1-1-2014

# Dielectric Elastomer Composites: Macroscopic Behavior and Instabilities

Morteza Hakimi Siboni
*University of Pennsylvania*, hakimi1364@gmail.com

# Dielectric Elastomer Composites: Macroscopic Behavior and Instabilities

**Abstract**
Dielectric Elastomers (DEs) are an interesting class of active materials that can exhibit coupled electrical and mechanical behaviors, for example they can respond to an external electric field by changing their shape or size. This unique property is known as electrostriction, and makes such materials promising candidates for a wide range of practical applications, and therefore there is a need for the design of DEs with enhanced electromechanical couplings. In this work we investigate the possibility of enhancing the electrostriction by making composites consisting of one or more family of filler phases in a soft dielectric host.

We use homogenization techniques to obtain estimates for the effective response of such DECs under general electrical and mechanical loading conditions. Next, we use the homogenization estimates developed in this work to investigate the effect of various microstructural parameters on the overall response of DECs. We also study failure of DECs as characterized by dielectric breakdown and/or the onset of material instabilities. Two types of material instabilities will be considered: Loss of Positive Definiteness (LPD) and Loss of Ellipticity (LE). Finally, we attempt an optimal design for the microstructure of DECs with enhanced electromechanical couplings, which are capable of achieving large electrostrictive strains before the failure. Our results show that composites consisting of a very small concentration of rigid circular fibers with vanishing contrast in the dielectric properties can achieve the largest electrostrictive strains before failure.

Finally, we attempt to study DECs in the post-bifurcated deformation regime. This is important since after the composite loses strong ellipticity, the solution of the homogenization problem may bifurcate into a lower energy (with generally softer mechanical response) solution, which is different from the pre-bifurcated solutions. This raises the interesting possibility of operating DECs in their softer post-bifurcated deformation regimes to further increase the maximum achievable electrostrictive strains.

**Degree Type**
Dissertation

**Degree Name**
Doctor of Philosophy (PhD)

**Graduate Group**
Mechanical Engineering & Applied Mechanics

**First Advisor**
Pedro Ponte Castañeda

**Keywords**
Bifurcation, Composites, Dielectric Elastomers, Homogenization Theory

**Subject Categories**
Engineering Mechanics | Mechanical Engineering

# DIELECTRIC ELASTOMER COMPOSITES: MACROSCOPIC BEHAVIOR AND INSTABILITIES

Morteza Hakimi Siboni

A DISSERTATION

in

Mechanical Engineering and Applied Mechanics

Presented to the Faculties of the University of Pennsylvania

in

Partial Fulfillment of the Requirements for the

Degree of Doctor of Philosophy

2014

Supervisor of Dissertation:

---

Pedro Ponte Castañeda, Professor
Department of Mechanical Engineering and Applied Mechanics

Graduate Group Chairperson:

---

Prashant K. Purohit, Associate Professor
Department of Mechanical Engineering and Applied Mechanics

Dissertation Committee:
John L. Bassani, Professor
Department of Mechanical Engineering and Applied Mechanics

Prashant K. Purohit, Associate Professor
Department of Mechanical Engineering and Applied Mechanics

**DIELECTRIC ELASTOMER COMPOSITES:**
**MACROSCOPIC BEHAVIOR AND INSTABILITIES**

*To My Parents & My Wife, Farzaneh*

# Acknowledgments

The completion of my PhD would not have been possible without the support and guidance of the following people. It is to them that I owe my deepest gratitude.

My adviser, Pedro Ponte Castañeda, who I have had the privilege of working with as a PhD student over the past five years. His immense knowledge, and his professionalism have been instrumental in inspiring and encouraging me during these years. I am indebted to him for all the hours he spent discussing science with me, assisting with my research projects, commenting on my writing, training me as a scientist, and most importantly for being patient with me.

My thesis committee members John Bassani and Prashant Pruhit, my qualification exam committee member Howard Hu, and my former adviser George Biros, I am grateful to you for all the help and support at various points during my PhD.

My lab members and friends, Evan Galipeau, Reza Avazmohammadi, Michalis Agoras, Qiwei Shi, David Argudo, and Sheng Mao. I am very fortunate to have such great office-mates. Our discussions became intense most of the times but they were always enlightening and enjoyable.

Maryeileen Banford, the MEAM Graduate Group coordinator, a truly kind person who has been helping me since the moment I entered Penn.

Mary Westervelt, the director of the Technical Communication Program of SEAS. I have attended two of Mary's courses while I was at Penn. One at the very beginning

of my PhD and another one half-way through, and both of them have taught me so much about technical writing/speaking. I am grateful to Mary for that.

My family, for all the sacrifices they have made for me. I truly love them and I wouldn't have made it this far without them.

And last, but certainly not least, my best friend and my wife, Farzaneh, who I met at Penn. Her love and support during these past five years were endless. These years of graduate school have not been an easy ride for, but we both learned a lot from each other. Farzaneh, you are the best outcome of my PhD, too!

ABSTRACT

DIELECTRIC ELASTOMER COMPOSITES: MACROSCOPIC BEHAVIOR AND INSTABILITIES

Morteza Hakimi Siboni

Pedro Ponte Castañeda

Dielectric Elastomers (DEs) are an interesting class of active materials that can exhibit coupled electrical and mechanical behaviors, for example they can respond to an external electric field by changing their shape or size. This unique property is known as electrostriction, and makes such materials promising candidates for a wide range of practical applications, and therefore there is a need for the design of DEs with enhanced electromechanical couplings. In this work we investigate the possibility of enhancing the electrostriction by making composites consisting of one or more family of filler phases in a soft dielectric host.

We use homogenization techniques to obtain estimates for the effective response of such DECs under general electrical and mechanical loading conditions. Next, we use the homogenization estimates developed in this work to investigate the effect of various microstructural parameters on the overall response of DECs. We also study failure of DECs as characterized by dielectric breakdown and/or the onset of material instabilities. Two types of material instabilities will be considered: Loss of Positive Definiteness (LPD) and Loss of Ellipticity (LE). Finally, we attempt an optimal design for the microstructure of DECs with enhanced electromechanical couplings, which are capable of achieving large electrostrictive strains before the failure. Our results show that composites consisting of a very small concentration of rigid circular fibers with vanishing contrast in the dielectric properties can achieve the largest electrostrictive strains before failure.

Finally, we attempt to study DECs in the post-bifurcated deformation regime. This is important since after the composite loses strong ellipticity, the solution of the homogenization problem may bifurcate into a lower energy (with generally softer mechanical response) solution, which is different from the pre-bifurcated solutions. This raises the interesting possibility of operating DECs in their softer post-bifurcated deformation regimes to further increase the maximum achievable electrostrictive strains.

# Contents

# List of Tables

# List of Figures

# Chapter 1

# Introduction

Electrostriction consists in the deformation of matter in response to externally applied electric stimuli, and it was first observed by Röntgen back in 1880 (Bar-Cohen 2004). Electro-Active Polymers (EAPs) are an interesting class of materials exhibiting this unique property (Bar-Cohen 2004, Carpi et al. 2010, Brochu & Pei 2010), and a large body of research has been dedicated in recent years to the development of EAPs with superior electromechanical properties. Being the closest man-made material to biological muscles, EAPs are also referred to as artificial muscles (Pelrine et al. 1998, Bar-Cohen 2004, Brochu & Pei 2010, Carpi et al. 2010). EAPs are now widely used in different industrial applications as actuators and sensors (Bar-Cohen 2004, Carpi et al. 2010). Other application areas for EAPs include active vibration damping in the automotive industry (Sarban et al. 2009), energy conversion (Ren et al. 2007), haptic devices (Ozsecen et al. 2010), tunable optical devices (Aschwanden & Stemmer 2006) and many others.

EAPs can be categorized into two main groups depending on the activation mechanism: field-activated and ionic EAPs. The coupled electro-elastic behavior in field-activated EAPs is the result of electrostatic forces between opposite charges created inside the dielectric (or on its outer boundaries) in the presence of external electric fields. Maxwell-type stresses are simple examples for this type of interactions (Cheng & Zhang 2008, Bar-Cohen 2004). Figure 1.1 shows a simple actuator consisting of a field-activated EAP sample sandwiched between two electrodes. As can be seen in

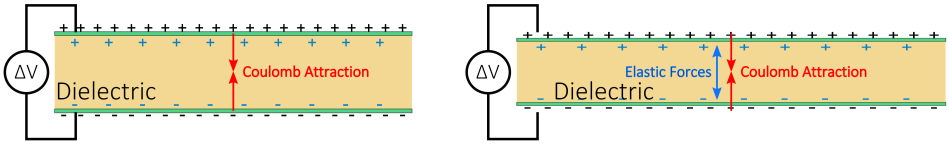


Figure 1.1: Schematics of a simple field-activated EAP deformed by Maxwell-like stresses. (left) Shows the accumulation of the free/bound charges on the electrodes and the development of Coulomb attraction between them, and (right) shows the deformed state in which the elastic forces counteract the Coulomb forces.

this figure, upon the application of an electric potential positive and negative charges accumulate on the electrodes. The Coulomb interactions among these charges cause the EAP to deform into a new state until the electrostatic forces are equilibrated with the elastic forces. On the other hand, the electromechanical coupling in ionic EAPs is the consequence of the diffusion of mobile ions (Park et al. 2008, Bar-Cohen 2004) in an external electric field. Figure 1.2 shows a simple actuator consisting of an ionic EAP sample. As shown in this figure, the distribution of Cations (positive

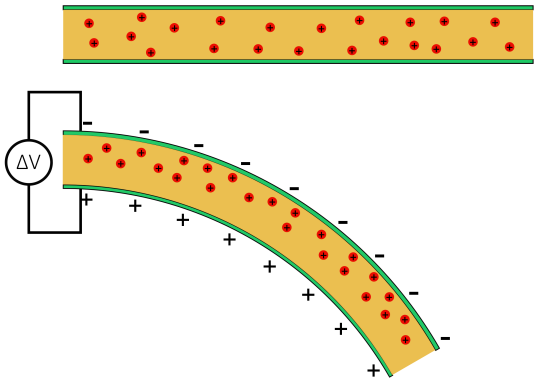


Figure 1.2: Schematics of a simple ionic EAP deformed in the presence of an electric field because of the redistribution of ions (Cations in this example). (top) Shows the EAP with a uniform distribution of ions, and (bottom) shows the EAP in the presence of the electric field in which the Cations are concentrated near the Anode.

ions) in the EAP sample is initially uniform. Upon the application of the electric field Cations in the sample move towards the Anode causing the density of positive charges to increase near the Anode and decrease near the Catode. As a result of this

the positive ions on one side of the sample experience larger repulsive forces compared to the other side, which in turn causes the sample to bend.

In this work we focus our attention to Dielectric Elastomers (DEs), which are an important class of field-activated EAPs with huge potential applications (Cheng & Zhang 2008) in different industries. As shown in Fig. 1.3, a simple dielectric elastomer actuator can be made by sandwiching a thin layer of dielectric elastomer between two compliant electrodes. When stimulated by an external voltage, the dielectric

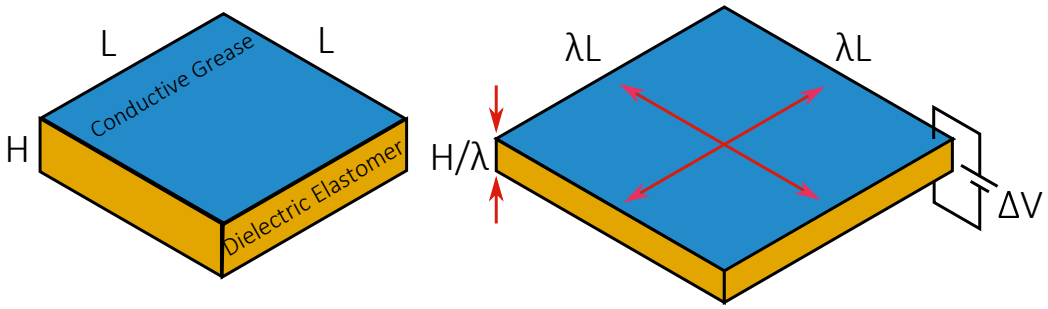


Figure 1.3: A simple dielectric actuator made out of the dielectric elastomer specimen sandwiched between two layers of conductive grease as the electrodes. (a) The actuator in the absence of electric fields, and (b) the actuator after the application of the electric fields.

elastomer contracts along the thickness while expanding its area (Bar-Cohen 2004, Carpi et al. 2010, Brochu & Pei 2010). Actuators that are capable of producing large electrostrictive strains are highly desirable for practical applications (Pelrine et al. 1998, Bar-Cohen 2004). The electrostrictive strains that have been reported for elastomers are usually fairly modest (in the order of 10% or less) (Sundar & Newnham 1992, Zhenyi et al. 1994, Carpi et al. 2008), while the operating electric fields are very large (in the order of $10^7$V/m). Furthermore, the performance of dielectric actuators operating at high voltages is severely restricted by dielectric breakdown, or an electromechanical (pull-in) instability followed by the dielectric breakdown (Stark & Garton 1955, Zhao & Suo 2008, Brochu & Pei 2010).

To remedy these limitations on the performance of DEs, different approaches have been proposed in the literature. Recently, the effect of the pre-stretch (Carpi et al. 2008) on the response and failure of thin ideal dielectrics, has been investi-

gated (Huang, Li, Foo, Zhu, Clarke & Suo 2012, Lu et al. 2012). This approach often involves stretching the dielectric elastomer by means of external (dead) loads in specific directions before applying the electric potential. However, the prescription of the dead load tractions often involves additional structural components, which may not be feasible in applications (e.g., see Fig. 1.4 for the experimental setup of Huang, Li, Foo, Zhu, Clarke & Suo (2012)).

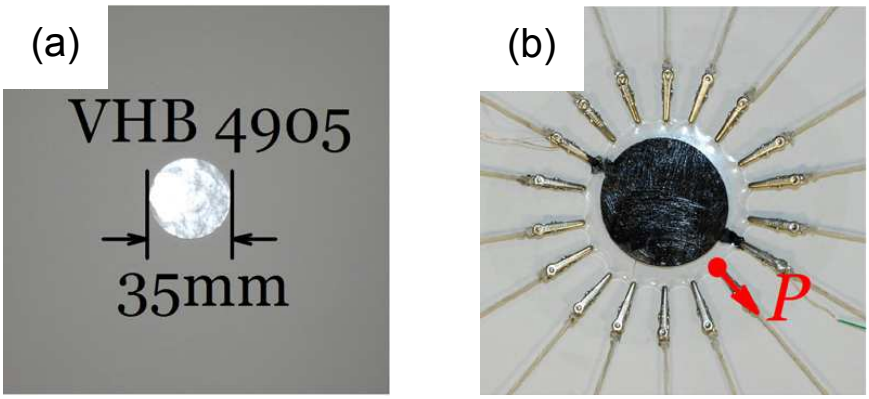


Figure 1.4: The experimental sample used in the work of Huang, Li, Foo, Zhu, Clarke & Suo (2012) for the experiments studying the effect of pre-stretch. (a) The specimen before the application of the dead load, and (b) the specimen after the application of the dead load. Note that the dead load is applied to the sample by means of the crocodile connectors and fixed-mass weights. The pictures in this figure are from the paper by Huang, Li, Foo, Zhu, Clarke & Suo (2012).

Another approach to improve the performance of dielectric actuators is to add one or more filler phases, which may have different elastic and electric properties, to a soft elastomeric host in order to make composites, known as Dielectric Elastomer Composites (DECs). As shown in schematic 1.5, the filler materials with different electric properties develops electric polarization in the presence of external electric fields. The polarized inhomogeneities then experience electrostatic forces, due to the dipole interactions among them (Shkel & Klingenberg 1998), and/or torques, due to the interactions with the external electric field (Landau et al. 1984, Siboni & Ponte Castañeda 2013). Theses forces/torques can then be translated into (potentially large) macroscopic deformations in the composite material, provided that the elastomeric host is chosen to be soft enough. The potential of this approach has been demonstrated recently in a series of experimental works. Thus, for example,

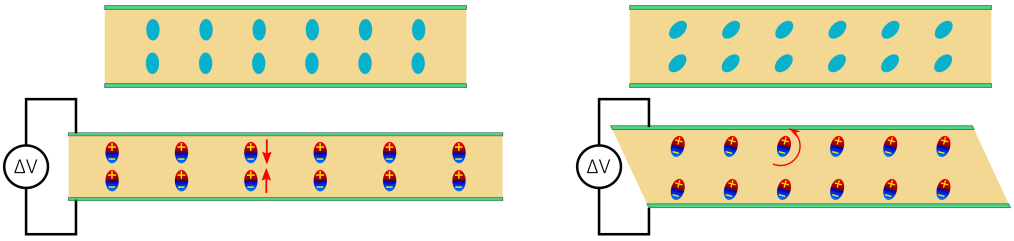


Figure 1.5: Schematics showing the dipolar interactions in DECs. (left) Shows the dipolar forces among the polarized inhomogeneities, causing the sample to undergo pure shear upon the application of the electric field, and (right) shows the dipolar torques experienced by polarized inhomogeneities, causing the sample to undergo simple shear.

Huang & Zhang (2004) have studied two-phase all-polymer composites consisting of poly(vinylidene fluoride-trifluoroethylene-chlorofluoro-ethylen) (or P(VDF-TrFE-CTFE), for short) as the matrix phase and polyanilie (or PANI, for short) conducting polymeric particles as the inclusion phase. They have been able to demonstrate significant improvements for electrostrictive strains of the composite near the percolation limit for the concentration of PANI particles (also see Huang et al. 2004, for a similar study for all organic three-component composites).

On the theoretical side, micromechanical approaches have been used to investigate the effective electro-active properties of DECs with various microstructures, making use of the classical small-strain formulation of electroelasticity (Landau et al. 1984). Thus, Shkel & Klingenberg (1998) have provided estimates for the deformation-dependent permittivity, as well as the electrostriction of isotropic dielectric solids. They used a mean-field approach to estimate the dipolar interactions at the microscopic level, and their analytical model for the effective deformation-dependent permittivity is in good agreement with their experiments (Shkel & Klingenberg 1998) for certain polymeric materials. On the other hand, Li & Rao (2004) and Rao & Li (2004) developed a micromechanical approach, which uses the "uniform field" concept of Benveniste & Dvorak (1992) to provide estimates for the effective electrostrictive coefficients of polymer-matrix composites with aligned and randomly oriented ellipsoidal inclusions. However, it was recognized (Li et al. 2004) that the effect of the field

fluctuations in the matrix phase, ignored in these works, could be important. More recently, Tian et al. (2012) have developed a rigorous method to compute the effective electro-elastic properties of composites in terms of coupled moments of the electrostatic and elastic fields in the composite. They also provided results for sequentially laminated composites, where such coupled moments could be computed explicitly. In the context of finite deformations, the state of the art for DECs is less advanced. Making use of the classical formulations of finite-strain electroelasticity (Toupin 1956), deBotton et al. (2007), Bertoldi & Gei (2011) and Rudykh & deBotton (2011) have obtained analytical estimates for the effective response and stability of DECs with layered microstructures at finite strains. More recently, Lu et al. (2012) have investigated soft dielectrics stiffened by long fibers. In their model, the effect of the fibers on the overall properties of the compound material is neglected and the fibers are assumed to constrain the deformation of the elastomeric matrix in the direction of the fibers in such a way that the sample is only allowed to undergo (2D) plane-strain deformations. Their experimental investigation of the problem demonstrates significant improvements for the maximum achievable electrostrictive strain before dielectric breakdown, consistent with earlier findings of Bolzmacher et al. (2006). The recent work of Lu et al. (2012) suggests that constraining the kinematics of an ideal dielectric into 2D plane-strain deformations eliminates the possibility of electromechanical instabilities typically observed in dielectrics subjected to equal biaxial loadings under general 3D conditions (Lu et al. 2012), hence enabling them to undergo larger stretches before dielectric breakdown.

The first objective of this work is to develop homogenization frameworks for the effective response of DECs with general particulate microstructures. Thus, in the context of infinitesimal deformations we propose a homogenization framework, which is capable of incorporating the effect of electric torques and particle rotations, in addition to dipolar interactions (Siboni & Ponte Castañeda 2013). It is remarked that unlike dipolar interactions which have no effect in the dilute limit for the concentration, we expect the electrostatic torques to have non-trivial effects even at dilute particle concentrations. We also demonstrated that the effective electrostrictive stress

for a DEC undergoing infinitesimal strains can be directly related to the first derivative of the effective deformation-dependent permittivity of the composite with respect to the macroscopic strain, which is consistent with the small-strain theory of Landau et al. (1984). In the context of finite deformations, we propose a homogenization theory for particulate DECs with random or periodic microstructures, also accounting for particle rotations due to the dipolar forces and torques (Ponte Castañeda & Siboni 2012).

Motivated by the findings of Lu et al. (2012), the second objective of this work is to apply the general homogenization theory for particulate DECs to fiber-constrained DECs. In particular we consider soft DEs stiffened by very hard (or rigid), aligned fibers in order to enforce 2D plane-strain conditions. However, unlike the recent work of Lu et al. (2012), where the fibers only act as structural elements to enforce the 2D plane-strain conditions, we take into account the effect of the fibers—through the disturbances in the local fields caused by them—on the overall electromechanical response of DECs. Thus, estimates will be obtained for the effective response of fibrous DECs undergoing finite deformations.

The third objective of this work is to investigate the possible development of electro-mechanical instabilities in DECs. The focus is on "material" instabilities that are intrinsic to the DECs, as characterized by their "macroscopic" or homogenized constitutive properties, and which involve macroscopically uniform fields. Thus, "structural" instabilities that are dependent on the geometry of the specimen, such as buckling, barreling, or wrinkling, will not be considered here. In particular, we will study loss of (incremental) positive definiteness (LPD) and loss of strong ellipticity (LE) of the electroelastic energy density. In the purely mechanical context (i.e., in finite elasticity), uniqueness and stability are characterized by the positive definiteness of a certain "exclusion" incremental energy functional (Hill 1957, Ogden 1997). In particular, it is known that loss of positive definiteness (LPD) is a necessary and sufficient condition for bifurcation under all-around dead loads (Hill 1967, Ogden 1997). On the other hand, loss of strong ellipticity signals the possible development of localized shear bands under displacement boundary conditions (Hill

1962, Rice 1976). Hill & Hutchinson (1975) investigated the bifurcation behavior of a broad class of incompressible, orthotropic solids subjected to plane-strain tension loadings. In addition, Ogden (1985) investigated the bifurcation and stability of homogeneous deformations in the plane-strain deformation of incompressible, hyperelastic solids subjected to dead-load tractions, including a global analysis of the problem. The works of Hill & Hutchinson (1975) and Ogden (1985) demonstrate that, under all-round dead loading, a variety of instability modes can occur while the energy-density function of the material is still strongly elliptic. However, it is known that the presence of an electric field can affect the onset of such instabilities in homogeneous ideal dielectric elastomers, when subjected to dead-load tractions. In particular, Zhao & Suo (2007) showed that the application of an electric field alone can lead to (snapping) instabilities of the maximum-load type in homogeneous dielectrics undergoing 3D equal bi-axial deformations. They further demonstrated that, the application of an equal bi-axial traction loading to the ideal dielectric can delay (or even completely remove) such instabilities. A more complete formulation of the stability and uniqueness problem in electroelasticity, generalizing the approach of Hill (1957) in finite elasticity and making use of the work of Dorfmann & Ogden (2010*b*), was initiated by Bertoldi & Gei (2011). Several authors have also begun to study instabilities in heterogeneous active materials. Building on earlier work for the purely mechanical problem (Geymonat et al. 1993), Bertoldi & Gei (2011) investigated loss of positive definiteness, as well as loss of strong ellipticity for DECs with layered microstructures, while Rudykh & deBotton (2011) studied the loss of strong ellipticity for such composites. In our work, we investigate the instabilites in fibrous DECs as characterized by the loss of positive definiteness and loss of strong ellipticity. We intend to complement the earlier works on the topic by providing a hopefully more complete discussion of the nature of the bifurcation modes for loading paths consisting of dead mechanical tractions in the presence of electric fields. To have a full picture for the response of fibrous DECs before failure, we also investigate the effect of dielectric breakdown on the overall performance of such composites.

The final objective of this work, is to obtain estimates for post-bifurcated response

of DECs and explore the possibilities therein. In particular, we would like to know whether it would be possible to operate DEC samples in their post-bifurcated–and often softer–deformation regime, and therefore achieve large electrostrictive strains by small changes in the electric fields.

The rest of this dissertation is divided into two parts: theory and applications. In the theory part of the dissertation we provide the necessary background materials on electreo-elasticity and homogenization. In the applications part we apply the general homogenization theory to sample application problems and report/discuss our findings. More details about the content of different chapters in each part are provided next.

In Chapter 2 we provide the background material on electroelasticity. In particular, we provide a thermodynamically consistent formulation for the governing and constitutive equations of electro-active materials in the absence of magnetic fields and motion. Both Lagrangian and Eulerian forms of the formulation will be provided for completeness. We also provide the incremental governing equations for EA materials in both Eulerian and push-forward forms, which are necessary for the stability analysis of such materials. Finally, we discuss material instabilities and dielectric breakdown (in the macroscopic sense) in EA materials with a given potential, which will later be applied to the effective potential of the DECs to study the onset of instabilities or failure in DECs.

Chapter 3 is concerned with the homogenization theory for electro-active composites. We start this chapter by providing a general variational formulation for the constitutive response of DECs, generalizing Hill's energy approach (Hill 1967) in the purely mechanical context. We then apply the general theory to a certain class of composites, namely two-phase composites with particulate microstructures. More specifically, we consider two-phase composites with periodic or random microstructures. For both periodic and random two-phase composites we first describe the initial microstructure of the composite and its evolution under general electro-mechanical loading conditions. Then, we introduce a partial decoupling strategy (generalizing the partial decoupling approximation of Ponte Castañeda & Galipeau (2011)), in order to

obtain the effective total energy of the DECs, with known microstructures and phase properties. In our decoupling strategy the total effective energy is the sum of the purely mechanical and purely electrostatic effective energies of the composite, which are linked together via some additional microstructural parameters. These additional microstructural parameters are then obtained by using an outer minimization. This decoupling strategy enables us to use available estimates for the purely mechanical effective energy of the composites along with Hashin-Shtrikman type estimates for the effecitve electrostatic energy, in order to obtain the effective total energy of the composite.

Chapter 4 provides a general framework for obtaining the effective response of DECs in the limit of infinitesimal deformations. More specifically, we show that the macroscopic total stress of a DEC can be obtained in terms of its deformation-dependent effective permittivity, consistent with earlier theoretical results (Landau et al. 1984, Shkel & Klingenberg 1998). We provide a simple, yet powerful tool which can be applied to DECs with generally different microstructures (i.e., laminated, fiber-reinforced, or particulate composites). In particular, in this chapter we focus our attention to DECs with particulate microstructures. Thus, we consider two-phase DECs consisting of aligned rigid inclusions distributed randomly in an "ideal dielectric" linear-elastic matrix (Zhao & Suo 2008). The inclusions are further assumed to have ellipsoidal shape and linear anisotropic dielectric behavior, and to be distributed with "ellipsoidal symmetry" (Ponte Castañeda & Willis 1995). Using the general framework developed in this work, we then provide estimates for the effective coupled electro-mechanical response of the above-described class of DECs, in the limit of infinitesimal deformations. We also provide some sample application problems to illustrate the theory developed in this chapter, and to investigate the effect of various microstructural parameters on the overall electro-active response of DECs.

In chapter 5, we will obtain homogenization estimates for the effective (macroscopic) response of fiber-constrained DECs undergoing finite deformations. More specifically, we consider DECs consisting of one family of aligned rigid fibers which are distributed with "elliptical symmetry" (Ponte Castañeda & Willis 1995) in an

ideal dielectric matrix. We then use available estimates (e.g., Lopez-Pamies & Ponte Castañeda 2006*a*) for the purely mechanical response of such composites at finite strains, along with a partial decoupling strategy/approximation (Ponte Castañeda & Siboni 2012) to estimate the effective electro-active response of such DECs. Having obtained an estimate for the effective response of the fiber-reinforced DECs, we then investigate the effect of different microstructural parameters on the response and possible failure of such composites, including susceptibility to electromechanical instabilities (through loss of positive definiteness), localization instabilities (through loss of ellipticity), and dielectric breakdown. The framework developed in this chapter also makes possible the development of a procedure for the optimal design of DECs capable of achieving large electrostrictive strains before failure. We also provide an example application to illustrate the theory developed in this chapter, and to investigate the effect of various microstructural parameters on the overall response and stability of fiber-constrained DECs.

In chapter 6, we further investigate the possible development of electro-mechanical instabilities in fiber-constrained DECs of the class described in chapter 5. The focus is on "material" instabilities that are intrinsic to the DECs, as characterized by their "macroscopic" or homogenized constitutive properties, and which involve macroscopically uniform fields. Thus, "structural" instabilities that are dependent on the geometry of the specimen, such as buckling, barreling, or wrinkling, will not be considered. In particular, we will study loss of (incremental) positive definiteness (LPD) and loss of strong ellipticity (LE) of the electroelastic energy density. This chapter is intended to complement the earlier works on the stability of DECs (deBotton et al. 2007, Bertoldi & Gei 2011, Rudykh & deBotton 2011) by providing a hopefully more complete discussion of the nature of the bifurcation modes for loading paths consisting of dead mechanical tractions in the presence of electric fields.

in chapter 7 we provide an explicit expression for the purely mechanical effective energy of fiber-constrained composites with prescribed in-plane rotations for the rigid fibers. This will be done by introducing a new variational problem in which the effects of external body couples are accounted for by means of uniform eigen-stress

fields for the fiber phase. Estimates for the new variational problem will be readily obtained using the "second-order" homogenization framework of Lopez-Pamies & Ponte Castañeda (2006*b*).

Chapter 8 is concerned with the effective response of DECs under non-aligned loading conditions. In particular in this chapter we make use of the partial decoupling strategy (PDS), introduced in earlier chapters, in order to study the response of DECs under general non-aligned loading conditions. Furthermore, we compare the response of DECs as obtained by the partial decoupling strategy with the corresponding results obtained by the partial decoupling approximation, to check the range of validity of such approximations. Finally, using the newly obtained PDS energies we obtain instability regions (regions corresponding to the loss of positive definiteness and the loss of ellipticity) for aligned DECs under aligned loadings and compare them with the corresponding results provided in chapter 5 and 6.

Finally, in chapter 9 we conclude this dissertation by providing a summary of what has been done in each chapter and our findings.

Unless otherwise mentioned, the following notations are used throughout this document for convenience. Scalars are denoted by italic Roman, $a$, or Greek letters, $\alpha$; vectors by boldface Roman letters, $\mathbf{b}$; second-order tensors by boldface italic Roman letters, $\boldsymbol{C}$, or boldface Greek letters, $\boldsymbol{\sigma}$; and fourth-order tensors by bared letters, $\mathbb{P}$. Where necessary, conventional index notation is adopted e.g., $b_i$, $C_{ij}$ and $P_{ijkl}$ are the Cartesian components of the vector $\mathbf{b}$, second order-tensor $\boldsymbol{C}$ and fourth-order tensor $\mathbb{P}$, respectively.

# Part I: Theory

# Chapter 2

# Background Materials on Electroelasticity

As their name suggests electro-active materials are defined as materials exhibiting coupled electrical and mechanical behaviors. Characterizing the constitutive behavior of electro-active materials requires a model for the interaction of the electric fields and matter. Modeling the response of deformable bodies to electric fields (or in general, to electromagnetic fields) has been a challenging scientific issue (e.g., see Maxwell 1873), and, as a consequence, different formulations have been proposed in the literature, which do not seem consistent at first glance. Despite the fact that there exist different formulations, it can be shown that under certain assumptions, all these formulations are equivalent (see, for example Hutter et al. 2006). We further emphasize that modeling the behavior of active materials at the continuum level requires a thermodynamically consistent constitutive description. The foundations for such a description were laid down by the pioneering work of (Toupin 1956), and since then a lot of progress has been made in the continuum description of electro-active materials. Modern developments on the topic include the works of Dorfmann & Ogden (2005), Mcmeeking & Landis (2005), Dorfmann & Ogden (2006), Suo et al. (2008). In this chapter, we present a brief summary of the governing/constitutive equations that are required for the purposes of this work. The rest of this chapter is organized as follows. In section 2.1 we provide the governing equations of electro-

elasto-statics in the absence of magnetic fields and current densities. In section 2.2 we provide a general form for the constitutive equations of a EA materials in terms of an energy density function (or potential). Section 2.3 is concerned with incremental governing equations of electroelasticity in both Lagrangian and push-forward forms. Finally, in section 2.4, we investigate the failure mechanisms in EA materials. In particular, we consider material instabilities (i.e., loss of positive definiteness and loss of strong ellipticity) as well as dielectric breakdown.

## 2.1 Governing equations

The response of a deformable electro-sensitive material can be described by the theory of electro-elasto-statics (e.g. Toupin 1956, Eringen & Maugin 1990, Kovetz 2000). Consider a homogeneous electro-elastic material occupying, in the absence of electric fields and mechanical loadings, a volume $\Omega_0$ in the reference configuration. Under the application of electric fields and mechanical loadings, a material point $\mathbf{X}$ in the reference configuration moves to a new $\mathbf{x}$ in the deformed configuration of the specimen, denoted by $\Omega$. For simplicity we exclude the possibility of gaps and/or interpenetration regions in the material throughout this chapter. This assumptions can be enforced by taking the map $\mathbf{x}(\mathbf{X})$, which takes the material forms from the reference configuration to the deformed one, to be continuous and one-to-one. Then, the deformation gradient tensor $\boldsymbol{F} = \operatorname{Grad}\mathbf{x}$ (with Cartesian components $F_{ij} = \partial x_i/\partial X_j$) characterizes the deformation of the material, and it is such that $J = \det\boldsymbol{F} > 0$. Finally, the material satisfies the conservation of mass equation, such that the material density in the deformed configuration becomes (in local form) $\rho = \rho_0/\det\boldsymbol{F}$, where $\rho_0$ denotes the material density in the reference configuration.

The equilibrium equations in Eulerian and Lagrangian forms are given by

$$\operatorname{div}\boldsymbol{T} + \rho\mathbf{f} = \mathbf{0}, \quad \text{and} \quad \operatorname{Div}\boldsymbol{S} + \rho_0\mathbf{f}_0 = 0, \tag{2.1}$$

respectively, with div and Div being the divergence operators in the deformed (i.e.,

with respect to $\mathbf{x}$) and reference (i.e., with respect to $\mathbf{X}$) configurations. In expressions (2.1), $\boldsymbol{T}$ is the *total* Cauchy stress tensor, $\boldsymbol{S} = J\boldsymbol{T}\boldsymbol{F}^{-T}$ is the (*first*) Piola-Kirchhoff stress tensor, and $\mathbf{f}$ and $\mathbf{f}_0$ are the given *mechanical* body force distributions in the deformed and reference configurations, respectively. The conservation of angular momentum requires symmetry of the Cauchy stress, i.e.,

$$\boldsymbol{T} = \boldsymbol{T}^T, \quad \text{or equivalently} \quad \boldsymbol{S}\boldsymbol{F}^T = \boldsymbol{F}\boldsymbol{S}^T. \tag{2.2}$$

The deformation gradient $\boldsymbol{F}$ and stress tensor $\boldsymbol{S}$ (or $\boldsymbol{T}$) may be discontinuous across material interfaces, but satisfy the jump conditions

$$[\![\boldsymbol{F}]\!] = \mathbf{a} \otimes \mathbf{N}, \quad \text{and} \qquad [\![\boldsymbol{S}]\!]\,\mathbf{N} = \mathbf{0} \ \left(\text{or } [\![\boldsymbol{T}]\!]\,\mathbf{n} = \mathbf{0}\right), \tag{2.3}$$

where $\mathbf{a}$ is a vector which can be determined from the solution of the problem, and $\mathbf{N}$ (or $\mathbf{n}$) is the normal to the interface in the reference (deformed) configuration.

It is important to emphasize that unlike the mechanical body forces (couples), which are externally prescribed, the electric body forces (couples) are manifestations of the electric fields that develop in the material, and therefore, need to be determined from the solution of the coupled electro-elastic problem. Therefore, for the purposes of the present investigation, we include the effects of electric body forces (couples) in the total stress. For this reason, the stresses $\boldsymbol{T}$ and $\boldsymbol{S}$ defined above, also include the electric effects, as it becomes clearer later on when we introduce the constitutive relations. Different formulations in which all or part of the electric contributions are described in terms of a body force or body couple in the above equilibrium equations are also available in the literature (Hutter et al. 2006), but such formulations are not considered here.

The true (or Eulerian) electric field $\mathbf{e}$ and electric displacement field $\mathbf{d}$ must satisfy Maxwell's equations, which, for quasi-static conditions, and in the absence of magnetic effects, are given by

$$\operatorname{curl}\mathbf{e} = \mathbf{0}, \quad \text{and} \quad \operatorname{div}\mathbf{d} = q, \tag{2.4}$$

where $q$ is the prescribed charge density (per unit volume in $\Omega$), and curl and div are the usual differential operators (with respect to $\mathbf{x}$). The Lagrangian form of the above equations is given by (Dorfmann & Ogden 2005)

$$\operatorname{Curl}\mathbf{E} = \mathbf{0}, \quad \text{and} \quad \operatorname{Div}\mathbf{D} = Q, \tag{2.5}$$

where $\mathbf{E} = \boldsymbol{F}^T\mathbf{e}$, $\mathbf{D} = J\boldsymbol{F}^{-1}\mathbf{d}$ and $Q = Jq$ are the "pull-back" versions of the true electric field $\mathbf{e}$, electric displacement field $\mathbf{d}$ and charge density $q$. The jump conditions for the electric fields are

$$[\![\mathbf{E}]\!] \times \mathbf{N} = 0 \ \left(\text{or } [\![\mathbf{e}]\!] \times \mathbf{n} = 0\right), \quad \text{and} \quad [\![\mathbf{D}]\!] \cdot \mathbf{N} = \Sigma \ \left(\text{or } [\![\mathbf{d}]\!] \cdot \mathbf{n} = \sigma\right), \tag{2.6}$$

where $\Sigma$ (or $\sigma$) is the prescribed charge per unit area in the reference (deformed) configuration.

## 2.2 Constitutive equations

The constitutive behavior of a homogeneous electro-elastic material has been described in many different ways (see Kovetz 2000, Hutter et al. 2006). However, the form developed by Dorfmann & Ogden (2005) (see also Suo et al. 2008) is most convenient for our purposes here. Thus, we introduce an energy-density function, or a potential $W(\boldsymbol{F}, \mathbf{D})$, such that the first Piola-Kirchhoff stress and the Lagrangian electric field may be obtained by

$$\boldsymbol{S} = \frac{\partial W}{\partial \boldsymbol{F}}(\boldsymbol{F}, \mathbf{D}), \quad \text{and} \quad \mathbf{E} = \frac{\partial W}{\partial \mathbf{D}}(\boldsymbol{F}, \mathbf{D}). \tag{2.7}$$

The energy function $W$ satisfies objectivity such that $W(\boldsymbol{Q}\boldsymbol{F}, \mathbf{D}) = W(\boldsymbol{F}, \mathbf{D})$, for all proper orthogonal tensors $\boldsymbol{Q}$, which implies that $W(\boldsymbol{F}, \mathbf{D}) = W(\boldsymbol{U}, \mathbf{D})$, with $\boldsymbol{F} = \boldsymbol{R}\boldsymbol{U}$ being the polar decomposition of $\boldsymbol{F}$.

It is also useful to introduce the Eulerian energy-density function $w(\boldsymbol{F}, \mathbf{d}) =$

$W(\boldsymbol{F}, \mathbf{D} = J\boldsymbol{F}^{-1}\mathbf{d})/J$, such that

$$W(\boldsymbol{F}, \mathbf{D}) = Jw(\boldsymbol{F}, \mathbf{d}). \tag{2.8}$$

It can then be shown that the Cauchy stress $\boldsymbol{T}$ and the true electric field $\mathbf{e}$ are given by

$$\boldsymbol{T} = \frac{\partial w}{\partial \boldsymbol{F}}\boldsymbol{F}^T + (w - \mathbf{e}\cdot\mathbf{d})\,\boldsymbol{I} + \mathbf{e}\otimes\mathbf{d}, \quad \text{and} \quad \mathbf{e} = \frac{\partial w}{\partial \mathbf{d}}(\boldsymbol{F}, \mathbf{d}). \tag{2.9}$$

Objectivity in this context implies that $w(\boldsymbol{Q}\boldsymbol{F}, \boldsymbol{Q}\mathbf{d}) = w(\boldsymbol{F}, \mathbf{d})$, for all proper orthogonal tensors $\boldsymbol{Q}$, or that $w(\boldsymbol{F}, \mathbf{d}) = u(\boldsymbol{F}^T\boldsymbol{F}, \boldsymbol{F}^T\mathbf{d})$, for some appropriately chosen function $u$. Using this it can be shown (see Kovetz 2000, for a similar calculation) that

$$\boldsymbol{T} = 2\boldsymbol{F}\frac{\partial u}{\partial \boldsymbol{F}^T\boldsymbol{F}}\boldsymbol{F}^T + (u - \mathbf{e}\cdot\mathbf{d})\,\boldsymbol{I} + 2\mathbf{e}\otimes_s\mathbf{d}, \tag{2.10}$$

where the symbol $\otimes_s$ is used to denote the symmetric dyadic product. Note that (2.10) makes it evident that the total Cauchy stress, as given by (2.9), is symmetric.

For materials with (internal) incompressiblity constraints (i.e. $C(\boldsymbol{F}) = \det\boldsymbol{F} - 1 = 0$) a hydrostatic pressure term is introduced in the expression for the Piola-Kirchhoff stress (Ogden 1997) while the expression for the Lagrangian electric field remains unchanged. Thus, for such materials equations (2.7) are updated as follows

$$\boldsymbol{S} = \frac{\partial W}{\partial \boldsymbol{F}}(\boldsymbol{F}, \mathbf{D}) - p\boldsymbol{F}^{-T}, \quad \text{and} \quad \mathbf{E} = \frac{\partial W}{\partial \mathbf{D}}(\boldsymbol{F}, \mathbf{D}). \tag{2.11}$$

The corresponding Eulerian equations (2.9), become

$$\boldsymbol{T} = \frac{\partial w}{\partial \boldsymbol{F}}\boldsymbol{F}^T - p\boldsymbol{I} + (w - \mathbf{e}\cdot\mathbf{d})\,\boldsymbol{I} + \mathbf{e}\otimes\mathbf{d}, \quad \text{and} \quad \mathbf{e} = \frac{\partial w}{\partial \mathbf{d}}(\boldsymbol{F}, \mathbf{d}), \tag{2.12}$$

where $w$ is defined as before with the replacement $J = 1$.

In this work we are mainly concerned with deriving macroscopic forms for the potentials of heterogeneous EA materials starting from the constitutive behavior of the phases. Hence, next we provide specific forms of the functions $W$ (or $w$) for the matrix and inclusion phases. In this work, it will be assumed that the matrix, labeled

with the superscript "1," is made of a dielectric elastomer, while the inclusions, labeled with the superscript "2," are made of much stiffer materials. The inclusions are assumed to be very stiff (rigid) compared to the soft elastomeric matrix. In fact, as it will become clearer later on, the inclusions are desired to have high dielectric coefficients for stronger electro-elastic couplings. However, naturally appearing materials (e.g., ceramics) with high dielectric coefficients also tend to be very stiff mechanically. As a consequence, and for simplicity, the inclusions will be assumed to be perfectly rigid in this work.

### 2.2.1 Dielectric elastomer matrix phase

For simplicity, the matrix phase is an "ideal dielectric elastomer" (Mcmeeking & Landis 2005, Zhao & Suo 2008) with a linear dielectric response described by the isotropic permittivity $\varepsilon^{(1)}$ that is taken to be independent of the deformation. Thus, the matrix material will be described here by an energy-density function (in the reference configuration) $W^{(1)}$ of the form

$$W^{(1)}\left(\boldsymbol{F},\mathbf{D}\right) = W^{(1)}_{me}\left(\boldsymbol{F}\right) + W^{(1)}_{el}\left(\boldsymbol{F},\mathbf{D}\right), \tag{2.13}$$

where $W^{(1)}_{me}\left(\boldsymbol{F}\right)$ is the usual (purely) mechanical stored-energy function of the elastomer and $W^{(1)}_{el}\left(\boldsymbol{F},\mathbf{D}\right)$ is the electrostatic part of the stored-energy function. For the purely mechanical stored energy we adopt the (incompressible) Gent (1996) model as specified by

$$W^{(1)}_{me}\left(\boldsymbol{F}\right) = -\frac{\mu^{(1)} J^{(1)}_m}{2} \ln\left(1 - \frac{I-d}{J^{(1)}_m}\right) \quad \text{with} \quad J = \det \boldsymbol{F} = 1,\ I = \operatorname{tr}\left(\boldsymbol{F}^T\boldsymbol{F}\right) \tag{2.14}$$

where $d$ specifies the dimension of the problem (i.e., $d = 2$ for 2D plain-strain problems and $d = 3$ for 3D problems), $\mu^{(1)}$ is the shear modulus of the elstomer and $J^{(1)}_m$, which specifies the limiting value for $I - d$, is the lock-up parameter. Note that the above purely mechanical energy density reduces to the (incompressible) Neo-Hookian model

as $J_m^{(1)} \to \infty$. The electrostatic stored energy of the ideal dielectrics can be written as

$$W_{el}^{(1)}(\boldsymbol{F}, \mathbf{D}) = \frac{1}{2\varepsilon^{(1)} J} (\boldsymbol{F}\mathbf{D}) \cdot (\boldsymbol{F}\mathbf{D}), \tag{2.15}$$

in the reference configuration. The Eulerian form of the above electrostatic energy function, as defined by $w_{el}^{(1)}(\mathbf{d}) = W_{el}^{(1)}(\boldsymbol{F}, J\boldsymbol{F}^{-1}\mathbf{d})/J$, is

$$w_{el}^{(1)}(\mathbf{d}) = \frac{1}{2\varepsilon^{(1)}} \mathbf{d} \cdot \mathbf{d}, \quad \text{and therefore} \quad \mathbf{e} = {\varepsilon^{(1)}}^{-1} \mathbf{d}. \tag{2.16}$$

which is consistent with the assumption that the dielectric response of the material is linear and independent of the deformation in the current configuration (i.e., $\varepsilon^{(1)}$ is a constant).

The total Cauchy stress, as defined by (2.9), for the above special form of the electro-active potential can be rewritten in the following more compact form

$$\boldsymbol{T} = \boldsymbol{T}^{me} + \boldsymbol{T}^{el}, \tag{2.17}$$

where

$$\boldsymbol{T}^{me} = \frac{\partial W_{me}^{(1)}}{\partial \boldsymbol{F}} \boldsymbol{F}^T - p\boldsymbol{I} \quad \text{and} \quad \boldsymbol{T}^{el} = \frac{1}{\varepsilon^{(1)}} \left[ \mathbf{d} \otimes \mathbf{d} - \frac{1}{2} (\mathbf{d} \cdot \mathbf{d}) \boldsymbol{I} \right] \tag{2.18}$$

are respectively the "purely mechanical" and "electrostatic" stresses in the material. Note that when the material is vacuum with permittivity $\varepsilon_0$, the electrostatic stress reduces to the Maxwell stress

$$\boldsymbol{T}^M = \varepsilon_0 \left[ \mathbf{e} \otimes \mathbf{e} - \frac{1}{2} (\mathbf{e} \cdot \mathbf{e}) \boldsymbol{I} \right]. \tag{2.19}$$

For this reason, the electrostatic stress $\boldsymbol{T}^{el}$ is sometimes referred to as the Maxwell stress in the material, and it is divergence free, just like the Maxwell stress $\boldsymbol{T}^M$. Finally, note that the decomposition provided in connection with expression (2.17) may not be generalized for all materials. For example, it will be shown later in this work that a composite made of a matrix material with constitutive behavior of the type (2.17) and rigid dielectric inclusions will *not* possess a constitutive response of

this form (and will, in fact, include additional terms coupling the deformation and electric fields in a non-trivial manner).

### 2.2.2 Rigid, polarizable particles

The behavior of the material in this case can be described by the energy function

$$W^{(2)}\left(\boldsymbol{F},\mathbf{D}\right)=W_{me}^{(2)}\left(\boldsymbol{F}\right)+W_{el}^{(2)}\left(\mathbf{D}\right). \tag{2.20}$$

The rigidity constraint is enforced by requiring $W_{me}^{(2)}$ to be zero when $\boldsymbol{F}$ is a pure rotation $\boldsymbol{R}^{(2)}$, and infinity otherwise. The electrostatic part of the energy for materials with linear dielectric behavior is taken to be of the standard form

$$W_{el}^{(2)}\left(\mathbf{D}\right)=\frac{1}{2}\mathbf{D}\cdot{\boldsymbol{\mathcal{E}}^{(2)}}^{-1}\mathbf{D}, \tag{2.21}$$

where $\boldsymbol{\mathcal{E}}^{(2)}$ is a constant, second-order tensor defining the anisotropic permittivity (or dielectric constant) of the material. Note that, because of objectivity, the tensor $\boldsymbol{\mathcal{E}}^{(2)}$ has to be independent of the deformation (or rotations for the special case of rigid particles), and is therefore a constant in the reference configuration. The corresponding energy function in the current configuration takes the form

$$w_{el}^{(2)}\left(\boldsymbol{R}^{(2)},\mathbf{d}\right)=\frac{1}{2}\mathbf{d}\cdot{\boldsymbol{\varepsilon}^{(2)}}^{-1}\mathbf{d} \tag{2.22}$$

where we have used objectivity, as well as the fact that for rigid materials $\boldsymbol{F}=\boldsymbol{R}^{(2)}$. In the above equation $\boldsymbol{\varepsilon}^{(2)}=\boldsymbol{R}^{(2)}\boldsymbol{\mathcal{E}}^{(2)}{\boldsymbol{R}^{(2)}}^{T}$ denotes the permittivity in the deformed configuration and depends on the rotation of the particle $\boldsymbol{R}^{(2)}$. Using (2.9), the Eulerian electric field $\mathbf{e}$ inside the rigid phase becomes

$$\mathbf{e}={\boldsymbol{\varepsilon}^{(2)}}^{-1}\mathbf{d}, \tag{2.23}$$

while the total stress becomes indeterminate. It is also important to mention that the second-order tensors $\boldsymbol{\mathcal{E}}^{(2)}$ and $\boldsymbol{\varepsilon}^{(2)}$ are positive definite, which is consistent with

the assumed convexity of the energy functions $W^{(2)}(\boldsymbol{F}, \mathbf{D})$ and $w^{(2)}(\boldsymbol{F}, \mathbf{d})$ in $\mathbf{D}$ and $\mathbf{d}$, respectively.

To obtain appropriate boundary conditions for the above-described electroelasticity problem one may use the jump conditions (2.3) and (2.6), taking into account the fact that neither the electric fields nor the stresses are zero outside the electro-elastic specimen, even if the specimen is surrounded by empty space (or vacuum). This is due to the fact that vacuum holds electric fields, and therefore also the (self-equilibrated) Maxwell stress, as pointed out by Dorfmann & Ogden (2005) and Bustamante et al. (2009).

## 2.3 Incremental formulation

In this section we provide the incremental governing equations of electroelasticity in both "Lagrangian" and "push-forward" forms. This is especially useful for the stability analysis of dielectric elastomers. The details for the development of such incremental equations can be found in the recent work of Dorfmann & Ogden (2010*a*). In the following, we only provide the necessary background information for the purposes of this chapter.

### 2.3.1 Lagrangian form

Given the static equilibrium state of the system as characterized by the deformation gradient $\boldsymbol{F}$ and (Lagrangian) electric displacement field $\mathbf{D}$, an (electromechanical) *increment* to this state can be obtained by superimposing a small (or incremental) displacement $\dot{\mathbf{x}}(\mathbf{X}, t)$ and a small (incremental) electric displacement field $\dot{\mathbf{D}}(\mathbf{X}, t)$ to the current state of the system. Note that here, the incremental quantities are marked by the overdot.

The incremental form of the governing equations $(2.1)_2$ and (2.5) can then be written as

$$\operatorname{Curl} \dot{\mathbf{E}} = 0, \quad \operatorname{Div} \dot{\mathbf{D}} = 0, \quad \text{and} \quad \operatorname{Div} \dot{\boldsymbol{S}} = \rho_0 \dot{\mathbf{x}}_{,tt}, \tag{2.24}$$

where $\dot{\mathbf{E}}$ and $\dot{\boldsymbol{S}}$ are the increments in $\mathbf{E}$ and $\boldsymbol{S}$ , respectively. Note that here we are assuming dead loads (i.e., constant body force and charges as the material deforms) such that $\dot{\mathbf{f}}_0 = 0$ and $\dot{Q} = 0$.

The incremental constitutive equations for unconstrained materials can be obtained by linearizing (2.7) with respect to the increments. Thus, we get

$$\dot{\boldsymbol{S}} = \mathbb{A}^0 \dot{\boldsymbol{F}} + \boldsymbol{\Gamma}^0 \dot{\mathbf{D}}, \quad \text{and} \quad \dot{\mathbf{E}} = \boldsymbol{\Gamma}^{0^T} \dot{\boldsymbol{F}} + \boldsymbol{M}^0 \dot{\mathbf{D}}, \tag{2.25}$$

where the fourth-order tensor $\mathbb{A}^0$ (the incremental (or tangent) elasticity at fixed $\mathbf{D}$), the third-order electromechanical coupling tensor $\boldsymbol{\Gamma}^0$, and the second-order tensor $\boldsymbol{M}^0$ (the inverse of the permittivity at fixed $\boldsymbol{F}$), are known as the incremental "electroelastic moduli" of electro-active materials. They are obtained from the second derivatives of the energy function via

$$A^0_{ijpq} := \frac{\partial^2 W}{\partial F_{ij} \partial F_{pq}}, \quad \Gamma^{0^T}_{pij} = \Gamma^0_{ijp} := \frac{\partial^2 W}{\partial F_{ij} \partial D_p}, \quad \text{and} \quad M^0_{ij} := \frac{\partial^2 W}{\partial D_i \partial D_j}, \tag{2.26}$$

and satisfy the following symmetries

$$A^0_{ijpq} = A^0_{pqij} \quad \text{and} \quad M^0_{ij} = M^0_{ji}. \tag{2.27}$$

Similarly, the incremental constitutive equations for materials with internal incompressiblity constraints can be obtained by linearizing (2.11) with respect to the increments. Thus, we get

$$\dot{\boldsymbol{S}} = \mathbb{A}^0 \dot{\boldsymbol{F}} + \boldsymbol{\Gamma}^0 \dot{\mathbf{D}} + p \boldsymbol{F}^{-T} \dot{\boldsymbol{F}}^T \boldsymbol{F}^{-T} - \dot{p} \boldsymbol{F}^{-T}, \quad \text{and} \quad \dot{\mathbf{E}} = \boldsymbol{\Gamma}^{0^T} \dot{\boldsymbol{F}} + \boldsymbol{M}^0 \dot{\mathbf{D}}, \tag{2.28}$$

where the moduli tensors are defined as before.

### 2.3.2 The "push-forward" form

One can also rewrite the above incremental equations in the deformed configuration via the "push-forward" versions of the increments

$$\dot{\boldsymbol{T}} := J^{-1}\dot{\boldsymbol{S}}\boldsymbol{F}^{T}, \quad \dot{\mathbf{d}} := J^{-1}\boldsymbol{F}\dot{\mathbf{D}}, \quad \text{and} \quad \dot{\mathbf{e}} := \boldsymbol{F}^{-T}\dot{\mathbf{E}}, \tag{2.29}$$

so that the incremental equilibrium equations in the deformed configuration become

$$\operatorname{curl}\dot{\mathbf{e}} = 0, \quad \operatorname{div}\dot{\mathbf{d}} = 0, \quad \text{and} \quad \operatorname{div}\dot{\boldsymbol{T}} = \rho\dot{\mathbf{u}}_{,tt}, \tag{2.30}$$

where $\mathbf{u}$ is the incremental displacement when written with respect to the deformed position $\mathbf{x}$, i.e.,

$$\mathbf{u} := \dot{\mathbf{x}}\left(\mathbf{X} = \mathbf{x}^{-1}(\mathbf{x}), t\right), \quad \text{and} \quad \mathbf{x}^{-1}() \text{ is the inverse of the map } \mathbf{x}(). \tag{2.31}$$

It is important to emphasize that equations (2.30) are definitions but not identities. Finally, the push-forward versions of the constitutive equations for unconstrained materials can be written as

$$\dot{\boldsymbol{T}} = \mathbb{A}\boldsymbol{H} + \boldsymbol{\Gamma}\dot{\mathbf{d}} \quad \text{and} \quad \dot{\mathbf{e}} = \boldsymbol{\Gamma}^{T}\boldsymbol{H} + \boldsymbol{M}\dot{\mathbf{d}}, \tag{2.32}$$

where $\boldsymbol{H} := \operatorname{grad}\mathbf{u} = \dot{\boldsymbol{F}}\boldsymbol{F}^{-1}$, and

$$A_{kmln} := J^{-1}F_{mi}F_{nj}A^{0}_{kilj}, \quad \Gamma_{ijt} := F_{ip}F^{-1}_{qt}\Gamma^{0}_{pjq}, \quad \text{and} \quad M_{kl} := JF^{-1}_{ik}F^{-1}_{jl}M^{0}_{ij}, \tag{2.33}$$

which satisfy the symmetry properties

$$A_{kmln} = A_{lnkm}, \quad \Gamma_{ijt} = \Gamma_{jit}, \quad \text{and} \quad M_{kl} = M_{lk}. \tag{2.34}$$

Likewise, the push-forward constitutive equations for incompressible materials can be written as

$$\dot{\boldsymbol{T}} = \mathbb{A}\boldsymbol{H} + \boldsymbol{\Gamma}\dot{\mathbf{d}} + p\boldsymbol{H}^{T} - \dot{p}\boldsymbol{I} \quad \text{and} \quad \dot{\mathbf{e}} = \boldsymbol{\Gamma}^{T}\boldsymbol{H} + \boldsymbol{M}\dot{\mathbf{d}}, \tag{2.35}$$

where the push-forward moduli are defined in (2.33).

## 2.4 Failure mechanisms in EA materials

To provide a complete picture for the analysis of (homogeneous or heterogeneous) electro-active materials, we need to address different failure mechanisms in such materials. This is especially important for the design of new materials with superior performance characteristics. In this work we consider three different failure mechanisms, namely *Loss of Positive Definiteness* (LPD) or loss of convexity, *Loss of strong Ellipticity* (LE) of the electroelastic energy, and *dielectric breakdown*. The first two can be recognized as "material" instabilities and they are best described in terms of incremental *electroelastic moduli tensors* of the EA material.

### 2.4.1 Material instabilities in dielectric elastomers

In this section we recall some results concerning the stability of dielectric elastomers (DEs) with given energy-density functions. Even though the stability prescriptions will be presented for homogeneous DEs, they can also be used for DECs, provided that a "macroscopic" energy-density function is available for such heterogeneous materials. In principle, instabilities could also take place at the "microscopic" level, but given the expected heterogeneity in the local fields inside the DECs, this possibility will not be considered in this work. Instead, we focus our attention only on intrinsic "material" instabilities, as defined by the homogenized or macroscopic constitutive relations for the DECs. Thus, geometry-dependent "structural" instabilities, such as buckling, barreling, or wrinkling, will not be considered here. In particular, two types of electromechanical instabilities will be considered: loss of positive definiteness (LPD), or loss of local convexity, and loss of strong ellipticity (LE). These instabilities are best described in terms of the electro-elastic incremental moduli, as defined in section 2.3, which also summarizes the incremental electroelasticity problem (Dorfmann & Ogden 2010*a*) for completeness.

*Loss of positive definiteness.* As already mentioned, a generalization of the exclu-

sion functional of Hill (1967) for electroelasticty was provided by Bertoldi & Gei (2011) (see also Zhao et al. 2007). Based on this criterion, Bertoldi & Gei (2011) argued that the critical bifurcation condition for all-around dead-load tractions/charges on the boundary reduces to loss of positive definiteness of the incremental electroelastic moduli, as defined by (2.26), thus providing a natural generalization of corresponding results for the purely elastic case (Hill 1967, Ogden 1997). More specifically, when the material is incompressible (as is the case in this work), for a given loading path (as determined by $p_s$, $\boldsymbol{F}_s$, $\mathbf{D}_s$, where $s$ is the loading parameter), the onset of the instability is determined when the "exclusion" condition

$$\mathcal{Q}^0 = \dot{\boldsymbol{F}} \cdot \mathbb{A}_s^0 \dot{\boldsymbol{F}} + p_s \mathrm{tr}\left[\left(\dot{\boldsymbol{F}}\boldsymbol{F}^{-1}\right)^2\right] + 2\dot{\boldsymbol{F}} \cdot \boldsymbol{\Gamma}_s^0 \dot{\mathbf{D}} + \dot{\mathbf{D}} \cdot \boldsymbol{M}_s^0 \dot{\mathbf{D}} > 0 \tag{2.36}$$

is first violated for at least one non-zero, critical pair $\left(\dot{\boldsymbol{F}}, \dot{\mathbf{D}}\right)$, where $\dot{\boldsymbol{F}}$ satisfies the incompressibility condition $\mathbf{tr}\left(\dot{\boldsymbol{F}}\boldsymbol{F}_s^{-1}\right) = 0$. In the above equation, the dotted quantities denote the increments, while $\mathbb{A}_s^0$, $\boldsymbol{\Gamma}_s^0$, and $\boldsymbol{M}_s^0$ are the electroelastic moduli defined in (2.26), evaluated at $\boldsymbol{F} = \boldsymbol{F}_s$ and $\mathbf{D} = \mathbf{D}_s$. The above quadratic form can also be written in push-forward form as

$$\mathcal{Q} = \mathcal{Q}^0/J = \boldsymbol{H} \cdot \mathbb{A}_s \boldsymbol{H} + 2\boldsymbol{H} \cdot \boldsymbol{\Gamma}_s \dot{\mathbf{d}} + \dot{\mathbf{d}} \cdot \boldsymbol{M}_s \dot{\mathbf{d}} + p_s \mathrm{tr}\left[\boldsymbol{H}^2\right], \tag{2.37}$$

where $\boldsymbol{H} \coloneqq \mathrm{grad}\mathbf{u} = \dot{\boldsymbol{F}}\boldsymbol{F}^{-1}$ denotes the gradient of the incremental displacement, defined in (2.31).

As pointed out by Hill (1967) in the purely mechanical context, the primary "eigenstates" associated with condition (2.36) can manifest themselves in essentially two ways. If the loading path is precisely orthogonal to the eigenmodal direction, a bifurcation is possible with or without exchange of stability. On the other hand, if the loading path is not of this special type, then a maximum, or limit load behavior is observed. In this work, we will refer to these two types of modes as "non-aligned" and "aligned," respectively. The second type of instability has been confirmed experimentally (Stark & Garton 1955, Lu et al. 2012), as well as theoretically (Zhao et al. 2007) for ideal dielectrics under 3D equal bi-axial loading conditions, where a maximum

is observed in the voltage. The existence of the maximum for the voltage is known to lead to the possibility of snapping behavior, followed by dielectric breakdown in voltage-controlled experiments (Zhao & Suo 2010). Loss of positive definiteness has also been studied for heterogeneous dielectrics with layered microstructures (Bertoldi & Gei 2011). Our goal in this work will be to consider, in some detail, the loss of positive definiteness of fibrous DECs subjected to bi-axial traction and prescribed charges on the surface (see chapter 6 for more details).

*Loss of strong ellipticity.* Generalizing earlier work for the purely mechanical case (Triantafyllidis & Maker 1985, Geymonat et al. 1993, Michel et al. 2010*a*), Bertoldi & Gei (2011) argued that loss of strong ellipticity of homogenized electro-elastic energy coincides with the onset of long-wavelength (or macroscopic) instabilities. Thus, in this work we will make use of loss of strong ellipticity to detect the possible development of localization instabilities in DECs. The loss of strong ellipticity in the context of electroelasticity is characterized by the loss of positive definiteness of the generalized electromechanical acoustic tensor (see Dorfmann & Ogden 2010*a*, for the definition). In particular, for incompressible electro-active materials, the generalized electromechanical acoustic tensor is given by

$$\hat{\boldsymbol{\gamma}}(\mathbf{n}) = \hat{\boldsymbol{Q}}(\mathbf{n}) - \hat{\boldsymbol{R}}(\mathbf{n})\,\hat{\boldsymbol{M}}^{-1}\hat{\boldsymbol{R}}^{T}(\mathbf{n}), \tag{2.38}$$

where the tensors $\hat{\boldsymbol{Q}}$, $\hat{\boldsymbol{R}}$ and $\hat{\boldsymbol{M}}$ are specific projections of the incremental moduli of the electro-active material onto the plane perpendicular to the unit vector $\mathbf{n}$. Specifically,

$$\begin{aligned}
&\hat{\boldsymbol{Q}}(\mathbf{n}) = \hat{\boldsymbol{I}}\boldsymbol{Q}(\mathbf{n})\,\hat{\boldsymbol{I}}, \quad \text{with} \quad Q_{ij}(\mathbf{n}) := A_{ipjq}n_p n_q \\
&\hat{\boldsymbol{R}}(\mathbf{n}) = \hat{\boldsymbol{I}}\boldsymbol{R}(\mathbf{n})\,\hat{\boldsymbol{I}}, \quad \text{with} \quad R_{ij}(\mathbf{n}) := \Gamma_{pij}n_p \\
&\hat{\boldsymbol{M}} = \hat{\boldsymbol{I}}\boldsymbol{M}\hat{\boldsymbol{I}},
\end{aligned} \tag{2.39}$$

where $\hat{\boldsymbol{I}} := \boldsymbol{I} - \mathbf{n}\otimes\mathbf{n}$ is the relevant projection operator. Thus, when the condition

$$\mathbf{m}\cdot\hat{\boldsymbol{\gamma}}(\mathbf{n})\,\mathbf{m} > 0, \tag{2.40}$$

ceases to hold (for any unit vector $\mathbf{m}$ satisfying the incompressibility condition $\mathbf{n}\cdot\mathbf{m} = 0$) for the first time, the material loses strong ellipticity. The vector $\mathbf{n}$ at which the tensor $\hat{\gamma}(\mathbf{n})$ loses positive definiteness, characterizes the normal to a localization plane (often referred to as the shear band). For composites with random microstructures, in the purely mechanical context, these instabilities are known to be the first to occur under prescribed displacement boundary conditions (Geymonat et al. 1993, Michel et al. 2010*a*). However, as we will see later on, they may also be the first to occur under dead load conditions for special types of loadings, since while loss of positive definiteness does not necessarily imply loss of ellipticity, the converse is always true and the two may happen simultaneously in some cases. In this connection, it is relevant to remark that in the purely mechanical context the loss of ellipticity condition may be obtained by checking the exclusion condition against rank-one (incremental) deformations of the form $\dot{\boldsymbol{F}} = f(\mathbf{X}\cdot\mathbf{B})\,\mathbf{a}\otimes\mathbf{B}$, where $f$ is an arbitrary function of its argument, and $\mathbf{a}$ and $\mathbf{B}$ are constant vectors (see Ogden 1997, for more details).

It is important to emphasize that, in this work, we will restrict our attention to loss of positive definiteness and loss of strong ellipticity in the *homogenized* response of the dielectric composite materials. (In principle, these conditions could also be applied locally at the level of the phases, but the "microscopic" fields inside the phases would be expected to be nonuniform, in which case the computation of the instability conditions would be much more difficult.) For this reason, the instabilities associated with the homogenized response are referred to as "macroscopic" instabilities, i.e., they are manifested in the material at length scales comparable to the size of the specimen. In addition, it is noted that the above conditions for LPD and LE can be further simplified for the purely mechanical case to obtain more explicit conditions for the onset of instabilities (see Appendix A for more details).

### 2.4.2 Dielectric breakdown

Dielectric breakdown corresponds to the instantaneous increase in the conductivity of dielectric insulators that happens when the magnitude of the electric field inside the dielectric reaches a critical value. Dielectric breakdown causes irreversible damages to

the EA material, and therefore must be avoided in applications. The safe operation of EA materials is ensured by requiring the maximum electric field in the material to be less than the breakdown field, denoted by $e_B$, i.e.

$$\max_{\text{sample}} |\mathbf{e}| < e_B. \tag{2.41}$$

This may be easily enforced for homogeneous EA samples where uniform fields can be assumed in most applications. For heterogeneous samples, however, one has to account for field magnifications due to the presence of heterogeneities. As it will be seen later on, the presence of heterogeneities can reduce the overall breakdown field of EA composites by a large factor.

## 2.5 Concluding remarks

In this chapter we have provided an overview for the governing equations of electroelasticity and constitutive response of homogeneous dielectric elastomers. The formulation used here for describing the governing equations is based on a total stress which includes both the mechanical and electrostatic surface forces. The constitutive response of dielectric elastomers were described via a potential energy which is assumed to be a function of the deformation gradient and the Lagrangian electric displacement field. We have also provided the incremental equations of electroelasticity along with conditions for predicting material instabilities and failure of electro-active materials.

# Chapter 3

# A Coupled Homogenization Framework

Effective medium theories have been used to model the behavior of DECs with various microstructures at both finite and infinitesimal deformations. For example, Shkel & Klingenberg (1998) have provided estimates for the deformation-dependent permittivity, as well as the electrostriction of isotropic dielectric solids. They used a mean-field approach to estimate the dipolar interactions at the microscopic level, and their analytical model for the effective deformation-dependent permittivity is in good agreement with their experiments (Shkel & Klingenberg 1998) for certain polymeric materials. Similarly, Li & Rao (2004) and Rao & Li (2004) have developed a micromechanical approach, which uses the "uniform field" concept of Benveniste & Dvorak (1992) to provide estimates for the effective electrostrictive coefficients of polymer-matrix composites with aligned and randomly oriented ellipsoidal inclusions. More recently, Tian et al. (2012) have developed a rigorous method to compute the effective electro-elastic properties of composites in terms of coupled moments of the electrostatic and elastic fields in the composite. They also provided results for sequentially laminated composites, where such coupled moments could be computed explicitly. In the context of finite deformations, the state of the art for DECs is less advanced. For example, deBotton et al. (2007), Bertoldi & Gei (2011) and Rudykh & deBotton (2011) have obtained analytical estimates for the effective response and stability of

DECs with layered microstructures at finite strains by making use of the classical formulations of finite-strain electroelasticity (Toupin 1956). In this chapter we provide a general homogenization theory for the coupled electro-elastic behavior of DECs. In particular, in section 3.1 we provide a variational formulation for the effective energy of DECs, generalizing the energy method of Hill (1972). In section 3.2 we consider two-phase DECs with random microstructures. More specifically, we describe the initial microstructure of the composite and its evolution. Then we introduce the partial decoupling strategy for obtaining the effective total electrostatic energy in terms of the effective purely mechanical energy and the effective (deformation-dependent) electrostatic energy. Finally, we provide Hashin-Schtricman type estimaes for the effective (deformation-dependent) permittivity of two-phase DECs with random microstructures , which may in turn be used along with availabe estimates for the purely mechanical energy to obtain the effect total energy of DECs. Section 3.3 provides the corresponding developments in the context of two-phase DECs with periodic microstructures.

## 3.1 The variational formulation

We consider a specimen $\Omega_0$ (in the reference configuration) made of the electro-active composite, which consists of $N$ homogeneous phases, occupying sub-domains $\Omega_0^{(r)}$ in $\Omega_0$. The distribution of the phases is described by the characteristic functions $\Theta_0^{(r)}$ $(r = 1, ..., N)$, such that $\Theta_0^{(r)}$ is equal to 1 for $\mathbf{X} \in \Omega_0^{(r)}$ and zero otherwise. Similarly, the specimen in its deformed configuration can be described by the characteristic functions $\Theta^{(r)}$ $(r = 1, ..., N)$, such that $\Theta^{(r)}(\mathbf{x}) = 1$ for $\mathbf{x} \in \Omega^{(r)}$ and zero otherwise, where $\Omega^{(r)}$ is the sub-domain of $\Omega$ (the deformed configuration of the specimen) that is occupied by phase $r$. Throughout this work, the electro-active composites are assumed to satisfy the *separation of length scales* hypothesis. In other words, it is assumed that the length scale at which the characteristic functions $\Theta_0^{(r)}$ vary (also referred to as the microscopic scale) is very small compared to the the size of the specimen $\Omega_0$ (or the macroscopic scale).

In this section, we develop a homogenization framework for the above-described electro-active composites with general microstructures in the quasi-static finite strain regimes. The basic idea is to generalize the heuristic approach of Hill (1972) in finite elasticity. Toward this goal, boundary conditions are prescribed that are consistent with "macroscopically uniform" fields in the composite. Here we enforce the conditions

$$\mathbf{x} = \bar{\boldsymbol{F}}\mathbf{X}, \quad \text{and} \quad \mathbf{D}\cdot\mathbf{N} = \bar{\mathbf{D}}\cdot\mathbf{N}, \quad \text{on} \quad \partial\Omega_0, \tag{3.1}$$

where $\bar{\boldsymbol{F}}$ and $\bar{\mathbf{D}}$ are a prescribed, constant tensor and vector, respectively, and $\mathbf{N}$ is the outward unit normal to the boundary of the composite specimen $\partial\Omega_0$. It then follows, by means of the divergence theorem, that the macroscopic averages (over $\Omega_0$) for the deformation gradient and electric displacement fields are given by

$$\langle \boldsymbol{F} \rangle_0 = \bar{\boldsymbol{F}}, \quad \text{and} \quad \langle \mathbf{D} \rangle_0 = \bar{\mathbf{D}}, \tag{3.2}$$

where $\langle\cdot\rangle_0$ has been used to denote a volume average in the reference configuration. This shows that $\bar{\boldsymbol{F}}$ and $\bar{\mathbf{D}}$ can be interpreted as the macroscopic, or average, deformation gradient and electric displacement field in the composite $\Omega_0$. Note that it is also possible to specify the electric field, or the traction on the boundary of the specimen. However, the boundary conditions (3.1) are preferred here since they lead to minimum-type variational formulations for the homogenization problem, because, as mentioned earlier, the associated potentials $W$ are convex in $\mathbf{D}$ and polyconvex in $\boldsymbol{F}$.

Given the boundary conditions (3.1) and the assumed separation of length scales, it is expected on physical grounds that the composite material will behave like the homogeneous medium with effective, or homogenized energy function $\tilde{W}$. Following the "energy" method of Hill (1972) for purely elastic composites, we define the homogenized potential for the electro-active composite as the volume average of the energy stored in the composite under application of the boundary conditions (3.1),

namely,

$$\tilde{W}\left(\bar{\boldsymbol{F}},\bar{\mathbf{D}}\right)=\min_{\boldsymbol{F}\in\mathcal{K}(\bar{\boldsymbol{F}})}\ \min_{\mathbf{D}\in\mathcal{D}_0(\bar{\mathbf{D}})}\langle W\left(\mathbf{X},\boldsymbol{F},\mathbf{D}\right)\rangle_0, \tag{3.3}$$

where $W\left(\mathbf{X},\boldsymbol{F},\mathbf{D}\right)$ is defined in terms of the uniform phase potentials $W^{(r)}\left(\boldsymbol{F},\mathbf{D}\right)$ via

$$W\left(\mathbf{X},\boldsymbol{F},\mathbf{D}\right)=\sum_{r=1}^{N}\Theta_0^{(r)}\left(\mathbf{X}\right)\ W^{(r)}\left(\boldsymbol{F},\mathbf{D}\right), \tag{3.4}$$

and where

$$\mathcal{K}\left(\bar{\boldsymbol{F}}\right)=\left\{\boldsymbol{F}\mid\exists\ \mathbf{x}=\mathbf{x}\left(\mathbf{X}\right)\ \text{with}\ \boldsymbol{F}=\operatorname{Grad}\mathbf{x}\ \text{in}\ \Omega_0,\ \mathbf{x}=\bar{\boldsymbol{F}}\mathbf{X}\ \text{on}\ \partial\Omega_0\right\}, \tag{3.5}$$

and

$$\mathcal{D}_0\left(\bar{\mathbf{D}}\right)=\left\{\mathbf{D}\mid\operatorname{Div}\mathbf{D}=\mathbf{0}\ \text{in}\ \Omega_0,\ \mathbf{D}\cdot\mathbf{N}=\bar{\mathbf{D}}\cdot\mathbf{N}\ \text{on}\ \partial\Omega_0\right\} \tag{3.6}$$

are, respectively, sets of admissible deformation gradients and electric displacement fields that are compatible with the boundary conditions (3.1).

It can be readily shown (see Bustamante et al. 2009) for a more general version of this variational principle including contributions from the surrounding vacuum) that the Euler-Lagrange equations associated with the variational problem (3.3) are precisely the equilibrium equation $(2.1)_2$ (with $\mathbf{f}_0=0$) and the Maxwell's equations (2.5). (Note that the energy contributions of the inhomogeneous terms, $\mathbf{f}_0$, $Q$, and $\Sigma$, are ignored since they have been assumed to vary on the macroscopic length scale, and have no effect on the homogenization problem.) Therefore, the minimizers (assuming that they exist) of the above problem are also solutions of the electro-elastic problem (described in the previous section) with boundary conditions (3.1). To the best of our knowledge, there exist no rigorous mathematical results for the existence of the minimizers for the above variational problem. However, as was recently argued by Ponte Castañeda & Galipeau (2011) for the analogous magneto-elasticity problem, it will be assumed here that the minimizers of the variational problem (3.3) exist at least for constitutive behaviors of the type discussed in chapter 2 for the ideal dielectric matrix and rigid particles.

For composites with periodic microstructures, or for random composite made out

of periodic repetitions of a representitive volume element (RVE), the general variational problem (3.3), can be equivalently written in terms of a periodic variational problem. Thus, let us denote the building block (or the elementary unit cell) of the composite by $\mathcal{U}_0$ in the reference configuration. For purely elastic composites in the finite-deformation regime, it is known (Braides 1985, Müller 1987) that the solution of the homogenization problem (3.3), although periodic, need not have the same period as the elementary unit cell $\mathcal{U}_0$. Thus, while it is expected that the minimum energy solution may be initially periodic on one cell, after a certain level of loading, the solution may develop microscopic (or pattern changing) instabilities and bifurcate into other solutions that may be periodic on a larger unit cell (or a super cell) $\mathbf{q}\mathcal{U}_0$ containing several elementary unit cells (see further below for more details). In such cases, the lowest value for the energy is obtained by "cooperative" interaction among several unit cells, after a certain level of loading. Therefore, the variational problem (3.3) for the effective energy of the electro-active composite with periodic microstructures under arbitrary loading conditions may be written in the form

$$\tilde{W}\left(\bar{\boldsymbol{F}}, \bar{\mathbf{D}}\right) = \min_{\mathbf{q}} \tilde{W}^{\mathbf{q}\mathcal{U}_0}\left(\bar{\boldsymbol{F}}, \bar{\mathbf{D}}\right), \quad \text{for} \quad \mathbf{q} = (q_1, q_2, q_3) \in \mathbb{N}^3, \tag{3.7}$$

where

$$\tilde{W}^{\mathbf{q}\mathcal{U}_0}\left(\bar{\boldsymbol{F}}, \bar{\mathbf{D}}\right) = \min_{\mathbf{u}' \in \mathbf{q}\mathcal{U}_0^{\#}} \min_{\mathbf{A}' \in \mathbf{q}\mathcal{U}_0^{\#}} \left\{ \frac{1}{|\mathbf{q}\mathcal{U}_0|} \int_{\mathbf{q}\mathcal{U}_0} W\left(\mathbf{X}; \bar{\boldsymbol{F}} + \nabla \mathbf{u}', \bar{\mathbf{D}} + \nabla \times \mathbf{A}'\right) d\mathbf{X} \right\} \tag{3.8}$$

is the effective energy associated with the super-cell $\mathbf{q}\mathcal{U}_0$. In this last expression, $\mathbf{u}'$ and $\mathbf{A}'$ are $\mathbf{q}\mathcal{U}_0$-periodic fluctuation functions, such that the deformation gradient and electric displacement trial fields are given by $\boldsymbol{F} = \bar{\boldsymbol{F}} + \operatorname{Grad} \mathbf{u}'$ and $\mathbf{D} = \bar{\mathbf{D}} + \operatorname{Curl} \mathbf{A}'$. Note that the minimizations over the sets of $\mathbf{q}\mathcal{U}_0$-periodic displacement and vector potential fluctuation fields (i.e., $\mathbf{u}'$ and $\mathbf{A}' \in \mathbf{q}\mathcal{U}_0^{\#}$) in expression (3.8) is equivalent to minimizations over the admissible sets (3.5) and (3.6) in expression (3.3).

Having defined the effective electro-elastic energy $\tilde{W}\left(\bar{\boldsymbol{F}}, \bar{\mathbf{D}}\right)$ of the composite, it can be shown by means of appropriate generalization of Hill's lemma (see, for

example, Castañeda & Suquet 1997) that the *average stress* and *average electric field*, determined by $\bar{\boldsymbol{S}} = \langle \boldsymbol{S} \rangle_0$ and $\bar{\mathbf{E}} = \langle \mathbf{E} \rangle_0$, are given by

$$\bar{\boldsymbol{S}} = \frac{\partial \tilde{W}}{\partial \bar{\boldsymbol{F}}}, \quad \text{and} \quad \bar{\mathbf{E}} = \frac{\partial \tilde{W}}{\partial \bar{\mathbf{D}}}, \tag{3.9}$$

respectively. As mentioned earlier, $\bar{\boldsymbol{F}}$ and $\bar{\mathbf{D}}$ correspond to the average (or macroscopic) deformation gradient and electric displacement fields in the composite. Therefore, expression (3.9) provides the macroscopic, or homogenized constitutive relations for the composite. In other words, similar to the local energy functions $W^{(r)}$, which characterize the response of the constituent phases, the effective energy function $\tilde{W}$, as defined by (3.3), completely describes the macroscopic response of the electroactive composite. Note that although, in general, energy will be stored (via the electric field) in the free space surrounding the specimen, as it is shown above, only the energy stored inside the specimen (i.e., $\tilde{W}$) needs to be considered in the homogenization problem. In addition, it is noted that $\tilde{W}$ is objective, which can be easily verified by making use of the objectivity of the phase potentials.

The Eulerian counterparts of the above effective constitutive equations for electroactive composites can be obtained in terms of the volume averages, denoted by $\langle \cdot \rangle$, of the true mechanical and electrical fields over the deformed configuration $\Omega$ of the composite. Thus, we define $\bar{\boldsymbol{T}} = \langle \boldsymbol{T} \rangle$, $\bar{\mathbf{d}} = \langle \mathbf{d} \rangle$ and $\bar{\mathbf{e}} = \langle \mathbf{e} \rangle$, which can be shown to satisfy the following relations:

$$\bar{\boldsymbol{T}} = \bar{J}^{-1} \bar{\boldsymbol{S}} \, \bar{\boldsymbol{F}}^T, \quad \bar{\mathbf{e}} = \bar{\boldsymbol{F}}^{-T} \bar{\mathbf{E}}, \quad \text{and} \quad \bar{\mathbf{d}} = \bar{J}^{-1} \bar{\boldsymbol{F}} \, \bar{\mathbf{D}}. \tag{3.10}$$

Furthermore, we define the effective Eulerian energy-density function $\tilde{w}\left(\bar{\boldsymbol{F}}, \bar{\mathbf{d}}\right) = \tilde{W}\left(\bar{\boldsymbol{F}}, \bar{J}\, \bar{\boldsymbol{F}}^{-1} \bar{\mathbf{d}}\right) / \bar{J}$. It then follows from equation $(3.10)_1$ that the average Cauchy stress is given by

$$\bar{\boldsymbol{T}} = \frac{\partial \tilde{w}}{\partial \boldsymbol{F}} \boldsymbol{F}^T + \left(\tilde{w} - \bar{\mathbf{e}} \cdot \bar{\mathbf{d}}\right) \boldsymbol{I} + \bar{\mathbf{e}} \otimes \bar{\mathbf{d}}. \tag{3.11}$$

Note that $\bar{\boldsymbol{T}}$ is symmetric, which can be shown from objectivity using arguments completely analogous to those used in connection with equation (2.10) to show the

symmetry of the local stress tensor $\boldsymbol{T}$. Also, it is easy to show, by means of $(3.10)_2$, that

$$\bar{\mathbf{e}} = \frac{\partial \tilde{w}}{\partial \bar{\mathbf{d}}}. \tag{3.12}$$

We remark that, we are not aware of mathematically rigorous results for the existence of solutions of the variational problem (3.3) (or (3.7) in the periodic case). However, at least for the material models discussed in Section 2.2 for the elastomeric matrix and rigid inclusion phases, which ensure quasi-convexity in $\boldsymbol{F}$ (for fixed $\mathbf{D}$) and convexity in $\mathbf{D}$ (for fixed $\boldsymbol{F}$), together with appropriate growth conditions, for the local potential $W$, it would be expected that results generalizing those of Müller (1987) and Geymonat et al. (1993) for purely mechanical systems should hold. Naturally, non-unique solutions would be expected to arise as a consequence of the possible development of "microscopic" and "macroscopic" instabilities (e.g. Michel et al. 2010*a*) as the deformation progresses.

In the next section, building on earlier works (Ponte Castañeda & Galipeau 2011, Ponte Castañeda & Siboni 2012), we propose a "partial decoupling strategy" in order to decouple the mechanical and electrostatic effects for electro-active composites with periodic and random microstructures. This will allow us to express the solution of the variational problem (3.3) (or (3.7) in the periodic case) for the effective stored-energy function of the electro-active composite in terms of the solutions of "purely mechanical" and "electrostatic" problems, coupled only through a finite set of microstructural variables, corresponding to the particle positions and orientations in the deformed configuration, which may be obtained by means of a finite-dimensional optimization process.

## 3.2 Homogenization estimates for two-phase particulate DECs with random microstructures

We consider a composite consisting of a random distribution of rigid, dielectric inclusions firmly embedded in an ideal dielectric elastomer matrix. The matrix is assumed

to be isotropic (both mechanically and electrically) and is capable of undergoing finite strains, as described by relations (2.13) and (2.15). For simplicity and ease of exposition, all the inclusions are assumed to be identical, but with arbitrary ellipsoidal shapes and general anisotropic dielectric properties, as characterized by relations (2.20) and (2.21). It is further assumed that the above-described electro-active composite has a stress-free configuration in the absence of deformation and electric fields (i.e., when $\boldsymbol{F} = \boldsymbol{I}$ and $\mathbf{D} = 0$), and that its mechanical behavior for small deformations is characterized by the conventional theory of linear elasticity. Under these conditions, we may expect a unique solution to the Euler-Lagrange equations associated with the variational problem (3.3), at least for sufficiently small deformations and electric fields (i.e., in the neighborhood of $\boldsymbol{F} = \boldsymbol{I}$ and $\mathbf{D} = 0$). However, after a certain amount of loading, this solution may become unstable and bifurcate (Geymonat et al. 1993) into a different (lower energy) solution.

In the following subsections, we will describe the initial microstructure of the composite in the reference configuration, the corresponding evolution of the microstructure, and finally a "partial decoupling" strategy to simplify the calculation of the effective stored-energy function of the composite (3.3) in the pre- and post-bifurcation regimes.

### 3.2.1 Initial microstructure

As depicted in Fig. 3.1 (left), the initial microstructure of the composite is obtained by a random distribution of aligned identical inclusions with ellipsoidal shapes, as defined by

$$\mathcal{I}_0 = \left\{ \mathbf{X} \mid \mathbf{X} \cdot \left( \boldsymbol{Z}_0^I \right)^{-2} \mathbf{X} \leq 1 \right\}. \tag{3.13}$$

Here the symmetric second-order tensor $\boldsymbol{Z}_0^I$ characterizes the shape and orientation of the inclusions in the reference configuration. Then, letting $\Theta_0^{(2)}(\mathbf{X})$ denote the characteristic function of a single ellipsoidal inclusion, and the random set $\{\mathbf{X}_\alpha\}$ denote the random positions of the inclusion centers, the characteristic function of

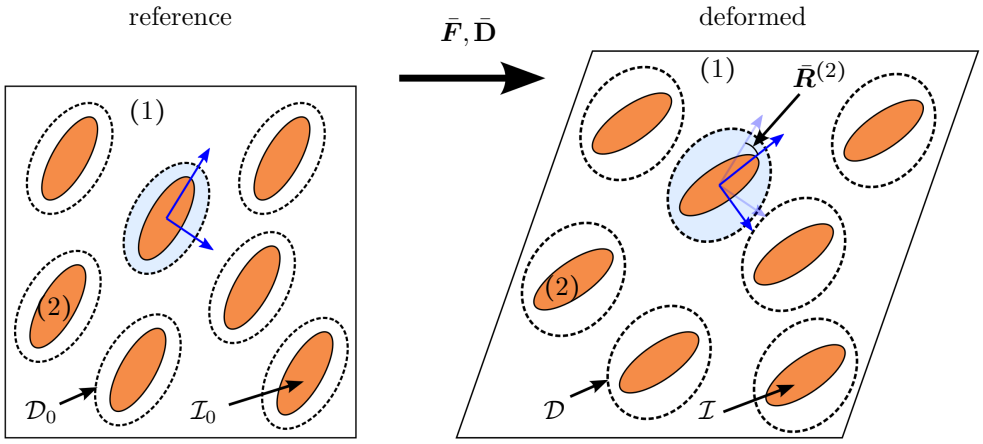


Figure 3.1: The random microstructure of two-phase particulate DECs in the reference (left) and deformed (right) configurations.

the inclusion phase may be written as follows

$$\Theta_0^{(2)}(\mathbf{X}) = \sum_{\alpha} \Theta_0^I(\mathbf{X} - \mathbf{X}_\alpha) = \int_{\Omega_0} \Theta_0^I(\mathbf{X} - \mathbf{Z})\, \psi_0(\mathbf{Z})\, d\mathbf{Z}, \tag{3.14}$$

where $\psi_0(\mathbf{Z}) := \sum_\alpha \delta(\mathbf{Z} - \mathbf{X}_\alpha)$ is the random density generated by the set of random point $\{\mathbf{X}_\alpha\}$. The probability density functions (PDFs) corresponding to the particle locations in the composite can then be obtained in terms of the ensemble averages of the random density $\psi_0(\mathbf{Z})$. Thus, letting $\langle\!\langle \cdot \rangle\!\rangle_0$ denote the ensemble average in the reference configuration, the PDF of finding and inclusion located at $\mathbf{Z}$ is defined by

$$p_0^I(\mathbf{Z}) := \langle\!\langle \psi_0(\mathbf{Z}) \rangle\!\rangle_0, \tag{3.15}$$

while the joint PDF of finding a pair of inclusions located at $\mathbf{Z}$ and $\mathbf{Z}'$ ($\mathbf{Z} \neq \mathbf{Z}'$) is defined by

$$p_0^{II}(\mathbf{Z}, \mathbf{Z}') := \langle\!\langle \psi_0(\mathbf{Z})\, \psi_0(\mathbf{Z}') \rangle\!\rangle_0 - \langle\!\langle \psi_0(\mathbf{Z}) \rangle\!\rangle_0\, \delta(\mathbf{Z} - \mathbf{Z}'). \tag{3.16}$$

It is remarked here that in general higher order PDFs can also be defined in order to describe the microstructure of the composite more accurately (see Milton 2001, for more details on higher order statistics). However, in this work we will make use of

Hashin-Shtrikman type homogenization estimates that are capable of accounting for microstructural details of the composite up to the two-point probabilities. Thus, to avoid the complications associated with higher order statistics, in this study we will only consider the effects of the first- and second- order PDFs defined above.

We assume that the composite is statistically isotropic (Milton 2001), such that $p_0^I(\mathbf{Z})$ is independent of the location, i.e.,

$$p_0^I(\mathbf{Z}) = p_0^I, \tag{3.17}$$

where $p_0^I$ denotes the number density of the inclusions in the reference configuration. Under the assumption of statistical isotropy the volume fraction of the inclusion phase in the reference configuration can be shown to be uniform and is given by

$$c_0^I = p_0^I |\Omega_0| . \tag{3.18}$$

Furthermore, we assume that the joint probability $p_0^{II}(\mathbf{Z}, \mathbf{Z}')$ is invariant under arbitrary translations, i.e.,

$$p_0^{II}(\mathbf{Z}, \mathbf{Z}') = p_0^{II}(\mathbf{Z} - \mathbf{Z}'), \tag{3.19}$$

and encompasses "ellipsoidal symmetry" (Ponte Castañeda & Willis 1995). Therefore, it will be assumed that $p_0^{II}$ depends on $\mathbf{Z}-\mathbf{Z}'$ via the combination $|\boldsymbol{Z}_0^D(\mathbf{Z} - \mathbf{Z}')|$, where $\boldsymbol{Z}_0^D$ is a symmetric second-order tensor characterizing the shape of the "distributional ellipses"

$$\mathcal{D}_0 = \left\{ \mathbf{X} \mid \mathbf{X} \cdot \left(\boldsymbol{Z}_0^D\right)^{-2} \mathbf{X} \leq 1 \right\}. \tag{3.20}$$

Note that in this context, statistical isotropy corresponds to the special case where $\boldsymbol{Z}_0^D = \boldsymbol{I}$. It is worthwhile to mention that in practice distribution of the inclusions can exhibit independent angular and radial behaviors. However, for cases where the initial distribution can be approximated as being ellipsoidal, simple analytical estimates may be obtained for the effective response of the composite, as will be seen later on, and hence the reason for the assumption of ellipsoidal symmetry.

### 3.2.2 Evolution of the microstructure

As depicted in Fig. 3.1, under the application of deformation and electric displacement fields, as described by the boundary conditions (3.1), the microstructure is expected to evolve in such a way that the particle positions and orientations, as well as the shape and size of the distribution, change with the applied deformation and electric field. Note that the particles will not change their size and shape, as they are rigid, but that their volume fraction can change, if the matrix material is compressible. Assuming that the matrix is capable of undergoing non-isochoric deformations (i.e., $\bar{J} = \det \bar{\boldsymbol{F}} \neq 1$), the volume fraction of the inclusion phase in the deformed configuration $c^I$, is given by

$$c^I = \left|\Omega^{(2)}\right| / |\Omega| = c_0^I / \bar{J}, \tag{3.21}$$

where we have used the fact that $|\Omega^{(2)}| = \left|\Omega_0^{(2)}\right|$ and $|\Omega| = \bar{J}\,|\Omega_0|$.

Under the application of the macroscopic mechanical and electrostatic loadings $\bar{\boldsymbol{F}}$ and $\bar{\mathbf{D}}$, the rigid inclusions are expected to change position and orientation, but their shape remains unchanged. Therefore, the microstructure of the composite in the deformed configuration is described by the deformed characteristic function

$$\Theta^{(2)}(\mathbf{x}) = \int_\Omega \Theta^I(\mathbf{x} - \mathbf{z})\, \psi(\mathbf{z})\, d\mathbf{z}, \tag{3.22}$$

where $\Theta^I(\mathbf{x})$ is the characteristic function of the single *rotated* inclusion, i.e.,

$$\mathcal{I} = \left\{ \mathbf{x} \mid \mathbf{x} \cdot \left(\boldsymbol{Z}^I\right)^{-2} \mathbf{x} \leq 1 \right\}, \quad \text{with} \quad \boldsymbol{Z}^I = \boldsymbol{R}^{I^T} \boldsymbol{Z}_0^I \boldsymbol{R}^I. \tag{3.23}$$

Here $\boldsymbol{R}^I$ denotes the rigid rotation of the inclusions and $\psi(\mathbf{z})$ denotes the random density associated with the set of random points $\{\mathbf{x}_\alpha\}$, which characterize the locations of the particle centers in the deformed configuration. It is emphasized here that both $\boldsymbol{R}^I$ and $\{\mathbf{x}_\alpha\}$ are expected to depend in a complicated manner on the local deformation gradient $\boldsymbol{F}$, which in turn is a function of $\bar{\boldsymbol{F}}$ and $\bar{\mathbf{D}}$. Dealing with the evolution of the microstructure in its full generality proves to be a very difficult task.

For this reason and in the spirit of developing simple homogenization estimates, the following simplifying assumptions will be made.

First, we assume that all the inclusions will rotate by the average rotation of the inclusion phase, denoted here by $\bar{\boldsymbol{R}}^{(2)}$, i.e.,

$$\boldsymbol{R}^I = \bar{\boldsymbol{R}}^{(2)}, \quad \text{for all inclusions.} \tag{3.24}$$

Note that for random distributions, individual inclusions will experience slightly different local fields and are expected to undergo slightly different rotations. Such slight misorientations from the average rotation $\bar{\boldsymbol{R}}^{(2)}$ may be incorporated into the homogenization estimates by means of an orientation distribution function, as was done by Racherla et al. (2010). Such generalizations are ignored in our work for simplicity.

Secondly, we assume that the evolution of the distribution is solely determined by the macroscopic mechanical loading, $\bar{\boldsymbol{F}}$, and is independent of the macroscopic electrostatic loading. Thus, it will be assumed here that the deformed joint probability density function $p^{II}(\mathbf{z}-\mathbf{z}')$ encompasses ellipsoidal symmetry, and therefore it depends on $\mathbf{z}-\mathbf{z}'$ via the combination $\left|\boldsymbol{Z}^{D^T}(\mathbf{z}-\mathbf{z}')\right|$. Here $\boldsymbol{Z}^D$ is a second-order tensor describing the deformed ellipsoidal shape of the distribution, i.e.,

$$\mathcal{D} = \left\{\mathbf{x} \mid \mathbf{x}\cdot\left(\boldsymbol{Z}^{D^T}\boldsymbol{Z}^D\right)^{-1}\mathbf{x} \le 1\right\}, \quad \text{with} \quad \boldsymbol{Z}^D = \bar{\boldsymbol{F}}\boldsymbol{Z}_0^D. \tag{3.25}$$

Similar to the inclusions, the evolution of the distribution is expected to depend on both the mechanical and electrostatic loadings, via the local deformation gradient. Therefore, in the context of random composites the deformed joint PDF is expected to depend on both $\bar{\boldsymbol{F}}$ and $\bar{\mathbf{D}}$, especially for large volume fractions of the inclusions. In addition, the joint PDF may also depend on higher-point statistics. As it was mentioned earlier, such higher-point statistics are ignored here since the estimates that are used in this work only account for two-point statistics, and hence the reason for the simplifying *ad hoc* assumption that the distribution of the inclusion remains ellipsoidal in the deformed configuration.

### 3.2.3 The partial decoupling strategy and approximation

In this section we provide a partial decoupling strategy to find the effective electro-elastic response of DECs described above. As we have seen in section 2.2, the potential energy for the ideal dielectric matrix and rigid inclusions can be split into a purely mechanical contribution $W_{me}^{(r)}(\boldsymbol{F})$ and an electrostatic contribution $W_{el}^{(r)}(\boldsymbol{F},\mathbf{D})$. By making use of the corresponding decompositions for $W^{(1)}$ and $W^{(2)}$ in expression (3.4) for the local energy of the composite, we obtain

$$W(\mathbf{X},\boldsymbol{F},\mathbf{D}) = W_{me}(\mathbf{X},\boldsymbol{F}) + W_{el}(\mathbf{X},\boldsymbol{F},\mathbf{D}), \tag{3.26}$$

where

$$W_{me}(\mathbf{X},\boldsymbol{F}) = \sum_{r=1}^{2} \Theta_0^{(r)}(\mathbf{X})\, W_{me}^{(r)}(\boldsymbol{F}) \quad \text{and} \quad W_{el}(\mathbf{X},\boldsymbol{F},\mathbf{D}) = \sum_{r=1}^{2} \Theta_0^{(r)}(\mathbf{X})\, W_{el}^{(r)}(\boldsymbol{F},\mathbf{D}). \tag{3.27}$$

Substituting the decomposition (3.26) into expression (3.3) for the homogenized potential, we obtain

$$\tilde{W}\left(\bar{\boldsymbol{F}},\bar{\mathbf{D}}\right) = \min_{\boldsymbol{F}\in\mathcal{K}(\bar{\boldsymbol{F}})} \min_{\mathbf{D}\in\mathcal{D}_0(\bar{\mathbf{D}})} \left\{\langle W_{me}(\mathbf{X},\boldsymbol{F})\rangle_0 + \langle W_{el}(\mathbf{X},\boldsymbol{F},\mathbf{D})\rangle_0\right\}, \tag{3.28}$$

where the admissible sets $\mathcal{K}\left(\bar{\boldsymbol{F}}\right)$ and $\mathcal{D}_0\left(\bar{\mathbf{D}}\right)$ are defined as before, and $\langle\cdot\rangle_0$ denotes the volume average in the reference configuration. It is observed that the first term on the right side of (3.28) is independent of the electric displacement field $\mathbf{D}$. Therefore, we can rewrite the variational problem (3.28) as follows

$$\tilde{W}\left(\bar{\boldsymbol{F}},\bar{\mathbf{D}}\right) = \min_{\boldsymbol{F}\in\mathcal{K}(\bar{\boldsymbol{F}})} \left\{\langle W_{me}(\mathbf{X},\boldsymbol{F})\rangle_0 + \tilde{W}_{el}\left(\bar{\mathbf{D}};\boldsymbol{F}\right)\right\}, \tag{3.29}$$

where

$$\tilde{W}_{el}\left(\bar{\mathbf{D}};\boldsymbol{F}\right) = \min_{\mathbf{D}\in\mathcal{D}_0(\bar{\mathbf{D}})} \langle W_{el}(\mathbf{X},\boldsymbol{F},\mathbf{D})\rangle_0 \tag{3.30}$$

is the homogenized electrostatic energy for a given (fixed) deformation field $\boldsymbol{F}$. It is important to emphasize that both terms on the right side of (3.29) depend on the

trial deformation field $\boldsymbol{F}$, and therefore the mechanical and electrostatic energies are coupled together and cannot be separated, in general. Thus, to make the dependence of $\tilde{W}_{el}\left(\bar{\mathbf{D}};\boldsymbol{F}\right)$ on the deformation more transparent, it is useful to rewrite the homogenized electrostatic energy in the current configuration, i.e.,

$$\tilde{W}_{el}\left(\bar{\mathbf{D}};\boldsymbol{F}\right) = \bar{J}\tilde{w}_{el}\left(\bar{\mathbf{d}};\boldsymbol{F}\right), \tag{3.31}$$

where $\bar{J} = \det \bar{\boldsymbol{F}}$ and

$$\tilde{w}_{el}\left(\bar{\mathbf{d}};\boldsymbol{F}\right) = \min_{\mathbf{d}\in\mathcal{D}(\bar{\mathbf{d}})} \left\langle \Theta^{(1)}\left(\mathbf{x}\right) w_{el}^{(1)}\left(\mathbf{d}\right) + \Theta^{(1)}\left(\mathbf{x}\right) w_{el}^{(2)}\left(\bar{\boldsymbol{R}}^{(2)},\mathbf{d}\right)\right\rangle. \tag{3.32}$$

In the above expression $w_{el}^{(1)}$ and $w_{el}^{(2)}$ are given by (2.16) and (2.22), respectively, $\langle\cdot\rangle$ is used to denote the volume average in the current configuration, and

$$\mathcal{D}\left(\bar{\mathbf{d}}\right) = \left\{\mathbf{d} \mid \operatorname{div}\mathbf{d} = \mathbf{0} \text{ in } \Omega,\ \mathbf{d}\cdot\mathbf{n} = \bar{\mathbf{d}}\cdot\mathbf{n} \text{ on } \partial\Omega\right\} \tag{3.33}$$

is the admissible set for the Eulerian electric displacement field $\mathbf{d}$.

Given the assumptions of subsection 3.2.2 for the evolution of the microstructure, it can be seen that the deformed characteristic functions $\Theta^{(1)}\left(\mathbf{x}\right)$ and $\Theta^{(2)}\left(\mathbf{x}\right)$ only depend on the macroscopic deformation $\bar{\boldsymbol{F}}$ and the average rotation of the inclusions $\bar{\boldsymbol{R}}^{(2)}$. Therefore, it is observed that by writing the homogenized electrostatic energy of the composite in its "more natural" Eulerian form the explicit dependence of $\tilde{w}_{el}$ on the local trial field $\boldsymbol{F}$ disappear. In other words, the homogenized Eulerian electrostatic energy is seen to depend on the deformation only via the macroscopic deformation $\bar{\boldsymbol{F}}$, which determines the shape of the distribution ellipses in the current configuration, and the average rotation of the inclusions $\bar{\boldsymbol{R}}^{(2)}$, i.e.,

$$\tilde{w}_{el}\left(\bar{\mathbf{d}};\boldsymbol{F}\right) = \tilde{w}_{el}\left(\bar{\mathbf{d}},\bar{\boldsymbol{F}};\bar{\boldsymbol{R}}^{(2)}\right). \tag{3.34}$$

Now by using the results (3.29) and (3.34), the variational problem (3.28) can be

rewritten as follows

$$\tilde{W}\left(\bar{\boldsymbol{F}},\bar{\mathbf{D}}\right)=\min_{\bar{\boldsymbol{R}}^{(2)}}\left\{\tilde{W}_{me}\left(\bar{\boldsymbol{F}};\bar{\boldsymbol{R}}^{(2)}\right)+\bar{J}\tilde{w}_{el}\left(\bar{\mathbf{d}},\bar{\boldsymbol{F}};\bar{\boldsymbol{R}}^{(2)}\right)\right\}, \tag{3.35}$$

where

$$\tilde{W}_{me}\left(\bar{\boldsymbol{F}};\bar{\boldsymbol{R}}^{(2)}\right)=\min_{\boldsymbol{F}\in\mathcal{K}'\left(\bar{\boldsymbol{F}},\bar{\boldsymbol{R}}^{(2)}\right)}\left\langle W_{me}\left(\mathbf{X},\boldsymbol{F}\right)\right\rangle_{0}. \tag{3.36}$$

In this last expression, $\mathcal{K}'\left(\bar{\boldsymbol{F}},\bar{\boldsymbol{R}}^{(2)}\right)$ denotes the set of admissible deformations inside the matrix phase that satisfy the affine condition on the boundary of the specimen, as given by $(3.1)_1$, and the prescribed rigid body motions at the interface of the inclusions with the matrix, as given by the rotation $\bar{\boldsymbol{R}}^{(2)}$. It is seen that the variational problems (3.32) and (3.36) are decoupled from each other, for the given rotation of the the inclusions, which is in turn obtained form the outer minimization in (3.35). For this reason we refer to (3.35) as the "partial decoupling strategy".

In summary, expression (3.35) for the effective energy $\tilde{W}\left(\bar{\boldsymbol{F}},\bar{\mathbf{D}}\right)$ along with expressions (3.32) and (3.36) for $\tilde{w}_{el}$ and $\tilde{W}_{me}$, show that for a given rotation $\bar{\boldsymbol{R}}^{(2)}$, the inner elastic and electrostatic problems can be solved independently of each other. Having solve these two decoupled variational problems, the outer minimization in (3.35) can be performed to obtain the *equilibrium* rotation $\bar{\boldsymbol{R}}^{(2)}$ as a function of the macroscopic loading $\bar{\boldsymbol{F}}$ and $\bar{\mathbf{D}}$, as well as the effective potential $\tilde{W}\left(\bar{\boldsymbol{F}},\bar{\mathbf{D}}\right)$ for the DEC.

As it is clear from equation (3.35), performing the outer minimization, requires the knowledge of explicit expressions in terms of the prescribed rotation $\bar{\boldsymbol{R}}^{(2)}$ for both $\tilde{W}_{me}$ and $\tilde{w}_{el}$. While this is relatively simple for the electrostatic part of the effective energy $\tilde{w}_{el}$, obtaining such explicit expressions for the effective mechanical energy, is more difficult. For this reason, it is advantageous to make use of the "partial decoupling approximation" of Ponte Castañeda & Galipeau (2011), which makes use of the solution of the purely mechanical problem to obtain approximate estimates for the above general problem. Thus, letting $\bar{\boldsymbol{R}}_{m}^{(2)}$ denote the minimizer of the purely

mechanical problem

$$\tilde{W}_{me}\left(\bar{\boldsymbol{F}}\right) = \min_{\bar{\boldsymbol{R}}^{(2)}} \tilde{W}_{me}\left(\bar{\boldsymbol{F}}, \bar{\boldsymbol{R}}^{(2)}\right), \tag{3.37}$$

it follows from (3.35) that

$$\tilde{W}\left(\bar{\boldsymbol{F}}, \bar{\mathbf{D}}\right) \leq \tilde{W}_{me}\left(\bar{\boldsymbol{F}}; \bar{\boldsymbol{R}}_m^{(2)}\right) + \bar{J}\tilde{w}_{el}\left(\bar{\mathbf{d}}, \bar{\boldsymbol{F}}; \bar{\boldsymbol{R}}_m^{(2)}\right). \tag{3.38}$$

Note that the right side of the inequality (3.38) can be treated as an estimate for the effective energy $\tilde{W}\left(\bar{\boldsymbol{F}}, \bar{\mathbf{D}}\right)$, which can be shown to become more accurate as the magnitude of the elastic interactions becomes large compared to the electrostatic interactions. Such conditions are expected to be met for small electric fields or for (mechanically) stiff matrix materials. A more rigorous argument for the above statement will be provided later on in this thesis. Finally, it is worthwhile to mention that the inequality (3.38) becomes an equality for the special case of DECs with aligned microstructure and under aligned mechanical and electrostatic loading conditions. This is because of the fact that under aligned loading conditions and when the microstructure of the composite is also aligned with the loading, the average rotation of the inclusions is zero (i.e., $\bar{\boldsymbol{R}}^{(2)} = \boldsymbol{I}$).

### 3.2.4 Hashin-Shtrikman estimates for the effective electrostatic energy of two-phase random DECs

In this subsection we provide Hashin-Shtrikman type estimates for the effective electrostatic energy of DECs with random microstructures. Assuming that an estimate is available for the effective purely mechanical energy of the composite, the partial decoupling strategy of the previous subsection can then be used to obtain the effective (coupled) electro-active energy of the composite.

The purely electrostatic homogenization problem (3.32) associated with $\tilde{w}_{el}$ for the electric behavior of the phases given by (2.16) and (2.22), reduces to

$$\tilde{w}_{el}\left(\bar{\mathbf{d}}, \bar{\boldsymbol{F}}; \bar{\boldsymbol{R}}^{(2)}\right) = \min_{\mathbf{d}\in\mathcal{D}(\bar{\mathbf{d}})} \left\langle \frac{1}{2}\mathbf{d}\cdot\boldsymbol{\varepsilon}^{-1}\left(\mathbf{x}\right)\left(\mathbf{d}\right)\right\rangle = \frac{1}{2}\bar{\mathbf{d}}\cdot\tilde{\boldsymbol{\varepsilon}}^{-1}\bar{\mathbf{d}}, \tag{3.39}$$

where $\tilde{\boldsymbol{\varepsilon}}$ is the homogenized permittivity of the composite in the deformed configuration. In (3.39), $\boldsymbol{\varepsilon}(\mathbf{x})$ is the local permittivity, and it is given by

$$\boldsymbol{\varepsilon}(\mathbf{x}) = \varepsilon^{(1)}\boldsymbol{I} + \Theta^{(2)}(\mathbf{x})\left(\boldsymbol{\varepsilon}^{(2)} - \varepsilon^{(1)}\boldsymbol{I}\right) \tag{3.40}$$

where

$$\varepsilon^{(1)}\boldsymbol{I} = \boldsymbol{\mathcal{E}}^{(1)} \quad \text{and} \quad \boldsymbol{\varepsilon}^{(2)} = \bar{\boldsymbol{R}}^{(2)}\boldsymbol{\mathcal{E}}^{(2)}\,\bar{\boldsymbol{R}}^{(2)\,T}, \tag{3.41}$$

denote the permittivity of the matrix and inclusion phases in the deformed configuration. Note that here, as described earlier in chapter 2, $\boldsymbol{\mathcal{E}}^{(1)}$ and $\boldsymbol{\mathcal{E}}^{(2)}$ are fixed (independent of the deformation) tensors corresponding to permittivities of the matrix and inclusion phases, respectively. It is also emphasized that here $\bar{\boldsymbol{R}}^{(2)}$ is treated as a given (fixed) rotation tensor.

Estimates for the effective permittivity of two-phase composites, defined by (3.39) with the constitutive behavior (3.40), and random microstructures with ellipsoidal symmetry, as described in section 3.2.2, can be obtained (Ponte Castañeda & Willis 1995) as follows

$$\tilde{\boldsymbol{\varepsilon}} = \varepsilon^{(1)}\boldsymbol{I} + c^I\left[\left(\boldsymbol{\varepsilon}^{(2)} - \varepsilon^{(1)}\boldsymbol{I}\right)^{-1} + \boldsymbol{P}\right]^{-1}. \tag{3.42}$$

Here, $c^I$ is the (current) volume fraction of the particles, and the microstructural tensor $\boldsymbol{P}$ is given (Ponte Castañeda & Willis 1995) by

$$\boldsymbol{P} = \boldsymbol{P}^I - c^I\boldsymbol{P}^D, \tag{3.43}$$

where $\boldsymbol{P}^I$ and $\boldsymbol{P}^D$ are Eshelby type microstructural tensors that encode the effect of the shape and distribution of the inclusions. For inclusions with general ellipsoidal shape, these microstructural tensors are given by

$$\boldsymbol{P}^I = \frac{\det \boldsymbol{Z}^I}{4\pi\varepsilon^{(1)}}\int_{|\boldsymbol{\xi}|=1}\boldsymbol{\xi}\otimes\boldsymbol{\xi}\left|\boldsymbol{Z}^I\boldsymbol{\xi}\right|^{-3}dS \quad \text{and} \quad \boldsymbol{P}^D = \frac{\det \boldsymbol{Z}^D}{4\pi\varepsilon^{(1)}}\int_{|\boldsymbol{\xi}|=1}\boldsymbol{\xi}\otimes\boldsymbol{\xi}\left|\boldsymbol{Z}^D\boldsymbol{\xi}\right|^{-3}dS. \tag{3.44}$$

It is emphasized that expression (3.42) for $\tilde{\boldsymbol{\varepsilon}}$ depends on the deformation via the dependence of the shape tensors $\boldsymbol{Z}^I$ and $\boldsymbol{Z}^D$, and the permittivity $\boldsymbol{\varepsilon}^{(2)}$ on the

deformation, as it is evident from equations (3.23), (3.25), and (3.41). Therefore, it is useful to define

$$\hat{\boldsymbol{P}}_0\left(\bar{\boldsymbol{U}}\right) := \boldsymbol{R}^p \hat{\boldsymbol{P}}_0^I \boldsymbol{R}^{pT} - c_0 \hat{\boldsymbol{P}}_0^D\left(\bar{\boldsymbol{U}}\right), \tag{3.45}$$

such that

$$\boldsymbol{P} = \frac{1}{\varepsilon^{(1)}} \bar{\boldsymbol{R}} \hat{\boldsymbol{P}}_0\left(\bar{\boldsymbol{U}}\right) \bar{\boldsymbol{R}}^T \tag{3.46}$$

to make the dependence of the $\boldsymbol{P}$-tensor on the deformation, more transparent. In (3.45) the new Eshelby tensors $\hat{\boldsymbol{P}}_0^I$ and $\hat{\boldsymbol{P}}_0^D\left(\bar{\boldsymbol{U}}\right)$ are defined as follows

$$\hat{\boldsymbol{P}}_0^I = \frac{\det \boldsymbol{Z}_0^I}{4\pi} \int_{|\boldsymbol{\xi}|=1} \boldsymbol{\xi} \otimes \boldsymbol{\xi} \left|\boldsymbol{Z}_0^I \boldsymbol{\xi}\right|^{-3} dS \quad \text{and} \quad \hat{\boldsymbol{P}}_0^D = \frac{\det \boldsymbol{Z}_0^D}{4\pi} \int_{|\boldsymbol{\xi}|=1} \boldsymbol{\xi} \otimes \boldsymbol{\xi} \left|\boldsymbol{Z}_0^D \bar{\boldsymbol{U}} \boldsymbol{\xi}\right|^{-3} dS, \tag{3.47}$$

and the rotation tensor $\boldsymbol{R}^p := \bar{\boldsymbol{R}}^T \bar{\boldsymbol{R}}^{(2)}$ on the right side of (3.45) characterizes the relative rotation of the fibers with respect to the macroscopic rotation $\bar{\boldsymbol{R}}$.

Using (3.46) and (3.41), the load dependent effective permittivity $\tilde{\boldsymbol{\varepsilon}}$, as given by (3.42), can be rewritten as follows

$$\tilde{\boldsymbol{\varepsilon}}\left(\bar{\boldsymbol{F}}; \bar{\boldsymbol{R}}^{(2)}\right) = \bar{\boldsymbol{R}} \tilde{\boldsymbol{\mathcal{E}}}\left(\bar{\boldsymbol{U}}; \bar{\boldsymbol{R}}^{(2)}\right) \bar{\boldsymbol{R}}^T, \tag{3.48}$$

where

$$\tilde{\boldsymbol{\mathcal{E}}}\left(\bar{\boldsymbol{U}}; \bar{\boldsymbol{R}}^{(2)}\right) = \varepsilon^{(1)} \boldsymbol{I} + \frac{c_0^I}{\bar{J}} \left[\boldsymbol{R}^p \left(\boldsymbol{\mathcal{E}}^{(2)} - \varepsilon^{(1)} \boldsymbol{I}\right)^{-1} \boldsymbol{R}^{pT} + \hat{\boldsymbol{P}}_0\left(\bar{\boldsymbol{U}}, \boldsymbol{R}^p\right) / \varepsilon^{(1)}\right]^{-1}. \tag{3.49}$$

As it is clear from (3.49), the deformation dependent permittivity $\tilde{\boldsymbol{\mathcal{E}}}\left(\bar{U}; \bar{\boldsymbol{R}}^{(2)}\right)$, depends on the deformation via $\bar{J}$, the relative particle rotation $\boldsymbol{R}^p$, and finally, the microstructural tensor $\hat{\boldsymbol{P}}_0\left(\bar{\boldsymbol{U}}, \boldsymbol{R}^p\right)$.

In conclusion, it follows the fully Lagrangian estimate

$$\tilde{W}_{el}\left(\bar{\boldsymbol{F}}, \bar{\mathbf{D}}; \bar{\boldsymbol{R}}^{(2)}\right) = \frac{1}{2\bar{J}} \bar{\mathbf{D}} \cdot \left[\bar{\boldsymbol{U}} \tilde{\boldsymbol{\mathcal{E}}}^{-1}\left(\bar{\boldsymbol{U}}; \bar{\boldsymbol{R}}^{(2)}\right) \bar{\boldsymbol{U}}\right] \bar{\mathbf{D}}, \tag{3.50}$$

for the effective (Lagrangian) electrostatic potential of the composite, for a given rotation $\bar{\boldsymbol{R}}^{(2)}$. Assuming that the corresponding estimate for $\tilde{W}_{me}\left(\bar{\boldsymbol{F}}; \bar{\boldsymbol{R}}^{(2)}\right)$ is also

known, the effective electro-active energy of the composite is obtained via

$$\tilde{W}\left(\bar{\boldsymbol{F}},\bar{\mathbf{D}}\right)=\min_{\bar{\boldsymbol{R}}^{(2)}}\left\{\tilde{W}_{me}\left(\bar{\boldsymbol{F}};\bar{\boldsymbol{R}}^{(2)}\right)+\tilde{W}_{el}\left(\bar{\boldsymbol{F}},\bar{\mathbf{D}};\bar{\boldsymbol{R}}^{(2)}\right)\right\}. \tag{3.51}$$

The stationary condition associated with the above minimization problem results in the following equation

$$\frac{\partial\tilde{W}_{me}}{\partial\bar{\boldsymbol{R}}^{(2)}}+\frac{\partial\tilde{W}_{el}}{\partial\bar{\boldsymbol{R}}^{(2)}}=0, \tag{3.52}$$

which can be solved for the equilibrium rotation of the inclusions as a function of the macroscopic deformation $\bar{\boldsymbol{F}}$ and macroscopic electric displacement field $\bar{\mathbf{D}}$, i.e.,

$$\bar{\boldsymbol{R}}^{(2)}_{eq}=\bar{\boldsymbol{R}}^{(2)}_{eq}\left(\bar{\boldsymbol{F}},\bar{\mathbf{D}}\right). \tag{3.53}$$

Finally, using (3.9), the macroscopic (Lagrangian) electric field $\bar{\mathbf{E}}$ and Piola-Kirchhoff stress $\bar{\boldsymbol{S}}$ corresponding to effective potential (3.51) can be obtained as follows

$$\bar{\mathbf{E}}=\frac{\partial\tilde{W}}{\partial\bar{\mathbf{D}}}=\frac{\partial\tilde{W}_{el}}{\partial\bar{\mathbf{D}}}\left(\bar{\boldsymbol{F}},\bar{\mathbf{D}};\bar{\boldsymbol{R}}^{(2)}\right)\Big|_{\bar{\boldsymbol{R}}^{(2)}=\bar{\boldsymbol{R}}^{(2)}_{eq}(\bar{\boldsymbol{F}},\bar{\mathbf{D}})},\quad\text{and}\quad\bar{\boldsymbol{S}}=\frac{\partial\tilde{W}}{\partial\bar{\boldsymbol{F}}}=\bar{\boldsymbol{S}}^{me}+\bar{\boldsymbol{S}}^{el}. \tag{3.54}$$

In the above equation

$$\begin{aligned}\bar{\boldsymbol{S}}^{me}&=\frac{\partial\tilde{W}_{me}}{\partial\bar{\boldsymbol{F}}}\left(\bar{\boldsymbol{F}};\bar{\boldsymbol{R}}^{(2)}\right)\Big|_{\bar{\boldsymbol{R}}^{(2)}=\bar{\boldsymbol{R}}^{(2)}_{eq}(\bar{\boldsymbol{F}},\bar{\mathbf{D}})}\\ \bar{\boldsymbol{S}}^{el}&=\frac{\partial\tilde{W}_{el}}{\partial\bar{\boldsymbol{F}}}\left(\bar{\boldsymbol{F}},\bar{\mathbf{D}};\bar{\boldsymbol{R}}^{(2)}\right)\Big|_{\bar{\boldsymbol{R}}^{(2)}=\bar{\boldsymbol{R}}^{(2)}_{eq}(\bar{\boldsymbol{F}},\bar{\mathbf{D}})}\end{aligned} \tag{3.55}$$

are, respectively, the purely mechanical (i.e., in the absence of electric fields) and electrostatic contributions of the (total) macroscopic Piola-Kirchhoff stress. Note that the derivatives in equations (3.54) and (3.55) are taken while holding $\bar{\boldsymbol{R}}^{(2)}$ fixed. The corresponding Eulerian expressions for the macroscopic total stress and electric field are provided in Appendix E.

## 3.3 Homogenization estimates for two-phase particulate DECs with periodic microstructures

In this subsection, we present the corresponding homogenization estimates for two-phase DECs with periodic microstructures. As before, the constitutive properties of the matrix and inclusion phases are described by relation (2.13) and (2.15), respectively, and all the inclusion are assumed to be identical, with arbitrary ellipsoidal shapes. We recall that, unique solutions are expected for the Euler-Lagrange equations associated with the variational problem (3.3), at least for sufficiently small deformation and electric fields (i.e., in the neighborhood of $\boldsymbol{F} = \boldsymbol{I}$ and $\mathbf{D} = 0$). Because of this, the solution of the variational problem is expected (Marcellini 1978) to be periodic with the same period as the elementary unit cell in the deformed configuration. After a certain amount of loading, this one-cell periodic solution may become unstable and bifurcate (Geymonat et al. 1993), in such a way that the deformation of the material will continue to be periodic, but on a larger unit cell (composed of possibly many elementary unit cells).

In the following subsections, we will describe the microstructure in the reference configuration, the corresponding evolution of the microstructure in both pre- and post-bifurcation regimes, and finally the corresponding periodic "partial decoupling strategy" for the calculation of the effective stored-energy function of periodic DECs in the pre- and post-bifurcation regimes.

### 3.3.1 Initial microstructure

As depicted in Fig. 3.2 (left), the initial microstructure of the composite is obtained by periodic repetition of a unit cell $\mathcal{U}_0$. Throughout this chapter, it is assumed that $\mathcal{U}_0$ is a parallelepiped defined by the lattice vectors $\mathbf{L}^i$ $(i = 1, 2, 3)$ in the reference configuration. For two-phase composites, the above microstructure is precisely characterized by periodic characteristic functions $\Theta_0^{(r)}(\mathbf{X})$ $(r = 1, 2)$, where the dependence on the

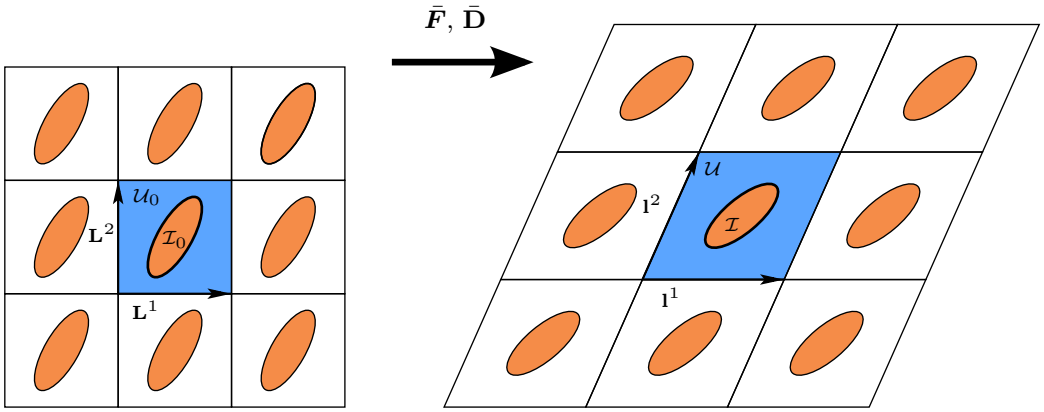


Figure 3.2: The periodic microstructure of two-phase particulate DECs in the reference (left) and deformed (right) configurations.

position vector $\mathbf{X}$ is fully determined by the unit cell $\mathcal{U}_0$, such that

$$\Theta_0^{(r)}(\mathbf{X}) = \Theta_0^{(r)}\left(\mathbf{X} + p_1\mathbf{L}^1 + p_2\mathbf{L}^2 + p_3\mathbf{L}^3\right) \text{ for all } p_1, p_2, p_3 \in \mathbb{Z}. \tag{3.56}$$

For future use, the reference reciprocal lattice (RL) vectors $\mathbf{K}^r$ are defined by

$$\mathbf{K}^r = 2\pi \frac{\mathbf{L}^s \times \mathbf{L}^t}{\mathbf{L}^1 \cdot (\mathbf{L}^2 \times \mathbf{L}^3)}, \tag{3.57}$$

where $(r, s, t)$ are the three even permutations of $(1, 2, 3)$.

Each unit cell $\mathcal{U}_0$, contains a single ellipsoidal inclusion, $\mathcal{I}_0$, located at its geometric center. Therefore, the characteristic function of the inclusion phase ($r = 2$) can be written as

$$\Theta_0^{(2)}(\mathbf{X}) = \sum_{p_1,p_2,p_3 \in \mathbb{Z}} \Theta_0^I\left(\mathbf{X} + p_1\mathbf{L}^1 + p_2\mathbf{L}^2 + p_3\mathbf{L}^3\right), \tag{3.58}$$

where $\Theta_0^I$ denotes the characteristic function of a single ellipsoidal inclusion, as defined by

$$\mathcal{I}_0 = \left\{\mathbf{X} \mid \mathbf{X} \cdot \left(\boldsymbol{Z}_0^I\right)^{-2} \mathbf{X} \leq 1\right\} \tag{3.59}$$

in terms of the symmetric, second-order tensor $\boldsymbol{Z}_0^I$.

It is important to note that with the above microstructure we would expect the homogenized results to depend on the volume fraction of the particles in the reference configuration $c_0^I = |\mathcal{I}_0| / |\mathcal{U}_0|$, the shape and orientation of the inclusions, described by

$\boldsymbol{Z}_0^I$, and the shape of the unit cell $\mathcal{U}_0$, described by the lattice vectors $\mathbf{L}^i$ $(i = 1, 2, 3)$ or, alternatively, the RL vectors $\mathbf{K}^r$ $(r = 1, 2, 3)$.

### 3.3.2 Evolution of the microstructure

Under the application of deformation and electric displacement fields, as described by the boundary conditions (3.1), the microstructure of the DEC is expected to evolve in such a way that the particle positions and orientations, as well as the shape and size of the unit cell, change with the applied deformation and electric field. Since the particles are rigid, their size and shape remains unchanged, but their volume fraction may change, if the matrix material is compressible. As already mentioned, the deformation of the composite should remain periodic on the elementary unit cell $\mathcal{U}_0$, at least for small enough values of the applied loading. For this reason, we first describe the evolution of the microstructure in the pre-bifurcation regime.

The deformed one-cell periodic structure, as depicted in Fig. 3.2 (right), is described by the characteristic functions

$$\Theta^{(r)}(\mathbf{x}) = \Theta^{(r)}\left(\mathbf{x} + p_1\mathbf{l}^1 + p_2\mathbf{l}^2 + p_3\mathbf{l}^3\right), \quad \text{for all } p_1, p_2, p_3 \in \mathbb{Z}, \tag{3.60}$$

where $\mathbf{l}^i$ $(i = 1, 2, 3)$ are the deformed lattice vectors. It follows from the assumed one-cell periodicity of the solution that these deformed lattice vectors can be related to the reference lattice vectors via the following identities

$$\mathbf{l}^i = \bar{\boldsymbol{F}}\mathbf{L}^i \quad \text{for} \quad i = 1, 2, 3. \tag{3.61}$$

Note that $\mathbf{l}^i$, as given by (3.61), completely characterize the evolution of the shape of the unit cell as well as the position of the particle centers. On the other hand, the deformed RL vectors $\mathbf{k}^r$ are given by

$$\mathbf{k}^r = 2\pi\frac{\mathbf{l}^s \times \mathbf{l}^t}{\mathbf{l}^1 \cdot (\mathbf{l}^2 \times \mathbf{l}^3)}, \tag{3.62}$$

where $(r, s, t)$ are again the three even permutations of $(1, 2, 3)$. Using (3.61) it can

be readily shown that

$$\mathbf{k}^r = \bar{\boldsymbol{F}}^{-T}\mathbf{K}^r \quad \text{for} \quad r = 1, 2, 3. \tag{3.63}$$

which relate the RL vectors in the deformed configuration to their reference counterparts. Assuming that the matrix is capable of undergoing non-isochoric deformations (i.e., $\bar{J} = \det \bar{\boldsymbol{F}} \neq 1$), the volume fraction of the inclusion phase in the deformed configuration $c^I = |\mathcal{I}| \,/\, |\mathcal{U}|$, is given by $c^I = c_0^I/\bar{J}$. Here, we have used the identity $|\mathcal{U}| = \bar{J}\,|\mathcal{U}_0|$ (this can be easily shown by using (3.61) to relate the lattice vectors in the deformed configuration to their reference counterparts), as well as the fact that the inclusions are rigid.

Excluding the possibility of pattern-changing instabilities, each unit cell $\mathcal{U}$ in the deformed configuration, will contain only one inclusion (denoted by $\mathcal{I}$ in the deformed configuration) at its geometric center. Therefore, the characteristic function of the inclusion phase ($r = 2$) in the deformed configuration $\Theta^{(2)}(\mathbf{x})$ can be written as

$$\Theta^{(2)}(\mathbf{x}) = \sum_{p_1,p_2,p_3\in\mathbb{Z}} \Theta^I\left(\mathbf{x} + p_1\mathbf{l}^1 + p_2\mathbf{l}^2 + p_3\mathbf{l}^3\right), \tag{3.64}$$

where $\Theta^I$ denotes the characteristic function of a single rotated inclusion in the deformed configuration, as given by

$$\mathcal{I} = \left\{\mathbf{x} \,|\, \mathbf{x}\cdot\left(\boldsymbol{Z}^I\right)^{-2}\mathbf{x} \leq 1\right\}, \quad \text{with} \quad \boldsymbol{Z}^I = \bar{\boldsymbol{R}}^I\,\boldsymbol{Z}_0^I\,\bar{\boldsymbol{R}}^{I\,T}. \tag{3.65}$$

Here, $\bar{\boldsymbol{R}}^I$ denotes the rotation of the inclusions and will depend on the macroscopic deformation $\bar{\boldsymbol{F}}$ as well as the macroscopic electric displacement field $\bar{\mathbf{D}}$.

In connection with the above result for the evolution of the microstructure, it is important to emphasize that since the macroscopic deformation $\bar{\boldsymbol{F}}$ is prescribed by the boundary conditions, and therefore, is known a priori, the deformed unit cell $\mathcal{U}$, and therefore, the location of the particle centers in the deformed configuration are known without the need to solve the coupled electro-elastic problem. However, the particle rotations $\bar{\boldsymbol{R}}^I$ have to be determined from the solution of the electro-elastic problem in terms of the applied deformation $\bar{\boldsymbol{F}}$ and electric displacement field $\bar{\mathbf{D}}$.

Having described the evolution of the microstructure in the pre-bifurcation one-cell periodic regime, we now proceed to describe the corresponding evolution of a super-cell $\mathbf{q}\mathcal{U}_0$ in the post-bifurcation regime.

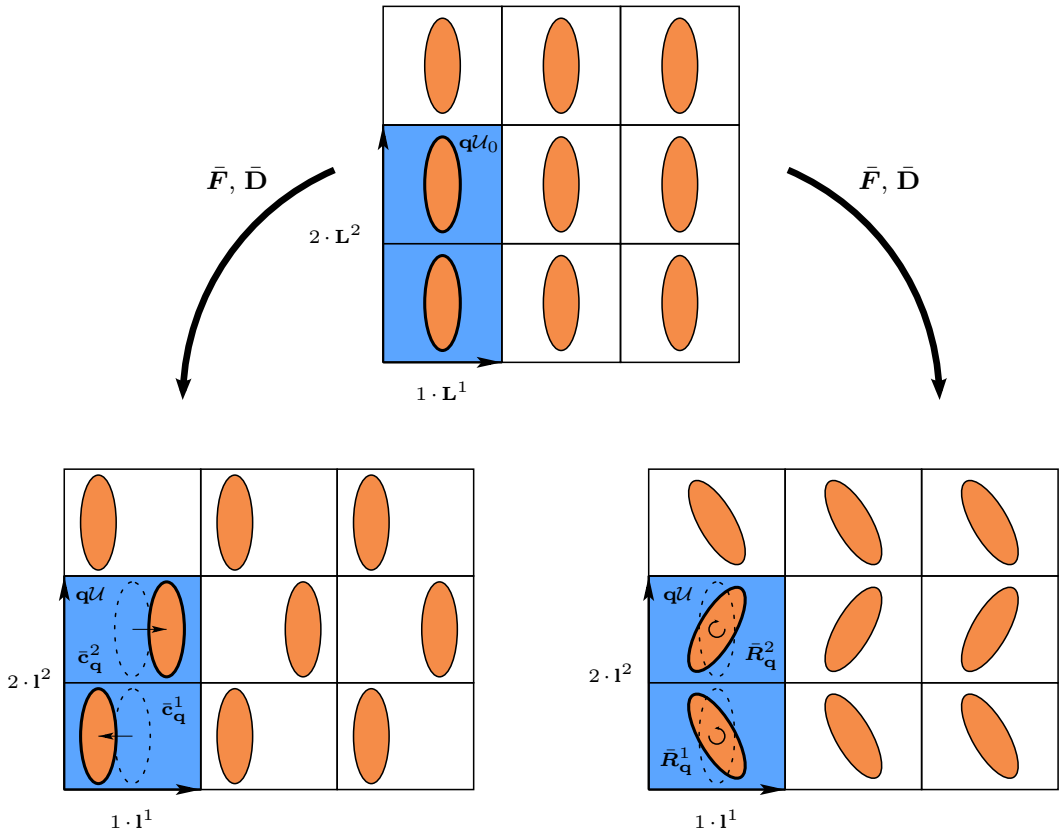


Figure 3.3: Initial, 1×1-cell periodic microstructure (top), and two possible 1×2-cell periodic, post-bifurcated microstructures (bottom).

As depicted in Fig. 3.3, the evolution of the shape of the super-cell $\mathbf{q}\mathcal{U}_0$ in the post-bifurcated regime can be completely described by

$$q_i \mathbf{l}^i = \bar{\boldsymbol{F}} \left( q_i \mathbf{L}^i \right) \quad \text{for} \quad i = 1, 2, 3 \quad \text{(no sum)}, \tag{3.66}$$

where $q_i \mathbf{l}^i$, for given $q_1, q_2, q_3$, are the lattice vectors of the deformed super-cell $\mathbf{q}\mathcal{U}$. Therefore, the $\mathbf{q}$-cell periodic microstructure of the composite in the deformed configuration can be described by the characteristic functions $\Theta^{(r)}_{\mathbf{q}}$ $(r = 1, 2)$, such that

$$\Theta^{(r)}_{\mathbf{q}} (\mathbf{x}) = \Theta^{(r)}_{\mathbf{q}} \left( \mathbf{x} + p_1 q_1 \mathbf{l}^1 + p_2 q_2 \mathbf{l}^2 + p_3 q_3 \mathbf{l}^3 \right), \quad \text{for all} \quad p_1, p_2, p_3 \in \mathbb{Z}. \tag{3.67}$$

It is important to emphasize that, unlike the one-cell periodic case where the particles all undergo the same rotations in the deformed configuration and their center locations are completely determined by the deformed unit cell, the particles in the super-cell may acquire different orientations and their positions will no longer be directly determined by the macroscopic deformation of the super-cell. For this reason, in addition to the evolution of the shape of the super-cell, as described by (3.66), we have to take into account these extra microstructural parameters when dealing with multi-cell periodic cases. These extra microstructural variables will be described here by a set of second-order orthogonal tensors $\bar{\boldsymbol{R}}^K_{\mathbf{q}}$ and vectors $\bar{\mathbf{c}}^K_{\mathbf{q}}$ corresponding, respectively, to the rotations and displacements of all the inclusions ($K = 1, ..., N_{\mathbf{q}}$) in the super-cell $\mathbf{q}\mathcal{U}_0$ (see Fig. 3.3).

### 3.3.3 The partial decoupling strategy and approximation

In this subsection, we implement the decoupling strategy for the variational problem (3.8) associated with the super cell $\mathbf{q}\mathcal{U}_0$. Then, the results will be specialized to the one-cell problem in order to obtain an estimate for pre-bifurcation effective energy.

Thus, similar to the random case, the position-dependent potential $W$ of the periodic composite, as defined by (3.4), can be split into two parts, such that

$$W(\mathbf{X}, \boldsymbol{F}, \mathbf{D}) = W_{me}(\mathbf{X}, \boldsymbol{F}) + W_{el}(\mathbf{X}, \boldsymbol{F}, \mathbf{D}), \tag{3.68}$$

where $W_{me}(\mathbf{X}, \boldsymbol{F})$ and $W_{el}(\mathbf{X}, \boldsymbol{F}, \mathbf{D})$ are given in expressions (3.27), except that now the corresponding periodic characteristic functions are used. Therefore, using the fact that $W_{me}$ is independent of $\mathbf{D}$, the variational statement (3.8) can be rewritten as

$$\tilde{W}^{\mathbf{q}\mathcal{U}_0}\left(\bar{\boldsymbol{F}}, \bar{\mathbf{D}}\right) = \min_{\mathbf{u}' \in \mathbf{q}\mathcal{U}_0^{\#}} \left\{ \frac{1}{|\mathbf{q}\mathcal{U}_0|} \int_{\mathbf{q}\mathcal{U}_0} W_{me}\left(\mathbf{X}; \bar{\boldsymbol{F}} + \nabla\mathbf{u}'\right) d\mathbf{X} + \tilde{W}_{el}^{\mathbf{q}\mathcal{U}_0}\left(\bar{\mathbf{D}}; \bar{\boldsymbol{F}} + \nabla\mathbf{u}'\right) \right\}, \tag{3.69}$$

where

$$\tilde{W}_{el}^{\mathbf{q}\mathcal{U}_0}\left(\bar{\mathbf{D}}; \bar{\boldsymbol{F}} + \nabla\mathbf{u}'\right) = \min_{\mathbf{A}' \in \mathbf{q}\mathcal{U}_0^{\#}} \left\{ \frac{1}{|\mathbf{q}\mathcal{U}_0|} \int_{\mathbf{q}\mathcal{U}_0} W_{el}\left(\mathbf{X}; \bar{\boldsymbol{F}} + \nabla\mathbf{u}', \bar{\mathbf{D}} + \nabla \times \mathbf{A}'\right) d\mathbf{X} \right\} \tag{3.70}$$

is the homogenized potential associated with the local potential $W_{el}(\mathbf{X}, \boldsymbol{F}, \mathbf{D})$, for a fixed trial field $\boldsymbol{F}(\mathbf{X}) = \bar{\boldsymbol{F}} + \nabla \mathbf{u}'$. It is important to note that both $W_{me}$ and $\tilde{W}_{el}^{\mathbf{q}\mathcal{U}_0}$ on the right-hand side of (3.69) depend on the trial deformation field $\boldsymbol{F}(\mathbf{X})$, and therefore, the mechanical and electric energy terms are coupled together and can not be interpreted as independent contributions in the total electro-mechanical energy. However, as it was the case in the context of random DECs, it is useful to rewrite the homogenized electrostatic energy in the current configuration, such that

$$\tilde{W}_{el}^{\mathbf{q}\mathcal{U}_0}\left(\bar{\mathbf{D}}; \boldsymbol{F}(\mathbf{X})\right) = \bar{J}\, \tilde{w}_{el}^{\mathbf{q}\mathcal{U}}\left(\bar{\mathbf{d}}; \boldsymbol{F}(\mathbf{X})\right), \tag{3.71}$$

where $\bar{J} = \det \bar{\boldsymbol{F}}$ and

$$\tilde{w}_{el}^{\mathbf{q}\mathcal{U}}\left(\bar{\mathbf{d}}; \boldsymbol{F}\right) = \min_{\mathbf{a}' \in \mathbf{q}\mathcal{U}^{\#}} \left\{ \frac{1}{|\mathbf{q}\mathcal{U}|} \int_{\mathbf{q}\mathcal{U}} \Theta_{\mathbf{q}}^{(1)}(\mathbf{x})\, w_{el}^{(1)}\left(\bar{\mathbf{d}} + \nabla \times \mathbf{a}'\right) + \Theta_{\mathbf{q}}^{(2)}(\mathbf{x})\, w_{el}^{(2)}\left(\bar{\boldsymbol{R}}_{\mathbf{q}}^{K}, \bar{\mathbf{d}} + \nabla \times \mathbf{a}'\right) d\mathbf{x} \right\}. \tag{3.72}$$

In this expression, $w_{el}^{(1)}$ and $w_{el}^{(2)}$ are given by (2.16) and (2.23), respectively, and $\mathbf{a}'$ denotes the periodic fluctuation of the electric vector potential in the deformed configuration. In addition, $\mathbf{q}\mathcal{U}$ denotes the super cell, and the $\Theta_{\mathbf{q}}^{(r)}(\mathbf{x})$ $(r = 1, 2)$ represent the $\mathbf{q}$-cell periodic characteristic functions of the phases in the deformed configuration. Note that the motions of the rigid particles in the super cell $\mathbf{q}\mathcal{U}$ are fully determined by translation vectors $\bar{\mathbf{c}}_{\mathbf{q}}^{K}$ of the particle centers, and rotation tensors $\bar{\boldsymbol{R}}_{\mathbf{q}}^{K}$ (cf. Fig. 3.3). Therefore, the characteristic functions $\Theta_{\mathbf{q}}^{(r)}$ will depend on the shape of the super cell $\mathbf{q}\mathcal{U}$, as well as on the above-defined translation vectors and rotation tensors.

It should be emphasized at this stage that writing the electric energy in its "more natural" Eulerian form (3.72) makes the explicit dependence on the deformation $\boldsymbol{F}(\mathbf{X})$ in the Lagrangian description (3.70) disappears. In other words, the electric energy $\tilde{w}_{el}^{\mathbf{q}\mathcal{U}}\left(\bar{\mathbf{d}}; \boldsymbol{F}(\mathbf{X})\right)$ depends on the deformation field $\boldsymbol{F}(\mathbf{X})$ only via the macroscopic deformation $\bar{\boldsymbol{F}}$, which determines the shape of the deformed super cell $\mathbf{q}\mathcal{U}$, and the positions and orientations of the rigid particles in the super cell, as given by

the vectors $\bar{\mathbf{c}}_{\mathbf{q}}^{K}$ and tensors $\bar{\boldsymbol{R}}_{\mathbf{q}}^{K}$, i.e.,

$$\tilde{w}_{el}^{\mathbf{q}\mathcal{U}}\left(\bar{\mathbf{d}};\boldsymbol{F}\left(\mathbf{X}\right)\right)=\tilde{w}_{el}^{\mathbf{q}\mathcal{U}}\left(\bar{\mathbf{d}},\bar{\boldsymbol{F}};\bar{\mathbf{c}}_{\mathbf{q}}^{K},\bar{\boldsymbol{R}}_{\mathbf{q}}^{K}\right). \tag{3.73}$$

Now, using the results (3.71) and (3.73), the variational problem (3.69) can be rewritten as

$$\tilde{W}^{\mathbf{q}\mathcal{U}_0}\left(\bar{\boldsymbol{F}},\bar{\mathbf{D}}\right)=\min_{\bar{\mathbf{c}}_{\mathbf{q}}^{K},\bar{\boldsymbol{R}}_{\mathbf{q}}^{K}}\left\{\tilde{W}_{me}^{\mathbf{q}\mathcal{U}_0}\left(\bar{\boldsymbol{F}};\bar{\mathbf{c}}_{\mathbf{q}}^{K},\bar{\boldsymbol{R}}_{\mathbf{q}}^{K}\right)+\bar{J}\,\tilde{w}_{el}^{\mathbf{q}\mathcal{U}}\left(\bar{\mathbf{d}},\bar{\boldsymbol{F}};\bar{\mathbf{c}}_{\mathbf{q}}^{K},\bar{\boldsymbol{R}}_{\mathbf{q}}^{K}\right)\right\}, \tag{3.74}$$

where

$$\tilde{W}_{me}^{\mathbf{q}\mathcal{U}_0}\left(\bar{\boldsymbol{F}};\bar{\mathbf{c}}_{\mathbf{q}}^{K},\bar{\boldsymbol{R}}_{\mathbf{q}}^{K}\right)=\min_{\mathbf{u}'\in\mathbf{q}\mathcal{U}_0^{\#\dagger}}\left\{\frac{1}{\left|\mathbf{q}\mathcal{U}_0^{\dagger}\right|}\int_{\mathbf{q}\mathcal{U}_0^{\dagger}}W_{me}\left(\mathbf{X};\bar{\boldsymbol{F}}+\nabla\mathbf{u}'\right)\,d\mathbf{X}\right\}. \tag{3.75}$$

In this last expression, $\mathbf{q}\mathcal{U}_0^{\#\dagger}$ denotes the set of $\mathbf{q}\mathcal{U}_0$-periodic fluctuation functions for the displacement field in the elastic matrix excluding the rigid inclusions (in their reference configuration), with prescribed rigid body motion on their boundaries, as determined by $\bar{\mathbf{c}}_{\mathbf{q}}^{K}$ and $\bar{\boldsymbol{R}}_{\mathbf{q}}^{K}$.

In conclusion, expression (3.74) for $\tilde{W}^{\mathbf{q}\mathcal{U}_0}\left(\bar{\boldsymbol{F}},\bar{\mathbf{D}}\right)$, together with (3.72) and (3.75) for $\tilde{w}_{el}^{\mathbf{q}\mathcal{U}}$ and $\tilde{W}_{me}^{\mathbf{q}\mathcal{U}_0}$, respectively, show that, for a given set of translation vectors $\bar{\mathbf{c}}_{\mathbf{q}}^{K}$ and rotations tensors $\bar{\boldsymbol{R}}_{\mathbf{q}}^{K}$, the inner elastic and electric problems can be solved independently of each other. Then, the outer minimization problem (with respect to $\bar{\mathbf{c}}_{\mathbf{q}}^{K}$ and $\bar{\boldsymbol{R}}_{\mathbf{q}}^{K}$) may be performed in order to obtain the effective potential $\tilde{W}^{\mathbf{q}\mathcal{U}_0}\left(\bar{\boldsymbol{F}},\bar{\mathbf{D}}\right)$ for the electro-active composite, as well as the equilibrium displacements and rotations of the inclusions in the super cell. We refer to expression (3.74) as the "partial decoupling strategy" for periodic DECs.

Performing the outer minimization in the variational problem (3.74) requires the knowledge of explicit expressions, in terms of $\bar{\mathbf{c}}_{\mathbf{q}}^{K}$ and $\bar{\boldsymbol{R}}_{\mathbf{q}}^{K}$ , for the effective potentials $\tilde{W}_{me}^{\mathbf{q}\mathcal{U}_0}$ and $\tilde{w}_{el}^{\mathbf{q}\mathcal{U}}$. In most cases, such explicit expressions are not easily obtained. However, using the solution of the purely mechanical problem, it is possible to generate approximate results for the above outer minimization problem.

Thus, letting $\bar{\mathbf{c}}_{\mathbf{q}m}^{K}$ and $\bar{\boldsymbol{R}}_{\mathbf{q}m}^{K}$ denote the particle translations and rotations in the

purely mechanical problem

$$\tilde{W}_{me}^{\mathbf{q}\mathcal{U}_0}\left(\bar{\boldsymbol{F}}\right) = \min_{\bar{\mathbf{c}}_{\mathbf{q}},\bar{\boldsymbol{R}}_{\mathbf{q}}} \tilde{W}_{me}^{\mathbf{q}\mathcal{U}_0}\left(\bar{\boldsymbol{F}};\bar{\mathbf{c}}_{\mathbf{q}},\bar{\boldsymbol{R}}_{\mathbf{q}}\right), \tag{3.76}$$

it follows from (3.74) that

$$\tilde{W}^{\mathbf{q}\mathcal{U}_0}\left(\bar{\boldsymbol{F}},\bar{\mathbf{D}}\right) \leq \tilde{W}_{me}^{\mathbf{q}\mathcal{U}_0}\left(\bar{\boldsymbol{F}};\bar{\mathbf{c}}_{\mathbf{q}m}^{K},\bar{\boldsymbol{R}}_{\mathbf{q}m}^{K}\right) + \bar{J}\,\tilde{w}_{el}^{\mathbf{q}\mathcal{U}}\left(\bar{\mathbf{d}},\bar{\boldsymbol{F}};\bar{\mathbf{c}}_{\mathbf{q}m}^{K},\bar{\boldsymbol{R}}_{\mathbf{q}m}^{K}\right), \tag{3.77}$$

which provides an estimate for the effective electro-active potential $\tilde{W}^{\mathbf{q}\mathcal{U}_0}\left(\bar{\boldsymbol{F}},\bar{\mathbf{D}}\right)$. The exact result (3.74), or the estimate (3.77) for the super-cell problem can then be used, via (3.7), to estimate the overall effective potential of the electro-active composite $\tilde{W}\left(\bar{\boldsymbol{F}},\bar{\mathbf{D}}\right)$ in the post-bifurcation regime.

Before the onset of any macroscopic or microscopic instabilities, the overall effective potential $\tilde{W}$ is expected to be given by the effective one-cell periodic potential, as defined by

$$\hat{W}\left(\bar{\boldsymbol{F}},\bar{\mathbf{D}}\right) = \tilde{W}^{\mathcal{U}_0}\left(\bar{\boldsymbol{F}},\bar{\mathbf{D}}\right) = \min_{\mathbf{u}'\in\mathcal{U}_0^{\#}} \min_{\mathbf{A}'\in\mathcal{U}_0^{\#}} \left\{ \frac{1}{|\mathcal{U}_0|} \int_{\mathcal{U}_0} W\left(\mathbf{X};\bar{\boldsymbol{F}}+\nabla\mathbf{u}',\bar{\mathbf{D}}+\nabla\times\mathbf{A}'\right) d\mathbf{X} \right\}, \tag{3.78}$$

where $\mathcal{U}_0^{\#}$ denotes the set of all one-cell periodic fluctuation functions for $\mathbf{u}'$ (or $\mathbf{A}'$). For small strains and small electric displacement fields (i.e., near $\bar{\boldsymbol{F}} = \boldsymbol{I}$ and $\bar{\mathbf{D}} = 0$), it is expected that

$$\tilde{W}\left(\bar{\boldsymbol{F}},\bar{\mathbf{D}}\right) = \hat{W}\left(\bar{\boldsymbol{F}},\bar{\mathbf{D}}\right). \tag{3.79}$$

However, as the macroscopic loadings ($\bar{\boldsymbol{F}}$ and $\bar{\mathbf{D}}$) increase, eventually we will have $\tilde{W}\left(\bar{\boldsymbol{F}},\bar{\mathbf{D}}\right) < \hat{W}\left(\bar{\boldsymbol{F}},\bar{\mathbf{D}}\right)$. Therefore, it is important to find a set of values for the macroscopic deformation and electric displacement fields, such that the condition (3.79) holds. Hence the reason for obtaining the one-cell periodic effective potential $\hat{W}$. Since the composite remains one-cell periodic in the pre-bifrucation regime each unit cell $\mathcal{U}$ will contain only one inclusion. Therefore, the translation of the particle will be known a priori (since the particle will remain at the center of the unit cell $\mathcal{U}$) and the rotation of the particle will be equal to the average rotation of all the

particles and is denoted by $\bar{\boldsymbol{R}}^{(2)}$. Therefore, we have that

$$\tilde{W}\left(\bar{\boldsymbol{F}},\bar{\mathbf{D}}\right)=\hat{W}\left(\bar{\boldsymbol{F}},\bar{\mathbf{D}}\right)=\min_{\bar{\boldsymbol{R}}^{(2)}}\left\{\hat{W}_{me}\left(\bar{\boldsymbol{F}};\bar{\boldsymbol{R}}^{(2)}\right)+\bar{J}\,\hat{w}_{el}\left(\bar{\mathbf{d}},\bar{\boldsymbol{F}};\bar{\boldsymbol{R}}^{(2)}\right)\right\}, \tag{3.80}$$

where $\hat{W}_{me}$ and $\hat{w}_{el}$ are effective one-cell potentials for the purely mechanical and purely electric problems for a fixed $\bar{\boldsymbol{R}}^{(2)}$, as determined by

$$\hat{W}_{me}\left(\bar{\boldsymbol{F}};\bar{\boldsymbol{R}}^{(2)}\right)=\min_{\mathbf{u}'\in\mathcal{U}_0^{\#\dagger}}\left\{\frac{1}{|\mathcal{U}_0^{\dagger}|}\int_{\mathcal{U}_0^{\dagger}}W_{me}\left(\mathbf{X};\bar{\boldsymbol{F}}+\nabla\mathbf{u}'\right)\,d\mathbf{X}\right\}, \tag{3.81}$$

and

$$\hat{w}_{el}\left(\bar{\mathbf{d}},\bar{\boldsymbol{F}};\bar{\boldsymbol{R}}^{(2)}\right)=\min_{\mathbf{a}'\in\mathcal{U}^{\#}}\left\{\frac{1}{|\mathcal{U}|}\int_{\mathcal{U}}\Theta^{(1)}(\mathbf{x})\,w_{el}^{(1)}\left(\bar{\mathbf{d}}+\nabla\times\mathbf{a}'\right)+\Theta^{(2)}(\mathbf{x})\,w_{el}^{(2)}\left(\bar{\boldsymbol{R}}^{(2)},\bar{\mathbf{d}}+\nabla\times\mathbf{a}'\right)d\mathbf{x}\right\}, \tag{3.82}$$

respectively. Here, the $\Theta^{(r)}$ $(r=1,2)$ are the one-cell periodic characteristic functions of the phases in the deformed configuration, as described earlier in Section 3.3.2, $\mathcal{U}$ is the unit cell in the deformed configuration, and $\mathcal{U}_0^{\dagger}$ is the unit cell in the reference configuration excluding the inclusion with the prescribed rigid body motion on the inner boundary (interface of the elastic matrix and the rigid inclusion), as determined by $\bar{\boldsymbol{R}}^{(2)}$.

Therefore, following the same procedure as for the **q**-cell periodic case, the overall effective potential of the composite (before the onset of microscopic instabilities) can be approximated as

$$\tilde{W}\left(\bar{\boldsymbol{F}},\bar{\mathbf{D}}\right)=\hat{W}\left(\bar{\boldsymbol{F}},\bar{\mathbf{D}}\right)\leq\hat{W}_{me}\left(\bar{\boldsymbol{F}};\bar{\boldsymbol{R}}_m^{(2)}\right)+\bar{J}\,\hat{w}_{el}\left(\bar{\mathbf{d}},\bar{\boldsymbol{F}};\bar{\boldsymbol{R}}_m^{(2)}\right), \tag{3.83}$$

where $\bar{\boldsymbol{R}}_m^{(2)}$ is the minimizer of the purely mechanical, one-cell, periodic problem

$$\hat{W}_{me}\left(\bar{\boldsymbol{F}}\right)=\min_{\bar{\boldsymbol{R}}^{(2)}}\hat{W}_{me}\left(\bar{\boldsymbol{F}};\bar{\boldsymbol{R}}^{(2)}\right). \tag{3.84}$$

It should be emphasized that the rotation $\bar{\boldsymbol{R}}_m^{(2)}$ minimizing the energy in this expression for $\hat{W}_{me}$ is precisely the rotation that would be induced in the purely mechanical

problem under an applied deformation $\bar{\boldsymbol{F}}$ (allowing the particle to rotate freely).

The estimate (3.83) for the macroscopic potential $\hat{W}$ (or (3.77) for $\tilde{W}^{\mathcal{qU}_0}$) is given in terms of two complementary contributions: the purely mechanical macroscopic potential $\hat{W}_{me}$ (or $\tilde{W}_{me}^{\mathcal{qU}_0}$) in the reference configuration and the purely electrostatic macroscopic potential $\hat{w}_{el}$ (or $\tilde{w}_{el}^{\mathcal{qU}}$) in the deformed configuration. However, these two contributions are only partially decoupled, since the electrostatic effective energy depends on the deformation field via $\bar{\boldsymbol{F}}$ and potentially the rigid body rotation and translation of the inclusions in the unit cell. For this reason we will refer to expression (3.83) (or (3.77)) as the "partial decoupling" approximation.

### 3.3.4 Hashin-Shtrikman estimates for the effective electrostatic energy of two-phase periodic DECs

The partial decoupling strategy/approximation introduced previously is especially useful when an estimate is available for the purely mechanical homogenization problem. Thus, assuming the availability of such an estimate for the purely mechanical effective energy, in this subsection we provide the Hashin-Shtrikman estimates for the electrostatic effective energy of DECs with periodic microstructures. This will be done for the one-cell periodic pre-bifurcation regime, for simplicity.

The purely electrostatic homogenization problem (3.82) associated with $\hat{w}_{el}$ for the electric behavior of the phases given by (2.16) and (2.22), reduces to

$$\hat{w}_{el}\left(\bar{\mathbf{d}},\bar{\boldsymbol{F}};\bar{\boldsymbol{R}}^{(2)}\right)=\min_{\mathbf{a}'\in\mathcal{U}^{\#}}\left\langle\frac{1}{2}\left(\bar{\mathbf{d}}+\nabla\times\mathbf{a}'\right)\cdot\boldsymbol{\varepsilon}^{-1}\left(\mathbf{x}\right)\left(\bar{\mathbf{d}}+\nabla\times\mathbf{a}'\right)\right\rangle_{\mathcal{U}}=\frac{1}{2}\bar{\mathbf{d}}\cdot\tilde{\boldsymbol{\varepsilon}}^{-1}\bar{\mathbf{d}},\tag{3.85}$$

where $\tilde{\boldsymbol{\varepsilon}}$ is the homogenized permittivity of the composite in the deformed configuration. In (3.85), $\boldsymbol{\varepsilon}\left(\mathbf{x}\right)$ is the periodic local permittivity, and it is given by an expression similar to (3.40), i.e.,

$$\boldsymbol{\varepsilon}\left(\mathbf{x}\right)=\varepsilon^{(1)}\boldsymbol{I}+\Theta^{(2)}\left(\mathbf{x}\right)\left(\boldsymbol{\varepsilon}^{(2)}-\varepsilon^{(1)}\boldsymbol{I}\right)\tag{3.86}$$

where $\Theta^{(2)}\left(\mathbf{x}\right)$ is now the periodic characteristic function for the inclusion phase, as

given by (3.64).

Estimates for the effective permittivity of two-phase composites, defined by (3.85) with the constitutive behavior (3.86), and one-cell periodic microstructures, as described in section 3.3.2, can be obtained by generalizing the "linear comparison" method of Ponte Castañeda & Willis (1995) for periodic composites , as follows

$$\tilde{\boldsymbol{\varepsilon}} = \varepsilon^{(1)}\boldsymbol{I} + c^I\left[\left(\boldsymbol{\varepsilon}^{(2)} - \varepsilon^{(1)}\boldsymbol{I}\right)^{-1} + \boldsymbol{P}\right]^{-1}. \tag{3.87}$$

Here, $c^I$ is the (current) volume fraction of the particles, and the microstructural tensor $\boldsymbol{P}$ is given (Nemat-Nasser & Hori 1993) (see also Nemat-Nasser et al. 1982) by the following infinite sum

$$\boldsymbol{P} = \frac{1}{\varepsilon^{(1)}}\sum_{\boldsymbol{\xi}\neq 0}\frac{1}{|\boldsymbol{\xi}|^2}\,(\boldsymbol{\xi}\otimes\boldsymbol{\xi})\,g(\boldsymbol{\xi})\,g(-\boldsymbol{\xi}), \tag{3.88}$$

where

$$\boldsymbol{\xi} = n_1\mathbf{k}^1 + n_2\mathbf{k}^2 + n_3\mathbf{k}^3 \quad \text{for all } n_i \in \mathbb{Z}. \tag{3.89}$$

are the RL points in the deformed configuration, and $g(\boldsymbol{\xi})$ is the volume average of $e^{i\mathbf{x}\cdot\boldsymbol{\xi}}$ over one inclusion. For an ellipsoidal inclusion with shape tensor $\boldsymbol{Z}^I$ in the deformed configuration, $g(\boldsymbol{\xi})$ is given (see Nemat-Nasser & Hori 1993) by

$$g(\boldsymbol{\xi}) = \frac{3}{\eta^3}(\sin\eta - \eta\cos\eta), \quad \text{where} \quad \eta = |\boldsymbol{Z}\boldsymbol{\xi}|. \tag{3.90}$$

Note that the above microstructural tensor depends on the deformation via the RL lattice points $\boldsymbol{\xi}$, as well as the shape tensor of the rigid inclusion in the deformed configuration $\boldsymbol{Z}^I$. Therefore, it is useful to rewrite the above expression for the electrostatic microstructural tensor $\boldsymbol{P}$ in terms of its reference counterpart $\boldsymbol{P}_0$ and the macroscopic loading, $\bar{\boldsymbol{F}}$ and $\bar{\mathbf{D}}$.

Using (3.63), it can be shown that the deformed RL points are related to their reference counterparts via

$$\boldsymbol{\xi} = \bar{\boldsymbol{F}}^{-T}\boldsymbol{\xi}_0, \quad \text{where} \quad \boldsymbol{\xi}_0 = n_1\mathbf{K}^1 + n_2\mathbf{K}^2 + n_3\mathbf{K}^3 \tag{3.91}$$

are the reference RL points corresponding to $\boldsymbol{\xi}$. In addition, assuming that the rotation of the particles $\bar{\boldsymbol{R}}^{(2)}$ is specified, $\boldsymbol{Z}^I$ can be written in terms of its reference counterpart $\boldsymbol{Z}_0^I$, via $(3.65)_2$. Therefore, (3.88) can be rewritten as follows

$$\boldsymbol{P} = \frac{1}{\varepsilon^{(1)}} \bar{\boldsymbol{R}} \hat{\boldsymbol{P}}_0 \left( \bar{\boldsymbol{U}}, \boldsymbol{R}^p \right) \bar{\boldsymbol{R}}^T, \tag{3.92}$$

where

$$\hat{\boldsymbol{P}}_0 = \bar{\boldsymbol{U}}^{-1} \left\{ \sum_{\boldsymbol{\xi}_0 \neq 0} \frac{1}{\left| \bar{\boldsymbol{U}}^{-1} \boldsymbol{\xi}_0 \right|^2} \left( \boldsymbol{\xi}_0 \otimes \boldsymbol{\xi}_0 \right) g\left( \boldsymbol{\xi}_0 \right) g\left( -\boldsymbol{\xi}_0 \right) \right\} \bar{\boldsymbol{U}}^{-1}. \tag{3.93}$$

In the above equation

$$g\left( \boldsymbol{\xi}_0 \right) = \frac{3}{\eta^3} \left( \sin \eta - \eta \cos \eta \right), \quad \text{where} \quad \eta = \left| \boldsymbol{Z}_0^I \boldsymbol{R}^{pT} \bar{\boldsymbol{U}}^{-1} \boldsymbol{\xi}_0 \right|. \tag{3.94}$$

In obtaining the above expression for $\hat{\boldsymbol{P}}_0$, we have used the polar decomposition $\bar{\boldsymbol{F}} = \bar{\boldsymbol{R}} \bar{\boldsymbol{U}}$ as well as the definition $\boldsymbol{R}^p = \bar{\boldsymbol{R}}^T \bar{\boldsymbol{R}}^{(2)}$ for the relative rotation.

Using (3.92) and (3.41), the load dependent effective permittivity $\tilde{\boldsymbol{\varepsilon}}$, as given by (3.87), can be rewritten as follows

$$\tilde{\boldsymbol{\varepsilon}} \left( \bar{\boldsymbol{F}}; \bar{\boldsymbol{R}}^{(2)} \right) = \bar{\boldsymbol{R}} \tilde{\boldsymbol{\mathcal{E}}} \left( \bar{\boldsymbol{U}}; \bar{\boldsymbol{R}}^{(2)} \right) \bar{\boldsymbol{R}}^T, \tag{3.95}$$

where

$$\tilde{\boldsymbol{\mathcal{E}}} \left( \bar{\boldsymbol{U}}; \bar{\boldsymbol{R}}^{(2)} \right) = \varepsilon^{(1)} \boldsymbol{I} + \frac{C_0^I}{\bar{J}} \left[ \boldsymbol{R}^p \left( \boldsymbol{\mathcal{E}}^{(2)} - \varepsilon^{(1)} \boldsymbol{I} \right)^{-1} \boldsymbol{R}^{pT} + \hat{\boldsymbol{P}}_0 \left( \bar{\boldsymbol{U}}, \boldsymbol{R}^p \right) / \varepsilon^{(1)} \right]^{-1}, \tag{3.96}$$

which is seen to be exactly identical to (3.49), with the only difference that now $\hat{\boldsymbol{P}}_0$ is given by (3.93).

Similar to the random case, the fully Lagrangian estimate for electrostatic energy is given by

$$\hat{W}_{el} \left( \bar{\boldsymbol{F}}, \bar{\mathbf{D}}; \bar{\boldsymbol{R}}^{(2)} \right) = \frac{1}{2\bar{J}} \bar{\mathbf{D}} \cdot \left[ \bar{\boldsymbol{U}} \tilde{\boldsymbol{\mathcal{E}}}^{-1} \left( \bar{\boldsymbol{U}}; \bar{\boldsymbol{R}}^{(2)} \right) \bar{\boldsymbol{U}} \right] \bar{\mathbf{D}}, \tag{3.97}$$

for a given (fixed) rotation $\bar{\boldsymbol{R}}^{(2)}$. Assuming that the corresponding estimate for $\hat{W}_{me} \left( \bar{\boldsymbol{F}}; \bar{\boldsymbol{R}}^{(2)} \right)$ is also known, the effective one-cell periodic electro-active energy of

the composite is obtained via

$$\tilde{W}\left(\bar{\boldsymbol{F}},\bar{\mathbf{D}}\right)=\min_{\bar{\boldsymbol{R}}^{(2)}}\left\{\hat{W}_{me}\left(\bar{\boldsymbol{F}};\bar{\boldsymbol{R}}^{(2)}\right)+\hat{W}_{el}\left(\bar{\boldsymbol{F}},\bar{\mathbf{D}};\bar{\boldsymbol{R}}^{(2)}\right)\right\}. \tag{3.98}$$

The stationary condition and constitutive relations associated with the above energy can be shown to be exactly identical to those of random two-phase DECs, as given by equations (3.52)-(3.55), where now the one-cell periodic energies $\hat{W}_{me}$ and $\hat{W}_{el}$ are used in the corresponding expressions.

## 3.4 Concluding remarks

In this chapter, we have proposed a homogenization framework for DECs at finite strains. In addition, this framework has been used to develop constitutive models for electro-active composites consisting of initially aligned, rigid dielectric particles distributed randomely or periodically in a dielectric elastomeric matrix. Assuming that the dielectric properties of the elastomer phase are isotropic and independent of the deformation, a decoupling strategy has been proposed. The strategy consists in writing the electro-elastic homogenization problem in terms of a "purely mechanical" homogenization problems in the reference configuration and a "purely electrostatic" homogenization problem in the deformed configuration, coupled only through a set of kinematic parameters describing the details of the microstructure in the deformed configuration (e.g., the particle positions and orientations within the appropriately defined unit cell in the deformed configuration in the periodic case). We have also shown that these results may be simplified further by taking the set of the kinematic parameters to be given by the solution of the purely mechanical problem when the microstructure is allowed to evolve freely as a result of the the imposed deformations. Such an approximation, also known as the "partial decoupling" approximation (first introduced by Ponte Castañeda & Galipeau 2011, in the context of magneto-elastic composites), is expected to become more accurate in the "stiff matrix" limit (i.e., when the matrix stiffness is large compared to the electric effects, so that the addi-

tional rotations due to the presence of the electric fields are negligible compared to the rotations induced by the deformation). Furthermore, as mentioned above the partial decoupling approximation is exact for the special case of aligned composites under aligned loading conditions. Finally, in the context of periodic composites we have provided the generalizations of the above-mentioned approach in the post-bifurcation regime, where the composite develops deformation patterns that are periodic on multiple cells.

The new estimates for the DECs developed in this chapter rely on corresponding estimates for the purely mechanical behavior of such material systems consisting of elastomers reinforced by aligned rigid inclusions. Such estimates may be obtained by means of the "second-order" linear comparison homogenization methods (Ponte Castañeda & Tiberio 2000, Lopez-Pamies & Ponte Castañeda 2006*b*) for composites with periodic (Brun et al. 2007, Michel et al. 2010*b*) or random (Lopez-Pamies & Ponte Castañeda 2006*b*) microstructures. In this chapter, estimates for the electrostatic energies have been obtained by adaptation of the Hashin-Shtrikman-type estimates of Ponte Castañeda et al. (1992) for random composites and Nemat-Nasser et al. (1982) for periodic composites. The resulting estimates lead to deformation-dependent predictions for the effective dielectric permittivity of the DECs, giving rise to "extra" stresses beyond the purely mechanical stress and the Maxwell-like stress in the composite. In other words, the macroscopic electromechanical response of the composite is not that of an "ideal dielectric" (Zhao & Suo 2008), even when the matrix material is assumed to be an ideal dielectric itself. This phenomenon has been linked to the deformation-induced configurational changes in the microstructure (i.e., change in the concentration or orientation of the inclusions or changes in the shape of the distribution) of the DEC. In this context, it is also relevant to note that the results of this chapter can be helpful in identifying the underlying microscopic mechanisms associated with the macroscopic behavior of electro-active composites. This in turn opens up the possibility of optimizing the relevant microstructural parameters to design DECs with enhanced properties (e.g., larger electrostrictive strains and controlled field-actuated stiffness), as will be seen later on in upcoming chapters.

# Part II: Applications

# Chapter 4

# DECs in the limit of infinitesimal deformations

In this chapter, we provide estimates for the effective response of Dielectric Ealstomer Composites (DECs) consisting of aligned ellipsoidal inclusions of a stiff dielectric material which are distributed randomly in an soft elastomeric matrix with "ellipsoidal" two-point statistics. The derivation of the results for the electro-mechanical response assumes linearized deformations, but includes non-linear (quadratic) terms in the electric fields. We investigate three different physical mechanisms contributing to the macroscopic electro-mechanical response of the composite: the intrinsic effect of the particles on the Maxwell stress, the inter-particle (dipole) interactions which are accounted for by evaluating the effect of the changes in the "shape" of the two-point probability functions with the deformation, and the effect of particle rotations and torques when the geometric and/or anisotropy axis of the particles are not aligned with the applied electric field. Several illustrative examples are provided to emphasize the relative importance of the different effects on the overall electrostriction of the composites for infinitesimal deformations. In particular, we provide results for the "compliant electrode" boundary conditions that are widely used in applications. We show that inter-particle interactions are synergistic with the intrinsic effect of the particles on the Maxwell stress, leading to significant enhancements in the electro-mechanical coupling of the DECs, especially at high particle concentrations. On

the other hand, the effect of electric torques on non-aligned particles is generally deleterious for electrostriction. The rest of this chapter is organized as follows. Section 4.1 provides a general framework for *anisotropic* electro-elastic materials in the context of infinitesimal deformation (Landau et al. 1984) by appropriately linearizing a thermodynamically consistent finite strain theory (Toupin 1956, Kovetz 1990, Hutter et al. 2006). In section 4.2 we introduce the general homogenization framework for DECs (Ponte Castañeda & Siboni 2012) in the infinitesimal deformation regime. Section 4.3 is concerned with the development of explicit estimates for the macroscopic response of two-phase DECs with random microstructures under general coupled electro-mechanical loading conditions. In section 4.4 we provide some sample applications to illustrate the theory developed in this chapter, and to investigate the effect of various microstructural parameters on the overall electro-active response of DECs.

## 4.1 Infinitesimal electroelasticity

Making use of the thermodynamically consistent, finite-deformation formulation of Chapter 2, here we obtain a suitably linearized theory (Landau et al. 1984) for anisotropic deformable dielectrics with zero or negligible piezo-electric coupling.

The deformation of a homogeneous electro-active material under the simultaneous action of mechanical and electrostatic loads is described by a continuous one-to-one map $\mathbf{x} = \mathbf{x}(\mathbf{X})$ between the (material) points in the reference ($\mathbf{X}$) and deformed ($\mathbf{x}$) configurations. In the infinitesimal limit, such deformations can be characterized by the displacement gradient $\nabla\mathbf{u}$, where $\mathbf{u} := \mathbf{x} - \mathbf{X}$ denotes the infinitesimal displacement. This displacement gradient can be decomposed into a symmetric part, $\boldsymbol{\epsilon} = \frac{1}{2}\left(\nabla\mathbf{u} + \nabla\mathbf{u}^T\right)$, and an antisymmetric part, $\boldsymbol{\omega} = \frac{1}{2}\left(\nabla\mathbf{u} - \nabla\mathbf{u}^T\right)$. They correspond, respectively, to the infinitesimal strain and rotation tensors.

The set of equations governing the Eulerian electric field $\mathbf{e}$ and electric displacement filed $\mathbf{d}$ are given by the Maxwell's equations (2.4) and the jump conditions (2.6). Similarly, the equations governing the (total) Cauchy stress $\boldsymbol{T}$, are given by

the conservation of linear and angular momentum equations (2.1) and (2.2), and the jump condition $(2.3)_2$. As it was mentioned earlier in Chapter 2, the total Cauchy stress $\boldsymbol{T}$ also includes the electrostatic effects (see further below for more details).

It is important to emphasize that the jump conditions for the electric fields and total stress can also be used at the interface of the specimen and the surrounding empty space to obtain appropriate boundary conditions for the problem. However, in doing so, one has to recognize that neither the electric fields nor the total stress are zero in the vacuum. In fact, it is well known that vacuum can carry the so-called Maxwell stress

$$\boldsymbol{T}_0^M = \varepsilon_0 \mathbf{e} \otimes \mathbf{e} - \frac{\varepsilon_0}{2} (\mathbf{e} \cdot \mathbf{e}) \boldsymbol{I}, \tag{4.1}$$

which is self-equilibrated (i.e., $\operatorname{div} \boldsymbol{T}_0^M = 0$). Therefore, the boundary condition for the stress can be written as

$$[\![\boldsymbol{T}]\!] \mathbf{m} + \mathbf{t}^{ex} = 0, \tag{4.2}$$

where $\mathbf{t}^{ex}$ denotes the externally applied mechanical traction on the boundary of the specimen. In case of having a prescribed displacement on the boundary, the same expression as in (4.2) can be used to obtain the external mechanical traction required to maintain that displacement.

The above set of governing equations is completed by introducing appropriate constitutive relations (Landau et al. 1984) for $\mathbf{e}$ and $\boldsymbol{T}$ in terms of $\mathbf{d}$ and $\nabla \mathbf{u}$. As shown in Appendix C, they can be obtained by suitably linearizing the corresponding constitutive relations for finite deformations. In particular, the electric constitutive equation may be written in the form

$$\mathbf{e} = \boldsymbol{\varepsilon}^{-1} (\boldsymbol{\epsilon}, \boldsymbol{\omega}) \mathbf{d}, \tag{4.3}$$

where

$$\boldsymbol{\varepsilon} (\boldsymbol{\epsilon}, \boldsymbol{\omega}) = \boldsymbol{\mathcal{E}}_0 + \boldsymbol{\omega} \boldsymbol{\mathcal{E}}_0 - \boldsymbol{\mathcal{E}}_0 \boldsymbol{\omega} + \mathbb{S} \boldsymbol{\epsilon} \tag{4.4}$$

is the permittivity in the deformed configuration, which can be seen to depend on both the strain $\boldsymbol{\epsilon}$ and the rotation $\boldsymbol{\omega}$. In this expression, $\boldsymbol{\mathcal{E}}_0$ is the permittivity of the

material in the reference (undeformed) configuration, and the fourth-order tensor $\mathbb{S}$ is defined by

$$S_{ijkl} = \left.\frac{\partial \mathcal{E}_{ij}(\boldsymbol{\epsilon})}{\partial \epsilon_{kl}}\right|_{\boldsymbol{\epsilon}=\mathbf{0}}, \tag{4.5}$$

where $\boldsymbol{\mathcal{E}}(\boldsymbol{\epsilon})$ is the "strain-dependent permittivity" in a fictitious frame that rotates with the material, as defined by expression (C.6). Note that $\mathbb{S}$ satisfies the symmetry properties $S_{ijkl} = S_{jikl} = S_{ijlk}$.

In the absence of electric fields, the mechanical response of the material is determined by the following expression for the "purely mechanical" stress

$$\boldsymbol{T}^{me} = \mathbb{C}\boldsymbol{\epsilon}, \tag{4.6}$$

where $\mathbb{C}$ is the standard elasticity modulus tensor, satisfying the usual major and minor symmetry relations. On the other hand, to describe the electro-mechanical response of the material under small deformations, we introduce a reference dielectric coefficient $\varepsilon$, a reference shear modulus $\mu$ and a reference electric field of magnitude $e$, and define the dimensionless parameter

$$\kappa = \frac{\varepsilon e^2}{\mu}, \tag{4.7}$$

serving to characterize the relative strengths of the electric and mechanical effects. Then, under the assumption that $\kappa$ is small, such that $\kappa \sim |\boldsymbol{\epsilon}|$, it is shown in Appendix C that the total stress can be written in the form

$$\boldsymbol{T} = \boldsymbol{T}^{me} + \boldsymbol{T}^{el}, \tag{4.8}$$

where $\boldsymbol{T}^{me}$ is the purely mechanical stress given by (4.6) and $\boldsymbol{T}^{el}$ is the "electrostatic" stress determined by equation (C.10). The electrostatic stress can, in turn, be decomposed into two parts (Krakovsky et al. 1999, Lee et al. 2005), namely,

$$\boldsymbol{T}^{el} = \boldsymbol{T}^{M} + \boldsymbol{T}^{es}, \tag{4.9}$$

where

$$\boldsymbol{T}^{M} = \frac{1}{2}\left(\mathbf{e}\otimes\mathbf{d}+\mathbf{d}\otimes\mathbf{e}\right) - \frac{1}{2}\left(\mathbf{e}\cdot\mathbf{d}\right)\boldsymbol{I}, \quad \text{and} \quad \boldsymbol{T}^{es} = -\frac{1}{2}\mathbb{S}^{\dagger}(\mathbf{e}\otimes\mathbf{e}), \tag{4.10}$$

are respectively the "Maxwell" and "electrostrictive" contributions to the total stress. Intuitively, the Maxwell contribution can be associated to the attractive forces between the opposite charges that are produced on the surface of the dielectric (or the conducting electrodes attached to it). On the other hand, the electrostrictive contribution is associated with dipole and other interactions intrinsic to the material, as already pointed out by Lee et al. (2005). The importance of these two contributions will be discussed in more detail later in this chapter.

It should be emphasized that the electric fields appearing in the above equation for the total stress are Eulerian variables, which depend on the deformation. In the limit of infinitesimal deformations, the Eulerian and Lagrangian descriptions of the electric field and electric displacement field are of course identical to zeroth order in the strain. However, as shown in Appendix C, the electromechanical coupling tensor $\mathbb{S}$ arises from the correction terms, and therefore the difference between the Eulerian and Lagrangian descriptions *cannot* simply be ignored.

## 4.2 Homogenization framework for the infinitesimal deformation limits

Like before we consider an electro-active composite specimen ($\Omega_0$ in the reference configuration) consisting of two or more homogeneous phases that satisfies the assumptions of *separation of length scale*. Our goal here is to obtain effective constitutive equations of such composites in the limit of infinitesimal deformations. Toward this goal, and consistent with macroscopically uniform fields inside a given "representative

volume element" of the composite, we prescribe the following boundary conditions

$$\begin{aligned} \mathbf{u} &= \bar{\boldsymbol{\epsilon}}\,\mathbf{X} + \bar{\boldsymbol{\omega}}\,\mathbf{X}, \quad \mathbf{X} \text{ on } \partial\Omega_0 \\ \mathbf{d}\cdot\mathbf{m} &= \bar{\mathbf{d}}\cdot\mathbf{m}, \qquad \mathbf{x} \text{ on } \partial\Omega, \end{aligned} \tag{4.11}$$

where $\bar{\boldsymbol{\epsilon}}$ and $\bar{\boldsymbol{\omega}}$ are respectively uniform symmetric and antisymmetric second-order tensors, while $\bar{\mathbf{d}}$ is a uniform vector. Note that the displacement boundary condition $(4.11)_1$ is prescribed in the reference configuration, while the electric boundary condition $(4.11)_2$ is given in the deformed configuration. Using the boundary conditions (4.11), it can be shown (via the divergence theorem) that

$$\langle \boldsymbol{\epsilon} \rangle_0 = \bar{\boldsymbol{\epsilon}}, \quad \langle \boldsymbol{\omega} \rangle_0 = \bar{\boldsymbol{\omega}}, \quad \text{and} \quad \langle \mathbf{d} \rangle = \bar{\mathbf{d}}, \tag{4.12}$$

where $\langle\cdot\rangle_0$ and $\langle\cdot\rangle$ denote the volume averages in the reference (i.e., over $\Omega_0$) and deformed (i.e., over $\Omega$) configurations. In other words, $\bar{\boldsymbol{\epsilon}}$, $\bar{\boldsymbol{\omega}}$ and $\bar{\mathbf{d}}$ can be thought of as the (uniform) macroscopic strain, rotation and electric displacement, respectively. Other types of boundary conditions could be used to define the homogenization problem which do not alter the final homogenized results, but they are not discussed here for brevity.

Given the above boundary conditions and the fact that the microstructure of the composite satisfies the *separation of length scales* hypothesis, it can be argued (Ponte Castañeda & Siboni 2012) that the composite behaves "effectively" as a homogeneous electro-active material of the type discussed in the previous section. Therefore, defining the macroscopic electric field and total stress in the composite by $\bar{\mathbf{e}} = \langle \mathbf{e} \rangle$ and $\bar{\boldsymbol{T}} = \langle \boldsymbol{T} \rangle$, respectively, the macroscopic constitutive relations for the composite are given by

$$\begin{aligned} \bar{\mathbf{e}} &= \tilde{\boldsymbol{\varepsilon}}^{-1}\left(\bar{\boldsymbol{\epsilon}}, \bar{\boldsymbol{\omega}}\right)\bar{\mathbf{d}} \\ \bar{\boldsymbol{T}} &= \tilde{\mathbb{C}}\bar{\boldsymbol{\epsilon}} - \frac{1}{2}\left(\bar{\mathbf{d}}\cdot\bar{\mathbf{e}}\right)\boldsymbol{I} + \frac{1}{2}\left(\bar{\mathbf{d}}\otimes\bar{\mathbf{e}} + \bar{\mathbf{e}}\otimes\bar{\mathbf{d}}\right) - \frac{1}{2}\tilde{\mathbb{S}}^{\dagger}\left(\bar{\mathbf{e}}\otimes\bar{\mathbf{e}}\right) \end{aligned} \tag{4.13}$$

where $\tilde{\mathbb{C}}$ denotes the effective stiffness of the composite, which is independent of the electric and deformation fields, and $\tilde{\boldsymbol{\varepsilon}}\left(\bar{\boldsymbol{\epsilon}}, \bar{\boldsymbol{\omega}}\right)$ denotes the effective deformation-

dependent permittivity of the composite, as defined by

$$\tilde{\boldsymbol{\varepsilon}}\left(\bar{\boldsymbol{\epsilon}},\bar{\boldsymbol{\omega}}\right)=\tilde{\boldsymbol{\mathcal{E}}}_0+\bar{\boldsymbol{\omega}}\tilde{\boldsymbol{\mathcal{E}}}_0-\tilde{\boldsymbol{\mathcal{E}}}_0\bar{\boldsymbol{\omega}}+\tilde{\mathbb{S}}\bar{\boldsymbol{\epsilon}}, \tag{4.14}$$

where $\tilde{\boldsymbol{\mathcal{E}}}_0$ is the effective permittivity of the DEC in the reference configuration and $\tilde{\mathbb{S}}$ is the corresponding effective electromechanical coupling tensor, which, as already mentioned, can be obtained by first determining the effective strain-dependent permittivity, as defined by (C.6), and then using the definition (4.5).

Note that, as it was the case for the homogeneous case, to be consistent with the assumptions of infinitesimal deformations the size of the electric fields has to be such that the parameter $\tilde{\kappa}=\frac{\varepsilon\bar{e}^2}{\mu}$ is small and the condition $\tilde{\kappa}\sim|\bar{\boldsymbol{\epsilon}}|$ holds. Furthermore, all the electric fields in the expression for the macroscopic total stress, $(4.13)_2$, have to be computed in the reference configuration.

For completeness, we also remark that the above-described homogenization framework is consistent with the small strain and rotations limit of the more general homogenization framework provided in Chapter 3 for finite strains, as expected. In addition, the effective constitutive relations (4.13) are consistent in form with the recent work of Tian et al. (2012), which provides a homogenization framework for small strains and rotations. In particular, consistent with (4.13), the corresponding expressions in this reference for the effective response do not contain piezoelectric contributions. (Note that such piezoelectric effects may be expected when the inclusions are ferroelectric exhibiting permanent polarizations.) On the other hand, the corresponding expression for the effective electromechanical coupling tensor $\tilde{\mathbb{S}}$ provided in Tian et al. (2012) is given in terms of the strain and electric field concentration tensors, instead of the derivative of the effective strain-dependent permittivity given in this work. However, although this remains to be shown rigorously, it is expected that these two results should be equivalent since the strain correction to the effective permittivity involves terms that are quadratic in the electric field and linear in the strain.

## 4.3 Estimates for two-phase DECs with random particulate microstructure

Here, we obtain explicit estimates for the effective constitutive response of DECs in the limit of infinitesimal deformations, including the effective stiffness and permittivity and the effective electro-active behavior.

### 4.3.1 Initial microstructure and constitutive behavior of the phases

We consider a two-phase DEC consisting of a matrix phase, denoted by the superscript "1", which could be electrically susceptible and an inclusion phase, denoted by the superscript "2". The concentrations of the matrix and inclusion phases in the reference configuration are thus given by

$$c_0^{(1)} = 1 - c_0 \quad \text{and} \quad c_0^{(2)} = c_0, \tag{4.15}$$

respectively. The inclusions are randomly distributed in the matrix, but are assumed to have identical ellipsoidal shape and orientation, so that they are geometrically characterized by ellipsoids $\mathcal{I}_0$, defined in (3.23) in terms of the shape tensor $\boldsymbol{Z}_0^I$. In addition, the inclusions are assumed to be very stiff (rigid) compared to the soft elastomeric matrix. In fact, as it will become clearer later on, the inclusions must have high dielectric coefficients in order for the DECs to exhibit large electro-active coupling. However, naturally appearing materials (e.g., ceramics) with high dielectric coefficients also tend to be very stiff mechanically. As a consequence, and for simplicity, the inclusions will be assumed to be perfectly rigid in this work.

The inclusions are distributed with "ellipsoidal symmetry" (Ponte Castañeda & Willis 1995). Therefore, as mentioned earlier, the two-point probability function for finding the centers of two inclusions separated by a vector $\mathbf{z}$ depends on $\mathbf{z}$ only through the combination $\left|(\boldsymbol{Z}_0^D)^{-T}\mathbf{z}\right|$, where $\boldsymbol{Z}_0^D$ is a symmetric, second-order tensor serving to define a "distributional ellipsoid" $\mathcal{D}_0$, as defined by (3.20).

Next we provide explicit forms for the constitutive equations of the matrix material as well as the dielectric inclusions in the infinitesimal context. Such constitutive equations can be obtained by appropriately linearizing the more general finite deformation expressions (2.13) and (2.20) of Chapter 2.

**Linear dielectric and elastic matrix phase:** It will be assumed in this chapter that the matrix has linear dielectric and elastic behavior. Furthermore, we assume that the dielectric properties of the matrix are isotropic and independent of the deformation. Such dielectrics are known in the literature as "ideal dielectrics" (Mcmeeking & Landis 2005, Zhao & Suo 2008). While for some materials it may be necessary to account for strain-dependent permittivities, for many others such effects may be safely neglected. As shown in Table 4.1, for the VBH elastomer (Wissler & Mazza 2007, Zhao & Suo 2008) the "intrinsic" electrostrictive effects (due to strain-dependent permittivities) are relatively small (i.e., less than 3%) at small strains compared to the Maxwell effects. Also note that for this specific elastomer the intrinsic electrostriction

| Material | $\varepsilon^{(1)}$[F/m] | $\mu^{(1)}$[MPa] | $3\epsilon/\kappa^{(1)}$ |
|---|---|---|---|
| VHB elastomer: | | | |
| Maxwell stress only | $4.68\varepsilon_0$ | $4.73\times10^{-2}$ | 1.000 |
| Maxwell & electrostrictive stresses | $4.68\varepsilon_0$ | $4.73\times10^{-2}$ | 0.973 |
| P(VDF_TrFE): | | | |
| Maxwell stress only | $68.5\varepsilon_0$ | $1.33\times10^{2}$ | 1.000 |
| Maxwell & electrostrictive stresses | $68.5\varepsilon_0$ | $1.33\times10^{2}$ | 1.579 |

Table 4.1: Electrostrictive strain $\epsilon$ (normalized by $\kappa^{(1)} = \varepsilon^{(1)}e^2/\mu^{(1)}$) for VHB elastomer (Wissler & Mazza 2007) and P(VDF_TrFE) polymer (Li & Rao 2004). Results are presented using the "ideal dielectric" approximation accounting only for Maxwell stresses (Zhao & Suo 2008), as well as for a more general model incorporating strain-dependent permittivities (Li & Rao 2004, Zhao & Suo 2008).

has an adverse effect, and therefore reduces the total electrostrictive strain. For comparison purposes, we also included the results of Li & Rao (2004) for P(VDF_TrFE), where the additional effects due to the intrinsic electrostriction of the material could not be neglected.

Thus, in this work the dielectric constitutive response of the matrix will be as-

sumed to be given by

$$\mathbf{e} = \varepsilon^{(1)^{-1}}\mathbf{d}, \tag{4.16}$$

where $\varepsilon^{(1)}$ denotes the constant (and isotropic) permittivity of the material. On the other hand, the total Cauchy stress for the ideal dielectric can be written in the form (4.8), where

$$\boldsymbol{T}^{me} = \mathbb{C}^{(1)}\boldsymbol{\epsilon}, \quad \text{and} \quad \boldsymbol{T}^{el} = \boldsymbol{T}^{M} = \frac{1}{\varepsilon^{(1)}}\left[\mathbf{d}\otimes\mathbf{d} - \frac{1}{2}(\mathbf{d}\cdot\mathbf{d})\boldsymbol{I}\right]. \tag{4.17}$$

In the first expression, $\mathbb{C}^{(1)}$ is a fully symmetric, fourth-order tensor representing the elasticity of the material, which for isotropic mechanical behavior can be written in terms of the shear modulus ($\mu^{(1)}$) and the Poisson's ratio ($\nu^{(1)}$) of the material. It should be remarked that the form (4.17) for the total stress is rather special in that it does not contain an electrostrictive component (i.e., $\boldsymbol{T}^{es}=0$ in expression (4.9) — cf. Tian et al. (2012), for example). Indeed, as it will be shown later on in this chapter, composites consisting of ideal dielectric matrices and rigid dielectric inclusions will exhibit a non-trivial effective electrostrictive component.

**Rigid dielectric inclusions:** A rigid material can only undergo a rigid displacement (a translation and a rotation). Therefore, in the limit of infinitesimal deformations, the displacement gradient for rigid materials reduces to a uniform infinitesimal rotation, i.e.,

$$\nabla\mathbf{u} = \boldsymbol{\omega}^{(2)}, \tag{4.18}$$

while the total stress becomes indeterminate (from the constitutive relation) inside such inclusions.

In the current configuration, the electric constitutive behavior for rigid materials simplifies to

$$\mathbf{e} = \boldsymbol{\varepsilon}^{(2)^{-1}}\mathbf{d}, \tag{4.19}$$

where $\boldsymbol{\varepsilon}^{(2)}$ is the (generally anisotropic) permittivity of the material in the current configuration. This permittivity in the current configuration is related to the corre-

sponding permittivity in the reference configuration, $\boldsymbol{\mathcal{E}}_0^{(2)}$, via

$$\boldsymbol{\varepsilon}^{(2)}\left(\boldsymbol{\omega}^{(2)}\right) = \boldsymbol{\mathcal{E}}_0^{(2)} + \boldsymbol{\omega}^{(2)}\boldsymbol{\mathcal{E}}_0^{(2)} - \boldsymbol{\mathcal{E}}_0^{(2)}\boldsymbol{\omega}^{(2)}, \tag{4.20}$$

where terms of order $\left(\boldsymbol{\omega}^{(2)}\right)^2$, or higher are ignored.

It should be emphasized here that because $\kappa$, as determined by expression (4.7), has been assumed to be small, it is expected that dielectric nonlinearities will not play a role for the matrix, or inclusions. In this sense, the assumption of linear dielectric behavior of the matrix and inclusion phases is consistent.

### 4.3.2 Evolution of the microstructure

Using the fact that the inclusions are rigid, the concentration of the inclusions in the deformed configuration is given by

$$c^{(2)} = c_0^{(2)}\left(1 - \mathrm{tr}\bar{\boldsymbol{\epsilon}}\right), \tag{4.21}$$

where terms of order $|\nabla\mathbf{u}|^2$ or higher are ignored.

As mentioned earlier, the rigid inclusions can, in general, undergo infinitesimal rotations. Given their identical shapes and orientations in the reference configuration, it seems reasonable to assume, for simplicity, that they will rotate with the average rotation in the inclusion phase (Ponte Castañeda & Galipeau 2011), as determined by the skew, second-order tensor $\bar{\boldsymbol{\omega}}^{(2)}$. Therefore, in the deformed configuration inclusions are described by the deformed ellipsoid $\mathcal{I}$, as given by (3.23), in terms of the deformed shape tensor given by

$$\boldsymbol{Z}^I = \left(\boldsymbol{I} + \bar{\boldsymbol{\omega}}^{(2)}\right)^T \boldsymbol{Z}_0^I \left(\boldsymbol{I} + \bar{\boldsymbol{\omega}}^{(2)}\right). \tag{4.22}$$

Under general electrostatic and mechanical loading of the system, the average particle rotation can be decomposed as

$$\bar{\boldsymbol{\omega}}^{(2)}\left(\bar{\boldsymbol{\epsilon}}, \bar{\boldsymbol{\omega}}, \bar{\mathbf{d}}\right) = \bar{\boldsymbol{\omega}}_{me}^{(2)}\left(\bar{\boldsymbol{\epsilon}}, \bar{\boldsymbol{\omega}}\right) + \bar{\boldsymbol{\omega}}_{el}^{(2)}\left(\bar{\boldsymbol{\epsilon}}, \bar{\boldsymbol{\omega}}, \bar{\mathbf{d}}\right). \tag{4.23}$$

where $\bar{\boldsymbol{\omega}}^{(2)}_{me}\left(\bar{\boldsymbol{\epsilon}}, \bar{\boldsymbol{\omega}}\right)$ is the "purely mechanical" rotation (i.e., the rotation in the absence of the electrostatic loadings) which depends solely on the macroscopic strain and rotation tensors. On the other hand, $\bar{\boldsymbol{\omega}}^{(2)}_{el}\left(\bar{\boldsymbol{\epsilon}}, \bar{\boldsymbol{\omega}}, \bar{\mathbf{d}}\right)$ is the extra rotation due to the presence of the electric fields, which, in general, can depend on both mechanical and electrostatic loadings. However, in the limit of infinitesimal deformations (i.e. when $\tilde{\kappa} \sim |\bar{\boldsymbol{\epsilon}}|$), the extra rotation due to the presence of the electrostatic fields must be independent of the macroscopic deformation (this can be shown by expanding $\bar{\boldsymbol{\omega}}^{(2)}$ to the first order in the dimensionless parameter $\tilde{\kappa}$ and then neglecting terms of order $\tilde{\kappa}^2$ or higher). Therefore, we can conclude that

$$\bar{\boldsymbol{\omega}}^{(2)}\left(\bar{\boldsymbol{\epsilon}}, \bar{\boldsymbol{\omega}}, \bar{\mathbf{d}}\right) = \bar{\boldsymbol{\omega}}^{(2)}_{me}\left(\bar{\boldsymbol{\epsilon}}, \bar{\boldsymbol{\omega}}\right) + \bar{\boldsymbol{\omega}}^{(2)}_{el}\left(\bar{\mathbf{d}}\right). \tag{4.24}$$

Although it is possible to obtain an explicit expression for the extra electrostatic rotation (e.g., see Siboni & Ponte Castañeda 2012), in the analyses that follow only the derivative of $\bar{\boldsymbol{\omega}}^{(2)}$ with respect to the deformation will be needed, and as a consequence it will not be necessary to obtain detailed expressions for $\bar{\boldsymbol{\omega}}^{(2)}_{el}\left(\bar{\mathbf{d}}\right)$.

As mentioned earlier in section 3.2.2, the evolution of the distribution is expected to depend in general on both the mechanical and electrostatic loadings, especially for large inclusion concentrations, where the strong mechanical and electrostatic interactions cannot be neglected. However, for consistency with the type of estimates that will be used in this work, and also for simplicity, we assume here that the distribution of the inclusions remains "ellipsoidal" in the deformed configuration, such that the distributional ellipsoid evolves solely as a consequence of the macroscopic deformation (Ponte Castañeda & Galipeau 2011).

Given the above assumptions, the ellipsoidal distribution of the inclusions in the deformed configuration is described by the deformed distributional ellipsoid $\mathcal{D}$, as given by (3.25) with the deformed shape tensor

$$\boldsymbol{Z}^D = \left(\boldsymbol{I} + \bar{\boldsymbol{\epsilon}} + \bar{\boldsymbol{\omega}}\right) \boldsymbol{Z}^D_0. \tag{4.25}$$

### 4.3.3 Estimates for the effective behavior of two-phase particulate DECs

In this subsection we provide estimates for the effective behavior of DECs in the limit of infinitesimal deformations. First, we provide explicit expressions for the effective stiffness, as well as for the average purely mechanical rotation of the particles. Next, we obtain the effective permittivity of DECs in the deformed configuration and also the effective strain-dependent permittivity. Finally, the effective electro-active behavior of DECs will be obtained using the theory described above.

#### Effective elastic behavior of DECs

As discussed earlier, in the limit of infinitesimal deformations and in the absence of electric fields, the effective elastic response of DECs is characterized by the effective elasticity tensor $\tilde{\mathbb{C}}$ of the composite. For composites reinforced with rigid particles, and exhibiting the above-described type of particulate microstructures consisting of aligned ellipsoidal inclusions (described by the shape tensor $\boldsymbol{Z}_0^I$) that are distributed with ellipsoidal symmetry (described by $\boldsymbol{Z}_0^D$), Ponte Castañeda & Willis (1995) developed the following estimate for the effective stiffness tensor

$$\tilde{\mathbb{C}} = \mathbb{C}^{(1)} + c_0 \left[ \mathbb{P}_{\mathcal{I}_0} - c_0 \mathbb{P}_{\mathcal{D}_0} \right]^{-1}, \tag{4.26}$$

where $\mathbb{C}^{(1)}$ is the stiffness of the matrix, and $\mathbb{P}_{\mathcal{I}_0}$ and $\mathbb{P}_{\mathcal{D}_0}$ are mechanical microstructural tensors respectively depending on the particle and distribution shape tensors $\boldsymbol{Z}_0^I$ and $\boldsymbol{Z}_0^D$. They are given by

$$P_{\mathcal{I}_0 ijpq} = \frac{\det \boldsymbol{Z}_0^I}{4\pi} \int_{|\boldsymbol{\xi}|=1} \xi_q \xi_j K_{ip}^{-1}(\boldsymbol{\xi}) \left| \boldsymbol{Z}_0^I \boldsymbol{\xi} \right|^{-3} \, dS, \tag{4.27}$$

where $K_{ip}(\boldsymbol{\xi}) = C_{ijpq}^{(1)} \xi_j \xi_q$, and a similar expression for $\mathbb{P}_{\mathcal{D}_0}$ with $\boldsymbol{Z}_0^I$ replaced by $\boldsymbol{Z}_0^D$. More explicit expressions for these microstructural tensors are provided in Appendix D for the special case of spheroidal inclusions. The estimate (4.26) may be viewed as a generalization of the dilute estimates of Eshelby (1957) to incorporate the effect of

two-point interactions among the particles. It also reduces to the Hashin & Shtrikman (1963) lower bound when the shape of the inclusions and distributions are both spherical.

For future reference, it is also noted that a corresponding expression (Kailasam & Ponte Castañeda 1998) for the average rotation of the particles is also available

$$\bar{\boldsymbol{\omega}}^{(2)}_{me} = \bar{\boldsymbol{\omega}} + \mathbb{W}^{(2)}\bar{\boldsymbol{\epsilon}}, \tag{4.28}$$

where

$$\mathbb{W}^{(2)} = -\left[\mathbb{R}_{\mathcal{I}_0}(\mathbb{P}_{\mathcal{I}_0})^{-1} - c_0\mathbb{R}_{\mathcal{D}_0}(\mathbb{P}_{\mathcal{I}_0})^{-1}\right]\left[\mathbb{I} - c_0\mathbb{P}_{\mathcal{D}_0}(\mathbb{P}_{\mathcal{I}_0})^{-1}\right]^{-1}, \tag{4.29}$$

is a fourth-order tensor, known as the rotation concentration tensor, and satisfies the symmetry properties $W^{(2)}_{ijkl} = W^{(2)}_{ijlk} = -W^{(2)}_{jikl}$. In equation (4.29), the fourth-order tensors $\mathbb{R}_{\mathcal{I}_0}$ and $\mathbb{R}_{\mathcal{D}_0}$ are also mechanical microstructural tensors, closely related to $\mathbb{P}_{\mathcal{I}_0}$ and $\mathbb{P}_{\mathcal{D}_0}$ and serving to characterize the rotation of the inclusions and the distributional ellipsoid, respectively (see Appendix D for explicit expressions for these tensors in the special case of spheroidal inclusions).

### Effective permittivity of DECs

Next we provide an explicit expression for the effective permittivity of the composite in the deformed configuration. We then linearize the obtained expression to first order in the deformation gradient to generate a corresponding expression of the form (4.14) for the effective permittivity of the composite, along with explicit expressions for $\tilde{\boldsymbol{\mathcal{E}}}_0$ and $\tilde{\mathbb{S}}$.

We begin by noting that estimates for the effective permittivity $\tilde{\boldsymbol{\varepsilon}}$ of two-phase particulate DECs with ellipsoidal microstructures described by the shape tensors $\boldsymbol{Z}^I$ and $\boldsymbol{Z}^D$ can be obtained (Ponte Castañeda & Willis 1995) as follows

$$\tilde{\boldsymbol{\varepsilon}}\left(\bar{\boldsymbol{\epsilon}}, \bar{\boldsymbol{\omega}}\right) = \varepsilon^{(1)}\boldsymbol{I} + c\left[\left(\boldsymbol{\alpha}^{(2)}\right)^{-1} - c\boldsymbol{P}_{\mathcal{D}}\right]^{-1}, \tag{4.30}$$

where

$$\boldsymbol{\alpha}^{(2)} = \left[\left(\boldsymbol{\varepsilon}^{(2)} - \varepsilon^{(1)}\boldsymbol{I}\right)^{-1} + \boldsymbol{P}_{\mathcal{I}}\right]^{-1} \tag{4.31}$$

has been introduced for convenience. In equations (4.30) and (4.31), $\boldsymbol{\varepsilon}^{(2)}$ denotes the permittivity of the inclusions, while $\boldsymbol{P}_{\mathcal{I}}$ and $\boldsymbol{P}_{\mathcal{D}}$ denote the electric microstructural tensors characterizing the geometry of the inclusions and their distribution, all in the deformed configuration. The above estimate for the effective permittivity provides a generalization of the well-known Maxwell-Garnett approximation (Garnett 1904), to which it reduces when the shape of the inclusions and the distribution are both spherical (isotropic). It also recovers the appropriate Hashin-Shtrikman bound (Hashin & Shtrikman 1962) in this special case. In addition, it is important to recall that certain geometric constraints (on the shape and concentration of the inclusions and the distributional ellipsoids) have to be satisfied for the above estimate to be valid (see Ponte Castañeda & Willis 1995, for more details).

The symmetric second-order tensor $\boldsymbol{P}_{\mathcal{I}}$ is given by

$$\boldsymbol{P}_{\mathcal{I}} = \frac{\det \boldsymbol{Z}^I}{4\pi\varepsilon^{(1)}} \int_{|\boldsymbol{\xi}|=1} \boldsymbol{\xi}\otimes\boldsymbol{\xi}\left|\boldsymbol{Z}^I\boldsymbol{\xi}\right|^{-3} \, dS(\boldsymbol{\xi}), \tag{4.32}$$

and $\boldsymbol{P}_{\mathcal{D}}$ is given by the same expression except that $\boldsymbol{Z}^I$ is replaced by $\boldsymbol{Z}^D$. Given the dependence of the shape tensors $\boldsymbol{Z}^I$ and $\boldsymbol{Z}^D$ on the deformation (discussed earlier), one can relate the microstructural tensors in the deformed configuration to their reference counterparts, i.e.,

$$\boldsymbol{P}_{\mathcal{I}} = \boldsymbol{P}_{\mathcal{I}_0} + \bar{\boldsymbol{\omega}}^{(2)}\boldsymbol{P}_{\mathcal{I}_0} - \boldsymbol{P}_{\mathcal{I}_0}\bar{\boldsymbol{\omega}}^{(2)}, \tag{4.33}$$

and

$$\boldsymbol{P}_{\mathcal{D}} = \hat{\boldsymbol{P}}_{\mathcal{D}_0} + \hat{\mathbb{P}}_{\mathcal{D}_1}\bar{\boldsymbol{\epsilon}} + \left(\mathrm{tr}\bar{\boldsymbol{\epsilon}}\right)\hat{\boldsymbol{P}}_{\mathcal{D}_0} + \bar{\boldsymbol{\omega}}\hat{\boldsymbol{P}}_{\mathcal{D}_0} - \hat{\boldsymbol{P}}_{\mathcal{D}_0}\bar{\boldsymbol{\omega}}, \tag{4.34}$$

where $\boldsymbol{P}_{\mathcal{I}_0}$ is the reference electric microstructural tensor of the inclusions with $\boldsymbol{Z}_0^I$ instead of $\boldsymbol{Z}^I$ in expression $(4.32)_1$, $\hat{\boldsymbol{P}}_{\mathcal{D}_0}$ is the reference distributional electric tensor, given by the same expression (4.32) with $\boldsymbol{Z}^I$ replaced by $\boldsymbol{Z}_0^D$. On the other hand,

$\hat{\mathbb{P}}_{\mathcal{D}_1}$, which encodes the corrections due to the change in the distribution, is given by

$$\hat{\mathbb{P}}_{\mathcal{D}_1} = -\frac{3}{2}\frac{\det \boldsymbol{Z}_0^D}{4\pi\varepsilon^{(1)}}\int_{|\boldsymbol{\xi}|=1} \boldsymbol{\xi}\otimes\boldsymbol{\xi}\otimes[\boldsymbol{\xi}'\otimes\boldsymbol{\xi}+\boldsymbol{\xi}\otimes\boldsymbol{\xi}']\left|\boldsymbol{Z}_0^D\boldsymbol{\xi}\right|^{-5} dS(\boldsymbol{\xi}), \tag{4.35}$$

where $\boldsymbol{\xi}' := \boldsymbol{Z}_0^{D^T}\boldsymbol{Z}_0^D\boldsymbol{\xi}$. Finally, it is important to mention that equations (4.33)-(4.35) are the linearized versions of the corresponding expressions in the context of finite deformations provided in previous chapter (see also Ponte Castañeda & Galipeau 2011).

Next, given the transformation rule (4.20) for the permittivity of the inclusions, and expression (4.33) for the inclusion microstructural tensors, it is evident that $\boldsymbol{\alpha}^{(2)}$, defined in equation (4.31), transforms as follows

$$\boldsymbol{\alpha}^{(2)} = \boldsymbol{A}^{(2)} + \bar{\boldsymbol{\omega}}^{(2)}\boldsymbol{A}^{(2)} - \boldsymbol{A}^{(2)}\bar{\boldsymbol{\omega}}^{(2)}, \tag{4.36}$$

where

$$\boldsymbol{A}^{(2)} = \left[\left(\boldsymbol{\mathcal{E}}_0^{(2)} - \varepsilon^{(1)}\boldsymbol{I}\right)^{-1} + \boldsymbol{P}_{\mathcal{I}_0}\right]^{-1}, \tag{4.37}$$

denotes the reference counterpart of $\boldsymbol{\alpha}^{(2)}$.

Then, substituting the expression (4.36) for $\boldsymbol{\alpha}^{(2)}$, along with the expressions (4.33) and (4.34) for the microstructural tensors, into (4.30), we confirm that $\tilde{\boldsymbol{\varepsilon}}(\bar{\boldsymbol{\epsilon}}, \bar{\boldsymbol{\omega}})$ is of the form given by expression (4.14), where

$$\tilde{\boldsymbol{\mathcal{E}}}_0 = \varepsilon^{(1)}\boldsymbol{I} + c_0\left[\left(\boldsymbol{A}^{(2)}\right)^{-1} - c_0\hat{\boldsymbol{P}}_{\mathcal{D}_0}\right]^{-1}, \tag{4.38}$$

is the effective permittivity of the DEC in the reference configuration and

$$\begin{aligned}\tilde{S}_{ijmn} = &-\delta_{mn}\tilde{\mathcal{K}}_{ij} + \tilde{\mathcal{K}}_{il}\left(\hat{\mathbb{P}}_{\mathcal{D}_1}\right)_{lkmn}\tilde{\mathcal{K}}_{kj} \\ &+\frac{1}{c_0}\tilde{\mathcal{K}}_{il}\left\{\left(\boldsymbol{A}^{(2)}\right)^{-1}_{ls}W^{(2)}_{skmn} - W^{(2)}_{ltmn}\left(\boldsymbol{A}^{(2)}\right)^{-1}_{tk}\right\}\tilde{\mathcal{K}}_{kj}\end{aligned} \tag{4.39}$$

is the electromechanical coupling tensor. Recall that $\tilde{\mathbb{S}}$ is defined in terms of the strain-dependent permittivity $\tilde{\boldsymbol{\mathcal{E}}}$ via its linearized approximation $\tilde{\boldsymbol{\mathcal{E}}}(\bar{\boldsymbol{\epsilon}}) = \tilde{\boldsymbol{\mathcal{E}}}_0 + \tilde{\mathbb{S}}\bar{\boldsymbol{\epsilon}}$. In

this expression, we have also used the short-hand notation

$$\tilde{\boldsymbol{\mathcal{K}}} = \left(\tilde{\mathcal{E}}_0 - \varepsilon^{(1)}\boldsymbol{I}\right), \tag{4.40}$$

and the components of the fourth-order tensor $\mathbb{W}^{(2)}$ are determined by expression (4.29).

**Effective electro-active behavior of DECs**

The macroscopic dielectric response of the DEC is given by

$$\bar{\mathbf{d}} = \tilde{\boldsymbol{\varepsilon}}^{-1}\bar{\mathbf{e}}, \tag{4.41}$$

where $\tilde{\boldsymbol{\varepsilon}}$ is defined in (4.14) with $\tilde{\boldsymbol{\mathcal{E}}}_0$ and $\tilde{\mathbb{S}}$ given by (4.38) and (4.39), respectively. Similarly, it is a simple matter to obtain the macroscopic total stress from expression $(4.13)_2$. The result can be written in the form

$$\bar{\boldsymbol{T}} = \bar{\boldsymbol{T}}^{me} + \bar{\boldsymbol{T}}^{M} + \bar{\boldsymbol{T}}^{es}, \tag{4.42}$$

where

$$\begin{aligned}
\bar{\boldsymbol{T}}^{me} &= \tilde{\mathbb{C}}\bar{\boldsymbol{\epsilon}}, \\
\bar{\boldsymbol{T}}^{M} &= \frac{1}{2}\left(\bar{\mathbf{d}}\otimes\bar{\mathbf{e}} + \bar{\mathbf{e}}\otimes\bar{\mathbf{d}}\right) - \frac{1}{2}\left(\bar{\mathbf{d}}\cdot\bar{\mathbf{e}}\right)\boldsymbol{I}, \text{ and} \\
\bar{\boldsymbol{T}}^{es} &= \frac{1}{2}\left(\bar{\mathbf{e}}\cdot\bar{\mathbf{p}}'\right)\boldsymbol{I} - \frac{1}{2}\hat{\mathbb{P}}^{\dagger}_{\mathcal{D}_1}(\bar{\mathbf{p}}'\otimes\bar{\mathbf{p}}') - \frac{1}{c_0}\mathbb{W}^{(2)\dagger}(\bar{\mathbf{q}}'\otimes_a\bar{\mathbf{p}}'),
\end{aligned} \tag{4.43}$$

are, respectively, the mechanical, Maxwell and electrostrictive contributions to the total stress. In these expressions, it is recalled that $\tilde{\mathbb{C}}$ is the macroscopic elasticity of the DEC, given by expression (4.26), $\mathbb{W}^{(2)}$ is the rotation concentration tensor, given by (4.29), and $\hat{\mathbb{P}}_{\mathcal{D}_1}$ is the electric microstructural tensor associated with changes in the ellipsoidal distribution of the particles, given by (4.35). In addition, $\bar{\mathbf{p}}'$ and $\bar{\mathbf{q}}'$ are related to the macroscopic polarization with respect to the matrix material[1] (instead

[1]Note that in electromagnetism theory the polarization in a dielectric is defined by $\mathbf{p} = \mathbf{d} - \varepsilon_0\mathbf{e}$.

of vacuum), and are given by

$$\bar{\mathbf{p}}' = \bar{\mathbf{d}} - \varepsilon^{(1)}\bar{\mathbf{e}} \quad \text{and} \quad \bar{\mathbf{q}}' = \left(\boldsymbol{A}^{(2)}\right)^{-1}\bar{\mathbf{p}}', \tag{4.44}$$

while the symbol $\otimes_a$ is used to denote the antisymmetric dyadic product. Note that $\bar{\boldsymbol{T}}^{es}$ is the consequence of the electro-elastic coupling arising in the composite from the presence of dielectric inclusions. (Recall that the matrix material has been assumed to be an ideal dielectric with $\boldsymbol{T}^{es} = \mathbf{0}$; cf. (4.17).) For the above specific microstructure, the terms on the right of equation $(4.43)_3$ can be respectively attributed to the change in the volume, the change in the distribution and the electrostatic torques that particles may experience. Also note that, as was mentioned earlier, the electric fields in the above equations are Eulerian variables, and therefore depend on the deformation. However, the corrections (due to the deformation) of the electric fields on the total macroscopic stress, as given by expressions (4.9) and (4.10), can be shown to be of higher order, and thus can be ignored in the computations. It is emphasized, once again, that such corrections are crucial nevertheless for the computation of the tensor $\tilde{\mathbb{S}}$ appearing in these expressions.

Next, we provide explicit expressions for the effective properties of DECs with special microstructures.

*Transversely isotropic DECs with non-aligned loadings.* Here we simplify the above general results to obtain explicit expressions for the effective response of two-phase DECs with transversely isotropic symmetry under non-aligned loading conditions. Toward this goal, we take the inclusions and the distribution to be spheroidal (ellipsoids of revolution) with the same aspect ratios $w_{\mathcal{I}_0} = w_{\mathcal{D}_0} := w$ and symmetry axes, as defined by the unit vectors $\mathbf{n}_{\mathcal{I}_0} = \mathbf{n}_{\mathcal{D}_0} := \mathbf{n}$. The corresponding shape tensors can then be written as

$$\boldsymbol{Z}_0^I = \boldsymbol{Z}_0^D = w \cdot \boldsymbol{\rho} + 1 \cdot \boldsymbol{\gamma}, \tag{4.45}$$

where

$$\boldsymbol{\rho} = \mathbf{n} \otimes \mathbf{n} \quad \text{and} \quad \boldsymbol{\gamma} = \boldsymbol{I} - \mathbf{n} \otimes \mathbf{n}, \tag{4.46}$$

are projection tensors characterizing the projections onto the symmetry axis $\mathbf{n}$, and the plane perpendicular to it. Furthermore, inclusions are electrically anisotropic with the transversely isotropic permittivity

$$\boldsymbol{\mathcal{E}}^{(2)} = \mathcal{E}_r^{(2)}\boldsymbol{\rho} + \mathcal{E}_s^{(2)}\boldsymbol{\gamma}, \tag{4.47}$$

where the subscripts "r" and "s" have been used to denote axial and transverse components, respectively. In addition, for simplicity and consistency with the properties of actual elastomers, we assume that the matrix is made out of an incompressible ideal dielectric elastomer with permittivity $\varepsilon^{(1)}$ and shear modulus $\mu^{(1)}$.

Given the above microstructure and constituent properties, the effective stiffness of the composite is obtained from expression (4.26) as follows

$$\tilde{\mathbb{C}} = 2\tilde{\mu}_p\mathbb{E}^{[3]} + 2\tilde{\mu}_n\mathbb{E}^{[4]} + 2\tilde{\mu}_a\mathbb{E}^{[a]}, \tag{4.48}$$

where

$$\tilde{\mu}_p = \mu^{(1)} + \frac{c_0}{1-c_0}\frac{1}{4m_p^p}, \quad \tilde{\mu}_n = \mu^{(1)} + \frac{c_0}{1-c_0}\frac{1}{4m_n^p}, \text{ and } \quad \tilde{\mu}_a = \mu^{(1)} + \frac{c_0}{1-c_0}\frac{1}{4m_a^p}, \tag{4.49}$$

are the effective transverse, axisymmetric, and longitudinal shear moduli, respectively. In the above expressions, the fourth-order tensors $\mathbb{E}^{[\alpha]}$ $(\alpha = 3, 4, a)$ and the constants $m_p^p$, $m_n^p$ and $m_a^p$ are defined in Appendix D.

The effective permittivity of the composite in the reference configuration, as determined by equation (4.38), becomes transversely isotropic, and can therefore be written as

$$\tilde{\boldsymbol{\mathcal{E}}}_0 = \tilde{\mathcal{E}}_{0r}\boldsymbol{\rho} + \tilde{\mathcal{E}}_{0s}\boldsymbol{\gamma}, \tag{4.50}$$

where

$$\tilde{\mathcal{E}}_{0r} = \varepsilon^{(1)} + \frac{c_0\varepsilon^{(1)}\left(\mathcal{E}_r^{(2)} - \varepsilon^{(1)}\right)}{\varepsilon^{(1)} + (1-c_0)(1-h)\left(\mathcal{E}_r^{(2)} - \varepsilon^{(1)}\right)}, \tag{4.51}$$

and

$$\tilde{\mathcal{E}}_{0s} = \varepsilon^{(1)} + \frac{c_0 \varepsilon^{(1)} \left( \mathcal{E}_s^{(2)} - \varepsilon^{(1)} \right)}{\varepsilon^{(1)} + \left(1 - c_0\right) \left(\frac{h}{2}\right) \left( \mathcal{E}_s^{(2)} - \varepsilon^{(1)} \right)} \tag{4.52}$$

are respectively the effective axial and transverse permittivities. On the other hand, the effective strain-dependent permittivity does not exhibit transversely isotropic symmetry for non-aligned loading conditions, and therefore no further simplifications can be made without the knowledge of the macroscopic strain. However, the fourth-order tensor $\tilde{\mathbb{S}}$, defined by equation (4.39), is a material property which exhibits transversely isotropic symmetry. It can therefore be written as

$$\begin{aligned} \tilde{\mathbb{S}} = & 2 \left( \hat{k}_p^p \tilde{\mathcal{K}}_s^2 - \tilde{\mathcal{K}}_s \right) \mathbb{E}^{[1]} + \left( \hat{n}^p \tilde{\mathcal{K}}_r^2 - \tilde{\mathcal{K}}_r \right) \mathbb{E}^{[2]} + 2 \hat{m}_p^p \tilde{\mathcal{K}}_s^2 \mathbb{E}^{[3]} \\ & + \left[ 2 \hat{m}_n^p - \frac{r}{4 c_0 m_n^p} \left( \left( \boldsymbol{A}^{(2)} \right)_r^{-1} - \left( \boldsymbol{A}^{(2)} \right)_s^{-1} \right) \right] \tilde{\mathcal{K}}_r \tilde{\mathcal{K}}_s \mathbb{E}^{[4]} \\ & + \left( \hat{l}^p \tilde{\mathcal{K}}_r^2 - \tilde{\mathcal{K}}_r \right) \mathbb{E}^{[5]} + \left( \hat{l}'^p \tilde{\mathcal{K}}_s^2 - \tilde{\mathcal{K}}_s \right) \mathbb{E}^{[6]}, \end{aligned} \tag{4.53}$$

where $\tilde{\mathcal{K}}_\alpha = \tilde{\mathcal{E}}_{0\alpha} - \varepsilon^{(1)}$ for $(\alpha = r, s)$ and the difference

$$\left( \boldsymbol{A}^{(2)} \right)_r^{-1} - \left( \boldsymbol{A}^{(2)} \right)_s^{-1} = \frac{2 - 3h\left(w\right)}{2\varepsilon^{(1)}} - \frac{\mathcal{E}_{0r}^{(2)} - \mathcal{E}_{0s}^{(2)}}{\left( \mathcal{E}_{0r}^{(2)} - \varepsilon^{(1)} \right) \left( \mathcal{E}_{0s}^{(2)} - \varepsilon^{(1)} \right)} \tag{4.54}$$

depends on the anisotropy of the inclusions. In equation (4.53), the fourth-order tensors $\mathbb{E}^{[\alpha]}$ $(\alpha = 1, \cdots, 6)$, the electric microstrucural tensor coefficients ($2\hat{k}_p^p$ ,$\hat{n}^p$, $2\hat{m}_p^p$, $2\hat{m}_n^p$, $\hat{l}^p$, $\hat{l}'^p$), the rotation coefficient $r$, $2m_n^p$, and the function $h\left(w\right)$ are given in Appendix D.

The electrostatic contribution to the total macroscopic stress depends on the direction of the electric field in the composite. Letting the macroscopic electric field be given by $\bar{\mathbf{e}} = \bar{e}\mathbf{n}'$, we can define the orthonormal coordinate system $\{\mathbf{n}, \mathbf{k}, \mathbf{t}\}$, such that $\mathbf{k} \coloneqq \left(\mathbf{n} \times \mathbf{n}'\right) / \left|\mathbf{n} \times \mathbf{n}'\right|$ and $\mathbf{t} \coloneqq \mathbf{n} \times \mathbf{k}$. Then the electrostatic contribution to the total macroscopic stress $\bar{\boldsymbol{T}}^{el}$ can be witten in the form

$$\bar{\boldsymbol{T}}^{el} = \bar{T}_{nn}^{el} \mathbf{n} \otimes \mathbf{n} + \bar{T}_{tt}^{el} \mathbf{t} \otimes \mathbf{t} + \bar{T}_{kk}^{el} \mathbf{k} \otimes \mathbf{k} + \bar{T}_{nt}^{el} \left( \mathbf{n} \otimes \mathbf{t} + \mathbf{t} \otimes \mathbf{n} \right), \tag{4.55}$$

where

$$\begin{aligned}
\bar{T}^{el}_{nn} &= \left(\tilde{\mathcal{K}}_r + \tilde{\mathcal{E}}_{0r} - \hat{n}^p \tilde{\mathcal{K}}^2_r\right) \bar{e}^2_n/2 + \left(\tilde{\mathcal{K}}_s - \tilde{\mathcal{E}}_{0s} - \hat{l}'^p \tilde{\mathcal{K}}^2_s\right) \bar{e}^2_t/2 \\
\bar{T}^{el}_{tt} &= \left(\tilde{\mathcal{K}}_r - \tilde{\mathcal{E}}_{0r} - \hat{l}^p \tilde{\mathcal{K}}^2_r\right) \bar{e}^2_n/2 + \left[\tilde{\mathcal{K}}_s + \tilde{\mathcal{E}}_{0s} - \left(\hat{k}^p_p + \hat{m}^p_p\right) \tilde{\mathcal{K}}^2_s\right] \bar{e}^2_t/2 \\
\bar{T}^{el}_{kk} &= \left(\tilde{\mathcal{K}}_r - \tilde{\mathcal{E}}_{0r} - \hat{l}^p \tilde{\mathcal{K}}^2_r\right) \bar{e}^2_n/2 + \left[\tilde{\mathcal{K}}_s - \tilde{\mathcal{E}}_{0s} - \left(\hat{k}^p_p - \hat{m}^p_p\right) \tilde{\mathcal{K}}^2_s\right] \bar{e}^2_t/2 \\
\bar{T}^{el}_{nt} &= \left\{\tilde{\mathcal{E}}_{0r} + \tilde{\mathcal{E}}_{0r} - \left[2\hat{m}^p_n - \frac{r}{4c_0 m^p_n}\left(\left(\boldsymbol{A}^{(2)}\right)^{-1}_r - \left(\boldsymbol{A}^{(2)}\right)^{-1}_s\right)\right]\right\} \bar{e}_n \bar{e}_n/2.
\end{aligned} \tag{4.56}$$

In these last expressions, $\bar{e}_t = \bar{\mathbf{e}} \cdot \mathbf{t}$ and $\bar{e}_n = \bar{\mathbf{e}} \cdot \mathbf{n}$ are the projection of the macroscopic electric field onto the $\mathbf{t}$ and $\mathbf{n}$ directions, respectively.

*Transversely isotropic DECs with aligned loadings.* If in addition to the transversely isotropic symmetry for the microstructure of the DECs, we assume that the loading conditions are also aligned with the microstructure more explicit expressions for the effective constitutive response of the DECs can be generated. Thus, we take the macroscopic electric field to be given by $\bar{\mathbf{e}} = \bar{e}\mathbf{n}$, and the macroscopic strain to be given by $\bar{\boldsymbol{\epsilon}} = \bar{\epsilon}_r \boldsymbol{\rho} - \frac{1}{2}\bar{\epsilon}_r \boldsymbol{\gamma}$. Note that $\bar{\boldsymbol{\epsilon}}$ is coaxial with the shape tensors (4.45), and also that, because of incompressibility, $\bar{\epsilon}_s = -\frac{1}{2}\bar{\epsilon}_r$. Then, it can be shown that the effective strain-dependent permittivity of the DECs is transversely isotropic, such that

$$\begin{aligned}
\tilde{\boldsymbol{\mathcal{E}}}\left(\bar{\boldsymbol{\epsilon}}\right) = &\left[\tilde{\mathcal{E}}_{0r} + \left(\tilde{\mathcal{E}}_{0r} - \varepsilon^{(1)}\right)^2 \left(\hat{n}^p - \hat{l}^p\right) \bar{\epsilon}_r\right] \boldsymbol{\rho} \\
&+ \left[\tilde{\mathcal{E}}_{0s} + \left(\tilde{\mathcal{E}}_{0s} - \varepsilon^{(1)}\right)^2 \left(\hat{l}'^p - \hat{k}^p_p\right) \bar{\epsilon}_r\right] \boldsymbol{\gamma},
\end{aligned} \tag{4.57}$$

where $\tilde{\mathcal{E}}_{0r}$ and $\tilde{\mathcal{E}}_{0r}$ are respectively the axial and transverse components of the effective permittivity in the reference configuration, as determined by equations (4.51) and (4.52). In the above equation $\hat{k}^p_p$, $\hat{n}^p$, $\hat{l}^p$ and $\hat{l}'^p$, which depend on the aspect ratio of the inclusions (or the distribution), are given in Appendix D.

The macroscopic electrostatic stress $\bar{\boldsymbol{T}}^{el}$ is also transversely isotropic for aligned loading conditions, so that

$$\bar{\boldsymbol{T}}^{el} = \bar{T}^{el}_r \boldsymbol{\rho} + \bar{T}^{el}_s \boldsymbol{\gamma}, \tag{4.58}$$

where

$$\bar{T}^{el}_r = \left[-\frac{\varepsilon^{(1)}}{2} + \tilde{\mathcal{E}}_{0r} - \frac{\hat{n}^p}{2}\left(\tilde{\mathcal{E}}_{0r} - \varepsilon^{(1)}\right)^2\right] \bar{e}^2, \tag{4.59}$$

and

$$\bar{T}_s^{el} = \left[ -\frac{\varepsilon^{(1)}}{2} - \frac{\hat{l}^p}{2} \left( \tilde{\mathcal{E}}_{0r} - \varepsilon^{(1)} \right)^2 \right] \bar{e}^2 \tag{4.60}$$

are respectively the axial and transverse components of $\bar{\boldsymbol{T}}^{el}$.

*Initially isotropic DECs.* For the special case of two-phase DECs with electrically isotropic spherical inclusions, which are embedded with spherical symmetry in an ideal dielectric elastomer matrix, the rotation concentration tensor $\mathbb{W}^{(2)}$ vanishes identically, and therefore simplified expressions for the effective permittivity and the electrostatic stress can be generated. Thus, denoting the permittivity of the matrix and its shear modulus by $\varepsilon^{(1)}$ and $\mu^{(1)}$, respectively, and the permittivity (in the reference configuration) of the inclusions by $\boldsymbol{\mathcal{E}}^{(2)} = \mathcal{E}^{(2)} \boldsymbol{I}$, the effective strain-dependent permittivity of the DECs can be written as

$$\tilde{\boldsymbol{\mathcal{E}}} \left( \bar{\boldsymbol{\epsilon}} \right) = \tilde{\mathcal{E}}_0 \boldsymbol{I} + a_1 \bar{\boldsymbol{\epsilon}} + a_2 \left( \operatorname{tr} \bar{\boldsymbol{\epsilon}} \right) \boldsymbol{I}. \tag{4.61}$$

In this expression,

$$\tilde{\mathcal{E}}_0 = \varepsilon^{(1)} + \frac{3 c_0 \varepsilon^{(1)} \left( \mathcal{E}^{(2)} - \varepsilon^{(1)} \right)}{3\varepsilon^{(1)} + \left( 1 - c_0 \right) \left( \mathcal{E}^{(2)} - \varepsilon^{(1)} \right)} \tag{4.62}$$

denotes the effective (isotropic) permittivity of the DEC in the reference configuration, and the coefficients $a_1$ and $a_2$ are respectively given by

$$a_1 = -\frac{2}{5} \frac{\left( \tilde{\mathcal{E}}_0 - \varepsilon^{(1)} \right)^2}{\varepsilon^{(1)}}, \quad \text{and} \quad a_2 = -\frac{1}{3} \frac{\left( \tilde{\mathcal{E}}_0 - \varepsilon^{(1)} \right) \left( \tilde{\mathcal{E}}_0 + 2\varepsilon^{(1)} \right)}{\varepsilon^{(1)}} + \frac{2}{15} \frac{\left( \tilde{\mathcal{E}}_0 - \varepsilon^{(1)} \right)^2}{\varepsilon^{(1)}}. \tag{4.63}$$

It is important to mention here that our result for the effective strain-dependent permittivity of initially isotropic DECs, as given by (4.61) and (4.63), agrees exactly with the result of Lee et al. (2005) for an isotropic distribution of spherical inclusions. However, the expression (4.62) for the effective permittivity in the reference configuration is different from the corresponding result in Lee et al. (2005) due to the fact that different methods have been used to estimate the effective properties.

The macroscopic electric stress for such composites is given by

$$\bar{\boldsymbol{T}}^{el} = \tilde{\mathcal{E}}_0 \bar{\mathbf{e}} \otimes \bar{\mathbf{e}} - \frac{\tilde{\mathcal{E}}_0}{2} (\bar{\mathbf{e}} \cdot \bar{\mathbf{e}}) \boldsymbol{I} - \frac{1}{2} [a_1 \bar{\mathbf{e}} \otimes \bar{\mathbf{e}} + a_2 (\bar{\mathbf{e}} \cdot \bar{\mathbf{e}}) \boldsymbol{I}], \tag{4.64}$$

where the first two terms on the right are recognized as the Maxwell stress in an ideal dielectric material with permittivity $\tilde{\mathcal{E}}_0$, and the other two are consequences of the change in the permittivity as the composite deforms. As expected, the form of the above expression for the macroscopic electric stress is also in agreement with the corresponding forms in Landau et al. (1984), Shkel & Klingenberg (1996).

*DECs in the dilute concentration limit.* In cases for which the concentration of the inclusion phase is sufficiently small, so that inter-particle interactions can be ignored, one may neglect terms of order $c_0^2$ and higher in the expressions for the effective constitutive response of the DECs to obtain the corresponding dilute estimates. For example, the effective macroscopic total stress in the limit of dilute concentrations becomes

$$\bar{\boldsymbol{T}} = \tilde{\mathbb{C}}^{dil} \bar{\boldsymbol{\varepsilon}} + \bar{\boldsymbol{T}}^{el}, \text{ where } \tilde{\mathbb{C}}^{dil} = \mathbb{C}^{(1)} + c_0 \left( \mathbb{P}^{(2)}_{\mathcal{I}_0} \right)^{-1} \tag{4.65}$$

denotes the effective stiffness (in the dilute limit) and

$$\begin{aligned} \bar{\boldsymbol{T}}^{el} = & \frac{1}{\varepsilon^{(1)}} \left[ -\frac{1}{2} \left( \bar{\mathbf{d}} \cdot \bar{\mathbf{d}} \right) \boldsymbol{I} + \bar{\mathbf{d}} \otimes \bar{\mathbf{d}} + \left( \bar{\mathbf{d}} \cdot \bar{\mathbf{p}}' \right) \boldsymbol{I} - \bar{\mathbf{d}} \otimes_s \bar{\mathbf{p}}' \right] \\ & - \frac{1}{\varepsilon^{(1)}} \left( \mathbb{P}^{(2)}_{\mathcal{I}_0} \right)^{-1} \mathbb{R}^{(2)\dagger}_{\mathcal{I}_0} \left( \bar{\mathbf{p}}' \otimes_a \bar{\mathbf{d}} \right), \end{aligned} \tag{4.66}$$

which is in agreement with finite strain results, when simplified for the limit of infinitesimal deformations and dilute concentrations (see Ponte Castañeda & Siboni 2012, for more details).

## 4.4 Results and discussion

In this section we investigate the response of two-phase, particulate DECs under the sole application of electric fields. More specifically, we study electrostriction in DEC samples subjected to a direct potential difference ($\Delta V$), which is applied via

a pair of electrodes which are in perfect contact with the composite specimen. The electrodes are assumed to be made of *electrically conducting grease* (as opposed to *metallic* conductors), and therefore they do not impose any mechanical constraints on the deformation of the sample. In addition, we will assume that the electrodes are perfect conductors in such a way that all the electric fields are identically zero in their interior.

As shown in Fig. 4.1(a), we consider a thin DEC sample, such that its height, which is aligned with the $X_2$ axis of the laboratory axes $\{X_1, X_2, X_3\}$, is much smaller than the other two dimensions. More specifically, we assume that the height of the sample, denoted by $d$, is much smaller than its characteristic length in the $X_3$-$X_1$ plane, denoted by $l$ (i.e., $d \ll l$). Given the condition $d \ll l$, we may expect to have uniform fields almost everywhere inside the composite except in the close vicinity of the side surfaces where fringing effects may occur. In fact, a straightforward numerical simulation suggests the existence of a "boundary layer" in this area with characteristic length $l_b \sim d$ where the electric fields are not uniform. In any event, in the developments that follow we take the macroscopic electric field inside the composite and away from the boundary layer to be a constant vector in the $X_2$ direction, i.e. $\bar{\mathbf{e}} = \bar{e}\hat{\mathbf{E}}_2$, where $\bar{e} = \Delta V/d$. It is remarked that such an approximation becomes more accurate as the ratio $d/l$ decreases. In addition, we assume that there are no externally applied mechanical tractions on the boundaries (i.e. the interfaces with the electrodes and the surrounding vacuum) of the sample.

In this work, for simplicity, we will only consider two-phase DECs with transversely isotropic symmetry. Also for simplicity, the inclusions are assumed to be electrically isotropic with permittivity $\boldsymbol{\mathcal{E}}^{(2)} = \mathcal{E}^{(2)}\boldsymbol{I}$, and, as shown in Fig. 4.1(b), of spheroidal shape characterized by an aspect ratio $w_{\mathcal{I}_0} = w$ and with symmetry axis $\mathbf{n}_{\mathcal{I}_0} = \mathbf{n}$. They are distributed with "spheroidal" symmetry with the same shape as the inclusions (i.e. $w_{\mathcal{D}_0} = w$ and $\mathbf{n}_{\mathcal{D}_0} = \mathbf{n}$) in an incompressible ideal dielectric matrix with permittivity $\varepsilon^{(1)}$ and shear modulus $\mu^{(1)}$. In addition, we take the symmetry axis of the DEC, which coincides with the symmetry axis of the inclusions $\mathbf{n}$, to be

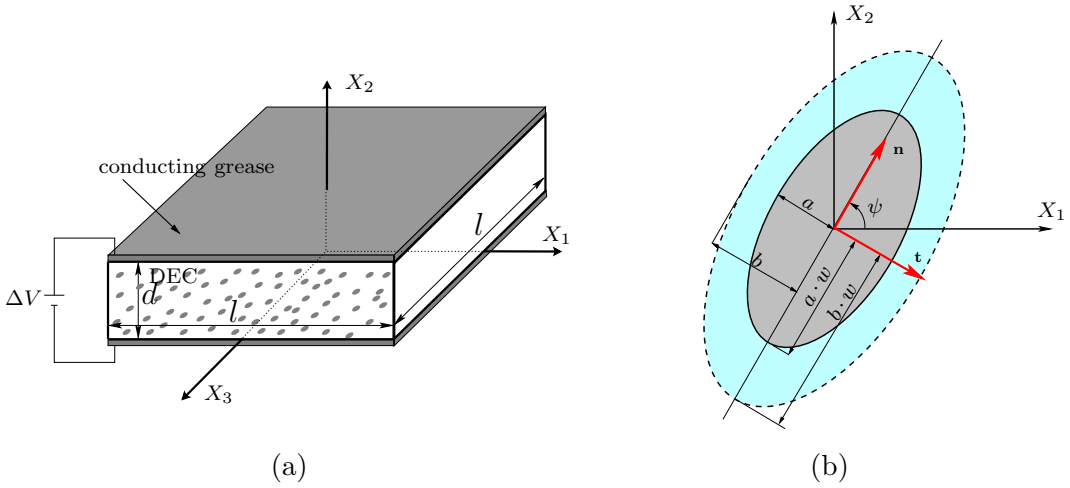


(a) (b)

Figure 4.1: (a) A thin DEC sample which is in perfect contact with two electrodes made out of conducting grease. (b) Geometry of the inclusions in the reference configuration. Here the solid line denotes the boundary of the inclusion and the dashed line denotes the distributional ellipsoid.

in the $X_1$-$X_2$ plane such that

$$\mathbf{n} = \cos\psi\hat{\mathbf{E}}_1 + \sin\psi\hat{\mathbf{E}}_2, \tag{4.67}$$

where the angle $\psi$ serves to characterize the initial orientation of the microstructure in the $X_1$-$X_2$ plane.

### 4.4.1 The effective permittivity and stiffness of DECs

To facilitate the discussion of the results pertaining the effective coupled electro-active properties of the DECs, we first provide some results for their effective dielectric permittivity and effective mechanical stiffness.

Figure 4.2 shows the dependence of the transverse and axial components of the effective permittivity on the concentration of the inclusion phase. As shown in this figure, the values of the effective permittivity range between the permittivity of the matrix (for $c_0 = 0$) and the permittivity of the inclusions (for $c_0 = 1$). Note that for the case of prolate inclusions the axial component of the permittivity is always larger than the transverse component, while for oblate inclusions the opposite is true. On

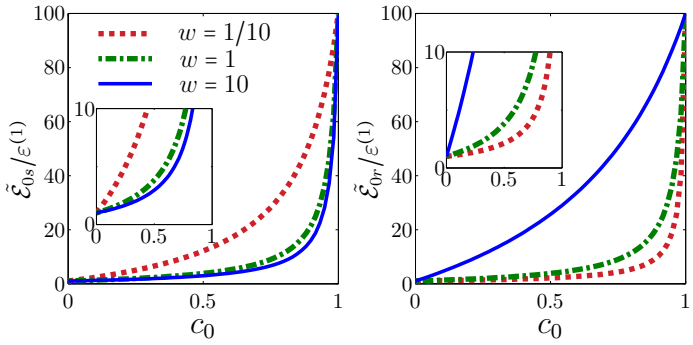


Figure 4.2: Plots for the transverse ($\tilde{\mathcal{E}}_{0s}$) and axial ($\tilde{\mathcal{E}}_{0r}$) components of the effective permittivity of the DEC as a function of the concentration of the inclusions, for different values of the aspect ratio. In these plots $\mathcal{E}^{(2)}/\varepsilon^{(1)} = 100$.

the other hand, for spherical inclusions, when the DEC is initially isotropic, the axial and transverse components of the permittivity are of course identical

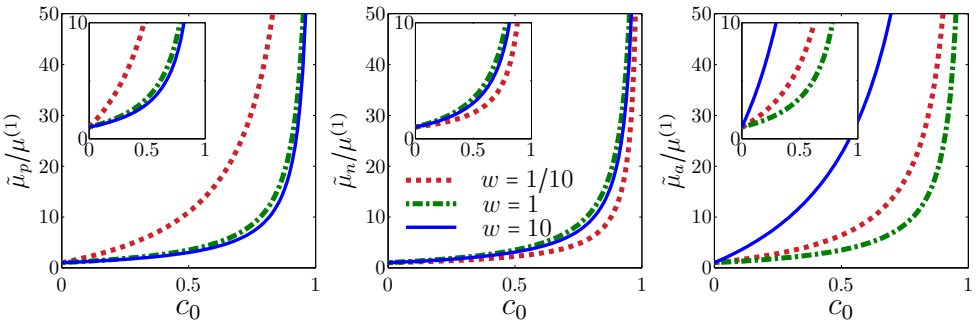


Figure 4.3: Plots for the effective transverse ($\tilde{\mu}_p$), longitudinal ($\tilde{\mu}_n$) and axisymmetric ($\tilde{\mu}_a$) shear moduli of the DEC as a function of the concentration of the inclusions, for different values of the aspect ratio. Note that in the limit when $c_0 \to 1$ all the shear moduli of the DEC tend to infinity since the inclusion phase is assumed to be rigid.

Figure 4.3 shows the corresponding plots for the transverse, longitudinal and axisymmetric shear moduli of the DEC as a function of the concentration of the inclusions. As can be seen in this figure, composites consisting of oblate ($w < 1$) inclusions have the largest transverse shear modulus, while composites with prolate ($w > 1$) inclusions have the largest longitudinal shear modulus. Note that in the limit when $c_0 \to 1$, the composite becomes mechanically rigid with all their shear moduli becoming unbounded.

### 4.4.2 The effective electro-active properties of DECs

This section is concerned with the effective electro-active properties of DECs. More specifically, we are interested in the electrostriction (i.e., the total strain that is observed in the DEC sample in the direction of the applied electric field).

Given the fact that there are no externally applied mechanical tractions on the boundaries of the specimen, the general traction boundary condition (4.2) can be specialized as follows. At the interface of the sample and the electrodes we have

$$\bar{\boldsymbol{T}}\mathbf{m} = 0, \tag{4.68}$$

where $\mathbf{m}$ is the unit normal to the interface and $\bar{\boldsymbol{T}}$ is the macroscopic total stress inside the sample. Note that since all the electric fields vanish inside the electrodes the Maxwell stress is identically zero, and it is for this reason that it does not appear in equation (4.68). The traction boundary conditions on the side surfaces are in general more complicated due to the fringing effects. However, recalling that the fringing effects occur only within a boundary layer with characteristic length $l_b\,(\sim d)$, which is much smaller than the size of the sample $l$, it is possible to show (again by resorting to a straightforward numerical simulation) that such fringing effects can be ignored, and to make use of the "equivalent" boundary condition

$$\bar{\boldsymbol{T}}\mathbf{m}' = 0, \tag{4.69}$$

where, once again, $\bar{\boldsymbol{T}}$ is the total macroscopic stress inside the specimen and $\mathbf{m}'$ is the unit normal to the side surfaces of the sample. The two conditions (4.68) and (4.69) simply imply that for the specific setup shown in Fig. 4.1(a) the *total* macroscopic stress has to be zero inside the DEC specimen, i.e.,

$$\bar{\boldsymbol{T}} = \mathbf{0}. \tag{4.70}$$

In other words, the deformation of the composite specimen, far from the boundary layer, is such that the elastic part of the total stress cancels out, exactly, the electro-

static stress that is developed inside the sample due to the presence of the electric field.

With the above assumptions for the microstructure of the DEC and the given boundary conditions, it can be easily argued that the macroscopic strain is uniform away from the boundary layer and it has the form

$$\bar{\boldsymbol{\epsilon}} = \begin{pmatrix} \bar{\epsilon}_{11} & \bar{\epsilon}_{12} & 0 \\ \bar{\epsilon}_{12} & \bar{\epsilon}_{22} & 0 \\ 0 & 0 & \bar{\epsilon}_{33} \end{pmatrix}, \tag{4.71}$$

where $\bar{\epsilon}_{ii}$ $(i = 1, 2, 3)$ are the normal strains and $\bar{\epsilon}_{12}$ is a shear strain. Note that since the inclusions are rigid and the matrix is incompressible the composite itself will be effectively incompressible in such a way that $\mathrm{tr}\bar{\boldsymbol{\epsilon}} = 0$. Then, using the condition (4.70) on the total macroscopic stress, together with the explicit expressions for the total macroscopic stress provided in the previous section, we can determine the components of the macroscopic strain for the given microstructure and loading conditions. In the following, results are provided for composites with transversely isotropic symmetry under both aligned and non-aligned loading conditions. Furthermore, we investigate the effect of different microstructural parameters, including the geometric and dielectric properties of the inclusions and their concentration, on the electrostriction of DECs (i.e. $\bar{\epsilon}_{22}$ in our case).

**Transversely isotropic DECs under aligned loading**

We start with a transversely isotropic DEC under aligned loading conditions (i.e. $\psi = 90°$). For this specific case, the symmetry axis of the composite is aligned with the direction of the macroscopic electric field (i.e., $\mathbf{n} = \hat{\mathbf{E}}_2$), and it follows that the electrostatic contribution to the total macroscopic stress is transversely isotropic with the symmetry axis being along the $X_2$ direction. Consequently, the macroscopic strain becomes coaxial with the microstructure and exhibits the same symmetry.

Thus, using the fact that the total stress $\bar{\boldsymbol{T}}$ vanishes inside (and away from the boundary layer) of the DEC, and the fact that the material is incompressible, it is

easily found that

$$\bar{\epsilon}_{22} = -2\bar{\epsilon}_{11} = -2\bar{\epsilon}_{33} = -\frac{\bar{T}_{22}^{el} - \bar{T}_{11}^{el}}{3\tilde{\mu}_a}, \tag{4.72}$$

where $\bar{T}_{11}^{el}$ and $\bar{T}_{22}^{el}$ are the relevant components of the electrostatic stress, and $\tilde{\mu}_a$ is the effective longitudinal shear modulus of the DEC.

The difference $\bar{T}_{22}^{el} - \bar{T}_{11}^{el}$ can be further decomposed into two contributions as follows

$$\bar{T}_{22}^{el} - \bar{T}_{11}^{el} = \bar{T}_{22}^{M} - \bar{T}_{11}^{M} + \bar{T}_{22}^{es} - \bar{T}_{11}^{es}, \tag{4.73}$$

where

$$\frac{\bar{T}_{22}^{M} - \bar{T}_{11}^{M}}{\varepsilon^{(1)}\bar{e}^2} = 1 + \frac{c_0}{\left(\Delta\varepsilon/\varepsilon^{(1)}\right)^{-1} + (1-c_0)\,(1-h)} \tag{4.74}$$

and

$$\frac{\bar{T}_{22}^{es} - \bar{T}_{11}^{es}}{\varepsilon^{(1)}\bar{e}^2} = \frac{\frac{6w^2(1-h)-3h}{4(w^2-1)}\, c_0^2}{\left[\left(\Delta\varepsilon/\varepsilon^{(1)}\right)^{-1} + (1-c_0)\,(1-h)\right]^2} \tag{4.75}$$

are the contributions due to the Maxwell and electrostrictive stresses, respectively. In these expressions, $\Delta\varepsilon := \mathcal{E}^{(2)} - \varepsilon^{(1)}$ and the parameter $h$ is defined in (D.9). Physically, the Maxwell component $\left(\bar{T}_{22}^{M} - \bar{T}_{11}^{M}\right)$ accounts for the attractive forces between the oppositely charged electrodes. Note that the Maxwell component is proportional to the axial component of the effective permittivity (i.e. $\tilde{\mathcal{E}}_{0_{22}}$ for the specific example of this section). On the other hand, the electrostrictive component accounts for the dipole-dipole interactions and is proportional to the quantity $\left(\tilde{\mathcal{E}}_{0_{22}} - \varepsilon^{(1)}\right)^2$. This last observation can be understood by recalling that in the presence of the electric fields the dielectric inclusions become polarized and that the dipole-dipole interactions are proportional to the size of the dipoles squared.

It is important at this stage to recall that the electrostrictive strain is non-zero even in the absence of dielectric particles (i.e. when $c_0 = 0$). This strain, which we denote by $\epsilon_m$, is given by

$$\epsilon_m = -\frac{1}{3}\frac{\varepsilon^{(1)}}{\mu^{(1)}}\bar{e}^2. \tag{4.76}$$

The strain $\epsilon_m$ is produced in the ideal dielectric matrix due to the Maxwell stress in the expression for the total stress, and is compressive.

In the following, we first investigate, in some detail, the relative importance of the Maxwell and the electrostrictive stresses on the electrostriction of DECs. We then consider the effect of different microstructural parameters on the electrostriction of DECs. The results will be shown normalized by the electrostrictive strain in the matrix material, i.e., by $\bar{\epsilon}_{22}/\epsilon_m$, in order to show the improvements in the effective electromechanical couplings over the ideal dielectric matrix.

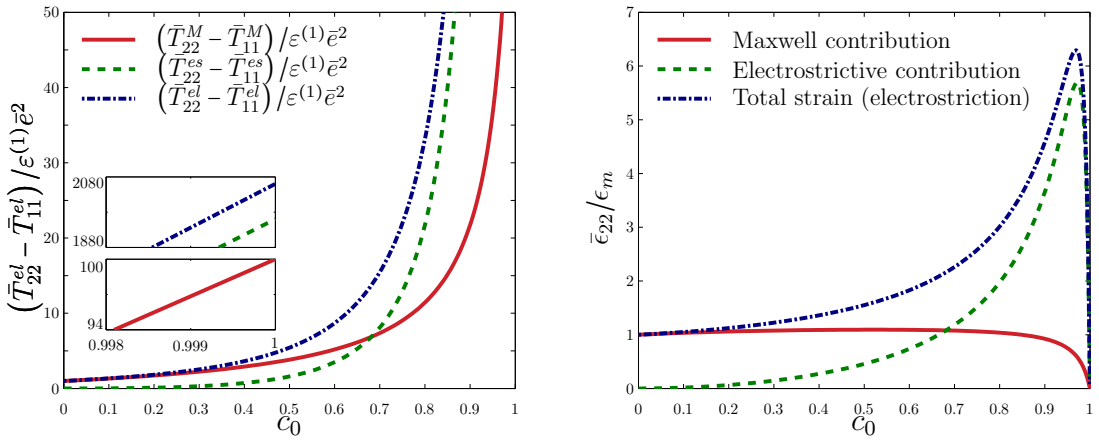


Figure 4.4: Plots for the different contributions to the electrostrictive strain (electrostriction) of DECs consisting of spherical ($w$ = 1) inclusions with permittivity $\mathcal{E}^{(2)}/\varepsilon^{(1)}$ = 100. (a) Results for the Maxwell and electrostrictive stress, as well as for the total electrostatic stress, as a function of the concentration, and (b) results for the corresponding contributions to the electrostriction.

Figure 4.4 shows results for the Maxwell and electrostrictive contributions to the stress, as well as the total electrostatic stress, along with the corresponding plots for the strains, for DECs consisting of spherical ($w$ = 1) inclusions with dielectric permittivity $\mathcal{E}^{(2)}/\varepsilon^{(1)}$ = 100. As shown in Fig. 4.4(a), for small volume fractions (i.e. $c_0 \lesssim 0.7$ in this case) the Maxwell effect is larger than the electrostrictive effect, while for larger volume fractions (i.e. $c_0 \gtrsim 0.7$) the electrostrictive effect becomes much larger than the Maxwell effect.

As mentioned earlier, the Maxwell stress accounts for the attractive force between the oppositely charged electrodes. This attractive force is proportional to the amount of charge on the electrodes which can be shown to be proportional to the effective

permittivity of the DEC. Therefore, the Maxwell stress increases with increasing the volume fraction of the highly dielectric inclusions. Note that the Maxwell stress is non-zero in the absence of inclusions (i.e., for the pure matrix) since even for this case there will be charges on the electrodes when the potential difference is applied. On the other hand, the electrostrictive stress is the result of the interactions between the polarized inclusions. As a consequence, it vanishes in the absence of dielectric particles (i.e., when $c_0 = 0$). It can be shown that the dipole-dipole interactions are inversely proportional to the third power of the relative distance of dipoles (Shkel & Klingenberg 1998). Hence, for small volume fractions ($c_0 \lesssim 0.7$ in this case) this effect is very weak, since the particles are far apart from each other. For higher concentrations ($c_0 \gtrsim 0.7$), however, this effect becomes very significant due to the fact that the particles are now closer to each other.

Figure 4.4(b) shows the plots for the strains corresponding to the Maxwell and electrostrictive contributions to the stress along with the total strain (i.e., the electrostriction). Note that the plots in this figure are simply obtained by dividing the plots in Fig. 4.4(a) by the effective longitudinal shear modulus of the DEC. As shown in this figure, for small volume fractions, the total strain is mainly the result of the Maxwell stress, while for larger volume fractions (i.e., as $c_0 \to 1$) the dominant contribution is due the electrostrictive stress. However, the material also becomes mechanically rigid as $c_0 \to 1$, and therefore the strain tends to zero in this limit. As a consequence, the maximum electrostriction is achieved for a relatively high concentration ($c_0 \sim 0.96$); it is larger than the strain in the homogeneous matrix under the same electric field by a factor of 6.

Thus far we have shown the importance of the electrostrictive part of the total stress for the overall electrostriction of the DECs, especially at large volume fractions. Next, we explore, in some detail, the effect of the various microstructural parameters on the electrostriction of DECs under aligned loading conditions.

Figure 4.5 shows results for the electrostriction as a function of the concentration of the inclusion phase for different values of $\mathcal{E}^{(2)}$, and for both spherical and prolate spheroidal shapes of the inclusions. As depicted in Fig. 4.5(a) for spherical inclusions

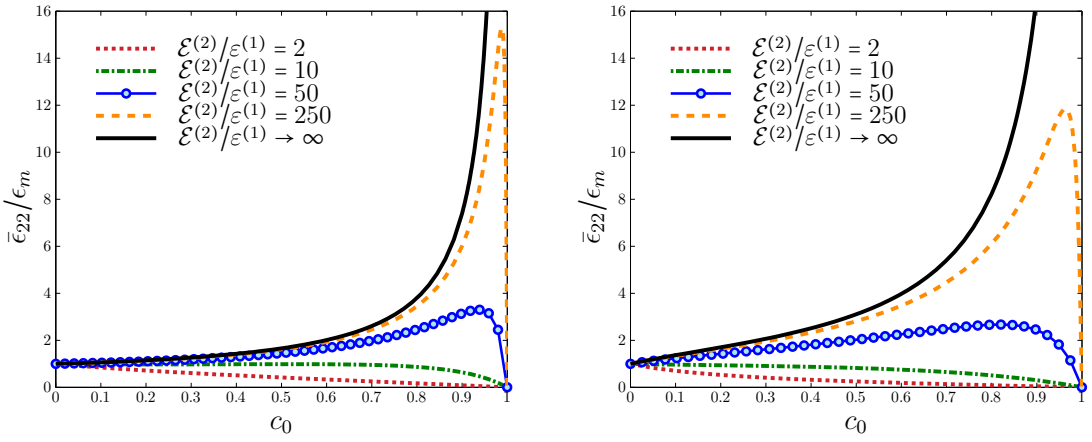


Figure 4.5: Plots for the electrostriction of a DEC with transversely isotropic symmetry under aligned loading conditions as a function of the concentration of the inclusions, for different values of the permittivity of the inclusions. (a) Results for spherical ($w = 1$) inclusions and (b) for prolate ($w = 3$) spheroidal inclusions.

and for finite, but large enough values of $\mathcal{E}^{(2)}$, the electrostriction increases monotonically to a maximum with increasing concentration, eventually decaying to zero due to the fact that the DEC becomes rigid in the limit as $c_0 \to 1$. For smaller values of $\mathcal{E}^{(2)}$, the mechanical stiffening effect of the rigid inclusions overwhelms the electrostatic effects, and therefore the composite exhibits no enhancement in the electro-active behavior compared to the pure matrix. Figure 4.5(b) shows the corresponding plots for the case of prolate spheroidal inclusions. As seen in this figure, the trends are more or less similar to the previous case. In addition, it is observed from these figures for both spherical and prolate spheroidal shapes for the inclusions that the largest strains are achieved in the limit as $\mathcal{E}^{(2)} \to \infty$.

Figure 4.6 shows the electrostriction as a function of the concentration for different values of the aspect ratio of the inclusions. Figure 4.6(a) shows results for $\mathcal{E}^{(2)}/\varepsilon^{(1)} = 100$. For $w \geq 1$, it can be seen that the electrostriction increases with increasing volume fraction of the inclusions until a maximum value, and then tends to zero with further increases in the volume fraction, again due to the mechanical stiffening effect of the rigid particles. For $w < 1$, on the other hand, more complicated trends are observed. For the specific examples provided in Fig. 4.6(a), the electrostriction

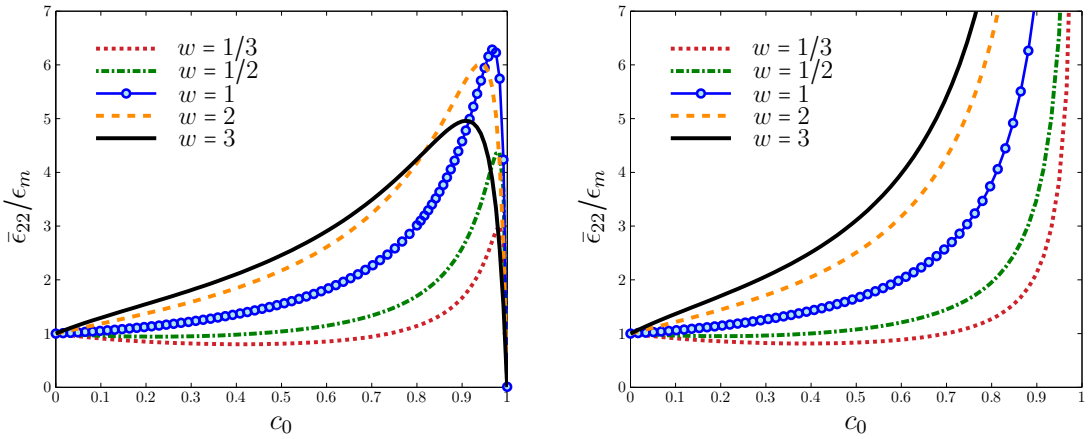


Figure 4.6: Plots for the electrostriction of a DEC with transversely isotropic symmetry under aligned loading conditions as a function of the concentration of the inclusions, for different values of the aspect ratio. (a) Results for $\mathcal{E}^{(2)}/\varepsilon^{(1)} = 100$ and (b) for $\mathcal{E}^{(2)}/\varepsilon^{(1)} \to \infty$.

decreases to a minimum, then increases to a maximum and finally decays to zero as the concentration of the inclusion phase further increases to 100%. Also, as can be seen in Fig. 4.6(b) for infinite permittivity of the inclusions, high electrostrictive strains can be achieved for both prolate and oblate shapes for sufficiently large volume fraction of the inclusion phase.

Figures 4.7(a) and (b) show the effect of the inclusion aspect ratio on the electrostriction for two different concentrations, $c_0 = 0.5$ and $c_0 = 0.75$, respectively. The main observation in this figure is that for finite values of $\mathcal{E}^{(2)}$ the electrostriction tends to zero as $w \to 0$ or $w \to \infty$, exhibiting a maximum for some prolate value of the aspect ratio $w$ that increases monotonically with increasing values of $\mathcal{E}^{(2)}$. Note that in the limit as $\mathcal{E}^{(2)} \to \infty$ the maximum value for the electrostriction shifts to $w \to \infty$. In this context, it is helpful to recall that the results corresponding to the limit as $\mathcal{E}^{(2)} \to \infty$ have been obtained by first taking the limit as the particles become rigid, and then taking the limit as $\mathcal{E}^{(2)} \to \infty$. As a consequence, proper care must be exercised in the interpretation of the results of this limiting case. In fact, the curve for $\mathcal{E}^{(2)} \to \infty$ should be interpreted as a limiting envelope for the family of curves for finite, fixed values of $\mathcal{E}^{(2)}$. In practical terms, the results of these figures show, for

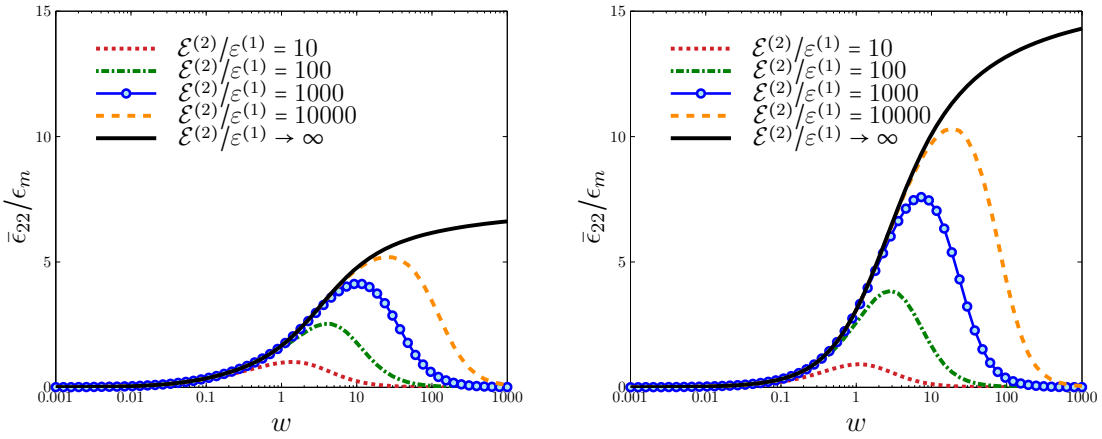


Figure 4.7: Plots for the electrostriction of a DEC with transversely isotropic symmetry under aligned loading conditions as a function of the aspect ratio of the inclusions, for different values of $\mathcal{E}^{(2)}/\varepsilon^{(1)}$. (a) Results for $c_0 = 0.5$ and (b) for $c_0 = 0.75$.

example, that for $\mathcal{E}^{(2)}/\varepsilon^{(1)} = 100$ strains in the order of $2.5\epsilon_m$ can be achieved for 50% volume fraction of rigid dielectric inclusions with an aspect ratio $w \sim 2$, or strains of order $4\epsilon_m$ for 75% volume fraction of rigid dielectric inclusions with aspect ratio $w \sim 3$.

The results shown in the prior figures suggest that the addition of highly dielectric particles can significantly enhance the effective electromechanical properties of DECs. Furthermore, it has been shown that there are "optimal" values of the concentration $c_0$, for fixed values of $\mathcal{E}^{(2)}/\varepsilon^{(1)}$ and $w$ (see Fig. 4.5), and of the aspect ratio $w$, for fixed values of $\mathcal{E}^{(2)}/\varepsilon^{(1)}$ and $c_0$ (see Fig. 4.7), for which the electrostriction reaches maximum values. It is then natural to look for global maxima for the electrostriction at each value of $\mathcal{E}^{(2)}/\varepsilon^{(1)}$. Fixing the ratio $\mathcal{E}^{(2)}/\varepsilon^{(1)}$, we can search for the values for $c_0$ and $w$ (denoted by $c_0^*$ and $w^*$) for which the electrostriction is largest. Thus, Fig. 4.8(a) shows the maximum electrostriction achievable in the aligned case as a function of the ratio $\mathcal{E}^{(2)}/\varepsilon^{(1)}$, while Fig. 4.8(b) shows the optimal values $c_0^*$ and $w^*$. In this context, it should be noted that the addition of particles with small dielectric permittivity (i.e. $\mathcal{E}^{(2)}/\varepsilon^{(1)} \lesssim 10$) does not lead to improvements in the overall electrostriction of the composite. However, for particles with higher di-

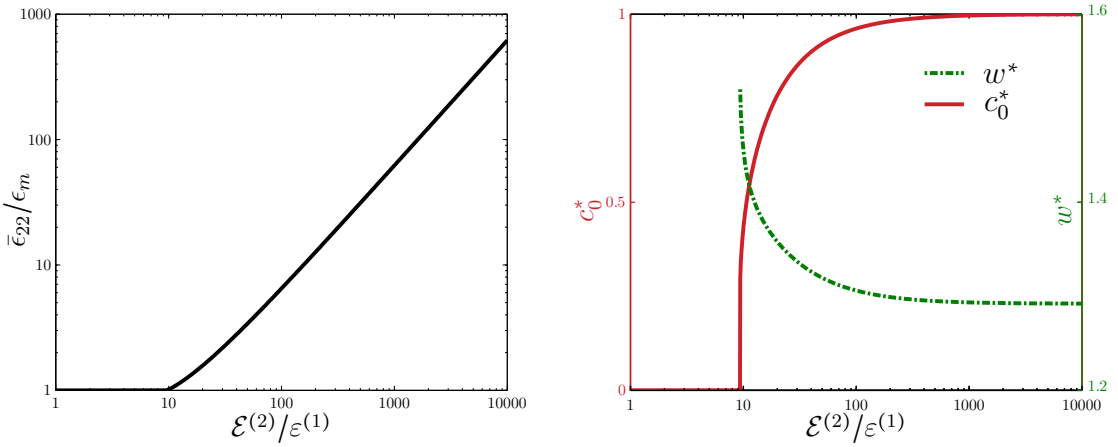


Figure 4.8: The maximum electrostriction achievable in the aligned case. (a) Maximum electrostriction as a function of the ratio $\mathcal{E}^{(2)}/\mathcal{E}^{(1)}$, and (b) concentration $c_0^*$ and aspect ratio $w^*$ at which the maximum occurs.

electric permittivity, large electrostrictive strains can be achieved for the right choices for the microstructural parameters. In fact, as can be deduced from Fig. 4.8, the electrostriction continues to increase (in a nearly linear fashion) for large values of the dielectric coefficient of the inclusion phase. Interestingly, the optimal value $c_0^*$ of the inclusion volume fraction tends to be closer and closer to 100%, suggesting some sort of percolation phenomenon (recall that the microstructures for the special type of homogenization estimates used in this work do not percolate until 100% concentration of the inclusion phase). On the other hand, the corresponding optimal value $w^*$ of the inclusion aspect ratio also tends to a limiting value, which is approximately 1.3.

### Transversely isotropic DECs under non-aligned loading

In this subsection, we consider two-phase, transversely isotropic DECs under non-aligned loading conditions (i.e. $0 \leq \psi < 90°$). For this more general case, the symmetry axis of the composite is not aligned with the direction of the macroscopic electric field and the electrostatic contribution to the total stress is no longer transversely isotropic. In fact, as has already been shown in the previous section, $\bar{\boldsymbol{T}}^{el}$ can be written in the

form given by equation (4.55) with respect to the orthonormal coordinate system defined by the unit vectors $\{\mathbf{t}, \mathbf{n}, \mathbf{k}\}$, where $\mathbf{k} = \hat{\mathbf{E}}_3$ in this case. Given the expression for $\bar{\boldsymbol{T}}^{el}$ and the fact that the total macroscopic stress vanishes inside the composite, it can be shown that

$$\bar{\boldsymbol{\epsilon}} = \bar{\epsilon}_{tt}\mathbf{t}\otimes\mathbf{t} + \bar{\epsilon}_{nn}\mathbf{n}\otimes\mathbf{n} + \bar{\epsilon}_{33}\mathbf{k}\otimes\mathbf{k} + \bar{\epsilon}_{nt}\left(\mathbf{n}\otimes\mathbf{t} + \mathbf{t}\otimes\mathbf{n}\right), \tag{4.77}$$

where

$$\begin{aligned}
\bar{\epsilon}_{nn} &= -\frac{\left[\tilde{\mathcal{E}}_{0r} + \frac{1}{2}\left(\hat{l}^p - \hat{n}^p\right)\tilde{\mathcal{K}}_r^2\right]\sin^2\psi}{3\tilde{\mu}_a}\bar{e}^2 + \frac{\left[-\frac{\tilde{\mathcal{E}}_{0s}}{2} + \frac{1}{2}\left(\hat{k}_p^p - \hat{l}'^p\right)\tilde{\mathcal{K}}_s^2\right]\cos^2\psi}{3\tilde{\mu}_a}\bar{e}^2,\\
\bar{\epsilon}_{tt} &= +\frac{\left(-\tilde{\mathcal{E}}_{0s} + \hat{m}_p^p\tilde{\mathcal{K}}_s^2\right)\cos^2\psi}{4\tilde{\mu}_p}\bar{e}^2 - \frac{\bar{\epsilon}_{nn}}{2}, \quad \bar{\epsilon}_{33} = -\frac{\left(-\tilde{\mathcal{E}}_{0s} + \hat{m}_p^p\tilde{\mathcal{K}}_s^2\right)\cos^2\psi}{4\tilde{\mu}_p}\bar{e}^2 - \frac{\bar{\epsilon}_{nn}}{2}, \text{ and}\\
\bar{\epsilon}_{nt} &= \frac{\left(\tilde{\mathcal{E}}_{0r} + \tilde{\mathcal{E}}_{0s} - 2\hat{m}_n^p\tilde{\mathcal{K}}_r\tilde{\mathcal{K}}_s\right)\sin\left(2\psi\right)}{8\tilde{\mu}_n}\bar{e}^2 + \frac{r\left(\left(\boldsymbol{A}^{(2)}\right)_r^{-1} - \left(\boldsymbol{A}^{(2)}\right)_s^{-1}\right)\tilde{\mathcal{K}}_r\tilde{\mathcal{K}}_s\sin\left(2\psi\right)}{32c_0m_n^p\tilde{\mu}_n}\bar{e}^2.
\end{aligned} \tag{4.78}$$

Note that the components of the strain with respect to the laboratory coordinate system $\{X_1, X_2, X_3\}$, in terms of the strains given in equation (4.78), can be easily obtained as follows

$$\begin{aligned}
\bar{\epsilon}_{11} &= \bar{\epsilon}_{tt}\sin^2\psi + \bar{\epsilon}_{nt}\sin 2\psi + \bar{\epsilon}_{nn}\cos^2\psi\\
\bar{\epsilon}_{22} &= \bar{\epsilon}_{tt}\cos^2\psi - \bar{\epsilon}_{nt}\sin 2\psi + \bar{\epsilon}_{nn}\sin^2\psi\\
\bar{\epsilon}_{12} &= \left(\bar{\epsilon}_{nn} - \bar{\epsilon}_{tt}\right)\sin\psi\cos\psi - \bar{\epsilon}_{nt}\cos 2\psi.
\end{aligned} \tag{4.79}$$

Figure 4.9 shows the effect of changing the orientation of the inclusions $\psi$ on the electrostriction. Figure 4.9(a) shows the electrostriction as a function of the aspect ratio for $c_0 = 0.75$, while Fig. 4.9(b) shows the corresponding plots for $c_0 = 0.9$. The main observation form these figures is that for fixed concentrations, the maximum electrostriction is achieved for aligned (i.e. $\psi = 90°$) microstructures. Another important observation can be made pertaining the limits $w \to 0$ and $w \to \infty$, which correspond, respectively, to laminated and fiber-reinforced composites. As shown in these figures, for aligned microstructures (see the solid lines in Fig. 4.9), the electrostriction vanishes identically for the above limits. This can be explained by

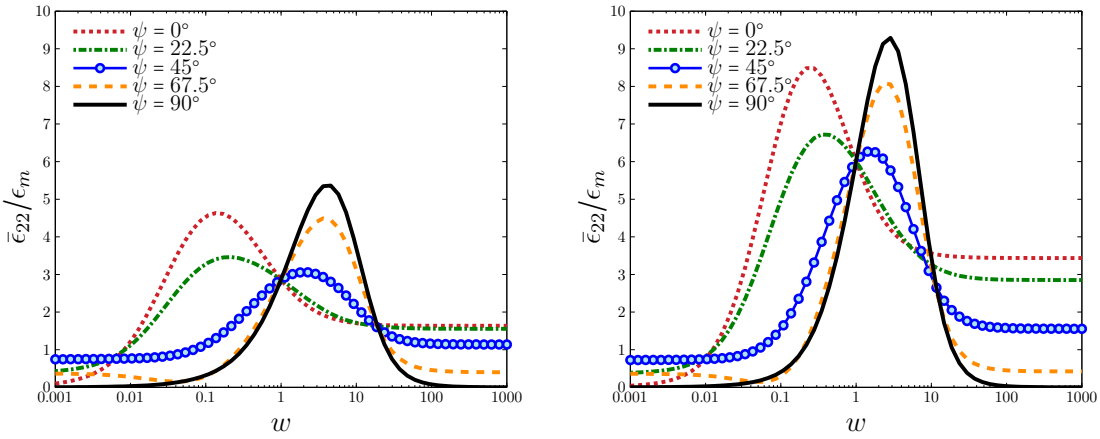


Figure 4.9: Plots for the electrostriction of a DEC with transversely isotropic symmetry under non-aligned loading conditions as a function of the aspect ratio of the inclusions, for different orientations $\psi$. (a) Results for $c_0 = 0.75$, and (b) for $c_0 = 0.9$. In these plots $\mathcal{E}^{(2)}/\varepsilon^{(1)} = 250$.

recalling that the inclusion phase is rigid and the matrix phase is incompressible, and therefore the DEC becomes effectively rigid in the limits where $w \to 0$ or $w \to \infty$. On the other hand, for non-aligned cases (i.e. $\psi \neq 90$) the electrostriction will be non-zero for laminated (or fiber-reinforced) DECs even when the inclusion phase is rigid. This is due to the fact that for laminated (or fiber-reinforced) composites under non-aligned loading conditions, there are shear modes of deformation available to the DEC which result in the non-trivial electrostriction observed in Fig. 4.9 for small (or large) values of the aspect ratio. It is noted that for non-aligned loading conditions the shear component of the macroscopic strain $\bar{\epsilon}_{12}$ is non-zero, and therefore, $\bar{\epsilon}_{22}$ plotted in Fig. 4.9 do not represent the maximum stain. However, we have confirmed that the general picture does not change significantly if we plot the maximum principal strain instead of $\bar{\epsilon}_{22}$.

## 4.5 Concluding remarks

In this chapter we have developed a general homogenization framework for DECs in the limit of infinitesimal deformations. The framework has been used to obtain

estimates for the effective response of two-phase DECs with random particulate microstructures. Our results show that the addition of highly dielectric yet stiff particles can enhance the electromechanical response of DECs, for appropriate choices of the relevant microstructural parameters. This is not a trivial result since the addition of highly dielectric but stiff particles to the dielectric elastomer matrix increases both the overall permittivity and the stiffness of the DEC. While a higher overall permittivity leads to an increased attractive force between the electrodes, the higher stiffness limits the overall electrostrictive strains that can be achieved. Consistent with the early theoretical results for electrostriction (Landau et al. 1984, Shkel & Klingenberg 1998), the framework developed in this work expresses the effective electromechanical coupling of the composite in terms of the derivative of the permittivity with respect to the strain, also incorporating the effect of particle rotations. In addition, it accounts for dipolar interactions between particles, as well as for the nonlinear coupling between the electric and mechanical fields. For these reasons, the new framework is expected to produce more accurate estimates than earlier estimates (Li & Rao 2004, Rao & Li 2004), especially when the field fluctuation in the matrix phase become significant (Li et al. 2004). On the other hand, while the framework developed in this work should be equivalent to the recently developed homogenization framework of Tian et al. (2012), the alternative expression for the electromechanical coupling in terms of the strain-dependent permittivity (instead of third moments of the electric and mechanical fields) has allowed the computation of such coupling constants for composites with general distributions of ellipsoidal inclusions, which is something that has not yet been possible with the formulation of Tian et al. (2012).

The specific estimates developed in this work are based on homogenization estimates of Ponte Castañeda & Willis (1995) for the effective stiffness and permittivity of a certain class of random particulate microstructures consisting of aligned ellipsoidal inclusions of a stiff dielectric material distributed in an soft elastomeric matrix with "ellipsoidal" two-point statistics. For the special case of spherical particles and isotropic (spherical) distributions, the estimate for the effective permittivity reduces to the well-known Maxwell-Garnett approximation (Garnett 1904), while both es-

timates for the effective permittivity and elasticity are known to be rigorous lower bounds (Hashin & Shtrikman 1962, 1963) for the class of statistically isotropic microstructures in this case. In addition, for the case of rigid, perfectly conducting inclusions, the estimates do not "percolate" until 100% concentration of the inclusions, which suggests that the estimates are more appropriate for polydisperse microstructures, such as the Hashin (Hashin & Shtrikman 1962) composite-sphere assemblage microstructure, than for monodisperse microstructures.

Be that as it may, our results show that the electrostriction under "soft electrode" conditions is compressive, and becomes strongest when the electric field is aligned with the long axis of the particles. This is because when the particles are not aligned with the field they tend to reorient themselves with the field producing a tensile contribution to the overall stretch which tends to oppose the compression applied by the electrodes. The results also show that for a fixed, sufficiently large dielectric coefficient for the particles (compared to that of the matrix) the strongest electrostriction is achieved for certain optimal values of the particle concentration ($0 < c_0^* < 1$) and aspect ratio ($1.2 < w^* < 1.6$). Moreover, it was found that the dipole interactions tend to become dominant (over the intrinsic effect of the particles on the Maxwell stress) at sufficiently large particle concentrations, and this is why the optimal particle concentration $c_0^*$ tends to be fairly high. In addition, it was found that the electrostriction increases monotonically with the dielectric coefficient of the particles (in fact, linearly, for large values of the particle dielectric coefficient), with the optimal values of the particle concentration and aspect ratio tending to 100% and $\sim 1.3$, respectively. This result is consistent with earlier findings (Huang et al. 2004), which suggest that the strongest electrostrictive effect occurs near percolation of the inclusion phase. However, as already noted, the estimates used in this work do not "percolate" until reaching 100% of the inclusion phase, and in this sense the results are consistent. On the other hand, high particle volume fractions would tend to produce dielectric breakdown of the elastomeric matrix phase, and it would be expected that lower concentrations of the inclusion phase should be used in practical applications.

In any event, the results of this chapter serves to provide some guidelines for the design of DECs with optimal electrostriction, at least for the special class of particulate microstructures used here. The general theory could also be used in combination with other types of homogenization estimates, such as the effective medium approximation (Bruggeman 1935), that would be perhaps more realistic for systems that percolate at a lower concentration of the inclusion phase. The theory could also be generalized to account for nonlinear susceptibilities for the matrix and inclusion phases, making use of corresponding results for nonlinear dielectrics (Ponte Castañeda 2001), as well as for finite deformations, using similar ideas for magnetorheological elastomers (Ponte Castañeda & Galipeau 2011). Finally, it should be noted that in the applications considered in this chapter we have ignored the possible strain-dependence for the permittivity of the matrix. Although for elastomeric materials this effect would be expected to be small and can be safely neglected, for other materials it may be necessary to account for this effect.

# Chapter 5

# Fiber-constrained DECs: Finite Deformation Response and Stability Analysis at Zero External Tractions

As mentioned earlier in chapter 1, the behavior of soft dielectrics stiffened by long fibers, have been studied recently by Lu et al. (2012) suggesting that constraining the kinematics of an ideal dielectric into 2D plane-strain deformations eliminates the possibility of electromechanical instabilities typically observed in dielectrics subjected to equal biaxial loadings under general 3D conditions (Lu et al. 2012), hence enabling them to undergo larger stretches before dielectric breakdown. Motivated by this finding, in this chapter we will consider DECs reinforced by very stiff, aligned fibers in order to enforce 2D plane-strain conditions. However, unlike the recent work of Lu et al. (2012), where the fibers only act as structural elements to enforce the 2D plane-strain conditions, here we take into account the effect of the fibers—through the disturbances in the local fields caused by them—on the overall electromechanical response of DECs. This will be done by using the homogenization framework of chapter 3 for coupled electro-elastic problems (see Ponte Castañeda & Siboni 2012,

for more details). In particular, we will develop estimates for the effective response of fiber-constrained DECs undergoing finite deformations. More specifically, we consider fibrous DECs consisting of a dielectric elastomer matrix phase constrained to undergo plane-strain deformations by means of aligned, long, rigid-dielectric fibers of elliptical cross section that are also aligned but randomly distributed in the transverse plane. We then use available estimates (e.g., Lopez-Pamies & Ponte Castañeda 2006*a*, Avazmohammadi & Ponte Castañeda 2013) for the purely mechanical response of such composites at finite strains, along with the partial decoupling strategy/approximation to estimate the effective electro-active response of such DECs. Having obtained an estimate for the effective response of the fiber-reinforced DECs, we then investigate the effect of different microstructural parameters on the response and possible failure of such composites, including susceptibility to electromechanical instabilities (through loss of positive definiteness), localization instabilities (through loss of ellipticity), and dielectric breakdown. The framework developed here also makes possible the development of a procedure for the optimal design of DECs capable of achieving large electrostrictive strains before failure. The rest of this chapter is organized as follows. Section 5.1 is concerned with the development of explicit estimates for the response of two-phase DECs with fibrous microstructures under aligned loading conditions. In this section, we first discribe the initial microstructure of the DECs and its evolution. Estimate for the effective mechanical and electrostatic energies will be provided next. Then, as argued in chapter 3, the effective total energy of the DEC is obtained using the partial decoupling approximation/strategy, and finally, we will specialize the general failure criteria described in chapter 2 for the fiber-constrained DECs undergoing 2D plane-strain deformations. In section 5.2 we provide an example application to illustrate the theory developed here, and to investigate the effect of various microstructural parameters on the overall response and stability of fiber-constrained DECs.

## 5.1 DECs consisting of long aligned fibers under aligned in-plane loadings

### 5.1.1 Initial microstructure

As shown in Fig. 5.1, we consider a two-phase DEC consisting of a matrix phase, denoted by the superscript "1", and an inclusion phase, denoted by the superscript"2". The matrix phase is assumed to be an ideal dielectric elastomer with the constitutive response of the form (2.13). The inclusion phase consists of one family of rigid aligned cylindrical particles (or fibers) with the constitutive response of the form (2.20). The concentrations of the matrix and inclusion phases in the reference configuration are denoted, respectively, by

$$c_0^{(1)} = 1 - c_0 \quad \text{and} \quad c_0^{(2)} = c_0. \tag{5.1}$$

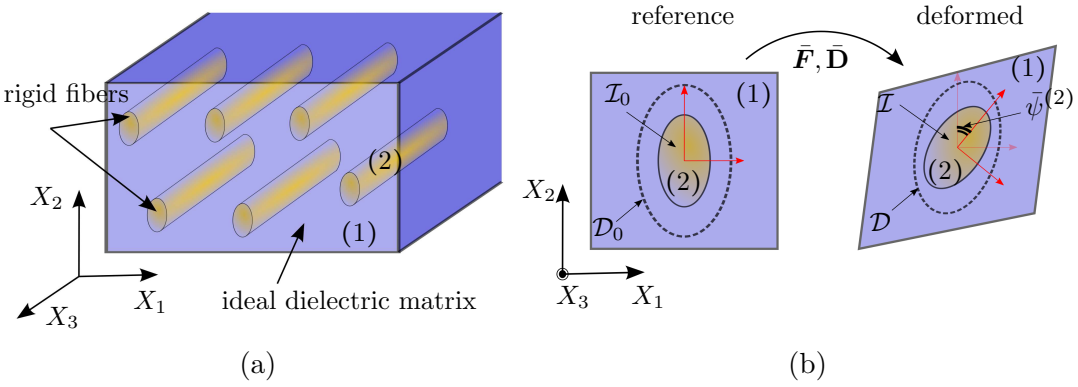


Figure 5.1: Schematic representation of two-phase fibrous DECs with random microstructures. (a) A DEC consisting of very long fibers, embedded firmly in an ideal dielectric matrix. (b) The microsructural information of the composite in the reference and deformed configurations.

The fibers (in the reference configuration) are aligned with the $X_3$ direction of the laboratory axis $\{X_1, X_2, X_3\}$ and are assumed to be very long such that their geometry is completely described by the shape of their cross-sections. In this work

we consider elliptical shapes for the cross-section of the fibers as characterized by

$$\mathcal{I}_0 = \{\mathbf{X} = (X_1, X_2)\,, \text{ such that } |\boldsymbol{Z}_0^{-T}\mathbf{X}| \leq 1\}\,, \tag{5.2}$$

where $\boldsymbol{Z}_0$ is a second-order tensor describing the shape (in the reference configuration) of the fibers.

Finally, we assume that the fibers are distributed with "elliptical symmetry" (Ponte Castañeda & Willis 1995). This means that the two-point probability function for finding two fibers separated by a vector $\mathbf{Z} = (Z_1, Z_2)$ depends on $\mathbf{Z}$ only through the combination $|(\boldsymbol{D}_0^{-T}\mathbf{Z})|$, where $\boldsymbol{D}_0$ is a symmetric, second-order tensor serving to define a "distributional ellipse" in the reference configuration via

$$\mathcal{D}_0 = \{\mathbf{X} = (X_1, X_2)\,, \text{ such that } |\boldsymbol{D}_0^{-T}\mathbf{X}| \leq 1\}\,. \tag{5.3}$$

Note that statistical isotropy can be achieved by setting $\boldsymbol{D}_0 = \boldsymbol{I}$, such that the two-point probability function depends on $\mathbf{Z}$ only via $|\mathbf{Z}|$, and the distributional ellipse becomes a circle. In this chapter, for simplicity, we assume that the shape of the distributional ellipses in the reference configuration is identical to the shape of the fibers such that $\boldsymbol{D}_0 = \boldsymbol{Z}_0$.

### 5.1.2 Evolution of the microstructure

Note that since the fibers are rigid the deformation along the fibers (i.e., the $X_3$ direction) is identically zero, and therefore the kinematics of the fiber-constrained DECs can be described by 2D plane-strain deformations in the plane perpendicular to the long axes of the fibers (i.e., $X_1$-$X_2$ plane).

The rigid fibers can, in general, undergo rotations in the $X_1$-$X_2$ plane. Given their identical cross-sections in the reference configuration, it seems reasonable to assume, for simplicity, that they will rotate with an average rotation denoted by the angle $\bar{\psi}^{(2)}$. Therefore, in the deformed configuration fibers are described by the shape of

their cross-sections via

$$\mathcal{I} = \{\mathbf{x} = (x_1, x_2)\,, \text{ such that } |\boldsymbol{Z}^{-T}\mathbf{x}| \leq 1\}\,, \tag{5.4}$$

where $\boldsymbol{Z}$ is the deformed counterpart of $\boldsymbol{Z}_0$, given by

$$\boldsymbol{Z} = \bar{\boldsymbol{R}}^{(2)}\boldsymbol{Z}_0\bar{\boldsymbol{R}}^{(2)^T} \quad \text{with} \quad \bar{\boldsymbol{R}}^{(2)} = \begin{bmatrix} \cos\bar{\psi}^{(2)} & -\sin\bar{\psi}^{(2)} \\ \sin\bar{\psi}^{(2)} & \cos\bar{\psi}^{(2)} \end{bmatrix} \tag{5.5}$$

Note that $\bar{\psi}^{(2)}$ will in general depend on both the macroscopic deformation and the macroscopic electric fields. However as mentioned earlier under the assumptions of the partial decoupling approximation, $\bar{\psi}^{(2)}$ will be determined from the solution of the purely mechanical homogenization problem, that is, we will take

$$\bar{\psi}^{(2)} \approx \bar{\psi}^{(2)}_{me} \tag{5.6}$$

where the purely mechanical fiber orientation $\psi^{(2)}_{me}$ will be given in the next subsection.

Similar to the fibers, the evolution of the distribution is expected to depend in general on both the mechanical and electrostatic loadings. As pointed out by Ponte Castañeda & Siboni (2012) in the context of DECs with periodic microstructures, the shape of the unit cell is expected to be controlled by the macroscopic deformation, at least up to the possible development of an instability. On the other hand, in the context of random microstructures, the above-defined two-point correlation functions would be expected to depend in a complicated way on the macroscopic fields, especially for large fiber concentrations. In addition, the two-point correlation functions would be expected to depend on higher-point statistics. However, given that the homogenization estimate that we will use below to estimate the macroscopic electrostatic response of the DECs makes use of only two-point correlation functions, in this work, we will make use of the *ad hoc* simplifying assumption that the inclusions remains distributed with "elliptical" symmetry in the deformed configuration, such that the distributional ellipses evolve solely as a consequence of the macroscopic

deformation (see Ponte Castañeda & Galipeau 2011, for an analogous assumption in the context of magneto-active elastomers).

Given the above assumptions, the elliptical distribution of the inclusions in the deformed configuration is described by the deformed distributional ellipse

$$\mathcal{D} = \{\mathbf{x} = (x_1, x_2)\,, \text{ such that } |\boldsymbol{D}^{-T}\mathbf{x}| \leq 1\}\,, \tag{5.7}$$

where

$$\boldsymbol{D} = \bar{\boldsymbol{F}}\boldsymbol{D}_0, \tag{5.8}$$

is the distributional shape tensor in the deformed configuration.

The incompressibility of the matrix phase along with the rigidity of the fibers imply overall incompressibility for the DECs considered in this chapter. Therefore, the concentration of the phases remain unchanged as the deformation progresses, such that

$$c^{(1)} = c_0^{(1)} = 1 - c_0, \quad \text{and} \quad c^{(2)} = c_0^{(2)} = c_0 \tag{5.9}$$

### 5.1.3 Estimates for the effective mechanical energy

An explicit expression for the effective mechanical energy of fiber-reinforced composites consisting of incompressible matrices and rigid aligned fibers may be obtained from the recent work of Lopez-Pamies & Ponte Castañeda (2006*a*). Given the incompressiblity of the matrix phase and rigidity of the fibers, it is obvious that the composite can only undergo pure shear in the $X_1$-$X_2$ plane. Recall that the macroscopic deformation $\bar{\boldsymbol{F}}$ can be decomposed as follows

$$\bar{\boldsymbol{F}} = \bar{\boldsymbol{R}}\bar{\boldsymbol{U}}, \tag{5.10}$$

where $\bar{\boldsymbol{R}}$ denotes the macroscopic rotation, $\bar{\boldsymbol{U}}$ is the right-stretch tensor. When referred to an underlying coordinates system (e.g., the laboratory axis $\{X_1, X_2\}$), the

macroscopic rotation $\bar{\boldsymbol{R}}$ can be represented by the matrix

$$\left[\bar{\boldsymbol{R}}\right] = \begin{bmatrix} \cos\bar{\psi} & -\sin\bar{\psi} \\ \sin\bar{\psi} & \cos\bar{\psi} \end{bmatrix}, \tag{5.11}$$

while the right-stretch tensor $\bar{\boldsymbol{U}}$ can be diagonalized as follows

$$\left[\bar{\boldsymbol{U}}\right] = \left[\bar{\boldsymbol{Q}}\right]\left[\bar{\boldsymbol{\Lambda}}\right]\left[\bar{\boldsymbol{Q}}\right]^T, \text{ where } \left[\bar{\boldsymbol{Q}}\right] = \begin{bmatrix} \cos\bar{\theta} & -\sin\bar{\theta} \\ \sin\bar{\theta} & \cos\bar{\theta} \end{bmatrix}, \text{ and } \left[\bar{\boldsymbol{\Lambda}}\right] = \begin{bmatrix} \bar{\lambda}_1 & 0 \\ 0 & \bar{\lambda}_2 \end{bmatrix}. \tag{5.12}$$

Here the angle $\bar{\psi}$ denotes the macroscopic in-plane rotation , $\bar{\theta}$ denotes the (in-plane) loading angle, and $\bar{\lambda}_1 := \bar{\lambda}$ and $\bar{\lambda}_2 := \bar{\lambda}^{-1}$ are the principal stretches corresponding to the macroscopic deformation $\bar{\boldsymbol{F}}$. Note that the incompressibility of the composite is enforced by the above choices for the principal stretches.

For the composites described earlier in this section and the above loading parameters the purely mechanical effective energy $\tilde{W}_{me}\left(\bar{\boldsymbol{F}}\right)$ is given by Lopez-Pamies & Ponte Castañeda (2006*a*) as follows

$$\tilde{W}_{me}\left(\bar{\boldsymbol{F}}\right) = \tilde{W}_{me}\left(\bar{\lambda},\bar{\theta}\right) = \left(c_0 - 1\right)\frac{\mu^{(1)}J_m}{2}\ln\left[1 - \frac{\hat{I}-2}{J_m}\right], \tag{5.13}$$

where

$$\begin{aligned} \hat{I} = {} & \frac{c_0\left(1+\bar{\lambda}^2\right)^2 + \left[1 + 2\left(c_0-2\right)c_0\bar{\lambda}^2 + \bar{\lambda}^4\right]w + c_0\left(1+\bar{\lambda}^2\right)^2 w^2}{\left(1-c_0\right)^2\bar{\lambda}^2 w} \\ & - \frac{c_0\left(\bar{\lambda}^4-1\right)\left(w^2-1\right)}{\left(1-c_0\right)^2\bar{\lambda}^2 w}\sin\left(\bar{\varphi}\right)\sin\left(\bar{\varphi}-2\bar{\theta}\right) - \frac{2c_0\left(1+\bar{\lambda}^2\right)\left(1+w^2\right)}{\left(1-c_0\right)^2\bar{\lambda}\,w}\cos\left(\bar{\varphi}\right). \end{aligned} \tag{5.14}$$

In the above equation

$$\bar{\varphi} := \bar{\psi}^{(2)}_{me} - \bar{\psi}, \tag{5.15}$$

denotes the relative (in-plane) rotation of the fibers (with respect to the macroscopic rotation $\bar{\psi}$), and satisfies the following identity

$$2\bar{\lambda}\left(1+w^2\right)\sin\left(\bar{\varphi}\right) - \left(\bar{\lambda}^2-1\right)\left(w^2-1\right)\sin\left[2\left(\bar{\varphi}-\bar{\theta}\right)\right] = 0. \tag{5.16}$$

In other words, equation (5.16), along with the definition (5.15), can be solved to obtain the average rotation of the fibers, $\bar{\psi}^{(2)}_{me}$, in the purely mechanical problem.

### 5.1.4 Estimates for the effective electrostatic energy

In this subsection, we obtain the electrostatic contribution to the effective energy for the fiber-constrained DECs. This task is best done by first computing the electrostatic energy in the deformed configuration and then transforming it back to the reference configuration. Hashin-Shtrikman type estimates for the electrostatic energy of a DEC (in the deformed configuration) with elliptical fibers (as described by the shape tensor $\boldsymbol{Z}$) which are distributed with elliptical symmetry (as described by the distributional shape tensor $\boldsymbol{D}$) can be obtained by following the work of Ponte Castañeda & Willis (1995). Thus, the effective electrostatic energy of the DECs can be written as

$$\tilde{w}_{el}\left(\bar{\boldsymbol{F}},\bar{\mathbf{d}}\right)=\frac{1}{2}\bar{\mathbf{d}}\cdot\tilde{\boldsymbol{\varepsilon}}^{-1}\bar{\mathbf{d}},\quad\text{where}\quad\tilde{\boldsymbol{\varepsilon}}\left(\bar{\boldsymbol{F}}\right)=\varepsilon^{(1)}\boldsymbol{I}+c^{(2)}\left[\left(\boldsymbol{\varepsilon}^{(2)}-\varepsilon^{(1)}\boldsymbol{I}\right)^{-1}+\boldsymbol{P}\right]^{-1}\tag{5.17}$$

is the deformation dependent homogenized permittivity of the composite with the local permittivity

$$\boldsymbol{\varepsilon}\left(\mathbf{x}\right)=\varepsilon^{(1)}\boldsymbol{I}+\Theta^{(2)}\left(\mathbf{x}\right)\left(\boldsymbol{\varepsilon}^{(2)}-\varepsilon^{(1)}\boldsymbol{I}\right).\tag{5.18}$$

In the above expressions, $\varepsilon^{(1)}$ is the permittivity of the matrix, and

$$\boldsymbol{\varepsilon}^{(2)}=\bar{\boldsymbol{R}}^{(2)}\boldsymbol{\mathcal{E}}^{(2)}\bar{\boldsymbol{R}}^{(2)^{T}}\tag{5.19}$$

is the permittivity of the fibers in the deformed configuration. The second-order tensor $\boldsymbol{P}$ is given by

$$\boldsymbol{P}=\boldsymbol{P}^{I}-c^{(2)}\boldsymbol{P}^{D},\tag{5.20}$$

where $\boldsymbol{P}^{I}$ and $\boldsymbol{P}^{D}$ are Eshelby type microstructural tensors that encode the effect of the shape and distribution of the fibers, respectively. They are given by

$$\boldsymbol{P}^{I}=\frac{\det\boldsymbol{Z}}{2\pi\varepsilon^{(1)}}\int_{|\boldsymbol{\xi}|=1}\boldsymbol{\xi}\otimes\boldsymbol{\xi}\left|\boldsymbol{Z}\boldsymbol{\xi}\right|^{-2}dS,\quad\text{and}\quad\boldsymbol{P}^{D}=\frac{\det\boldsymbol{D}}{2\pi\varepsilon^{(1)}}\int_{|\boldsymbol{\xi}|=1}\boldsymbol{\xi}\otimes\boldsymbol{\xi}\left|\boldsymbol{D}\boldsymbol{\xi}\right|^{-2}dS.\tag{5.21}$$

It is emphasized that expression (5.17) for $\tilde{\boldsymbol{\varepsilon}}$ depends on the deformation via the dependence of the shape tensors $\boldsymbol{Z}$ and $\boldsymbol{D}$, and the permittivity $\boldsymbol{\varepsilon}^{(2)}$ on the deformation, as it is evident from equations (5.5), (5.8), and (5.19). Therefore, it is useful to define

$$\hat{\boldsymbol{P}}_0\left(\bar{\boldsymbol{U}}\right) := \boldsymbol{R}^p \hat{\boldsymbol{P}}_0^I \boldsymbol{R}^{p^T} - c_0 \hat{\boldsymbol{P}}_0^D\left(\bar{\boldsymbol{U}}\right), \tag{5.22}$$

such that

$$\boldsymbol{P} = \frac{1}{\varepsilon^{(1)}} \bar{\boldsymbol{R}} \hat{\boldsymbol{P}}_0\left(\bar{\boldsymbol{U}}\right) \bar{\boldsymbol{R}}^T \tag{5.23}$$

to make the dependence of the $\boldsymbol{P}$-tensor on the deformation, more transparent. In (5.22) the new Eshelby tensors $\hat{\boldsymbol{P}}_0^I$ and $\hat{\boldsymbol{P}}_0^D\left(\bar{\boldsymbol{U}}\right)$ are defined as follows

$$\hat{\boldsymbol{P}}_0^I = \frac{\det \boldsymbol{Z}_0}{2\pi} \int_{|\boldsymbol{\xi}|=1} \boldsymbol{\xi} \otimes \boldsymbol{\xi} \left|\boldsymbol{Z}_0 \boldsymbol{\xi}\right|^{-2} dS \quad \text{and} \quad \hat{\boldsymbol{P}}_0^D = \frac{\det \boldsymbol{D}_0}{2\pi} \int_{|\boldsymbol{\xi}|=1} \boldsymbol{\xi} \otimes \boldsymbol{\xi} \left|\boldsymbol{D}_0 \bar{\boldsymbol{U}} \boldsymbol{\xi}\right|^{-2} dS, \tag{5.24}$$

and the rotation tensor $\boldsymbol{R}^p\left(\bar{\boldsymbol{U}}\right) := \bar{\boldsymbol{R}}^T \bar{\boldsymbol{R}}^{(2)}$ on the right side of (5.22) characterizes the relative rotation of the fibers with respect to the macroscopic rotation $\bar{\boldsymbol{R}}$. When referred to the underlying laboratory axis $\{X_1, X_2\}$, the relative rotation is represented by

$$\left[\boldsymbol{R}^p\left(\bar{\boldsymbol{U}}\right)\right] = \begin{bmatrix} \cos\bar{\varphi} & -\sin\bar{\varphi} \\ \sin\bar{\varphi} & \cos\bar{\varphi} \end{bmatrix}, \tag{5.25}$$

where $\bar{\varphi} = \bar{\psi}^{(2)} - \bar{\psi}$ is the relative in-plane rotation of the fibers with respect to the macroscopic rotation. Note that in the computations that follow we make the substitution $\bar{\psi}^{(2)} \simeq \bar{\psi}_{me}^{(2)}$ in accordance with the partial decoupling approximation, discussed earlier.

Substituting (5.22) along with (5.19) into $(5.17)_2$, we obtain

$$\tilde{\boldsymbol{\varepsilon}}\left(\bar{\boldsymbol{F}}\right) = \bar{\boldsymbol{R}} \tilde{\boldsymbol{\mathcal{E}}}\left(\bar{\boldsymbol{U}}\right) \bar{\boldsymbol{R}}^T, \tag{5.26}$$

where

$$\tilde{\boldsymbol{\mathcal{E}}}\left(\bar{\boldsymbol{U}}\right) = \varepsilon^{(1)} \boldsymbol{I} + \frac{c_0}{\bar{J}} \left\{ \boldsymbol{R}^p \left(\boldsymbol{\mathcal{E}}^{(2)} - \varepsilon^{(1)} \boldsymbol{I}\right)^{-1} \boldsymbol{R}^{p^T} + \frac{1}{\varepsilon^{(1)}} \hat{\boldsymbol{P}}_0\left(\bar{\boldsymbol{U}}\right) \right\}^{-1} \tag{5.27}$$

is the effective permittivity in a coordinate system that is rotated by the macroscopic

rotation. Then, the effective electrostatic energy $\tilde{W}_{el}\big(\bar{\boldsymbol{F}},\bar{\mathbf{D}}\big) = \tilde{w}_{el}\big(\bar{\boldsymbol{F}},\bar{\mathbf{d}}\big)/\bar{J}$, can be obtained as follows

$$\tilde{W}_{el}\big(\bar{\boldsymbol{F}},\bar{\mathbf{D}}\big) = \frac{1}{2\bar{J}}\bar{\mathbf{D}}\cdot\Big[\bar{\boldsymbol{U}}\tilde{\boldsymbol{\mathcal{E}}}^{-1}\big(\bar{\boldsymbol{U}}\big)\bar{\boldsymbol{U}}\Big]\bar{\mathbf{D}}. \tag{5.28}$$

The above estimate for the effective electrostatic energy and the estimate (5.13) for the effective mechanical energy can be used to obtain the effective electromechanical energy of the composites via expression (3.38).

### 5.1.5 Constitutive response of the DECs

Having the explicit expressions for $\tilde{W}_{me}$ and $\tilde{W}_{el}$, one can compute the effective constitutive response of the DECs by following the prescriptions of section 3. Thus, it is obtained that

$$\bar{\mathbf{E}} = \frac{\partial\tilde{W}_{el}}{\partial\bar{D}}, \quad \text{and} \quad \bar{\boldsymbol{S}} = \bar{\boldsymbol{S}}^{me} + \bar{\boldsymbol{S}}^{el}, \tag{5.29}$$

where

$$\bar{\boldsymbol{S}}^{me} = \frac{\partial\tilde{W}_{me}}{\partial\bar{\boldsymbol{F}}} - \bar{p}\bar{\boldsymbol{F}}^{-T} \quad \text{and} \quad \bar{\boldsymbol{S}}^{el} = \frac{\partial\tilde{W}_{el}}{\partial\bar{\boldsymbol{F}}} \tag{5.30}$$

are, respectively, the purely mechanical (i.e., in the absence of the electric fields) and electrostatic contributions to the macroscopic Piola-Kirchhoff stress. It is noted that the hydrostatic pressure term $-\bar{p}\bar{\boldsymbol{F}}^{-T}$ on the right side of equation $(5.30)_1$ accounts for the overall incompressibility of the composite. The corresponding Eulerian expressions for the macroscopic total stress and electric field are provided in E.

### 5.1.6 Failure analysis of the fiber-constrained DECs under aligned loading conditions

Here, we provide explicit conditions for characterizing the onset of instabilities in fiber-reinforced DECs undergoing 2D plane-strain deformations, by specializing the more general conditions of section 2.4.

*Loss of convexity of the homogenized energy.* As was the case for the homogeneous

electro-active materials, the loss of convexity in DECs can be characterized by the loss of positive definiteness (LPD) of the effective electroelastic energy of the DECs. Such conditions in general depend on the loading path, and therefore simplified expressions may not be obtained without the knowledge of the loading path. In the next section of this chapter, we focus our attention on aligned loadings of the type specified by the macroscopic fields

$$\left[\bar{\boldsymbol{F}}\right] = \begin{bmatrix} \bar{\lambda} & 0 \\ 0 & \bar{\lambda}^{-1} \end{bmatrix} \quad \text{and} \quad \bar{\mathbf{D}} = \bar{D}\hat{\mathbf{E}}_2. \tag{5.31}$$

Thus, the loss of convexity criterion will be provided next for loadings of the form (5.31).

Recall that the increments for the 2D plane-strain problem can be characterized by the vector

$$\boldsymbol{\delta} := \left(u_{1,1}, u_{1,2}, u_{2,1}, \dot{d}_1, \dot{d}_2\right), \tag{5.32}$$

where $u_{i,j}$ $(i,j = 1,2)$ are the components of the (incremental) displacement gradient and $\dot{d}_i$ $(i = 1,2)$ are the components of the incremental electric displacement. (Note that $u_{2,2} = -u_{1,1}$, due to the incompressibility conditions.) Thus, the positive definiteness of the quadratic form (2.37) can be determined by evaluating the sign of the eigenvalues of the Hessian

$$\mathcal{H}_{ij} := \frac{\partial^2 \mathcal{Q}}{\partial \delta_i \partial \delta_j}. \tag{5.33}$$

When at least one of the eigenvalues vanishes for the first time, in a given loading path, the material loses convexity. We refer to the eigenvector corresponding to the vanishing eigenvalue as the (eigen-) mode of instability. For the aligned loadings of the form (5.31), two modes can be recognized for the loss of convexity: *aligned* and *non-aligned* modes. For the aligned mode, the eigenvector corresponding to the vanishing eigenvalue is parallel to the loading direction (i.e., only the $u_{1,1}$ and $\dot{d}_2$ components of $\boldsymbol{\delta}$ are non-zero), while for the non-aligned mode, the eigenvector corresponding to the vanishing eigenvalue is precisely orthogonal to the loading direction (i.e., only the $u_{1,2}$, $u_{2,1}$, and $\dot{d}_1$ components of $\boldsymbol{\delta}$ are non-zero). As pointed out by Hill (1967)

in the purely mechanical context, when the eigenmodal directions have a projection along the loading directions, as it is the case for the aligned modes here, a maximum or limit load behavior is expected. On the other hand, when the eigenmodes are orthogonal to the loading directions, as it is the case for the non-aligned modes here, a bifurcation is possible.

It is worthwhile to mention that in the absence of external mechanical tractions, the conditions for the possible development of aligned loss of convexity modes have been considered by Zhao et al. (2007) for ideal dielectrics and by Bertoldi & Gei (2011) for laminated EAPCs, leading to the conditions that

$$\frac{\partial^2 \tilde{W}}{\partial \bar{\lambda}^2} = 0, \quad \text{or} \quad \frac{\partial^2 \tilde{W}}{\partial \bar{\lambda}^2} \times \frac{\partial^2 \tilde{W}}{\partial \bar{D}_2^2} = \left( \frac{\partial^2 \tilde{W}}{\partial \bar{\lambda} \partial \bar{D}_2} \right)^2 . \tag{5.34}$$

The non-aligned mode, however, will correspond to other types of instabilities not discussed in the works mentioned above. Such non-aligned instability modes in the absence of external tractions correspond to a trivial rotational instability that can be safely ignored (see Truesdell & Noll 2004, for more details). On the other hand, when the external tractions are non-zero, the non-aligned modes may not be ignored, as will be discussed elsewhere. It should be emphasized that here we are mainly interested in cases with zero external tractions, where the aligned LPD modes are the only ones that are relevant. However, the non-aligned LPD modes will also be included in the discussion of the results, for completeness.

*Loss of strong ellipticity of the homogenized energy.* The loss of strong ellipticity of DECs can be characterized by the loss of positive definiteness of the generalized acoustic tensor defined by (2.38), where the incremental moduli are obtained from the second derivatives of the homogenized energy $\tilde{W}$ as opposed to $W$. Under the assumption of 2D plane-strain deformations with aligned microstructures, and under aligned loading conditions of the form (5.31), the condition (2.40) can be further simplified. Thus, the DEC can be shown to be strongly elliptic when the polynomial

$$a_6^* \xi^6 + a_4^* \xi^4 + a_2^* \xi^2 + a_0^* = 0, \tag{5.35}$$

has no real roots. The coefficient in (5.35) are given (Rudykh & deBotton 2011) by

$$\begin{aligned}
a_6^* &:= \tilde{A}_{2121}\tilde{M}_{22} - \tilde{\Gamma}_{122}^2 \\
a_4^* &:= \tilde{A}_{2121}\tilde{M}_{11} + \left[\tilde{A}_{1111} + \tilde{A}_{2222} - 2\left(\tilde{A}_{2112} + \tilde{A}_{2211}\right)\right]\tilde{M}_{22} - \left(\tilde{\Gamma}_{112} + \tilde{\Gamma}_{121}\right)^2 \\
a_2^* &:= \left[\tilde{A}_{1111} + \tilde{A}_{2222} - 2\left(\tilde{A}_{2211} + \tilde{A}_{2112}\right)\right]\tilde{M}_{11} + \tilde{A}_{1212}\tilde{M}_{22} + 2\tilde{\Gamma}_{121}\left(\tilde{\Gamma}_{112} + \tilde{\Gamma}_{121}\right) \\
a_0^* &:= \tilde{A}_{1212}\tilde{M}_{11} - \tilde{\Gamma}_{121}^2,
\end{aligned} \tag{5.36}$$

where the components of the effective electromechanical moduli ($\tilde{\mathbb{A}}$, $\tilde{\boldsymbol{\Gamma}}$, $\tilde{\boldsymbol{M}}$) are defined by expressions similar to (2.33) and (2.26), except that $W$ is replaced by $\tilde{W}$. It is remarked that loss of strong ellipticity implies loss of convexity but the opposite is not necessarily true.

*Dielectric breakdown of the DEC.* The condition for the safe operation of a general electro-active material is given by inequality (2.41). Therefore, the breakdown occurs for a DEC when the equality in (2.41) holds. The maximum electric field for the class of DEC of interest here under aligned loadings of the form (5.31) is expected to take place at the top of the fibers. This critical value may be easily obtained by noting that the Hashin-Shtrikman-type estimates used in this work for the electric fields are uniform inside the fibers. Thus, the vertical component (in the $X_2$ direction) of the electric field inside the fibers is given by

$$\bar{e}^{(2)} = \frac{\varepsilon^{(1)}\bar{e}}{\varepsilon^{(1)} + \left(\mathcal{E}^{(2)} - \varepsilon^{(1)}\right)\left(\frac{1}{1+w} - c_0^{(2)}\frac{\bar{\lambda}^2}{\bar{\lambda}^2+w}\right)}. \tag{5.37}$$

where $\bar{e}$ is the corresponding vertical component of the macroscopic electric field.

Then, the electric field in the dielectric elastomer immediately outside and on top of the fibers can be obtained by means of the jump condition for the electric displacement, i.e., $\mathcal{E}^{(2)}\bar{e}^{(2)} = \varepsilon^{(1)}e_{max}^{(1)}$, so that the maximum value of the electric field is given by

$$e_{max}^{(1)} = \frac{\mathcal{E}^{(2)}\bar{e}}{\varepsilon^{(1)} + \left(\mathcal{E}^{(2)} - \varepsilon^{(1)}\right)\left(\frac{1}{1+w} - c_0^{(2)}\frac{\bar{\lambda}^2}{\bar{\lambda}^2+w}\right)}. \tag{5.38}$$

In the following sections, use will be made of expression (5.38), together with the inequality (2.41), to estimate the overall electric strength of the DECs.

## 5.2 Results and discussion

In this section, we investigate the effective response and possible failure instabilities in the fiber-constrained DECs with elliptical microstructures discussed earlier, under aligned loadings of the form (5.31). Toward this end, we consider a dielectric actuator, consisting of a fiber-constrained DEC that is in perfect contact with two electrodes. The electric field is applied to the DEC sample by means of a direct potential difference ($\Delta V$) between the electrodes, which are made of *electrically conducting grease* (as opposed to metallic conductors), so that the deformation of the DEC is not constrained by them. Finally, we assume that the electrodes are perfect conductors such that all the electric fields are identically zero inside them.

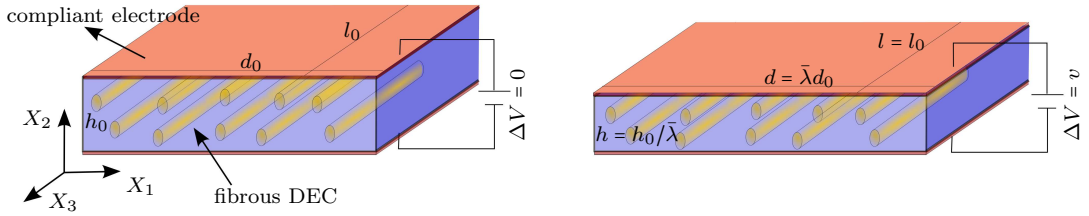


(a) reference (b) deformed

Figure 5.2: Schematic representation of a dielectric actuator made out of a thin DEC layer sandwiched between two compliant electrodes. (a) The actuator in the reference configuration ($\Delta V = 0$), and (b) the actuator in the deformed configuration ($\Delta V = v \neq 0$).

As shown in Fig. 5.2(a), we consider a dielectric actuator, which is aligned with the laboratory axis $\{X_1, X_2, X_3\}$ in its undeformed state (i.e., when $\Delta V = 0$). We assume that the height of the sample is small compared to its width and depth, such that $h_0 \ll d_0, l_0$. The microstructure of the DEC consists of one family of identical cylindrical fibers with their longest axis parallel to the $X_3$ direction. The fibers are assumed to have a general elliptical cross-section aligned with the coordinate axis in the $X_1$-$X_2$ plane, see Fig. 5.3(a). Thus, their geometry (in the reference configuration) is characterized by the aspect ratio of the cross section, denoted by $w = b_0^i/a_0^i$. The initial distribution of the fibers in the reference configuration has elliptic symmetry with the same shape as the fiber cross-sections, such that $w_0^d = b_0^d/a_0^d = w$. For simplicity,

the fibers are assumed to have an isotropic dielectric response, characterized by the permittivity $\boldsymbol{\mathcal{E}}^{(2)} = \mathcal{E}^{(2)}\boldsymbol{I}$, and the matrix phase is assumed to be an incompressible ideal dielectric elastomer with permittivity $\varepsilon^{(1)}$ and a mechanical response of the Gent form (2.14) with shear modulus $\mu^{(1)}$ and strain-locking parameter $J_m$.

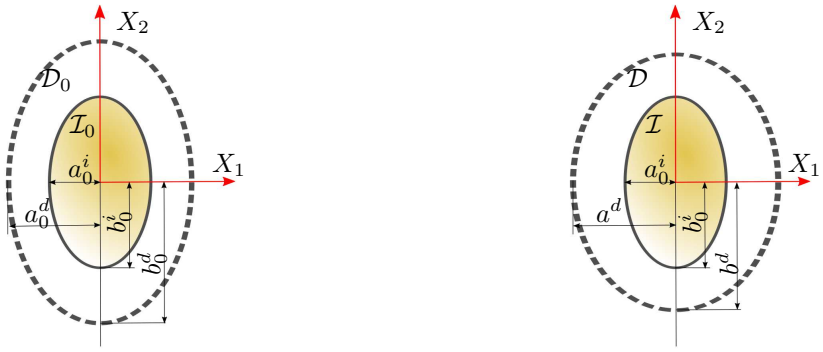


(a) reference (b) deformed

Figure 5.3: Microstructural details of the fiber-constrained DEC in the (a) reference and (b) deformed configurations.

As shown in Fig. 5.2(b), upon the application of the potential difference $\Delta V = v$, the actuator is expected to deform into a new configuration characterized by the macroscopic deformation gradient specified by $(5.31)_1$. Given the assumptions discussed in the context of the evolution of the microstructure in section 5.1.2, it would be expected that the microstructure of the DEC would remain aligned under the specific loading conditions of this section, at least up to the possible onset of any macroscopic instabilities. (In particular, this means that the average orientation of the fibers would be expected to remain aligned, while the orientation of specific fibers may differ from the average.) In addition, the geometry of the fibers in the deformed configuration is characterized by the same aspect ratio $w$, since the fibers are assumed to be rigid (see Fig. 5.3(b)). For simplicity, as mentioned in the previous section, we assume that the distribution of the fibers evolves with the macroscopic deformation, and therefore maintains its elliptical symmetry in the deformed configuration, with

current aspect ratio given by

$$w^d = \frac{b^d}{a^d} = \frac{\bar{\lambda}^{-1}\, b_0^d}{\bar{\lambda}\, a_0^d} = \bar{\lambda}^{-2} w. \tag{5.39}$$

Given that the height of the sample is much smaller than its width, we can assume uniform macroscopic electric fields everywhere inside the composite specimen except near the side surfaces where fringing effects are expected to occur. In fact, as already pointed out by Siboni & Ponte Castañeda (2013), a straightforward numerical simulation demonstrates the existence of a boundary layer with characteristic thickness $l_b \sim h_0$ in the vicinity of the samples side surfaces, where the electric fields are not uniform. Thus, in the limit as $h_0/d_0$ becomes small, we can take the Eulerian electric field to be macroscopically uniform inside the sample in its deformed state, such that $\bar{\mathbf{e}} = \bar{e}\hat{\mathbf{E}}_2$, where $\bar{e} = v/h$. Unless stated otherwise, we assume that there are no externally applied mechanical tractions on the boundaries of the actuator. Note that here $h = h_0/\lambda$ denotes the deformed height of the sample, as depicted in Fig. 5.2(b).

As shown before in the context of infinitesimal strains, under the electrode boundary conditions the total macroscopic stress in the DEC is identically zero such that

$$\bar{\boldsymbol{T}} = 0. \tag{5.40}$$

Taking into account the overall incompressibility of the composite, equation (5.40) further simplifies to

$$\bar{T}_{11} - \bar{T}_{22} = 0 \quad \text{and} \quad \bar{T}_{12} = 0, \tag{5.41}$$

which can be used to determine the macroscopic stretch $\bar{\lambda}$ as a function of the voltage $v$.

For the above-mentioned perfectly aligned case, we can split the components of the total stress as

$$\bar{T}_{11} - \bar{T}_{22} = \left(\bar{T}_{11}^{me} - \bar{T}_{22}^{me}\right) + \left(\bar{T}_{11}^{el} - \bar{T}_{22}^{el}\right) \quad \text{and} \quad \bar{T}_{12} = \bar{T}_{12}^{me} + \bar{T}_{12}^{el}. \tag{5.42}$$

The mechanical contributions to the total stress are given by

$$\bar{T}_{11}^{me} - \bar{T}_{22}^{me} = \bar{\lambda}\,\frac{\partial \tilde{W}_{me}}{\partial \bar{\lambda}} \quad \text{and} \quad \bar{T}_{12}^{me} = 0, \tag{5.43}$$

where

$$\frac{\partial \tilde{W}_{me}}{\partial \bar{\lambda}} = \frac{\mu^{(1)}\left[\left(c_0 + w + c_0 w^2\right)\left(\bar{\lambda}^4 - 1\right) - \left(c_0 + c_0 w^2\right)\left(\bar{\lambda}^3 - \bar{\lambda}\right)\right]}{\bar{\lambda}^3 w\left(1 - c_0\right)\left[1 - \left(\hat{I}_a - 2\right)/J_m\right]}. \tag{5.44}$$

In the above equation $\hat{I}_a$ is obtained by making the replacements $\bar{\theta} = \bar{\varphi} = 0$ in expression (5.14) for $\hat{I}$. Similarly, the electrostatic contributions are given by

$$\bar{T}_{11}^{el} - \bar{T}_{22}^{el} = \bar{\lambda}\,\frac{\partial \tilde{W}_{el}}{\partial \bar{\lambda}} \quad \text{and} \quad \bar{T}_{12}^{el} = 0, \tag{5.45}$$

where

$$\frac{\partial \tilde{W}_{el}}{\partial \bar{\lambda}} = -\left[\frac{\tilde{\mathcal{E}}_{22}}{\varepsilon^{(1)}} + \frac{c_0 \bar{\lambda}^2 w}{\left(\bar{\lambda}^2 + w\right)^2}\left(\frac{\tilde{\mathcal{E}}_{22}}{\varepsilon^{(1)}} - 1\right)^2\right]\varepsilon^{(1)}\bar{\lambda}\bar{E}^2. \tag{5.46}$$

In the above equation, $\bar{E} := v/h_0$ is the average nominal (Lagrangian) electric field and

$$\tilde{\mathcal{E}}_{22}\left(\bar{\lambda}\right) = \varepsilon^{(1)} + c_0\left[\frac{1}{\mathcal{E}^{(2)} - \varepsilon^{(1)}} + \frac{1}{\varepsilon^{(1)}}\left(\frac{1}{1+w} - \frac{c_0\bar{\lambda}^2}{\bar{\lambda}^2 + w}\right)\right]^{-1} \tag{5.47}$$

is the (principal) effective permittivity of the composite in the direction of the applied electric field ($X_2$).

Corresponding results for an ideal dielectric elastomer with Gent-type mechanical response, under the assumption of 2D plane-strain deformation, may be obtained by setting $c_0 = 0$ in the above equations. Thus, for the pure elastomer matrix, we have that

$$\bar{T}_{11}^{me} - \bar{T}_{22}^{me} = \frac{\mu^{(1)}\left(\bar{\lambda}^2 - \bar{\lambda}^{-2}\right)}{1 - \left(\bar{\lambda}^2 + \bar{\lambda}^{-2} - 2\right)/J_m}, \quad \text{and} \quad \bar{T}_{11}^{el} - \bar{T}_{22}^{el} = \bar{T}_{11}^{M} - \bar{T}_{22}^{M} = -\varepsilon^{(1)}\bar{\lambda}^2\bar{E}^2. \tag{5.48}$$

For comparison purposes, we also include the corresponding results for 3D equal biaxial loading of the ideal dielectric, as shown in Fig. 5.4. They are given by (see

Lu et al. 2012, for example)

$$\bar{T}^{me}_{11} - \bar{T}^{me}_{22} = \frac{\mu^{(1)}\left(\bar{\lambda}^2 - \bar{\lambda}^{-4}\right)}{1 - \left(2\bar{\lambda}^2 + \bar{\lambda}^{-4} - 3\right)/J_m}, \quad \text{and} \quad \bar{T}^{el}_{11} - \bar{T}^{el}_{22} = \bar{T}^{M}_{11} - \bar{T}^{M}_{22} = -\varepsilon^{(1)}\bar{\lambda}^4\bar{E}^2. \tag{5.49}$$

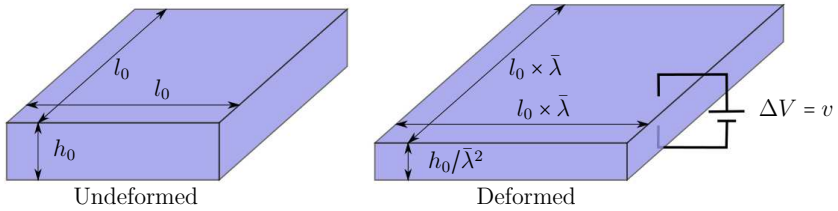


Figure 5.4: Schematics for an ideal dielectric under the 3D equal biaxial loading conditions, in the reference (left) and current (right) configurations.

In the following subsection, we present results for the effective response and failure of fiber-constrained DECs under the soft electrode boundary conditions described above. We start by comparing the response of the fiber-constrained DECs with the response of the homogeneous ideal dielectrics (under both 2D plane-strain and 3D equal biaxial loading conditions). Then we investigate the effect of the concentration, aspect ratio, and permittivity of the fibers on the behavior and stability of DECs. Next, we discuss briefly the effect of a very specific form of external mechanical tractions on the response and failure of DECs. Finally, we optimize the microstructure to achieve the maximum possible electrostriction before any of the failure criteria are met for the composite.

### 5.2.1 Effective response of the DECs

In this subsection, we discuss the main characteristics of the overall response of DECs consisting of aligned rigid fibers with permittivity $\boldsymbol{\mathcal{E}}^{(2)} = \mathcal{E}^{(2)}\boldsymbol{I}$, and Gent-type ideal dielectric matrices with permittivity $\varepsilon^{(1)}$, shear modulus $\mu^{(1)}$ and strain-locking parameter $J_m$. Figure 5.5 shows the effective electromechanical response of the fiber-constrained DECs with different fiber concentrations, including the special case when $c_0 = 0$ corresponding to plane deformations of the pure elastomer matrix. In addition, results for an ideal dielectric subjected to the 3D equibiaxial loading condition

of Fig. 5.4 are included in Fig. 5.5 for comparison purposes. Figure 5.5(a) shows the mechanical stress and the electrostatic stress (normalized by $\bar{E}^2$) as functions of the lateral stretch $\bar{\lambda}$. Figures 5.5(b) and 5.5(c) respectively show the macroscopic (Lagrangian or nominal) electric and electric displacement fields, both as a function of the lateral stretch $\bar{\lambda}$. Finally, Fig. 5.5(d) shows the macroscopic electric field as a function of the macroscopic electric displacement. This last plot is simply obtained by replacing $\bar{\lambda}$ in Fig. 5.5(b) with $\bar{D}\left(\bar{\lambda}\right)$ in Fig. 5.5(c).

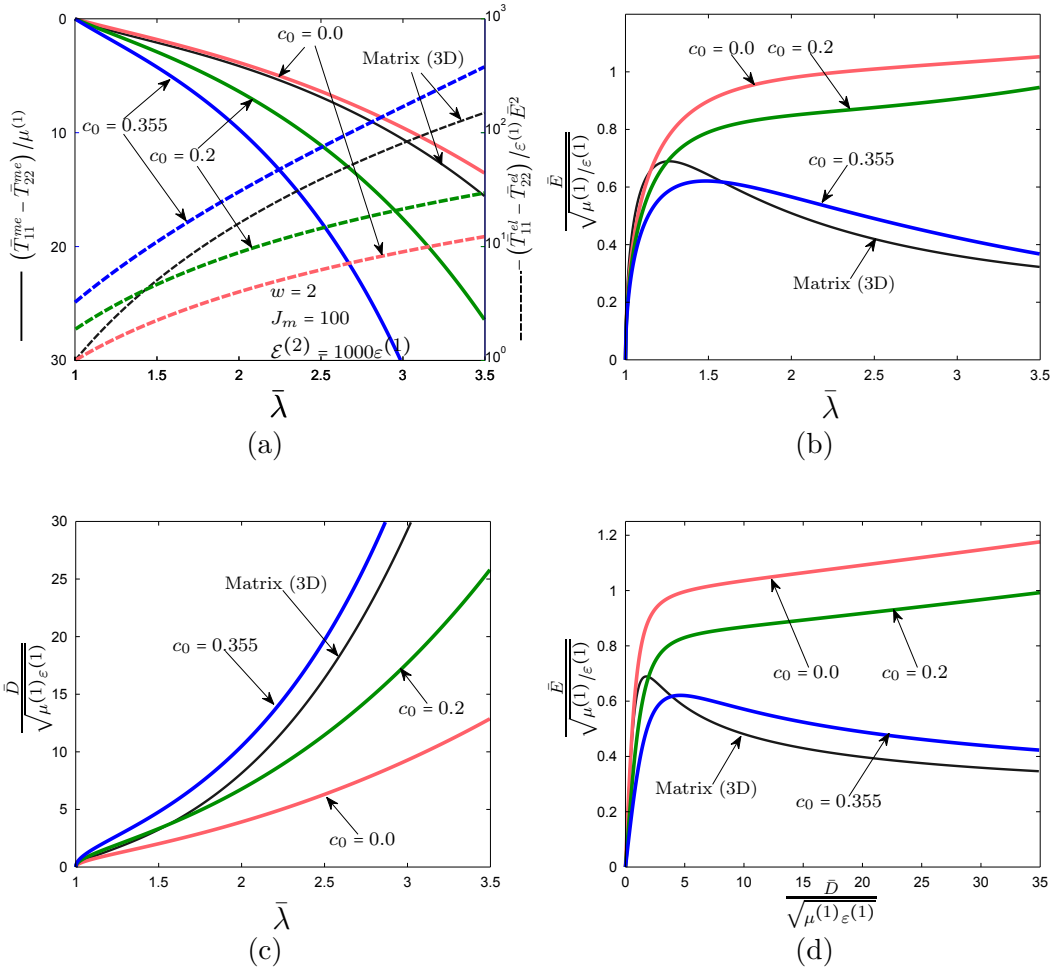


Figure 5.5: The effective response of fiber-constrained DECs with different concentrations, as well as the response for an ideal dielectric under the 3D loading condition. (a) The mechanical and electrostatic stresses as functions of the lateral stretch, (b) the nominal electric field as a function of the lateral stretch, (c) the nominal electric displacement as a function of the lateral stretch, and (d) the nominal electric field as a function of the nominal electric displacement. In this figure $J_m = 100$, $w = 2$, and $\mathcal{E}^{(2)}/\varepsilon^{(1)} = 1000$.

We start our discussion of the results by comparing the response of the pure (matrix) ideal dielectric for the 2D (i.e., when $c_0 = 0$) and 3D loading conditions. As shown in Fig. 5.5(a), the difference between the mechanical stresses for the 2D and 3D setups is relatively small for all values of $\bar{\lambda}$. The difference between the electrostatic stresses (normalized by $\bar{E}^2$), however, is very significant for large values of $\bar{\lambda}$. This is due to the fact that in the 3D setup the thickness of the sample reduces at a faster rate (by a factor of $\bar{\lambda}^{-2}$ compared to $\bar{\lambda}^{-1}$ for the 2D setup) as the deformation progresses. Therefore, at fixed $\bar{\lambda}$, the 3D setup requires a much smaller $\bar{E}$ (or applied voltage) to satisfy the equilibrium condition. Another important observation here is the non-monotonic behavior of the $\bar{E}$-$\bar{\lambda}$ curve for the 3D setup, as can be seen in Fig. 5.5(b). It is well known (Zhao & Suo 2007) that in a voltage-controlled experiment the material may experience an electromechanical instability at the maximum in the response curve shown in Fig. 5.5(b). Note that the points in the response curve after the maximum are not stable (as will be discussed in more detail below). Thus, at the maximum point, a further increase in the applied voltage forces the sample to "snap" to a stable branch with a much larger lateral stretch. This in turn may result in a dramatic increase in the electric field inside the sample, causing the sample to undergo dielectric breakdown. On the other hand, as noted by Lu et al. (2012), this non-monotonic behavior is not observed for the 2D case. Therefore, one may be able to safely increase the voltage up to the breakdown of the material and achieve higher strains. However, this would require a mechanism to constrain the material to 2D plane-strain deformations. While this may be achieved by means of external structures, it may not be feasible from the applications point of view. Another method for achieving the 2D plane-strain deformations, which has been proposed recently (see Lu et al. 2012, for example), is to make use of stiff fibers to constrain the deformation of the material along the fiber directions. Recent experimental and theoretical studies (Huang, Lu, Zhu, Clarke & Suo 2012, Bolzmacher et al. 2006) show the potential usefulness of this approach.

As shown in Fig. 5.5(a), the addition of the fibers makes the composite mechanically stiffer and therefore, at a given stretch, composites with higher concentrations

carry larger (in magnitude) mechanical stresses. The magnitude of the electrostatic contribution to the total stress also increases with increasing the concentration. As can be seen in Fig. 5.5(b), the $\bar{E}$-$\bar{\lambda}$ curves for composites with small concentrations are similar to that of the homogeneous matrix under the assumption of 2D plane-strain deformations. For higher concentrations, more complex behaviors are observed. Thus, when the concentration is high enough, a non-monotonic response for the nominal electric field as a function of the stretch may be seen (e.g., in Fig. 5.5(b), see the curve for $c_0 = 0.355$). This can be explained by means of the dipole interactions between the polarized fibers. It is well-known that the dipole interactions are inversely proportional to the third power of the average distance between the dipoles in 3D (see Shkel & Klingenberg 1998). Similarly, one can show that the interactions between long fibers are inversely proportional to the second power of the average distance between the fibers. At low concentrations, the fibers are far apart from each other and the interactions are small. As the concentration increases, the average distance between the fibers decreases, and the dipole interactions become more significant. Hence, despite the fact that the presence of rigid fibers makes the composite mechanically stiffer, composites with higher concentrations of the fibers often require less voltage to attain a given lateral stretch.

As shown in Fig. 5.5(c), unlike the corresponding results for the nominal electric field, the results for the nominal electric displacement are monotonic for all values of the concentration, as well as for the ideal dielectric under the 3D loading conditions. Recall that the electric displacement corresponds to the amount of charge accumulated on the electrodes. Therefore, in charge-controlled experiments (Keplinger et al. 2010) one may be able to achieve any stretch without developing electromechanical instabilities, due to the one-to-one relationship between the electric displacement and the macroscopic stretch. There are also studies suggesting the possibility of phase transitions in charge-controlled experiments when a non-monotonic response is observed for the nominal electric field as a function of the macroscopic stretch, despite the fact that the nominal electric displacement is monotonic (see Zhao et al. 2007, Zhou et al. 2008, for more details). In any event, in the discussions to follow, we

focus our attention on voltage-controlled conditions, which seem to be more relevant in applications.

Finally, as can be seen in Fig. 5.5(d), the $\bar{E}$-$\bar{D}$ curves are non-monotonic when the concentration of the fibers is large enough (see the plot for $c_0$ = 0.355), and also for the matrix under the 3D loading conditions. This is easily explained by recalling the non-monotonic behavior of the $\bar{E}$-$\bar{\lambda}$ curves and the monotonic behavior of the $\bar{D}$-$\bar{\lambda}$ curves. Once again, it is noted that the portions of the $\bar{E}$-$\bar{D}$ curves with negative slope correspond to unstable states, as will be seen further below.

Thus far we have discussed the main characteristics for the effective response of DECs and compared them with the response of ideal dielectrics under both 2D and 3D loading conditions. We have also identified the dipole interactions as the main mechanism for the electromechanical couplings in fiber-constrained DECs. In the following subsections, we investigate the effect of different microstructural parameters on the response and stability of fiber-constrained DECs the electrode boundary conditions in more detail.

### 5.2.2 The effect of the fiber volume fraction

Figure 5.6 shows the response curves for DECs with different concentrations of circular fibers, along with the corresponding failure regions. The microstructural features of the composite are specified in the figure. Figure 5.6(a) shows the voltage (recall that the applied voltage is proportional to the nominal electric field) as a function of the macroscopic stretch. As can be seen in this figure for small concentrations the curves are monotonic, while for larger concentrations non-monotonic behaviors are observed. Also note that a much smaller voltage is required to keep the sample at equilibrium for large (but smaller than the lock-up) stretches. As mentioned earlier, larger volume fractions lead to a significant reduction in the average distance between the fibers, and therefore enhance the dipole interactions between them. Finally, as the concentration of the fibers increases the composite locks up earlier, as expected.

The rest of the plots in Fig. 5.6 depict the effect of the concentration on failure of the DECs. Thus, in Figs. 5.6(b)-5.6(d), the non-convex regions associated with

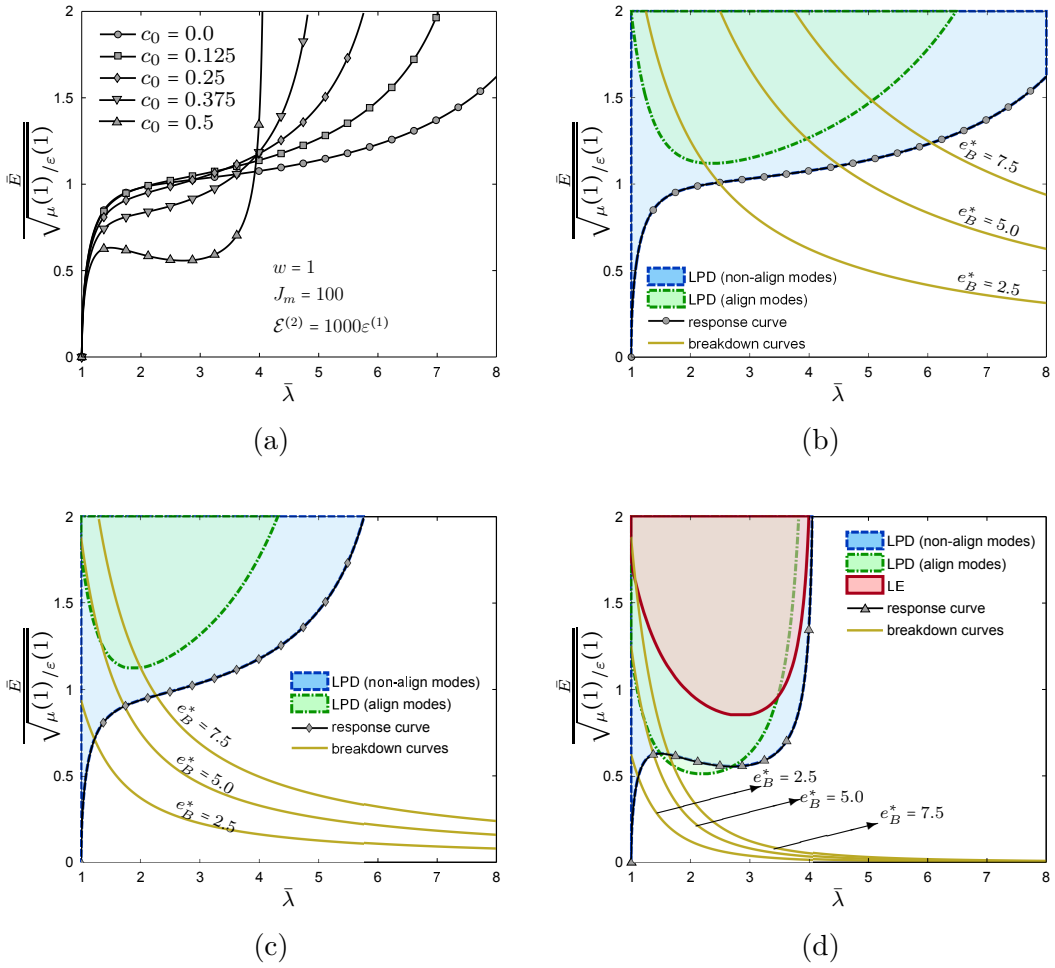


Figure 5.6: The response and failure of DECs consisting of circular fibers. (a) The response curves for different concentrations, and the failure regions for (b) $c_0 = 0.0$, (c) $c_0 = 0.25$, and (d) $c_0 = 0.5$. In this figure $J_m = 100$, $w = 1$, and $\mathcal{E}^{(2)}/\varepsilon^{(1)} = 1000$.

the aligned eigenmodes are shaded by the color green with dash-dotted boundaries, the non-convex regions associated with the non-aligned eigenmodes are shaded by the color blue with dashed boundaries, and the non-elliptic regions are shaded by the color red with solid boundaries. Note that the boundary of each of the instability regions signals the possible onset of the corresponding failure mode. In addition, the breakdown curves are shown for three different values of the (normalized) electric strength of the matrix, $e_B^* := e_B/\sqrt{\mu^{(1)}/\varepsilon^{(1)}}$.

Figure 5.6(b) shows the failure regions for the ideal dielectric matrix. As shown in this figure, the boundary of the non-convex domain associated with non-aligned

modes coincides exactly with the response curve of the ideal dielectric. As mentioned earlier, in the absence of external mechanical tractions, such non-aligned instability modes correspond to trivial rotational instabilities that can be safely ignored. The non-convex domain associated with the aligned modes, on the other hand, never intersects the response curve of an ideal dielectric under 2D loading conditions, and therefore for an ideal dielectric in the absence of external tractions the first failure encountered is the dielectric breakdown. Thus, the ideal dielectric can attain relatively large electrostriction before breakdown. However, as mentioned earlier, in order to achieve plane-strain deformations, it is necessary to use rigid fibers to constrain the deformation of the sample in one direction ($X_3$ in our case). As shown in Fig. 5.6(c) for moderate concentrations ($c_0$ = 0.25) of circular fibers, the failure regions are qualitatively similar to those of the homogeneous ideal dielectric. The main difference, however, is that the addition of dielectric fibers dramatically reduces the overall electric strength of the DEC. This is due to the field magnifications inside the matrix in the vicinity of the highly dielectric fibers. Thus, as shown in Fig. 5.6(d) for high enough concentrations ($c_0$ = 0.5), the response curve crosses into the aligned non-convex domain. In this connection, it should be recalled that the response curve crosses the non-convex region for the first time when the maximum voltage is reached. The eigenmode for the instability at the intersection of the response curve and the non-convex region (also for all the point on the boundary of the non-convex region) is of the aligned type, as discussed earlier. This type of instability in the purely mechanical context typically corresponds to a "maximum load" instability in samples under dead loads (e.g., see Hill 1967). The portion of the response curve that falls into the non-convex region has negative slope suggesting an electromechanical instability (as mentioned earlier). An important consequence of this is that, in a voltage-controlled experiment, increasing the voltage beyond the maximum value in the response curve causes the sample to snap into the stable branch of the response curve. However, the sample experiences breakdown while snapping into the stable branch, which may be undesirable in applications. Finally, for sufficiently high concentrations, non-elliptic regions appear in the picture, although the response curve never crosses into the non-

elliptic region for the specific case shown in Fig. 5.6(d). However, it is remarked that the boundary of the non-elliptic region corresponds to the onset of localization instabilities in the DECs. In the specific example shown here the acoustic tensor $\hat{\gamma}(\mathbf{n})$ vanishes for $\mathbf{n} = \hat{\mathbf{E}}_2$, which means that the plane of the band is parallel to the electrodes. In this connection, it should also be noted that the elliptic region falls completely within the non-convex region for the composite shown in Fig. 5.6(d). In other words, loss of strong ellipticity implies loss of convexity, but the converse is not necessarily true, as already mentioned.

### 5.2.3 The effect of the fiber aspect ratio

Figure 5.7 shows the response curves for DECs consisting of elliptical fibers with the longer (in-plane) axis parallel to the field direction $X_2$, together with the corresponding failure regions. The microstructural details of the composite are specified in the figure. Figure 5.7(a) shows the voltage-stretch curves for different values of the aspect ratio. As can be seen in this figure, as the aspect ratio of the fibers increases, less voltage is required to keep the sample in equilibrium at a given stretch. This can be explained by noting that fibers with elongated cross-sections in the direction of the applied electric field ($X_2$) attain higher polarizations, which in turn results in stronger dipole interactions. Therefore, for composites with $w > 1$, larger stretches may be achieved with smaller electric fields. However, as was the case for composites with high concentrations of circular inclusions (before locking up), the non-monotonic behavior observed for large fiber aspect ratios may also result in electromechanical instabilities, as will be discussed in more detail below.

As shown in Figs. 5.7(b)-5.7(d), increasing the aspect ratio while keeping the volume fraction fixed has qualitatively the same effect on the DEC failure regions as increasing the volume fraction for a fixed aspect ratio, except that a new loss of ellipticity region is now observed near the zero-voltage axis, consistent with the results of Lopez-Pamies & Ponte Castañeda (2006*a*) for the purely mechanical case. We emphasize that this newly developed loss of ellipticity region falls exactly on top of a non-convex region of the non-aligned type. Finally, it should be noted that,

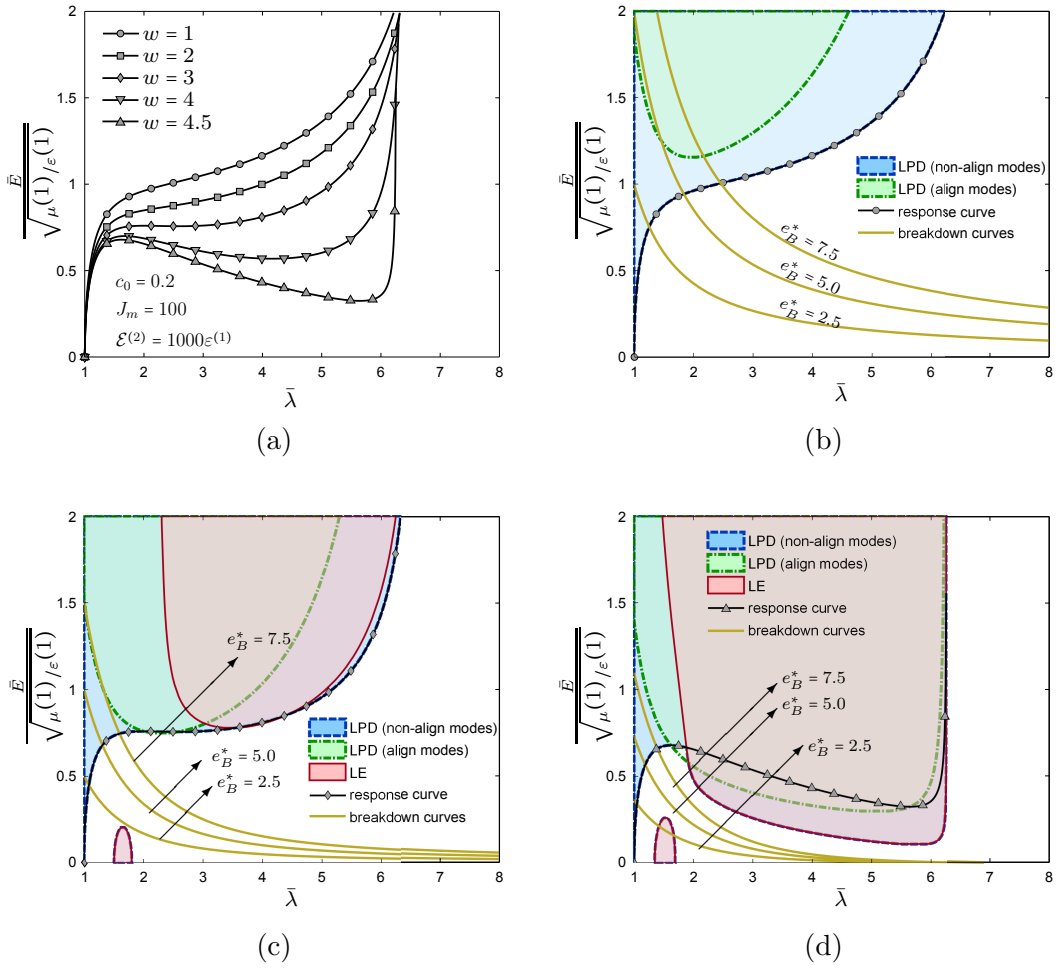


Figure 5.7: The effect of the fiber aspect ratio on the response and failure of fiber-constrained DECs. (a) The response curves for different aspect ratios, and the failure regions for (b) $w = 1$, (c) $w = 3$, and (d) $w = 4.5$. In this figure $J_m = 100$, $c_0 = 0.2$, and $\mathcal{E}^{(2)}/\varepsilon^{(1)} = 1000$.

for all the cases considered in these figures, the critical (first) failure mechanisms to be observed as the voltage is increased is the dielectric breakdown. Although the fiber aspect ratio significantly affects the other failure mechanisms, its effect on the dielectric breakdown controls the largest amount of stretch that can be generated by the application of a potential difference, with the result that increasing aspect ratios lead to breakdown failure at smaller overall stretches.

Thus far we have shown that for composites consisting of fibers with $w > 1$, where the longer (in-plane) axis is aligned with the field direction, the main limiting factor for the performance is breakdown or the snap-through followed by dielectric

breakdown. In the following we consider cases where $w < 1$ (i.e., fibers with the longer axis perpendicular to the field direction). Note that such DECs require higher voltages to achieve a desired stretch. However, the reduction in the overall breakdown field of the composite is less severe in the case of "flat" (i.e., $w < 1$) fibers. Therefore, we are able to operate the composite at higher voltages and achieve higher strains.

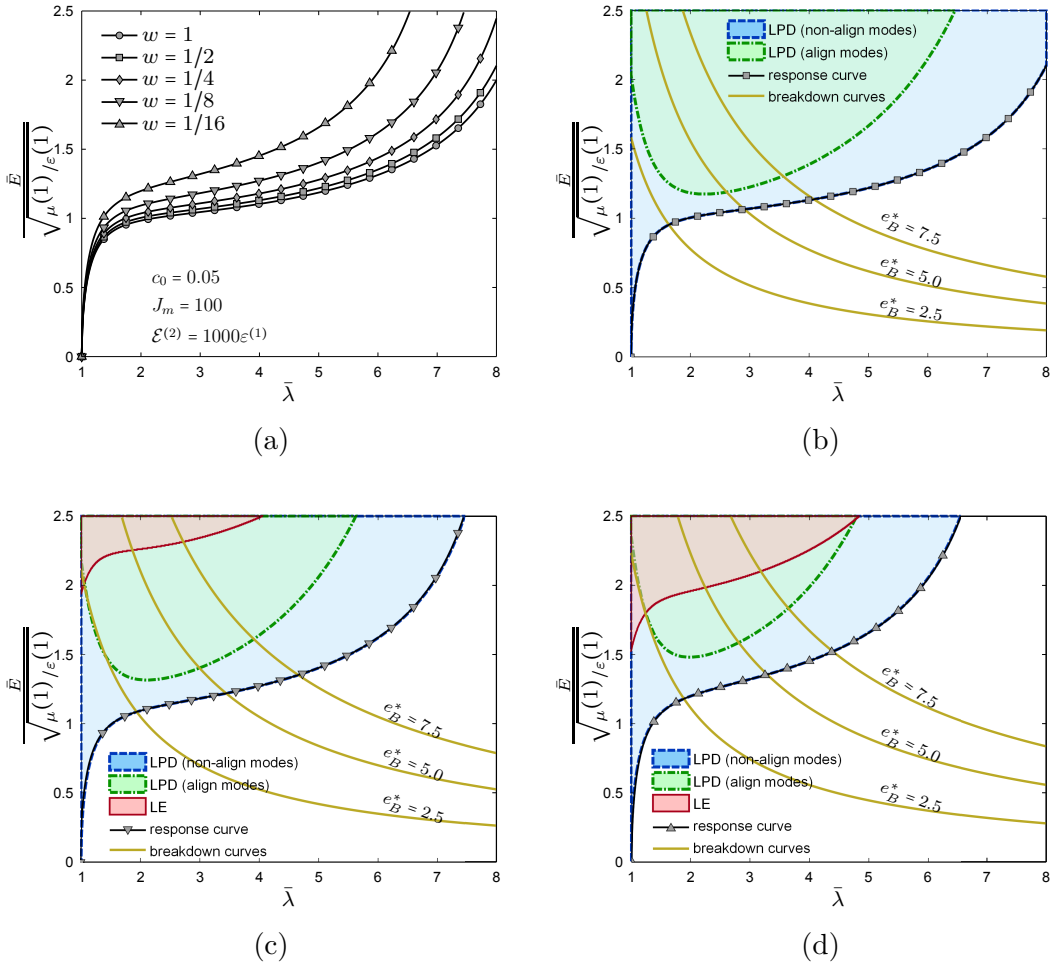


Figure 5.8: The effect of fiber aspect ratio on the response and failure of fiber-constrained DECs. (a) The response curves for different aspect ratios, and the failure regions for (b) $w = 1/2$, (c) $w = 1/8$, and (d) $w = 1/16$. In this figure $J_m = 100$, $c_0 = 0.05$, and $\mathcal{E}^{(2)}/\varepsilon^{(1)} = 1000$.

Figure 5.8 shows the corresponding results for composites consisting of a small concentration of fibers ($c_0 = 5\%$) with $w \leq 1$. In this case, the dipole interactions are small, and as can be seen in Fig. 5.8(a), higher voltages are required to achieve a given stretch for composites consisting of fibers with $w < 1$. This is easily understood

by recalling the stiffening effect of fibers with $w < 1$ (note that in the limit as $w \to 0$ the fibers tend to rigid layers and the composite becomes effectively rigid due to the incompressibility of the matrix). The corresponding failure domains for DECs with different aspect ratios ($w < 1$) are shown in Figs. 5.8(b)-5.8(d), where it can also be seen that the response curves are always monotonic and the critical failure mechanism is again the dielectric breakdown. It is emphasized that a small concentration of flat fibers minimizes the adverse effect of the dielectric breakdown while constraining the composite to plane-strain conditions. This, in turn, enables the composite to withstand higher voltages and attain larger strains. Finally, for small enough aspect ratios the composite may lose ellipticity in purely electric loading paths (i.e., when $\bar{\lambda} = 1$ is held fixed and $\bar{E} > 0$ is increased). This is because of the destabilizing effect of the torque exerted on the fibers by the electric field. More precisely, for cases when $w < 1$ (i.e., when the longer in-plane axes of the fibers is perpendicular to the field) a small perturbation in the orientation of the fibers may cause them to rotate toward stable configurations.

### 5.2.4 The effect of the fiber permittivity

Figure 5.9 shows the response curves for DECs consisting of circular fibers with different permittivities, along with the corresponding failure regions. The microstructural details of the composite are specified in the figure. Figure 5.9(a) shows the voltage-stretch curves for different values of the ratio $\mathcal{E}^{(2)}/\varepsilon^{(1)}$. As shown in this figure, as the ratio increases, less voltage is required to keep the sample in equilibrium at a given stretch. This can be explained by noting that fibers with higher permittivities attain higher polarizations, which in turn results in stronger dipole interactions. Therefore, composites with $\mathcal{E}^{(2)}/\varepsilon^{(1)} > 1$ may achieve larger stretches with smaller electric potentials. However, the maximum achievable stretch is limited by the same failure mechanisms discussed earlier. Thus, as shown in Figs. 5.9(b)-5.9(d), when the effects of the dielectric breakdown are taken into account, composites with vanishing dielectric contrast (i.e., when $\mathcal{E}^{(2)} = \varepsilon^{(1)}$) can achieve the largest stretch before failing. For composites with non-zero contrasts in the dielectric properties of the phases, the

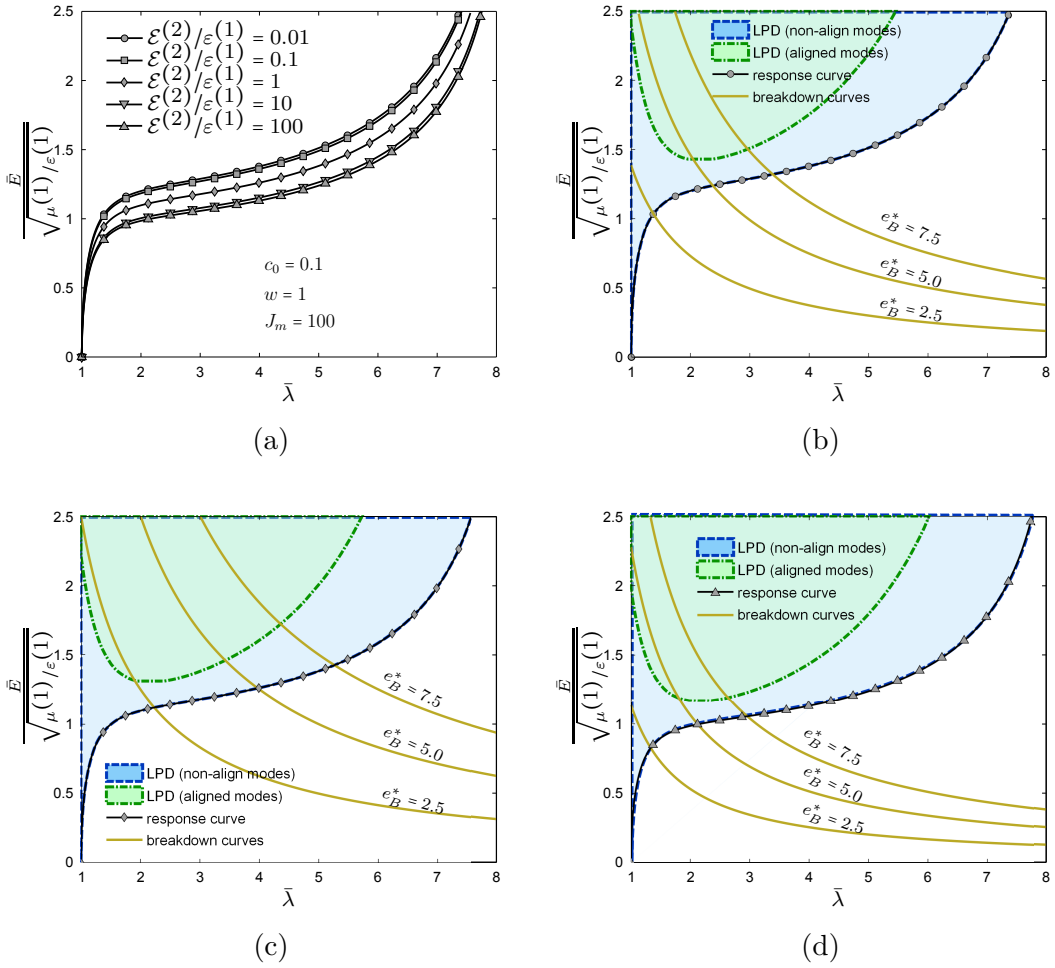


Figure 5.9: The effect of the fiber permittivity on the response and failure of fiber-constrained DECs. (a) The response curves for different permittivity of the fibers, and the failure regions for (b) $\mathcal{E}^{(2)}/\varepsilon^{(1)} = 0.01$, (c) $\mathcal{E}^{(2)}/\varepsilon^{(1)} = 1$, and (d) $\mathcal{E}^{(2)}/\varepsilon^{(1)} = 100$. In this figure $J_m = 100$, $c_0 = 0.1$, and $w = 1$.

maximum attainable stretch before dielectric breakdown decreases due to the field-magnification effects. Note, however, that the reduction in the maximum achievable stretch is less severe for cases with $\mathcal{E}^{(2)}/\varepsilon^{(1)} < 1$, as can be seen in Fig. 5.9(b).

### 5.2.5 The effect of external mechanical tractions

Here we briefly consider the effect of aligned (with the coordinate axis) external tractions of the form

$$\bar{T}_{11} = \bar{t}_1 \geq 0, \quad \text{and} \quad \bar{T}_{22} = \bar{t}_2 = 0, \tag{5.50}$$

on the response and failure of a DEC with finite concentration of fibers with circular or elliptical cross-sections. For such tractions, we can easily modify (5.41) to obtain the new response curve of the composite. While the non-elliptic regions and the breakdown curves are independent of the loading conditions, the non-convex regions may, in general, depend on the external loading. However, for the (dead-load) tractions of the form (5.50), the non-convex regions, too, remain unchanged.

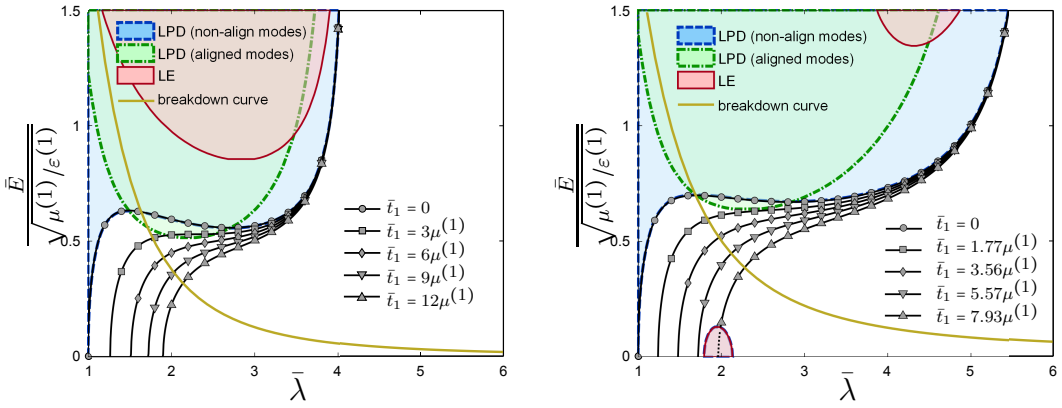


Figure 5.10: The effect of the external mechanical tractions of the form $\bar{t}_1 \geq 0$ and $\bar{t}_2 = 0$ on the behavior of fiber-constrained DECs. (a) The response curves along with the failure regions for a composite consisting of circular ($w = 1$) fibers with $c_0 = 0.5$, and (b) the response curves along with the failure regions for a composite consisting of elliptical ($w = 2$) fibers with $c_0 = 0.3$. In this figure $J_m = 100$, $\mathcal{E}^{(2)}/\varepsilon^{(1)} = 1000$, and the electric strength of the matrix is $e_B^* = 7.5$.

Figures 5.10(a) and 5.10(b) show the response curves and the corresponding failure regions for composites consisting of circular ($w = 1$) and elliptical ($w = 2$) fibers, respectively. In both cases, the response curves in the absence of the external traction cross into the aligned non-convex domains, and therefore can develop electromechanical instabilities as the voltage is increased. As the traction $\bar{t}_1$ increases, the response curves tend to fall completely within the stable domain. Therefore, it can be concluded that a positive traction in the $X_1$ direction has an stabilizing effect on fiber-constrained DECs. The stabilizing effect of the (dead-load) tractions has also been reported for ideal dielectrics under equal biaxial loading conditions (see for example Zhao & Suo 2010, Lu et al. 2012). However, it is noted that the response

curve may cross the non-elliptic region for high values of the traction (e.g., in Fig. 5.10(b) see the curve corresponding to $\bar{t}_1 = 7.93\mu^{(1)}$). Finally, note that even though the maximum attainable stretch increases for samples under external tractions, the portion of the deformation achieved solely by the application of the electric potential (or the eletrostrictive strain) is still relatively small. In fact, it is smaller than for the non-pre-stretched case. For this reason, this option will not be pursued further in this work.

### 5.2.6 Optimization of the microstructure

In the previous sections, we have investigated the effects of microstructural parameters on the performance of fiber-constrained DECs. We have demonstrated that increasing the concentration or aspect ratio of the fibers enhances the electromechanical coupling in the DECs due to dipole interactions. However, the performance (i.e., the maximum achievable strain) of DECs with high concentrations or aspect ratios was shown to be severely restricted by dielectric breakdown, due to the field magnification effects of fibers. For this reason, we have also provided results for the effect of contrast in the dielectric properties of the fiber and matrix phases. According to our results, the adverse effect of the fibers on the overall breakdown field of the composite is minimized (or absent altogether) for small (or vanishing) contrast in the dielectric permittivities of the phases. It is remarked that, at zero contrast, the overall breakdown field for the composite reduces to the breakdown field of the homogeneous matrix. Inspired by the above findings, we attempt next an optimal design for the microstructure of fiber-constrained DECs in order to achieve the largest possible electrostriction before failure.

Figure 5.11 displays the effects of the microstructural parameters $w$ and $\mathcal{E}^{(2)}/\varepsilon^{(1)}$ on the "terminal" stretch of DECs, as determined by the dielectric breakdown. More specifically, Figs. 5.11(a) and 5.11(b) show the terminal stretch as a function of the aspect ratio for $c_0 = 0.01$ and $c_0 = 0.1$, respectively, while Figs. 5.11(c) and 5.11(d) show the terminal stretch as a function of the ratio $\mathcal{E}^{(2)}/\varepsilon^{(1)}$ for $c_0 = 0.01$ and $c_0 = 0.1$, respectively.

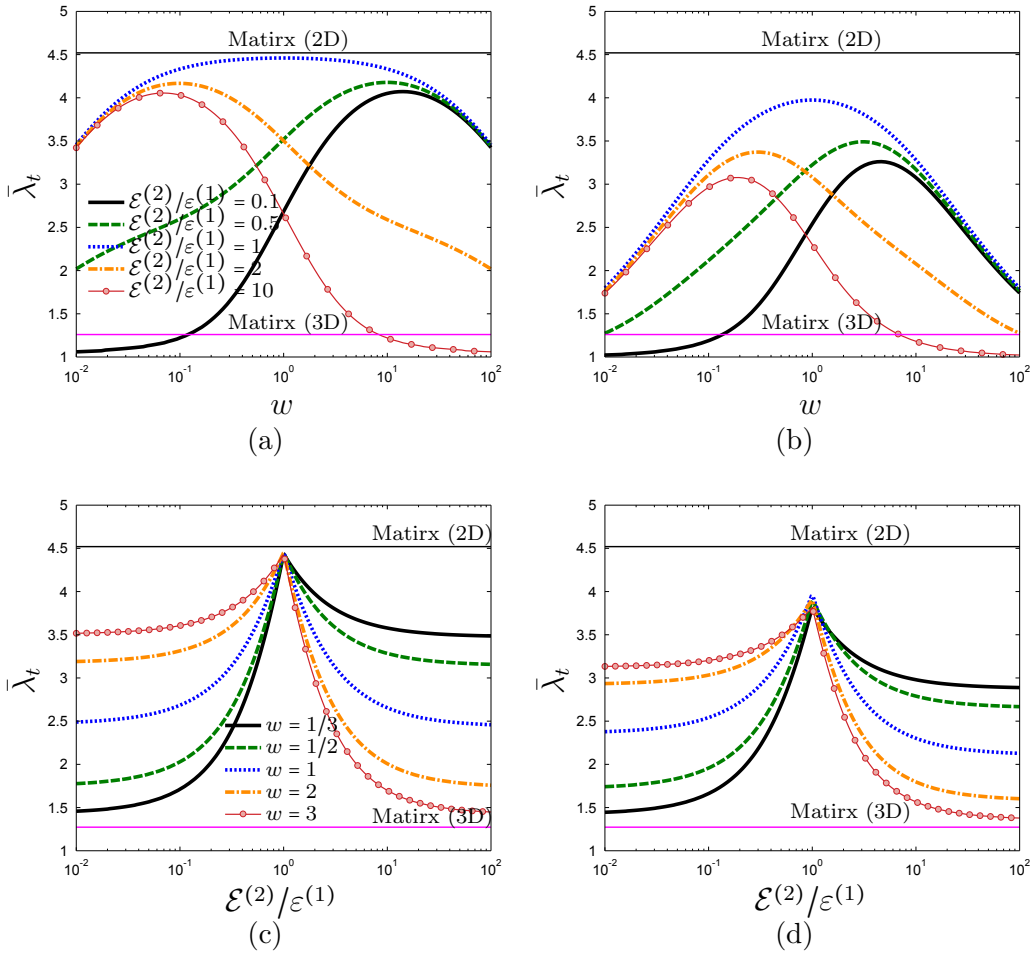


Figure 5.11: The effect of the microstructure on the terminal stretch as obtained by the dielectric breakdown. Results for the ideal dielectic under both 2D (plane-strain) and 3D (equal biaxial) loading conditions are also shown for comparison purposes. Results for the terminal stretch as a function of the aspect ratio for different values of the permittivity are given in plot (a) for $c_0 = 0.01$ and in plot (b) for $c_0 = 0.1$. Results for the terminal stretch as a function of the permittivity ratio for different values of the aspect ratio are given in plot (c) for $c_0 = 0.01$ and in plot (d) for $c_0 = 0.1$. In this figure $J_m = 100$ and $e_B^* = 5$.

As can be seen in Figs. 5.11(a) and 5.11(b), composites consisting of circular (i.e., $w = 1$) fibers with zero contrast in the dielectric permittivities (i.e., $\mathcal{E}^{(2)}/\varepsilon^{(1)} = 1$) can attain the largest electrostrictive strains before undergoing dielectric breakdown. Thus, the DECs with circular cross-section fibers and vanishing dielectric contrast achieve nearly 100% of the matrix stretch for 1% fiber volume fraction, while they achieve nearly 75% of the matrix stretch for 10% volume fraction. It is also observed

from these figures that for DECs with non-zero dielectric contrast the maximum stretch is achieved for $w \neq 1$, depending on the values of the other two microstructural parameters. For example, for $c_0 = 0.1$ and $\mathcal{E}^{(2)}/\varepsilon^{(1)} = 0.1$ the maximum stretch of $\bar{\lambda}_t^{max} \simeq 3.26$ is achieved for elongated (in the direction of the applied electric field) elliptical fibers with aspect ratio $w \simeq 4.64$, while for $c_0 = 0.1$ and $\mathcal{E}^{(2)}/\varepsilon^{(1)} = 10$ the maximum stretch of $\bar{\lambda}_t^{max} \simeq 3.08$ is achieved for flat fibers with aspect ratio $w \simeq 0.19$. Note that the electric fields at which these maximum stretches are achieved are $\bar{E}^{max}/\sqrt{\mu^{(1)}/\varepsilon^{(1)}} \simeq 1.38$ when $\mathcal{E}^{(2)}/\varepsilon^{(1)} = 0.1$, and $\bar{E}^{max}/\sqrt{\mu^{(1)}/\varepsilon^{(1)}} \simeq 1.24$ when $\mathcal{E}^{(2)}/\varepsilon^{(1)} = 10$. For the same concentration ($c_0 = 0.1$) of circular fibers, the electric field necessary to achieve the maximum stretch is $\bar{E}^{max}/\sqrt{\mu^{(1)}/\varepsilon^{(1)}} \simeq 1.26$.

On the other hand, as can be seen in Figs. 5.11(c) and 5.11(d), $\bar{\lambda}_t$ is highly sensitive to changes in the ratio $\mathcal{E}^{(2)}/\varepsilon^{(1)}$ in the neighborhood of the optimal value (i.e., $\mathcal{E}^{(2)}/\varepsilon^{(1)} = 1$). Therefore, it is very important in practical applications to try to match as closely as possible the dielectric properties of the fiber and matrix phases, while still maintaining a significant stiffness contrast between the soft elastomer and the stiffer fibers, so as to effectively constrain the overall deformation in the out-of-plane direction. In this connection, Table 5.1 shows the dielectric and stiffness properties of commercially available materials satisfying the above-mentioned conditions for the design of DECs that are capable of achieving large field-induced stretches.

| Material | $\varepsilon/\varepsilon_0$ | $\mu$[MPa] |
|---|---|---|
| Matrix: | | |
| VHB 4910 (by 3M) | 4.5 – 4.8 | 0.1 – 3.0 |
| Fibers: | | |
| Nylon 6 | 2.6 – 38.0 | 17 – 4100 |
| Nylon 66 | 3.0 – 14.0 | 40 – 3900 |

Table 5.1: Candidate materials for the soft matrix and for the stiff fibers that may be chosen to satisfy the zero dielectric contrast ( $\mathcal{E}^{(2)}/\varepsilon^{(1)} \sim 1$) and infinite stiffness contrast ($\mu^{(2)}/\mu^{(1)} \to \infty$) conditions. The properties for the matrix material are taken form Carpi et al. (2008) and the properties for the fiber materials are taken from the website www.matweb.com.

Finally, it should be emphasized that even though smaller concentrations of fibers lead to larger overall electrostriction, the fiber concentration has to be sufficiently

large for the fibers to be able to support the stresses necessary to enforce the 2D plane-strain constraint. Thus, the optimal concentration will also depend on the tensile strength of the fibers.

## 5.3 Concluding remarks

In this chapter we have obtained homogenization estimates for the electromechanical response of fiber-constrained DECs consisting of one family of aligned rigid dielectric fibers firmly embedded in an ideal dielectric matrix. Toward this end, we have used the decoupling strategy/approximation of Ponte Castañeda & Siboni (2012), together with analytical estimates of Lopez-Pamies & Ponte Castañeda (2006*a*) for the purely mechanical response of fiber-reinforced composites at finite strains. Using the homogenization estimates obtained in this work, we have thoroughly investigated the effects of microstructural parameters, such as the concentration and aspect ratio of the fibers, as well as of the dielectric contrast, on the overall response of DECs. In particular, we have shown that increasing the volume fraction or aspect ratio (in the direction of the applied field) of the fibers significantly enhances the electromechanical coupling in fiber-constrained DECs, due to the effects of dipolar interactions. Therefore, DECs consisting of high concentrations of fibers or large aspect ratios for the fibers require, in general, smaller voltages to achieve a given deformation state.

In addition, we have investigated the effect of microstructure on the stability and failure of fiber-constrained DECs. It has been shown that while low concentrations of fibers, serving to constrain the deformation in the plane transverse to the fibers, can be used to prevent the development of electromechanical instabilities, sufficiently high concentrations of fibers can lead to the generation of such instabilities, which are manifested by a snap-through behavior, similar to that observed in pure dielectric elastomers undergoing more general 3D deformations. In addition, it has been found that high fiber concentrations and/or large fiber aspect ratios can lead to a dramatic reduction on the overall breakdown field that the DEC can withstand, due to the field-magnification effect of the fibers. As a consequence, dielectric breakdown has

been identified as the main limiting factor in the performance of these fiber-reinforced DECs.

For this reason, we have also considered the effect of the fiber permittivity on the macroscopic response and failure instabilities in these DECs. According to our theoretical predictions, composites with smaller contrasts in the dielectric constant of the phases can actually achieve higher overall electrostrictive strains before failure. In fact, for composites with vanishingly small dielectric contrast, the overall breakdown field becomes that of the pure matrix phase, and as a consequence such composites can withstand larger applied electric fields and achieve larger electrostrictive strains.

We have also considered the effect of externally applied mechanical tractions on the response and stability of DECs. Our results show that the application of external tractions in the direction perpendicular to the applied electric field (and to the fibers) can be used to reduce, or eliminate altogether the possible development of electromechanical (or snap-through) instabilities, characterized by loss of positive definiteness with aligned eigenmodes, in agreement with similar findings for homogeneous ideal dielectrics under 3D equal-biaxial loading conditions (Lu et al. 2012). However, although the terminal stretch before breakdown increases with increasing traction, the portion of the stretch that is solely due to the electric potential (i.e., the electrostriction) is still relatively small. In this context, it is also important to note that for composites consisting of elliptical fibers with the longer (in-plane) axis aligned with the electric field, the mechanical traction cannot be increased arbitrarily since the composite may experience shear localization instabilities, as determined by the loss of strong ellipticity condition. This suggest the possibility of using electric fields to control the onset of these instabilities, which may be desirable in certain applications. The effect of external mechanical tractions will be studied in more details in the next chapter.

Inspired by the above findings for the effect of the various material and microstructural parameters, we have developed a systematic procedure for the optimal design of DECs that are capable of achieving large electrostrictions—in excess of 100% strain—before failure. Due to the severe restrictions imposed by dielectric breakdown, com-

posites consisting of a very small concentration of rigid circular fibers with vanishing contrast in the dielectric properties can achieve the largest electrostrictive strains. It is emphasized, however, that although smaller fiber concentrations result in larger electrostrictive strains, the concentration of the fibers cannot be arbitrarily small. In fact, there exists a critical value for the concentration, which depends on the tensile strength of the fiber material, to ensure that the fibers do not break and the constraint of 2D plane-strain deformations is satisfied for the DECs. The optimized microstructures suggested by our analytical model are found to be generally consistent with recent experimental findings of Lu et al. (2012) and Bolzmacher et al. (2006).

# Chapter 6

# Fiber-constrained DECs: Finite Deformation Response and Stability Analysis at Non-zero (Dead) External Tractions

In the previous chapter we investigated the effective response and stability of fiber-constrained DECs under the electrode boundary conditions (i.e., when the external mechanical tractions are identically zero and a potential difference is applied across the DEC sample via the compliant electrodes). In this chapter we investigate the possible development of instabilities in a certain class of dielectric elastomer composites (DECs) subjected to all-around dead electromechanical loading. Like before, the DECs consist of a dielectric elastomer matrix phase constrained to plane-strain deformations by means of aligned, long, rigid-dielectric fibers of elliptical cross section that are also aligned but randomly distributed in the transverse plane. The focus in this chapter is on "material" instabilities that are intrinsic to the DECs, as characterized by their "macroscopic" or homogenized constitutive properties, and which involve macroscopically uniform fields. Thus, "structural" instabilities that are dependent on the geometry of the specimen, such as buckling, barreling, or wrinkling,

will not be considered here. In particular, we will study loss of (incremental) positive definiteness (LPD) and loss of strong ellipticity (LE) of the electroelastic energy density. In the purely mechanical context (i.e., in finite elasticity), uniqueness and stability are characterized by the positive definiteness of a certain "exclusion" incremental energy functional (Hill 1957, Ogden 1997). In particular, it is known that loss of positive definiteness (LPD) is a necessary and sufficient condition for bifurcation under all-around dead loads (Hill 1967, Ogden 1997). On the other hand, loss of strong ellipticity signals the possible development of localized shear bands under displacement boundary conditions (Hill 1962, Rice 1976). Hill & Hutchinson (1975) investigated the bifurcation behavior of a broad class of incompressible, orthotropic solids subjected to plane-strain tension loadings. In addition, Ogden (1985) investigated the bifurcation and stability of homogeneous deformations in the plane-strain deformation of incompressible, hyperelastic solids subjected to dead-load tractions, including a global analysis of the problem. The works of Hill & Hutchinson (1975) and Ogden (1985) demonstrate that, under all-round dead loading, a variety of instability modes can occur while the energy-density function of the material is still strongly elliptic. However, it is known that the presence of an electric field can affect the onset of such instabilities in homogeneous ideal dielectric elastomers, when subjected to dead-load tractions. In particular, Zhao & Suo (2007) showed that the application of an electric field alone can lead to (snapping) instabilities of the maximum-load type in homogeneous dielectrics undergoing 3D equal bi-axial deformations. They further demonstrated that, the application of an equal bi-axial traction loading to the ideal dielectric can delay (or even completely remove) such instabilities. A more complete formulation of the stability and uniqueness problem in electro-elasticity, generalizing the approach of Hill (1957) in finite elasticity and making use of the work of Dorfmann & Ogden (2010*b*), was initiated by Bertoldi & Gei (2011). Instabilities in heterogeneous active materials have also been studied recently by several authors. For example, building on earlier work for the purely mechanical problem (Geymonat et al. 1993), Bertoldi & Gei (2011) investigated loss of positive definiteness, as well as loss of strong ellipticity for DECs with layered microstructures, while

Rudykh & deBotton (2011) studied the loss of strong ellipticity for such composites. In this chapter, we investigate the instabilites in fibrous DECs of the class described in the previous chapter, as characterized by the loss of positive definiteness and loss of strong ellipticity. We hope to complement the earlier works on the topic by providing a more complete discussion of the nature of the bifurcation modes for loading paths consisting of dead mechanical tractions in the presence of electric fields. The rest of this chapter is organized as follows. In section 6.1 we describe the problem of a fiber-constrained DEC under the dead electromechanical loading conditions. In sections 6.2 and 6.3 we study DECs with (initially) isotropic microstructions and DECs with anisotropic microstructures, respectively. Finally in section 6.4 we study the effect of microstructural parameters on the instabilities of DECs under dead electromechanical loads.

## 6.1 Instability analysis of fiber-constrained DECs under aligned dead loadings

In this section, we consider DECs that are constrained by aligned rigid fibers of elliptical cross section and subjected to all-around dead mechanical loads and charges. Motivated by possible applications as dielectric actuators, we assume that the surface charges are applied by means of "soft electrodes" (e.g., conducting grease), which are in perfect contact with the DEC sample, so that the electric displacement field is applied to the DEC sample via the surface charges $+\sigma$ and $-\sigma$ on the electrodes, as depicted in Fig. 6.1.

As depicted in Fig. 6.1(a), it is assumed that fibers in the undeformed state of the DEC (i.e., in the absence of mechanical tractions and surface charge densities) are aligned with the laboratory axis, as defined by $\{X_1, X_2, X_3\}$. More specifically, the cylindrical fibers have their long axis parallel to the $X_3$ direction, while their elliptical cross-sectional shape is aligned with the coordinate axis in the $X_1$-$X_2$ plane and has aspect ratio $w = b_0^i/a_0^i$, as shown in Fig. 5.3(a). In addition, the fibers are distributed

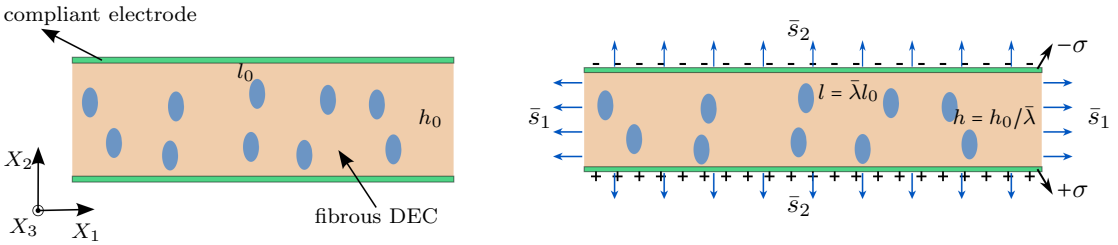


(a) reference (b) deformed

Figure 6.1: Schematic representation of a dielectric actuator made out of a thin DEC layer sandwiched between two compliant electrodes. (a) The actuator in the reference configuration with initial dimensions $l_0$ by $h_0$, and (b) the actuator in the deformed configuration with current dimensions $l_0\bar{\lambda}$ by $h_0/\bar{\lambda}$, after application of the nominal tractions $\bar{s}_1$ and $\bar{s}_2$, and the surface charge density $\sigma$.

with elliptical symmetry with the same initial shape as the fiber cross-sections (i.e., $w_0^d = b_0^d/a_0^d = w$). For simplicity, the matrix is assumed to be an incompressible ideal dielectric with permittivity $\varepsilon^{(1)}$ and mechanical response of the Gent type (2.14) with shear modulus $\mu^{(1)}$ and strain-locking parameter $J_m$, while the rigid fibers are assumed to have a linear isotropic dielectric response with isotropic permittivity $\boldsymbol{\mathcal{E}}^{(2)} = \mathcal{E}^{(2)}\boldsymbol{I}$.

We are interested in the stability behavior of the DECs under the application of all-around dead loads and charges. As depicted in Fig. 6.1(b), the nominal external traction $\bar{\mathbf{s}}^{ex}$, labelled here $\bar{\mathbf{s}}$, for simplicity, is given by

$$\bar{\mathbf{s}} = \begin{bmatrix} \bar{s}_1 & 0 \\ 0 & \bar{s}_2 \end{bmatrix} \mathbf{N}, \tag{6.1}$$

where $\bar{s}_1$ and $\bar{s}_2$ are prescribed independently of the deformation. Correspondingly, an electric displacement field is prescribed by means of surface charge densities $-\sigma$ and $+\sigma$ on the top and bottom electrodes, respectively. In practical applications, it is common to use thin samples, such that $h_0/l_0 \ll 1$. Therefore, it is reasonable to assume that the stress and electric displacement fields are (macroscopically) uniform everywhere inside, except perhaps near the side surfaces where fringing effects are expected to occur (see Siboni & Ponte Castañeda 2013, for more details). Note that, due to the presence of the conducting electrodes all the electric fields, and therefore the Maxwell stress, are identically zero in the region surrounding the DEC sample.

Thus, the traction jump condition (2.3) reduces to

$$\bar{\boldsymbol{S}}\mathbf{N} = \bar{\mathbf{s}}, \tag{6.2}$$

where $\bar{\boldsymbol{S}}$ denotes the macroscopic nominal stress inside the DEC and $\bar{\mathbf{s}}$ is the externally applied mechanical traction defined in (6.1). Given the above assumptions, the macroscopic Piola-Kirchhoff (nominal) stress $\bar{\boldsymbol{S}}$ inside the DEC sample—before any instabilities—can be shown to be given by

$$\bar{\boldsymbol{S}} = \begin{bmatrix} \bar{s}_1 & 0 \\ 0 & \bar{s}_2 \end{bmatrix}. \tag{6.3}$$

The Lagrangian (nominal) electric displacement field will be aligned with the vertical direction (as defined by the unit vector $\hat{\mathbf{E}}_2$), and therefore given by

$$\bar{\mathbf{D}} = \bar{D}\,\hat{\mathbf{E}}_2, \tag{6.4}$$

where $\bar{D}$ is prescribed by means of the surface charge densities independently of the deformation. It is important to note in this context that thin samples are prone to wrinkling instabilities in the $X_1$-$X_3$ plane under compressive tractions in the $X_1$ direction. As mentioned earlier in the text, the focus of the current study is on intrinsic "material" instabilities, and therefore such structural bifurcation modes will not be considered here.

On account of the material symmetry of the DECs and of the "aligned" character of the traction (6.1) and electric displacement (6.4), the DEC sample is expected to deform—at least up to the possible onset of an instability—into a new configuration described by the (macroscopic) deformation gradient

$$\left[\bar{\boldsymbol{F}}\right] = \begin{bmatrix} \bar{\lambda} & 0 \\ 0 & \bar{\lambda}^{-1} \end{bmatrix}, \tag{6.5}$$

where use has been made of the incompressibility of the material. Correspondingly,

it is assumed that (on the average) the rigid fibers (of fixed aspect ratio $w$) in the DEC remain aligned with the applied fields up until the onset of the first macroscopic instability (see Fig. 5.3(b)). In addition, consistent with equation (5.8), the distribution of the fibers evolves with the macroscopic deformation and therefore remains elliptical and aligned with the loading, such that the deformed distribution aspect ratio is given by

$$w^d = \frac{b^d}{a^d} = \frac{\bar{\lambda}^{-1} b_0^d}{\bar{\lambda} a_0^d} = \bar{\lambda}^{-2} w. \tag{6.6}$$

It is also remarked for later use that the Cauchy tractions are of the form

$$\bar{\mathbf{t}} = \begin{bmatrix} \bar{t}_1 & 0 \\ 0 & \bar{t}_2 \end{bmatrix} \mathbf{n}, \tag{6.7}$$

where $\bar{t}_1 = \bar{s}_1 \bar{\lambda}$ and $\bar{t}_2 = \bar{s}_2 / \bar{\lambda}$.

Given the traction boundary conditions (6.1) (or equivalently (6.7)), the macroscopic constitutive equations (5.29) and (5.30) can be used to determine the macroscopic stretch $\bar{\lambda}$ and Lagrange multiplier $\bar{p}$ as functions of the applied tractions $\bar{t}_1$ and $\bar{t}_2$, and the macroscopic electric displacement field $\bar{D}$. For the above-mentioned perfectly aligned loading case, and up to the possible development of an instability, we have that

$$\bar{t}_1 - \bar{t}_2 = \bar{\lambda} \frac{\partial \tilde{W}_{me}}{\partial \bar{\lambda}} + \bar{\lambda} \frac{\partial \tilde{W}_{el}}{\partial \bar{\lambda}} \quad \text{and} \quad 2\bar{p} = -\left(\bar{t}_1 + \bar{t}_2\right) + \tilde{A}_{1212} + \tilde{A}_{2121} - \tilde{A}_{1221}, \tag{6.8}$$

where

$$\frac{\partial \tilde{W}_{me}}{\partial \bar{\lambda}} = \frac{\mu^{(1)} \left[ \left(c + w + cw^2\right) \left(\bar{\lambda}^4 - 1\right) - \left(c + cw^2\right) \left(\bar{\lambda}^3 - \bar{\lambda}\right) \right]}{\bar{\lambda}^3 w \left(1 - c\right) \left[ 1 - \left(\hat{I}_a - 2\right) / J_m \right]} \tag{6.9}$$

and

$$\frac{\partial \tilde{W}_{el}}{\partial \bar{\lambda}} = -\left[ \frac{\varepsilon^{(1)}}{\tilde{\mathcal{E}}_{22}} + \frac{c\bar{\lambda}^2 w}{\left(\bar{\lambda}^2 + w\right)^2} \left( 1 - \frac{\varepsilon^{(1)}}{\tilde{\mathcal{E}}_{22}} \right)^2 \right] \varepsilon^{(1)^{-1}} \bar{\lambda}^{-3} \bar{D}^2. \tag{6.10}$$

In these equations, $\hat{I}_a$ is obtained by making the replacements $\bar{\theta} = \bar{\varphi} = 0$ in expression (5.14) for $\hat{I}$, and the components of the effective moduli $\tilde{\mathbb{A}}$ are obtained by expressions

(2.33) and (2.26) $W$ being replaced by $\tilde{W}$. In addition,

$$\tilde{\mathcal{E}}_{22}\left(\bar{\lambda}\right) = \varepsilon^{(1)} + c\left[\frac{1}{\mathcal{E}^{(2)} - \varepsilon^{(1)}} + \frac{1}{\varepsilon^{(1)}}\left(\frac{1}{1+w} - \frac{c\bar{\lambda}^2}{\bar{\lambda}^2 + w}\right)\right]^{-1} \tag{6.11}$$

is the principal macroscopic permittivity of the composite in the direction of the applied electric displacement (i.e., the $X_2$ direction). The macroscopic constitutive equations (5.29) can also be used to determine the macroscopic electric field

$$\bar{\mathbf{E}} = \bar{E}\,\hat{\mathbf{E}}_2, \quad \text{with} \quad \bar{E} = \tilde{\mathcal{E}}_{22}\bar{D}. \tag{6.12}$$

Given the above preliminaries, we are now ready to investigate the possible onset of loss of convexity and of strong ellipticity in the fiber-constrained DECs subjected to aligned dead-load traction/charge conditions. We also explore the effect of the relevant microstructural variables (aspect ratio and concentration of the fibers) on the onset of instabilities (or in general shape of the failure regions) for such DECs. For the "principal" solution described by expressions (6.1) through (6.12), the loss of convexity and strong ellipticity conditions can be simplified further as discussed next.

*Loss of convexity of the incremental homogenized energy.* As already mentioned in the previous section the increments for plane-strain problems can be defined by the vector $\boldsymbol{\delta}$, defined in (5.32), in terms of the components of the incremental displacement gradient and incremental electric displacement. Then we argued that the positive definiteness of the quadratic form (2.37) can be determined by evaluating the sign of the eigenvalues of the Hessian defined in equation (5.33). Thus, we have shown that the DEC loses convexity when at least one of the eigenvalues first vanishes in a given loading path. Two types of modes have been identified for the loss of convexity: *aligned* and *non-aligned* modes. For the aligned modes, the eigenvector corresponding to the vanishing eigenvalue is "aligned" with the direction of the loading (i.e., only the $u_{1,1}$ and $\dot{d}_2$ components of $\boldsymbol{\delta}$ are non-zero), while for the non-aligned modes, the eigenvector corresponding to the vanishing eigenvalue is orthogonal to the loading

(i.e., only the $u_{1,2}$, $u_{2,1}$, and $\dot{d}_1$ components of $\boldsymbol{\delta}$ can be non-zero). By making use of expressions (6.8), it can be shown that the stability criteria for the aligned LPD modes can be written as

$$\frac{\partial^2\tilde{W}}{\partial\bar{\lambda}^2} - 2\bar{\lambda}^{-2}\bar{t}_2 > 0, \quad \text{and} \quad \left(\frac{\partial^2\tilde{W}}{\partial\bar{\lambda}^2} - 2\bar{\lambda}^{-2}\bar{t}_2\right)\frac{\partial^2\tilde{W}}{\partial\bar{D}_2^2} - \left(\frac{\partial^2\tilde{W}}{\partial\bar{\lambda}\partial\bar{D}_2}\right)^2 > 0, \tag{6.13}$$

so that an aligned instability will take place when one of the conditions in (6.13) is first violated. Note that the above condition reduce to the conditions (5.34) of chapter 5, in the absence of external tractions (i.e., when $\bar{t}_2 = 0$). If the first inequality is violated, the instability is purely mechanical and corresponds to a turning point in the nominal tractions. On the other hand, when the second inequality is violated, the instability is electro-mechanical and generally corresponds to a maximum in the nominal electric field. In particular, when $\bar{t}_2 = 0$, these conditions reduce to corresponding conditions first identified by Zhao et al. (2007) for ideal dielectrics and by Bertoldi & Gei (2011) for laminated DECs. The non-aligned modes, however, will correspond to other types of bifurcation instabilities apparently not considered in the earlier works. As we will see below, such non-aligned bifurcation instabilities can take place before the aligned limit-point-type instabilities in many cases. Finally, it is noted that more explicit expressions are given in A for the loss of convexity instabilities in the purely mechanical context. Such results are of course entirely consistent with the results of Hill (1967) and Ogden (1985) for the purely mechanical cases.

*Loss of strong ellipticity of the homogenized energy.* Recall that the conditions for the loss of strong ellipticity are independent of the loading conditions. Therefore, for the special case of aligned composites under alignded loading conditions, the strong ellipticity of the homogenized energy (or its violation) is determined, by evaluating the roots of the polynomial (5.35).

As it was the case in the previous chapter, in the results presented in the figures below, the "non-convex" regions associated with "aligned" instability modes are shaded by the color green with dash-dotted boundaries, while the non-convex regions associated with "non-aligned" bifurcation modes are shaded by the color blue with

solid boundaries. For completeness, the "non-elliptic" regions, which are shaded by the color red with dashed boundaries, are also shown in the figures. It is emphasized here that the boundaries of the unstable regions signal the onset of the corresponding instabilities. For simplicity, we use dimensionless forms for the plots, where the normalization factors depend on the properties of the matrix phase. In particular, we use here the dimensionless quantities

$$\frac{\bar{t}}{\mu^{(1)}}, \quad \frac{\bar{D}}{\sqrt{\mu^{(1)}\varepsilon^{(1)}}}, \quad \text{and} \quad \frac{\bar{E}}{\sqrt{\mu^{(1)}/\varepsilon^{(1)}}}$$

to denote, respectively, the normalized traction, electric displacement field, and electric field. For comparison purposes, sample normalization factors are provided in Table 6.1 for typical elastomers used in practical applications. Note that for a specific matrix material, one can calculate the normalization factors, and therefore obtain the range for the external stimuli associated with instabilities by referring to the normalized results in the plots that follow.

| Material | $\varepsilon^{(1)}/\varepsilon_0$ | $\mu^{(1)}$[MPa] | $\sqrt{\mu^{(1)}\varepsilon^{(1)}}$[C/m$^2$] | $\sqrt{\mu^{(1)}/\varepsilon^{(1)}}$[MV/m] |
|---|---|---|---|---|
| VHB 4910 (by 3M) | 4.7 | 1.6 | $8.2\times10^{-3}$ | 196 |
| Natural Rubber | 2.6 | 0.6 | $3.5\times10^{-3}$ | 156 |

Table 6.1: Typical soft dielectric elastomers and the corresponding normalization factors. The properties for VHB 4910 are taken form Carpi et al. (2008) and the properties for Natural Rubber are taken from the website www.matweb.com.

## 6.2 Isotropic DECs and comparison with homogeneous ideal dielectrics

We start our discussion by comparing the results for a homogeneous ideal dielectric (i.e., $c = 0$) to that of a DEC with (initially) isotropic microstructure (i.e., $w = 1$ and $c = 0.3$). Thus, Fig. 6.2 shows the failure regions in the space of principal Cauchy tractions, $\bar{t}_1$ vs. $\bar{t}_2$, for different values of the normalized electric displacement $\bar{D}/\sqrt{\varepsilon^{(1)}\mu^{(1)}}$.

Figures 6.2(a) and 6.2(b) show results for $\bar{D} = 0$ (i.e., the purely mechanical case). As can be seen from these figures, the stability region is roughly a band bounded by two hyperbolic-looking curves that closely hug the $\bar{t}_1$ and $\bar{t}_2$ axes. Note that the stability maps are symmetric with respect to the line $\bar{t}_1 = \bar{t}_2$ in the absence of electric fields, consistent with the isotropic behavior of the material. In particular, it is observed that the response remains stable for uniaxial tension along either axis. It is also remarked that the stable region is significantly larger (in area) for the case of isotropic composites compared to that of the ideal dielectric. This somewhat counter-intuitive observation can be explained by recalling that the addition of rigid fibers to the pure matrix significantly enhances the overall stiffness, and therefore the composite can sustain higher stresses before the onset of instabilities.

For the isotropic cases with no applied electric fields shown in Figs. 6.2(a) and 6.2(b), the first instabilities take place by loss of positive definiteness (LPD) and involve non-aligned modes corresponding to bifurcation instabilities that are orthogonal to the loading path and consist of infinitesimal rotations superimposed on shears at 45° to the loading directions. In these figures (and in the figures that follow) the modes are shown schematically by means of icons at sample points on the boundary of the instability regions. As can also be seen from the figures, the boundary of the instability region corresponding to the aligned LPD modes is entirely engulfed by the outer non-aligned LPD region, except for the critical point $\bar{t}_1 = \bar{t}_2 = \bar{t}_c > 0$, where the two regions just touch. At this special point, which corresponds to equibiaxial tension and has been considered in a detailed local and non-local analysis by Ogden (1985), there is a symmetry-breaking bifurcation where the rotationally invariant principal solution (with macroscopic stretch $\bar{\lambda} = 1$) suddenly allows for a pure shear ($\bar{\lambda} \neq 1$) at an indeterminate angle. Note that the instability takes place at a critical $\bar{t}_c \approx 2\mu^{(1)}$ for the ideal dielectric and $\bar{t}_c \approx 4\mu^{(1)}$ for the specific composite shown in the figure. Interestingly, non-aligned instabilities can also take place for compressive loadings, including when one of the principal tractions is tensile. However, the point at the origin where $\bar{t}_1 = \bar{t}_2 = 0$ is special. At this point, the instability mode for both the ideal dielectric and the isotropic DEC is an incremental deformation of

the form ($u_{1,2} = -u_{2,1}$), which corresponds to a *special* rotational mode that can be safely ignored (Truesdell & Noll 2004). As we move away from this point along the boundary of the inner non-aligned LPD region, the mode of the instability evolves into a compound one consisting of combinations of an infinitesimal rotation and a pure shear at 45° angle. Furthermore, the pure shear changes sign as we go from one side of the point $\bar{t}_1 = \bar{t}_2 = 0$ to the other side. Finally, it is noted that, for these purely mechanical loadings, explicit expressions are given in A. In particular, the boundary of the aligned region (denoted by the dash-dot line) corresponds to the violation of condition (A.9), while the boundary of the non-aligned region (denoted by solid lines) corresponds to the violation of conditions (A.11).

Figures 6.2(c) and 6.2(d) show the corresponding results when a non-zero electric displacement field is applied (in the $X_2$ direction). It is observed that the presence of the electric field breaks the symmetry of the unstable region about the symmetry line $\bar{t}_1 = \bar{t}_2$, and results in the closing of the stable band along the $\bar{t}_2$ axis. In particular, different from the previous purely mechanical cases, the materials can now become unstable on loading paths of the type $\bar{t}_1 = 0$ and $\bar{t}_2 = \bar{t} > 0$. (Note that due to the stiffening effect of the rigid fibers, the onset of instabilities for loading paths of the form $\bar{t}_1 = const.$ and $\bar{t}_2 = \bar{t} > 0$ occurs at larger values of the traction $\bar{t}_2$ for the composite, compared to the ideal dielectric matrix.) The unaligned mode at the onset of this instability is a simple shear along the $X_2$ direction (with $u_{2,1} \neq 0$), accompanied by a non-zero increment in the electric displacement along the $X_1$ direction (with $\dot{d}_1 \neq 0$), which is represented by a (solid) arrow in the corresponding icon. For the critical point $\bar{t}_1 = \bar{t}_2 = \bar{t}_c > 0$, we again observe two modes for the instabilities. A non-aligned mode consisting of a pure shear at 45° accompanied by an increment in the electric displacement field in the $X_1$ direction, and an aligned mode consisting of a pure shear aligned with the coordinate axes and an increment in the electric displacement field in the $X_2$ direction. Similar to the previous case, the instability modes for all the other points on the boundary of the non-aligned region with non-symmetric loading (i.e., $\bar{t}_1 \neq \bar{t}_2$) consist of a pure shear at 45° and an infinitesimal rotation, along with an increment in the electric displacement in the $X_1$ direction.

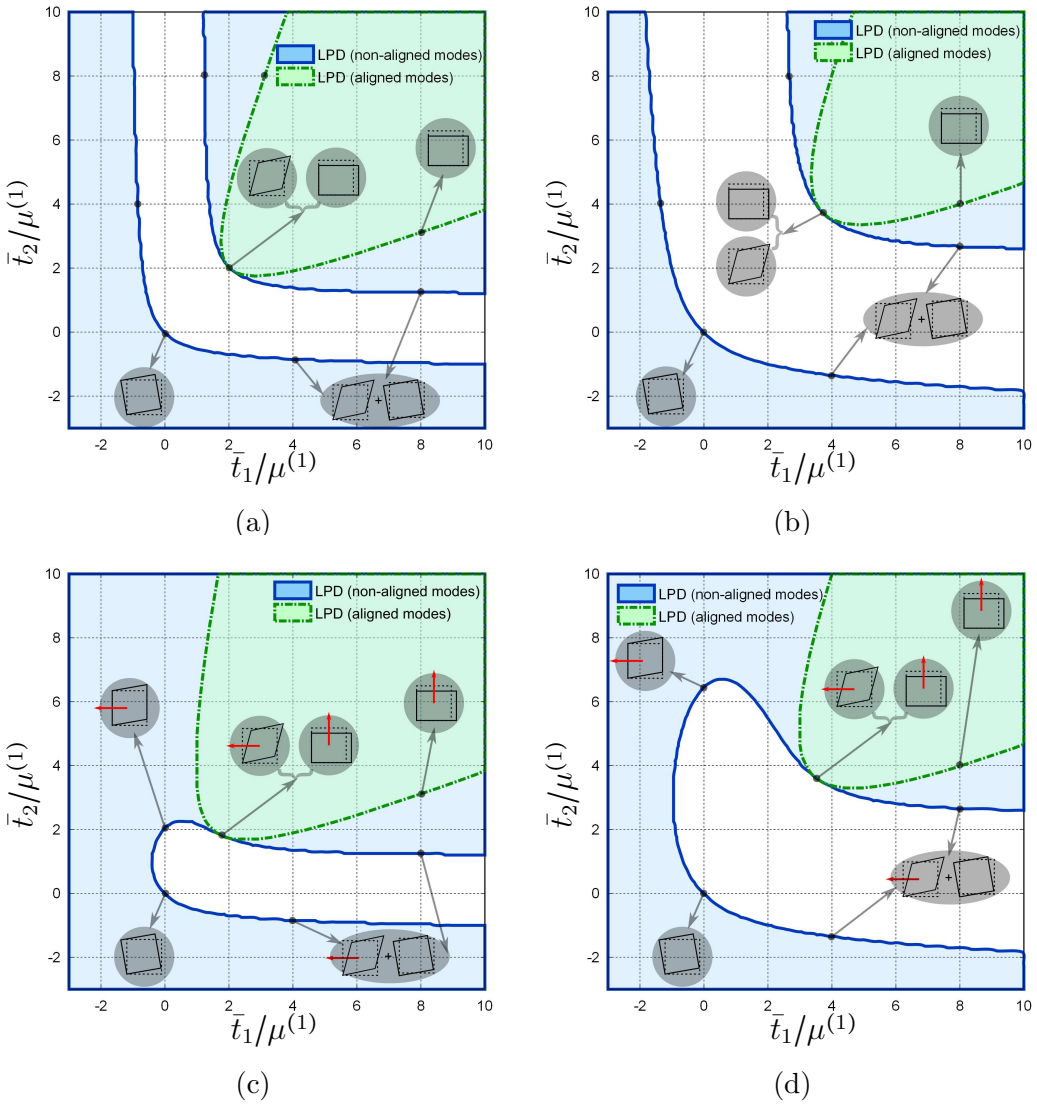


Figure 6.2: This figure shows the stability and various instability regions (on the $\bar{t}_1$-$\bar{t}_2$ plane) for isotropic cases. (a) Ideal dielectric and $\bar{D}/\sqrt{\varepsilon^{(1)}\mu^{(1)}} = 0$, (b) initially isotropic composite and $\bar{D}/\sqrt{\varepsilon^{(1)}\mu^{(1)}} = 0$, (c) ideal dielectric and $\bar{D}/\sqrt{\varepsilon^{(1)}\mu^{(1)}} = 0.5$, and (d) initially isotropic composite and $\bar{D}/\sqrt{\varepsilon^{(1)}\mu^{(1)}} = 0.5$. In this figure $J_m = 100$, and for the composite $c = 0.3$, $w = 1$, and $\mathcal{E}^{(2)}/\varepsilon^{(1)} = 1000$.

However, the special rotational instability persists for $\bar{t}_1 = \bar{t}_2 = 0$ as the electric field $\bar{D}$ is increased. Note that such loading paths are neutrally stable. Finally, it should also be noted that while the isotropic DECs are strongly elliptic for all tractions when the electric field vanishes, they may lose strong ellipticity for sufficiently high electric fields (not shown in the figures).

## 6.3 DECs with anisotropic microstructures

Figure 6.3 shows the stability and various instability regions for DECs with aligned elliptical fibers as a function of the Cauchy tractions, $\bar{t}_1$ vs. $\bar{t}_2$, for different values of the electric displacement field $\bar{D}$, which is again applied in the vertical ($X_2$) direction. In these figures, the aspect ratio and concentration of the fibers are fixed ($w = 2$, $c = 0.355$) and the long in-plane axis of the fibers is along the vertical direction and therefore aligned with the applied electric field.

As observed in Fig. 6.3(a) for the purely mechanical case ($\bar{D} = 0$), the failure regions are no longer symmetrically distributed relative to the equibiaxial loading line, as a consequence of the anisotropy induced by the elliptical fibers. Compared to the prior results for circular fibers ($w = 1$) shown in Fig. 6.2(b), the following observations can be made. First, the stability region now closes up along the $\bar{t}_1$ axis, while the corresponding area along the $\bar{t}_2$ axis is left largely unchanged. Second, the boundary of the stability region is still determined by the onset of unaligned LPD instabilities. However, while the aligned LPD region no longer coincides with the unaligned LPD boundary for equibiaxial loading—the aligned LPD region now being fully contained within the outer unaligned LPD region—the non-aligned LPD region now touches on the boundary of a new loss of strong ellipticity (LE) region for uniaxial tension along the horizontal direction. Thus, for uni-axial tension along the $X_1$ direction, the DEC loses positive definiteness and strong ellipticity at the same time ($\bar{t}_2 = 0$ and $\bar{t}_1 = \bar{t}_c > 0$). These LE instabilities, which were first observed by Lopez-Pamies & Ponte Castañeda (2006*a*), take place when the tangent shear modulus transverse to the long axis of the fibers vanishes and correspond to localization bands with shear

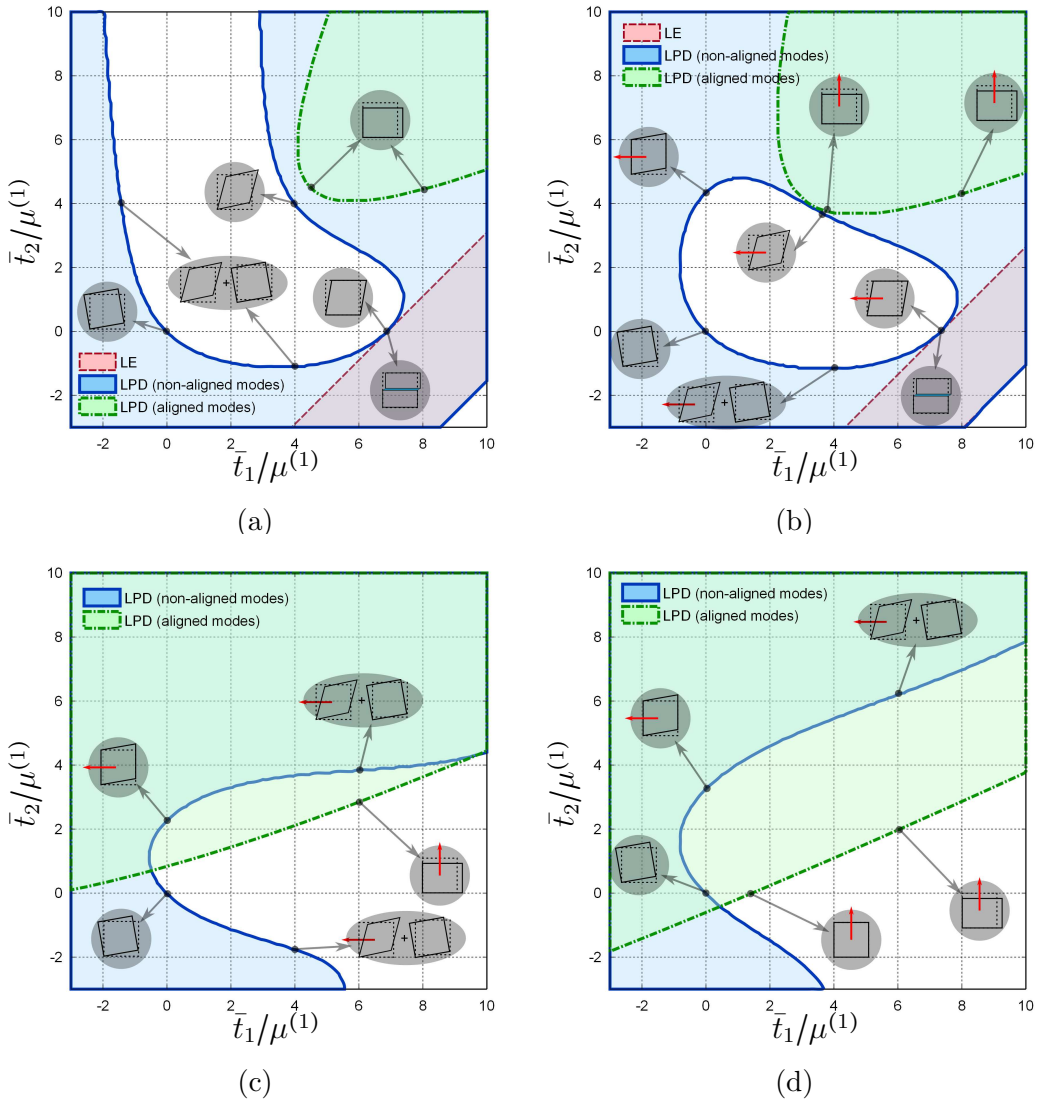


Figure 6.3: This figure shows the stability and various instability regions (on the $\bar{t}_1$-$\bar{t}_2$ plane) for different values of the electric displacement. (a) $\bar{D}/\sqrt{\varepsilon^{(1)}\mu^{(1)}} = 0$, (b) $\bar{D}/\sqrt{\varepsilon^{(1)}\mu^{(1)}} = 1.15$, (c) $\bar{D}/\sqrt{\varepsilon^{(1)}\mu^{(1)}} = 3.45$, and (d) $\bar{D}/\sqrt{\varepsilon^{(1)}\mu^{(1)}} = 5.75$. In this figure $w = 2$, $c = 0.355$, $J_m = 100$, and $\mathcal{E}^{(2)}/\varepsilon^{(1)} = 1000$.

along the $X_1$ direction, as illustrated by the icon in the figure. On the other hand, the mode of the unaligned LPD branch corresponds to a simple shear also aligned with the $X_1$ direction.

As the electric displacement field $\bar{D}$ is progressively increased in Figs. 6.3(b) to 6.3(d), the following observations can be made. First, for relatively small values of $\bar{D}$, the stability region closes up along the $\bar{t}_2$ axis, leading to a closed (i.e., bounded) stability domain, but then for larger values of $\bar{D}$, it opens up along the $\bar{t}_1$ direction. Second, the LE instability region shifts to the right and eventually disappears with the opening of the stability region along the $\bar{t}_1$ direction. Third, the aligned LPD region, which was completely engulfed by the unaligned LPD region for $\bar{D} = 0$, starts to shift down and to the left in the figure, first touching the unaligned LPD region near the equibiaxial loading line, but then partially overtaking it as $\bar{D}$ is further increased, and eventually enclosing the unloaded state $\bar{t}_1 = \bar{t}_2 = 0$. In connection with this last observation, it is important to emphasize that limit load instabilities are therefore to be expected for a mechanically unloaded sample at sufficiently large electric displacement fields. It is also interesting to observe that the application of an electric field along the fiber direction can generate electric torques that tend to stabilize the fibers against possible rotations, and thus delays the instability for tensile loading along the $X_1$ direction (see Galipeau & Ponte Castañeda 2013, for similar observations in the context of magneto-active elastomers). The instability modes for several representative points are shown in these plots. Note that the modes in the presence of an electric field may include increments in the relevant components of the electric displacement field (i.e., in the $X_1$ direction for non-aligned modes and in the $X_2$ direction for the aligned modes).

Figure 6.4 shows the corresponding results for DECs consisting of elliptical fibers with their long axis perpendicular to the applied electric displacement field, which is still being applied along the $X_2$ direction (i.e., $w < 1$). Figure 6.4(a) shows the results for the purely mechanical case (i.e., when $\bar{D} = 0$). As can be seen from this figure, the stability and various instability regions are similar to those of the Fig. 6.3(a) except that the role of the tractions $\bar{t}_1$ and $\bar{t}_2$ is interchanged. This is to be

expected from the symmetry of the problem and implies that the LE instability is now encountered for uni-axial tension along the $X_2$ direction, and that the normal to the shear band is in the $X_1$ direction. Figures 6.4(b) to 6.4(d) depict the effect of increasing electric displacement $\bar{D}$ (still applied in the $X_2$ direction) on the various failure regions. The following observation can be made. First, as $\bar{D}$ increases, the

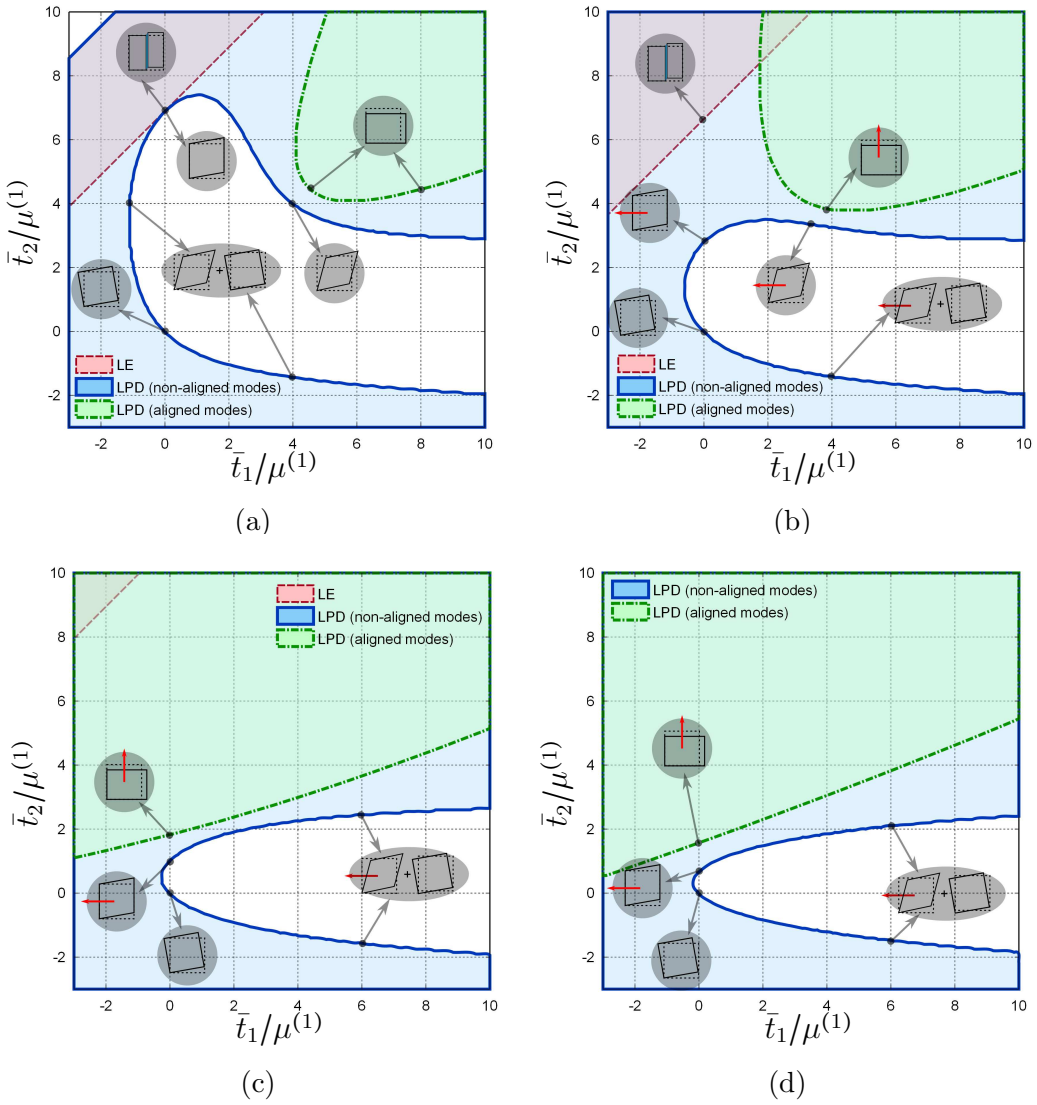


Figure 6.4: This figure shows the stability and various instability regions (on the $\bar{t}_1$-$\bar{t}_2$ plane) for different values of the electric displacement. (a) $\bar{D}/\sqrt{\varepsilon^{(1)}\mu^{(1)}} = 0$, (b) $\bar{D}/\sqrt{\varepsilon^{(1)}\mu^{(1)}} = 1.15$, (c) $\bar{D}/\sqrt{\varepsilon^{(1)}\mu^{(1)}} = 3.45$, and (d) $\bar{D}/\sqrt{\varepsilon^{(1)}\mu^{(1)}} = 5.75$. In this figure $w = 1/2$, $c = 0.355$, $J_m = 100$, and $\mathcal{E}^{(2)}/\varepsilon^{(1)} = 1000$.

stability region becomes more tightly aligned with the $\bar{t}_1$ axis, meaning that for given

$\bar{t}_1$ smaller values of $\bar{t}_2$ are allowed. Second, the aligned LPD region shifts a bit down and to the left, but never quite catches up with the stability region, so that the first instability cannot be of the aligned type for these cases with $w < 1$. Third, the LE region initially shifts down slightly, making it easier for such instabilities to take place for tensile loadings along the $X_2$ direction, but then shifts up for larger values of $\bar{D}$, eventually tending to disappear. This is due to the fact that fibers tend to align their larger (in-plane) axis with the external field and are therefore electrostatically unstable when a field is applied in the transverse direction (along the $X_2$ direction here). However, for sufficiently large fields, the compressive Maxwell stresses (in the vertical direction), which increase with the square of the field and tend to stabilize the fibers against rotations, preclude the LE instabilities from taking place. In any case, the LE region becomes completely surrounded by the unaligned LPD region and therefore the first instability is always of the unaligned LPD type for prescribed all-around dead loads. (If displacement boundary conditions were to be applied instead, then it would be expected that the LE instabilities could be critical.) An important implication of all these observations is that for $w < 1$ the behavior is completely stable for uniaxial tensile loads in the horizontal direction. This is unlike the case of $w > 1$, where instabilities are expected for uniaxial tension along the $X_1$ direction either at low enough values of the fields, or at sufficiently high values of the field.

## 6.4 The effect of microstructural parameters on the stability

In this subsection we investigate the effect of the volume fraction of the fibers and their aspect ratio on the stability of fiber-constrained DECs. For simplicity, and consistent with practical applications for dielectric actuators, we will consider only uni-axial loadings along the $X_1$ direction (i.e., $\bar{t}_1 \neq 0$ and $\bar{t}_2 = 0$), in the presence of non-zero electric displacement fields in the $X_2$ direction. Once again, it is recalled that for thin actuators, compressive tractions ($\bar{t}_1 < 0$) would be expected to lead to

(structural) wrinkling instabilities, which are outside of the scope of this work.

Figure 6.5 shows $\bar{D}$ vs. $\bar{t}_1$ maps of the stability and various instability regions for different values of the fiber aspect ratio. As can be deduced from Fig. 6.5(a), for DECs consisting of fibers with $w = 1/4$, the material is stable when

$$\bar{t}_1 \geq 0 \quad \text{for all} \quad \bar{D} \geq 0. \tag{6.14}$$

In this context, it should be noted that such DECs are neutrally stable when no traction is applied to the boundary, i.e., when $\bar{t}_1 = 0$. (Recall that this situation corresponds to *special* rotational modes mentioned earlier.) However, as soon as a negative traction is applied to the material, the behavior becomes unstable triggering unaligned LPD modes. It is also important to mention that for the cases where $w < 1$, the DECs may lose strong ellipticity for sufficiently negative tensions (or compressions). Figure 6.5(b) shows the corresponding results for DECs with circular fibers ($w = 1$). Similar to the previous case, all the points on and above the $\bar{t}_1 = 0$ line are stable. It is also observed that the material is always strongly elliptic in this case. On the other hand, as can be seen in Fig. 6.5(c), for DECs consisting of elliptical fibers with $w > 1$ ($w = 2$ for the specific DEC in this figure), the material may lose ellipticity for a critical $\bar{t}_1 = \bar{t}_1^c > 0$, when the electric displacement field is smaller than a certain limiting value ($\bar{D}^c/\sqrt{\varepsilon^{(1)}\mu^{(1)}} \approx 1.2$ for the case shown here). It is also observed that the critical traction $\bar{t}_1^c$ increases with increasing electric displacement field up to a critical value $\bar{D}^c$, beyond which (for $\bar{D} > \bar{D}^c$) the composite is always strongly elliptic. Once again this is due to the stabilizing effect of the electrostatic torques on the fibers when their larger (in-plane) axis is aligned with the applied electric field. For a larger aspect ratio ($w = 4$), as shown in Fig. 6.5(d), the behavior for small values of $\bar{D}$ is similar to that for the previous case ($w = 2$), although the LE region is slightly larger with LE being observed for slightly lower values of $\bar{t}_1$ and slightly larger values of $\bar{D}$. However, for larger values of $\bar{D}$, it can be seen that the DEC can not only lose ellipticity again (at sufficiently large values of $\bar{D}$), but it can also exhibit aligned LPD instabilities for moderate values of $\bar{D}$ and $\bar{t}_1$. We will come

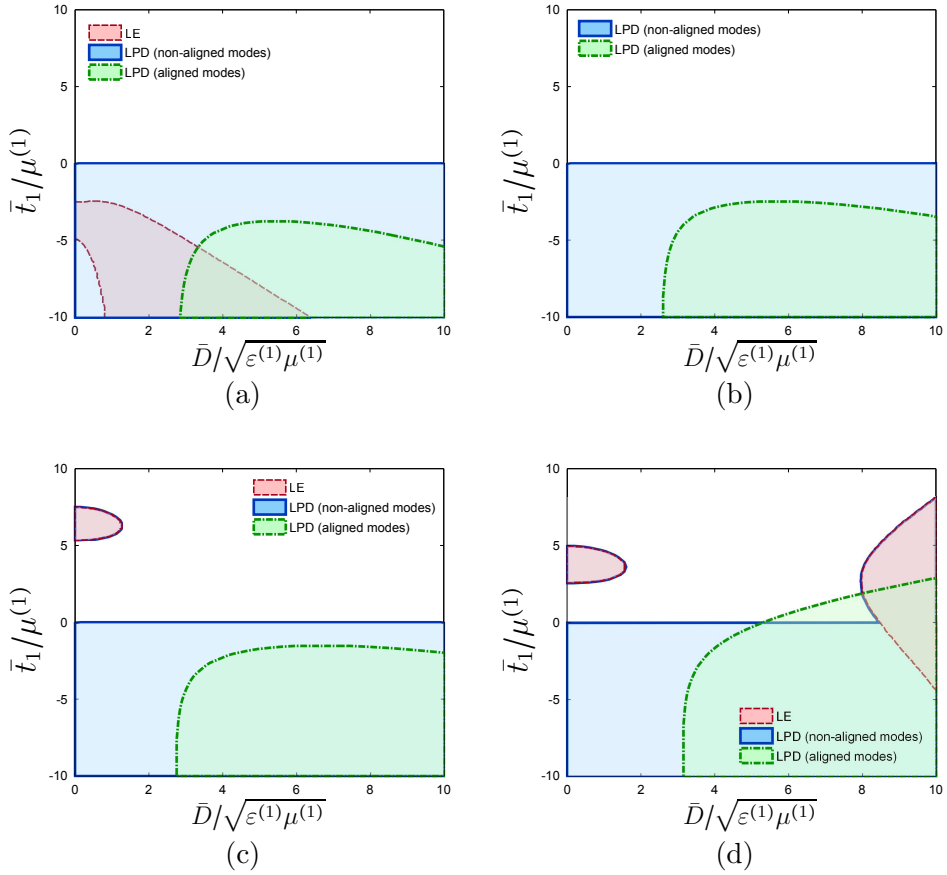


Figure 6.5: This figure shows the stability and various instability regions (on the $\bar{D}$-$\bar{t}_1$ plane) for different values of the aspect ratio of the fibers. (a) $w = 1/4$, (b) $w = 1$, (c) $w = 2$, and (d) $w = 4$. In this figure $c = 0.2$, $J_m = 100$, and $\mathcal{E}^{(2)}/\varepsilon^{(1)} = 1000$.

back to this point at the end of this section.

Figure 6.6 shows the corresponding stability and instability regions on maps of $\bar{D}$ vs. $\bar{t}_1$, for different values of the fiber concentration for composites with aspect ratio $w = 2$. As shown in this figure, there is always a value for the electric displacement field below which the material can lose strong ellipticity at a critical traction $\bar{t}_1 = \bar{t}_1^c > 0$. Similar to the previous case this critical traction increases with increasing electric field, due to the stabilizing effect of the electrostatic torques on the fibers. It is also important to mention that for a fixed electric displacement (below the limiting value), the critical traction $\bar{t}_1^c$ increases with increasing the concentration. Again, this can be explained by noting that composites with higher concentrations are much stiffer. Therefore, even though composites with higher concentrations lose ellipticity

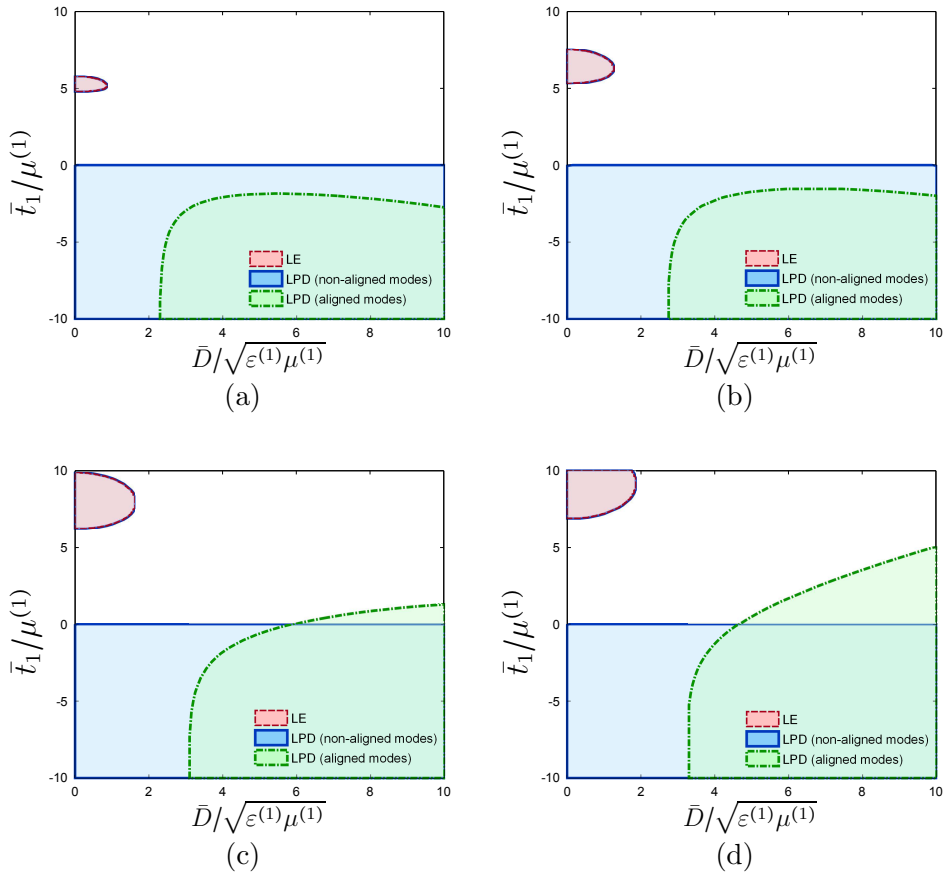


Figure 6.6: This figure shows the stability and various instability regions (on the $\bar{D}$-$\bar{t}_1$ plane) for different values of the concentration. (a) $c = 0.1$, (b) $c = 0.2$, (c) $c = 0.3$, and (d) $c = 0.355$. In this figure $w = 2$, $J_m = 100$, and $\mathcal{E}^{(2)}/\varepsilon^{(1)} = 1000$.

at smaller stretches, the critical tractions are larger for higher concentrations. Finally, it is observed that for the even larger concentrations shown in Figs. 6.6(c) and 6.6(d), the aligned LPD instability region extends beyond the $\bar{t}_1$ axis. This means that, for sufficiently high fiber concentrations, the DECs may become unstable under traction-free conditions by simply increasing the applied electric displacement field.

Figure 6.7 presents results for DECs subjected to increasing electric field $\bar{D}$ under fixed (dead) nominal tractions $\bar{s}_1 = \bar{t}_1/\bar{\lambda}$ and $\bar{s}_2 = 0$ for two different aspect ratios: $w = 4.5$ (figures on left) and $w = 1/4.5$ (figures on right). As can be seen from Figs. 6.7(a) and 6.7(c) for $w = 4.5$, the application of the electric field $\bar{D}$ (along the long axis of the fibers) results in increasing stretch $\bar{\lambda}$ along the $X_1$ direction for all values of the pre-stress $\bar{s}_1$, while the Cauchy tractions can increase, or decrease depending on whether $\bar{s}_1$ is positive or negative. For zero pre-stress, the behavior is (neutrally) stable up to the point where the aligned LPD region is crossed corresponding to a maximum load type behavior, as depicted by the green cross on the corresponding nominal electric field $\bar{E}$ curve shown in Fig. 6.7(e). As the nominal traction is increased ($\bar{s}_1/\mu^{(1)} = 1$), the onset of the maximum is delayed, as can be seen in Fig. 6.7(e), but a shear localization instability, labelled with red circles, is actually possible when the fixed nominal traction path first crosses the LE instability region on the right. As the nominal traction is increased further $\bar{s}_1/\mu^{(1)} = 2$), the DEC can actually become unstable at zero applied electric field ($\bar{D} = 0$), since the material exhibits purely mechanical instabilities of the shear localization type. However, the figure also suggest that the application of an electric field can actually stabilize the material (by leaving the LE region on the left) up until a sufficiently large value, at which the LE region on the right is traversed. Alternatively, application of negative tractions, independent of whether or not an electrical field is applied, immediately leads to unstable behavior. On the other hand, as can be seen from Figs. 6.7(b), 6.7(d) and 6.7(f) for $w = 1/4.5$, when the fibers are orthogonal to the applied electric field, the behavior is completely stable for zero or positive values of the nominal traction $\bar{s}_1$, while it becomes unstable for compressive values ($\bar{s}_1 < 0$). Also, as shown in Fig. 6.7(f), the points where the fixed nominal traction paths cross the aligned

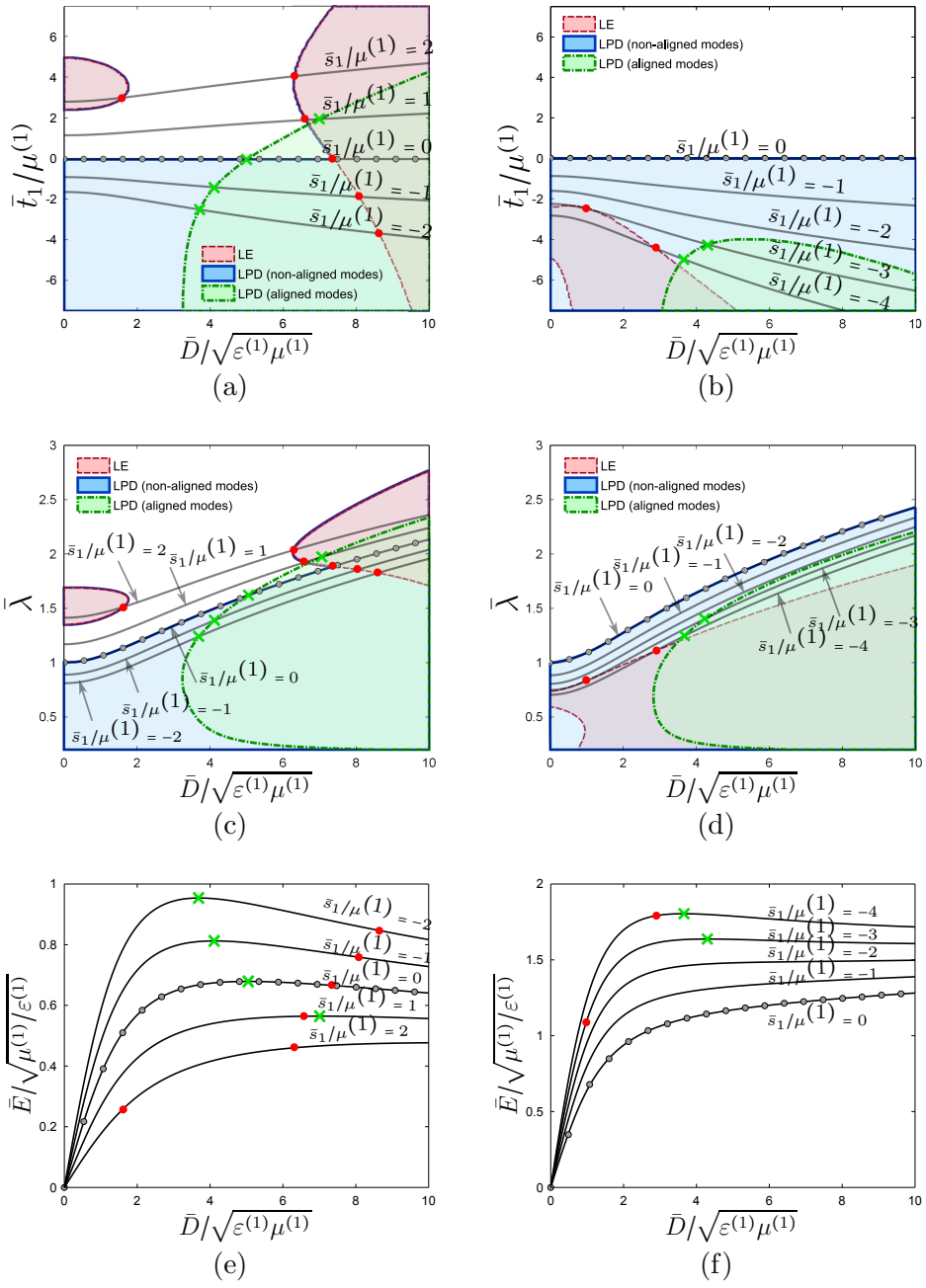


Figure 6.7: This figure shows the response of DECs under constant nominal tractions in the $X_1$ direction, $\bar{s}_1 = \bar{t}_1/\bar{\lambda}$ and $\bar{s}_2 = \bar{t}_2 = 0$. (a) Instability regions and constant $\bar{s}_1$ curves on the $\bar{D} - \bar{t}_1$ plane for $w = 4.5$, (b) instability regions and constant $\bar{s}_1$ curves on the $\bar{D} - \bar{t}_1$ plane for $w = 1/4.5$, (c) instability regions and constant $\bar{s}_1$ curves on the $\bar{D} - \bar{\lambda}$ plane for $w = 4.5$, (d) instability regions and constant $\bar{s}_1$ curves on the $\bar{D} - \bar{\lambda}$ plane for $w = 1/4.5$, (e) $\bar{E}$-$\bar{D}$ curves for different values of $\bar{s}_1$ for $w = 4.5$, and (f) $\bar{E}$-$\bar{D}$ curves for different values of $\bar{s}_1$ for $w = 1/4.5$. In this figure $c = 0.2$, $J_m = 100$, $\mathcal{E}^{(2)}/\varepsilon^{(1)} = 1000$, and the symbols "×" and "•" denote the intersection of the corresponding response curve with the boundary of the aligned and elliptic regions, respectively.

LPD regions still correspond to maxima on the $\bar{E}$ versus $\bar{D}$ plots, but the behavior is already unstable, as just pointed out. Finally, it should be noted that the results shown in Fig. 6.7(c) are qualitatively similar to results presented by Bertoldi & Gei (2011) for laminated dielectric elastomer composites. This is not too surprising in view of the fact that layered microstructures can be recovered from our results in the limit as $w \to \infty$. However, because of the randomness of the microstructure in our DECs, "microscopic" periodic modes (Geymonat et al. 1993) are not relevant here.

## 6.5 Concluding remarks

In this work we have carried out a preliminary investigation on the possible development of instabilities in a certain class of fiber-constrained dielectric elastomer composites subjected to all-around dead electromechanical loading under plane-strain conditions. Three types of "material" instabilities were considered: loss of positive definiteness (LPD) with "aligned" eigenmodes, loss of positive definiteness with "non-aligned" eigenmodes, and loss of strong ellipticity (LE). Loss of positive definiteness simply corresponds to the loss of local convexity of the homogenized electro-elastic stored-energy function for the DECs (Bertoldi & Gei 2011). For the aligned cases, the (local) convexity is lost for increments that are aligned with the loading direction, and typically manifest themselves as "limit load" behavior either in the mechanical or electrical response, while for the non-aligned case the convexity is lost for increments that are orthogonal to the loading direction, and could correspond to bifurcations from the principal solution. The loss of strong ellipticity, on the other hand, corresponds to loss of positive definiteness of the electromechanical acoustic tensor (Dorfmann & Ogden 2010*a*) and manifests itself by the onset of highly localized shear band instabilities. Loss of ellipticity normally takes place after loss of convexity, but the two can occur simultaneously for special circumstances.

Our results show that the stability of the DECs depends sensitively on the loading conditions (i.e., the applied tractions on the sample and electric displacement fields in the $X_2$ direction) and is also affected by the microstructure of the DECs (i.e., the

volume fraction of the fibers and their aspect ratio). It is worth mentioning that for the range of tractions considered in our work, the strain-locking parameter does not have a significant effect on the onset of instabilities. According to our results, only the first two types of LPD instabilities are normally observed for DECs with in-plane isotropic microstructures, corresponding to randomly distributed fibers of circular cross-section, including as a special case the ideal dielectric matrix phase. However, anisotropy of the in-plane microstructure—in the form of fibers of elliptical cross section that are aligned with the loading directions—allows for the possible development of shear localization instabilities under conditions involving compressive electromechanical stresses along the long (in-plane) axis of the fibers. More specifically, it is found that the non-aligned LPD instabilities typically precede aligned LPD and LE instabilities, especially for in-plane isotropic microstructures, but aligned (limit load) LPD and LE instabilities can also be critical for composites with anisotropic microstructures. In this context, it should be noted that the possible development of non-aligned LPD bifurcation instabilities appears to have been ignored in prior analysis of the problem for ideal dielectric (Zhao & Suo 2007, Zhao et al. 2007) and layered dielectrics (Bertoldi & Gei 2011, Rudykh & deBotton 2011). Fortunately, however, such instabilities can usually be avoided by orienting the long (in-plane) axis of the fibers parallel to the tensile stress direction and orthogonal to the applied electric field. It should also be noted that our work can be considered a generalization of the plane-strain works of Huang, Li, Foo, Zhu, Clarke & Suo (2012) for (isotropic) ideal dielectric elastomers and of Bertoldi & Gei (2011) for (anisotropic) layered dielectrics in that both limits can be recovered in principle by taking the elliptical cross section of the fibers to be circular ($w = 1$) or flat ($w = 0$), respectively. (In the first case, the fiber concentration $c$ must also be taken to be infinitesimal to compare with the corresponding results of Huang, Li, Foo, Zhu, Clarke & Suo (2012)). Our work also provides new results in the purely mechanical context for all-around dead tractions of the fiber-reinforced elastomers with non-circular (i.e., elliptical) cross section, where the in-plane response is orthotropic (Hill & Hutchinson 1975). Thus, our work also provides a specific example generalizing the results of Ogden (1985) for in-plane

isotropic response, although a global analysis was not attempted here.

Finally, it should be noted that the results of this chapter can be generalized in at least two ways. First, compliant fibers could be used instead of rigid fibers in order to reduce the overall stiffness of the DECs while taking advantage of the dipolar interactions between the fibers. Second, particulate DECs consisting of rigid spheroidal inclusions could also be considered by making use of the purely mechanical effective energy of such composites obtained in a recent work by Avazmohammadi & Ponte Castañeda (2013). Such generalizations are beyond the scope of this work and will be pursued elsewhere. In addition, it should be recalled that dielectric breakdown must be considered in the design of microstructures for optimal performance (Bertoldi & Gei 2011, Siboni & Ponte Castañeda 2014). This will be left for future work, but based on the recent results of Siboni & Ponte Castañeda (2014) for mechanically unloaded dielectric elastomer composites, we anticipate that dielectric breakdown will also play an important role in curtailing the range of allowable electric fields for mechanical loaded systems, especially when large contrasts in the dielectric properties of the constituents are involved.

# Chapter 7

# Purely Mechanical Problem with Prescribed Rotation for the Inclusion Phase

In the previous two chapters we have studied the fiber-constrained DECs with aligned microstructures under aligned electromechanical loading conditions. For such cases we have argued that the torque applied on the dielectric inclusions is identically zero, and thus the effective total energy has been obtained by simply adding the purely mechanical and (deformation-dependent) electrostatic energies. This observation has significantly simplified the procedure for obtaining the effective electrostatic energy of aligned DECs.

For the more general non-aligned cases, it is well-known that the dielectric inclusions experience non-zero torques in the presence of electric fields (Landau et al. 1984, Siboni & Ponte Castañeda 2012). Such non-zero electrical torques may cause the inclusions to undergo extra rotations (in addition to the rotations caused by the mechanical deformations) in the presence of electric fields. When the relative strength of the electrostatic and elastic fields are comparable, so are the relative magnitude of the extra electrostatic rotations and the purely mechanical rotations. For this reason, the extra rotations caused by the electrostatic torques may not be ignored and one has to make use of the more general Partial Decoupling Strategy of section 3.2.

It is recalled that the PDS scheme of section 3.2 applies to DECs with particulate microstructures consisting of rigid inclusions firmly embedded in an ideal dielectric matrix. For this specific class of DECs we have shown in section 3.2 that the effective energy may be obtained by the following miminization problem

$$\tilde{W}\left(\bar{\boldsymbol{F}},\bar{\mathbf{D}}\right)=\min_{\bar{\boldsymbol{R}}^{(2)}}\left\{\tilde{W}_{me}\left(\bar{\boldsymbol{F}};\bar{\boldsymbol{R}}^{(2)}\right)+\tilde{W}_{el}\left(\bar{\boldsymbol{F}},\bar{\mathbf{D}};\bar{\boldsymbol{R}}^{(2)}\right)\right\}. \tag{7.1}$$

As it is evident from the above equation, obtaining the effective electro-elastic energy via the above minimization problem requires explicit expressions for the energies $\tilde{W}_{me}\left(\bar{\boldsymbol{F}};\bar{\boldsymbol{R}}^{(2)}\right)$ and $\tilde{W}_{el}\left(\bar{\boldsymbol{F}},\bar{\mathbf{D}};\bar{\boldsymbol{R}}^{(2)}\right)$. Recall that $\tilde{W}_{me}\left(\bar{\boldsymbol{F}};\bar{\boldsymbol{R}}^{(2)}\right)$ corresponds to the effective purely mechanical energy of a composite under the macroscopic mechanical load, denoted by $\bar{\boldsymbol{F}}$, and prescribed (average) rotations on the inclusion phase. Similarly, $\tilde{W}_{el}\left(\bar{\boldsymbol{F}},\bar{\mathbf{D}};\bar{\boldsymbol{R}}^{(2)}\right)$ corresponds to the effective electrostatic energy of the composite under the macroscopic electromechanical load, denoted by $\bar{\boldsymbol{F}}$ and $\bar{\mathbf{D}}$, and prescribed rotations for the inclusions.

In this chapter we provide a general procedure for obtaining the effective mechanical energy of two-phase composites consisting of one family of rigid inclusions in an elastomeric matrix, where the rotation of the inclusions is prescribed a priori. Then explicit expressions will be obtained for fiber-reinforced composites undergoing 2D deformations in the plane perpendicular to the long axes of the fibers. The results of this chapter can be thought of as the generalization of the second-order results of Lopez-Pamies & Ponte Castañeda (2006*a*), in which the fibers are freely evolving as a consequence of the macroscopic mechanical loading, characterized by $\bar{\boldsymbol{F}}$. The explicit expressions obtained in this chapter will be readily used in the following chapter to obtain the effective energy of fiber-constrained DECs under general non-aligned electromechanical loading conditions by using the above-described decoupling strategy. The rest of this chapter is organized as follows. In section 7.1 we describe the variational problem concerned with the effective purely mechanical energy $\tilde{W}_{me}\left(\bar{\boldsymbol{F}};\bar{\boldsymbol{R}}^{(2)}\right)$ and explain our solution procedure. In section 7.2 we introduce a new variational problem in which the phase energies are modified to account for constant per phase

eigen-stresses. We also establish a relationship between such eigen-stresses and the externally applied body couples. Section 7.3 is concerned with applying the second-order homogenization framework of Lopez-Pamies & Ponte Castañeda (2006*b*) to the new variational problem with eigen-stress. Finally, in section 7.4 we make use of the estimates obtained for the new variational problem, in order to obtain the corresponding estimates for composites with prescribed (average) rotations for the inclusions.

## 7.1 Problem formulation and solution procedure

As mentioned earlier in section 3.2 the effective mechanical energy of two-phase composites with specified (average) rotations for the rigid inclusions, denoted here by $\bar{\boldsymbol{R}}^{(2)}$, can be obtained via the following variational problem

$$\tilde{W}_{me}\left(\bar{\boldsymbol{F}};\bar{\boldsymbol{R}}^{(2)}\right)=\min_{\bar{\boldsymbol{F}}\in\mathcal{K}'\left(\bar{\boldsymbol{F}},\bar{\boldsymbol{R}}^{(2)}\right)}\left\langle W_{me}\left(\mathbf{X},\boldsymbol{F}\right)\right\rangle_0 \tag{7.2}$$

where $\langle\rangle_0$ denotes the volume average in the reference (undeformed) configuration and the local energy density in terms of phase energies is given by

$$W_{me}\left(\mathbf{X},\boldsymbol{F}\right)=\boldsymbol{\Theta}^{(1)}\left(\mathbf{X}\right)W_{me}^{(1)}\left(\boldsymbol{F}\right)+\boldsymbol{\Theta}^{(2)}\left(\mathbf{X}\right)W_{me}^{(2)}\left(\boldsymbol{F}\right). \tag{7.3}$$

In (7.2), $\mathcal{K}'\left(\bar{\boldsymbol{F}},\bar{\boldsymbol{R}}^{(2)}\right)$ denotes the set of admissible deformation maps, $\mathbf{x}\left(\mathbf{X}\right)$, that satisfy the affine displacement condition on the boundary of the specimen, i.e.,

$$\mathbf{x}=\bar{\boldsymbol{F}}\mathbf{X}\quad\text{for}\quad\mathbf{X}\in\partial\Omega_0, \tag{7.4}$$

and rigid body rotations in the inclusion phase, i.e.,

$$\boldsymbol{F}\left(\mathbf{X}\right)=\bar{\boldsymbol{R}}^{(2)}\quad\text{for}\quad\mathbf{X}\in\Omega_0^{(2)}. \tag{7.5}$$

Recall that in the standard variational problem for obtaining the effective energy

of two-phase composites, as given by

$$\tilde{W}_{me}\left(\bar{\boldsymbol{F}}\right) = \min_{\mathcal{K}(\bar{\boldsymbol{F}})} \left\langle W_{me}\left(\mathbf{X}, \boldsymbol{F}\right)\right\rangle_0, \tag{7.6}$$

the inclusions are allowed to evolve (or rotate in the rigid case) "freely", and their evolution is the consequence of the macroscopic deformation $\bar{\boldsymbol{F}}$ (e.g., see Lopez-Pamies & Ponte Castañeda 2006*b*, Lopez-Pamies & Ponte Castañeda 2006*a*, for the details of obtaining the evolution). Unlike the standard variational problem (7.6), where the inclusions are free to evolve, the rotation of the inclusions in (7.2) is set to a desired value, denoted here by $\bar{\boldsymbol{R}}^{(2)}$. Note that, in practice, the desired (average) rotation $\bar{\boldsymbol{R}}^{(2)}$ for the inclusion phase may be achieved by the application of external body couples (e.g., the electrostatic torques experienced by the dielectric inclusions in DECs when an electric field is present). In other words, there is a correspondence between the rotation $\bar{\boldsymbol{R}}^{(2)}$ and the torque applied on the inclusion phase.

Solving the variational problem (7.2) requires generating trial displacement fields that are in the admissible set $\mathcal{K}'\left(\bar{\boldsymbol{F}}, \bar{\boldsymbol{R}}^{(2)}\right)$. This proves to be a difficult task given the random nature of the microstructure in the problem at hand. For this reason we choose to obtain the solution of problem (7.2), indirectly, by solving a new variational problem. In particular, given the one-to-one correspondence between the rotation $\bar{\boldsymbol{R}}^{(2)}$ in (7.2) and the external body couples applied on the inclusion, we will consider a homogenization problem in which the affine displacement (7.4) is applied on the boundary of the specimen, while and external body couple is applied on the inclusions. It is emphasized that for this newly defined problem the trial deformation fields no longer need to satisfy the condition (7.5), but have to be compatible with rigid rotations in the inclusion phase. Furthermore, the effect of the external body couples applied on the inclusion phase will be accounted for by introducing a uniform eigen-stress for the inclusion phase[2]. The main advantage of using an

[2]The variational formulations of a continuum in the presence of an external body couple $\mathbf{c}^0\left(\mathbf{X}\right)$ can be written (e.g., see equation (29) in Merlini 1997) as

$$\int_{\Omega_0} \delta W_{me}\left(\boldsymbol{F}, \mathbf{X}\right) dV = \int_{\Omega_0} \operatorname{ax}\left[\delta \boldsymbol{F} \boldsymbol{F}^{-1}\right] \cdot \mathbf{c}^0\left(\mathbf{X}\right) dV, \quad \text{where} \quad \left(\operatorname{ax}[\boldsymbol{A}]\right)_k := -\frac{1}{2}\epsilon_{ijk} A_{ij}.$$

eigen-stress formulation (instead of directly using body couples) is that the resulting variational problem can be cast into a form exactly similar to the standard problem (7.6), but with appropriately modified phase energies. This will in turn enable us to conveniently apply the available "second-order" homogenization prescriptions (Lopez-Pamies & Ponte Castañeda 2006*b*, Lopez-Pamies & Ponte Castañeda 2006*a*), in order to obtain homogenization estimates for the problem at hand.

In the following we first introduce a new variational problem with modified energies for the phases to account for the effect of eigen-stresses. Using ideas from the theory of continuum mechanics, we then explain the connection between the eigen-stresses and body couples. Having established such connections we then proceed to the solutions of the new variational problem using the "second-order" framework of Lopez-Pamies & Ponte Castañeda (2006*b*). Finally, recalling that there exists a one-to-one correspondence between the body couples applied on the inclusion phase and the (average) rotation $\bar{\boldsymbol{R}}^{(2)}$, we obtain the solution of the original variational problem (7.2).

## 7.2 A variational problem with eigen-stress and the connection with body couples

In this section we define a new variational problem in terms of the modified phase energies. The modified energies are obtained by adding a linear term to the original energy in order to account for the effect of (external) eigen-stresses on each phase. This will be done for general $N$-phase composites, first, and then specializations to two-phase composites will be provided. For simplicity, we drop the subscript "me" for the purely mechanical energies in the rest of this section.

Thus, the new variational problem is defined as follows

$$\tilde{W}_*\left(\bar{\boldsymbol{F}}\right) = \min_{\boldsymbol{F}\in\mathcal{K}\left(\bar{\boldsymbol{F}}\right)} \left\langle W_*\left(\boldsymbol{F},\mathbf{X};\boldsymbol{M}\right)\right\rangle, \tag{7.7}$$

However, for convenience, in this work we make use of an eigen-strain formulation to account for the effects of external body couples.

where the modified energy $W_*$ is defined by

$$W_*\left(\boldsymbol{F},\mathbf{X};\boldsymbol{M}\right) \coloneqq W\left(\boldsymbol{F},\mathbf{X}\right)+\boldsymbol{M}\left(\mathbf{X}\right)\cdot\boldsymbol{F} \tag{7.8}$$

and $\boldsymbol{M}\left(\mathbf{X}\right)$ is a constant per phase tensor field (or eigen-stress), which can be related to the body couples. This can be easily shown by first noting that the Euler-Lagrange equations associated with (7.7) can be written as

$$\mathrm{Div}\boldsymbol{S}_* = 0 \quad \text{in} \quad \Omega_0, \quad \text{or} \quad \mathrm{div}\boldsymbol{T}_* = 0 \quad \text{in} \quad \Omega, \tag{7.9}$$

where

$$\boldsymbol{S}_* \coloneqq \partial W_*/\partial\boldsymbol{F} \quad \text{and} \quad \boldsymbol{T}_* \coloneqq J^{-1}\boldsymbol{S}_*\boldsymbol{F}^T, \tag{7.10}$$

are, respectively, the (first) Piola-Kirchhoff and Cauchy stresses associated with the modified energy (7.8). Next we make use of the integral form for the equilibrium of angular momentum for an arbitrary body part, as given by

$$\int_{\partial\mathcal{B}_0}\mathbf{x}\times\left(\boldsymbol{S}_*\mathbf{N}\right)dS = \int_{\mathcal{B}_0}\rho^0\mathbf{c}^0\left(\mathbf{X}\right)dV, \quad \text{and} \quad \int_{\partial\mathcal{B}}\mathbf{x}\times\left(\boldsymbol{T}_*\mathbf{n}\right)ds = \int_{\mathcal{B}}\rho\mathbf{c}\left(\mathbf{x}\right)dv, \tag{7.11}$$

in the reference and current configurations, respectively. Here, $\mathcal{B}_0$ denotes the arbitrary body part in the reference (undeformed) configuration with unit outward normal $\mathbf{N}$, while $\mathcal{B}$ denotes the corresponding body part in the current (deformed) configuration with unit outward normal $\mathbf{n}$. Using an appropriate form of the divergence theorem and the fact that the domain of integration in integrals of (7.11) is arbitrary, it follows that

$$\boldsymbol{S}_*\boldsymbol{F}^T - \boldsymbol{F}\boldsymbol{S}_*^T = \rho^0\boldsymbol{C}^0\left(\mathbf{X}\right), \quad \text{or} \quad \boldsymbol{T}_*^T - \boldsymbol{T}_* = \rho\boldsymbol{C}\left(\mathbf{x}\right) \tag{7.12}$$

where

$$C^0_{mn}\left(\mathbf{X}\right) \coloneqq -\varepsilon_{mni}c^0_i\left(\mathbf{X}\right) \quad \text{and} \quad C_{mn}\left(\mathbf{x}\right) \coloneqq -\varepsilon_{mni}c_i\left(\mathbf{x}\right), \tag{7.13}$$

are, respectively, anti-symmetric second-order tensors corresponding to the vector of

body couple in the reference configuration, $\mathbf{c}^0(\mathbf{X})$, and in the deformed configuration, $\mathbf{c}(\mathbf{x})$.

Now to see the connection between the eigen-stresses and body couples, we make the replacement

$$\boldsymbol{S}_* = \boldsymbol{S} + \boldsymbol{M}(\mathbf{X}) \quad \text{where} \quad \boldsymbol{S} := \frac{\partial W}{\partial \boldsymbol{F}}, \tag{7.14}$$

into $(7.12)_1$. Thus, the following relationship between the local eigen-stress $\boldsymbol{M}(\mathbf{X})$ and the local body couple $\boldsymbol{C}^0(\mathbf{X})$ is obtained, i.e.,

$$\boldsymbol{M}(\mathbf{X})\boldsymbol{F}^T - \boldsymbol{F}\boldsymbol{M}^T(\mathbf{X}) = \rho^0 \boldsymbol{C}^0(\mathbf{X}), \tag{7.15}$$

where we have used the objectivity of the potential $W(\boldsymbol{F}, \mathbf{X})$ to make the replacement $\boldsymbol{S}\boldsymbol{F}^T - \boldsymbol{F}\boldsymbol{S}^T = 0$. The corresponding Eulerian form of (7.15) can also be obtained as follows

$$\boldsymbol{m}(\mathbf{X}) - \boldsymbol{m}^T(\mathbf{X}) = \rho \boldsymbol{C}(\mathbf{x}), \quad \text{where} \quad \boldsymbol{m}(\mathbf{x}) := J^{-1}\boldsymbol{M}(\mathbf{x})\boldsymbol{F}^T, \tag{7.16}$$

such that

$$\boldsymbol{T}_* = \boldsymbol{T} + \boldsymbol{m}(\mathbf{x}). \tag{7.17}$$

In other words, the eigen-stress $\boldsymbol{M}(\mathbf{x})$, when written in the Eulerian form, corresponds to the anti-symmetric part of the the Cauchy stress and is equal to the body couple.

It is emphasized here that unlike $\boldsymbol{M}(\mathbf{X})$, which is taken to be uniform within each phase of the composite, the local body couple $\boldsymbol{C}^0(\mathbf{X})$ will not in general be uniform within each phase of the composite due to the potential dependence of the local deformation gradient $\boldsymbol{F}$ on $\mathbf{X}$. However, as will be seen later on, the homogenization estimates used in this work predict uniform deformation fields in the inclusion phase (i.e., $\boldsymbol{F}(\mathbf{X}) = \bar{\boldsymbol{F}}^{(2)}$ for $\mathbf{X} \in \Omega_0^{(2)}$), and for such cases the body couple corresponding to the uniform eigen-stress in the inclusion phase turns out to be uniform. Finally, note that in the variational problem (7.7) the admissible deformations need not satisfy the condition (7.5), but have to be compatible with rigid rotations of the inclusions.

## 7.3 Second-order estimates for the new variational problem

An estimate for the solution of the non-linear variational problem (7.7), can be obtained by using the "second-order" homogenization method (Lopez-Pamies & Ponte Castañeda 2006*b*, Lopez-Pamies & Ponte Castañeda 2006*a*). The basic idea behind the "second-order" method is to make use of an appropriately chosen linear comparison composite (LCC) with the same microstructure as the non-linear composite to obtain an estimate for the variational problem (7.7). Details of the "second-order" homogenization method can be found in Lopez-Pamies & Ponte Castañeda (2006*b*), Lopez-Pamies & Ponte Castañeda (2006*a*).

Given the fact that the form of the new variational problem (7.7) is exactly identical to the problem addressed in the aforementioned papers, estimates for (7.7) may be conveniently obtained by replacing $W(\boldsymbol{F},\mathbf{X})$ by the modified energy $W_*(\boldsymbol{F},\mathbf{X};\boldsymbol{M})$ in the appropriate expressions of Lopez-Pamies & Ponte Castañeda (2006*b*). Thus, as argued by Lopez-Pamies & Ponte Castañeda (2006*b*), the "principal" solution (before the onset of instabilities) associated with the variational problem (7.7) can be obtained via the stationary problem

$$\hat{W}_*\left(\bar{\boldsymbol{F}}\right) = \underset{\boldsymbol{F}\in\mathcal{K}\left(\bar{\boldsymbol{F}}\right)}{\text{stat}} \sum_{r=1}^{N} c_0^{(r)} \left\langle W_*^{(r)}\left(\boldsymbol{F};\boldsymbol{M}^{(r)}\right)\right\rangle^{(r)}, \tag{7.18}$$

where the constitutive properties of each phase are taken to be uniform and as usual $\mathcal{K}\left(\bar{\boldsymbol{F}}\right)$ denotes the set of admissible deformation gradients, satisfying the affine boundary condition on the boundary of the specimen. Following the prescriptions of Lopez-Pamies & Ponte Castañeda (2006*b*), an estimate for the principal solution is obtained as follows

$$\hat{W}_*\left(\bar{F}\right) \approx \underset{\mathbb{L}^{(s)}}{\text{stat}} \left\{ \hat{W}_{*T}\left(\bar{\boldsymbol{F}};\boldsymbol{F}^{(s)},\boldsymbol{M}^{(s)},\mathbb{L}^{(s)}\right) + \sum_{r=1}^{N} c_0^{(r)} V_*^{(r)}\left(\boldsymbol{F}^{(r)},\boldsymbol{M}^{(r)},\mathbb{L}^{(r)}\right)\right\}. \tag{7.19}$$

In the above equation $\hat{W}_{*T}$ is the homogenized energy of an LCC with the same

microstructure as the non-linear composite but with the following linear local energy

$$W_{*T}(\boldsymbol{F},\mathbf{X};\boldsymbol{M}) = \sum_{r=1}^{N} \Theta^{(r)}(\mathbf{X})\, W_{*T}^{(r)}\left(\boldsymbol{F};\boldsymbol{M}^{(r)}\right), \tag{7.20}$$

where the phase energies are given by

$$\begin{aligned} W_{*T}^{(r)}(\boldsymbol{F}) &:= W_{*T}^{(r)}\left(\boldsymbol{F}^{(r)}\right) + \mathcal{L}_{*}^{(r)}\left(\boldsymbol{F}^{(r)}\right)\cdot\left(\boldsymbol{F}-\boldsymbol{F}^{(r)}\right) \\ &\quad + \frac{1}{2}\left(\boldsymbol{F}-\boldsymbol{F}^{(r)}\right)\cdot\mathbb{L}^{(r)}\left(\boldsymbol{F}-\boldsymbol{F}^{(r)}\right), \text{ where } \mathcal{L}_{*}^{(r)}(\boldsymbol{F}) := \frac{\partial}{\partial \boldsymbol{F}} W_{*}^{(r)}(\boldsymbol{F}). \end{aligned} \tag{7.21}$$

In the above expressions for the phase energies, $\boldsymbol{F}^{(r)}$ and $\mathbb{L}^{(r)}$ are, respectively, reference deformation gradients and moduli tensors for each phase that will be determined from the analysis that follows. Note that the linear phase energies $W_{*T}^{(r)}$, defined in (7.21), correspond to fictitious linear thermoelastic materials with constitutive response of the form

$$\boldsymbol{S}_{*} = \mathcal{L}_{*}^{(r)}\left(\boldsymbol{F}^{(r)}\right) + \mathbb{L}^{(r)}\left(\boldsymbol{F}-\boldsymbol{F}^{(r)}\right). \tag{7.22}$$

The corrector functions $V_{*}^{(r)}$ on the right side of (7.19) account for the non-linearity of the phase energies, and they are defined by

$$V_{*}^{(r)}\left(\boldsymbol{F}^{(r)},\boldsymbol{M}^{(r)},\mathbb{L}^{(r)}\right) := \underset{\hat{F}^{(r)}}{\operatorname{stat}}\left\{W_{*}^{(r)}\left(\hat{F}^{(r)}\right) - W_{*T}^{(r)}\left(\hat{F}^{(r)}\right)\right\}. \tag{7.23}$$

Estimates for the effective energy of general $N$ phase linear thermoelastic composites may be obtained by using the work of Ponte Castañeda & Tiberio (2000). As will be seen later on, in this work we are interested in two-phase particulate composites, and for this special class such estimates for the LCC can be easily obtained by appropriate generalizations of Levin (1967) relations. Such generalizations along with other necessary calculations pertaining two-phase linear thermoelastic composites are provided in Appendix F.

Next, using the stationary conditions associated with (7.19) and (7.23), the effective energy of the non-linear composites with local energies of the form $W_{*}(\boldsymbol{F},\mathbf{X};\boldsymbol{M})$

is obtained as follows

$$\hat{W}_*\left(\bar{\boldsymbol{F}}\right) = \sum_{r=1}^{N} c_0^{(r)} \left\{ W_*^{(r)}\left(\hat{\boldsymbol{F}}^{(r)}\right) + \mathcal{L}_*^{(r)}\left(\boldsymbol{F}^{(r)}\right) \cdot \left(\bar{\boldsymbol{F}}^{(r)} - \hat{\boldsymbol{F}}^{(r)}\right) \right\}. \tag{7.24}$$

The stationary conditions associated with equations (7.19) and (7.23) read, respectively, as follows

$$\frac{\partial \hat{W}_{*T}}{\partial \mathbb{L}^{(r)}} + c_0^{(r)} \frac{\partial V_*^{(r)}}{\partial \mathbb{L}^{(r)}} = 0. \tag{7.25}$$

$$\mathcal{L}_*^{(r)}\left(\hat{\boldsymbol{F}}^{(r)}\right) - \mathcal{L}_*^{(r)}\left(\boldsymbol{F}^{(r)}\right) = \mathbb{L}^{(r)}\left(\hat{\boldsymbol{F}}^{(r)} - \boldsymbol{F}^{(r)}\right), \tag{7.26}$$

The condition (7.25) can be further simplified to obtain

$$\boldsymbol{C}_{\boldsymbol{F}}^{(r)} = \left(\hat{\boldsymbol{F}}^{(r)} - \boldsymbol{F}^{(r)}\right) \otimes \left(\hat{\boldsymbol{F}}^{(r)} - \boldsymbol{F}^{(r)}\right) - \left(\bar{\boldsymbol{F}}^{(r)} - \boldsymbol{F}^{(r)}\right) \otimes \left(\bar{\boldsymbol{F}}^{(r)} - \boldsymbol{F}^{(r)}\right) \tag{7.27}$$

where $\boldsymbol{C}_{\boldsymbol{F}}^{(r)} := \left\langle \left(\boldsymbol{F} - \bar{\boldsymbol{F}}^{(r)}\right) \otimes \left(\boldsymbol{F} - \bar{\boldsymbol{F}}^{(r)}\right) \right\rangle^{(r)}$ is the fluctuation of the deformation gradient in phase $r$.

### 7.3.1 Specialization to two-phase particulate composites consisting of compliant phases

In this section we specialize the general results, obtained in previous subsections, for the case of two-phase particulate composites with random microstructures, as described in section 3.2. Thus, assuming that $\boldsymbol{M}(\mathbf{X})$ is identically zero in the matrix phase, i.e.,

$$\boldsymbol{M}(\mathbf{X}) = \begin{cases} \mathbf{0} & \text{for } \mathbf{X} \in \Omega_0^{(1)} \\ \boldsymbol{M}^{(2)} & \text{for } \mathbf{X} \in \Omega_0^{(2)} \end{cases}, \tag{7.28}$$

the local energy (7.8) for the special case of two-phase particulate composites reduces to

$$W_*\left(\boldsymbol{F}, \mathbf{X}; \boldsymbol{M}^{(2)}\right) = \Theta^{(1)}(\mathbf{X})\, W^{(1)}(\boldsymbol{F}) + \Theta^{(2)}(\mathbf{X})\, W^{(2)}(\boldsymbol{F}) + \Theta^{(2)}(\mathbf{X}) \left(\boldsymbol{M}^{(2)} \cdot \boldsymbol{F}\right). \tag{7.29}$$

Substituting the local energy (7.29) into (7.24), the effective non-linear energy of two-phase composites is obtained as follows

$$\begin{aligned}\hat{W}_* = (1-c_0)\left\{W^{(1)}\left(\hat{\boldsymbol{F}}^{(1)}\right) + \mathcal{L}^{(1)}\left(\boldsymbol{F}^{(1)}\right)\cdot\left(\bar{\boldsymbol{F}}^{(1)} - \hat{\boldsymbol{F}}^{(1)}\right)\right\} \\ + c_0\left\{W^{(2)}\left(\hat{\boldsymbol{F}}^{(2)}\right) + \mathcal{L}^{(2)}\left(\boldsymbol{F}^{(2)}\right)\cdot\left(\bar{\boldsymbol{F}}^{(2)} - \hat{\boldsymbol{F}}^{(2)}\right) + \boldsymbol{M}^{(2)}\cdot\bar{\boldsymbol{F}}^{(2)}\right\},\end{aligned} \tag{7.30}$$

where

$$\mathcal{L}^{(r)}\left(\boldsymbol{F}^{(r)}\right) := \frac{\partial W^{(r)}}{\partial \boldsymbol{F}}\left(\boldsymbol{F}^{(r)}\right) \quad \text{for} \quad r = 1, 2. \tag{7.31}$$

Next we provide prescriptions for the calculation of the unknowns $\bar{\boldsymbol{F}}^{(1)}$, $\bar{\boldsymbol{F}}^{(2)}$, $\hat{\boldsymbol{F}}^{(1)}$, and $\hat{\boldsymbol{F}}^{(2)}$. To this end we note that for two phase composites the average of the deformation gradient over phase one, $\bar{\boldsymbol{F}}^{(1)}$, in terms of $\bar{\boldsymbol{F}}^{(2)}$ can be obtained as follows

$$\bar{\boldsymbol{F}}^{(1)} = \frac{1}{1-c_0}\left(\bar{\boldsymbol{F}} - c_0\bar{\boldsymbol{F}}^{(2)}\right). \tag{7.32}$$

The average $\bar{\boldsymbol{F}}^{(2)}$ for the special case of two-phase particulate composites may be obtained by substituting

$$\boldsymbol{T}^{(1)} := \mathcal{L}^{(1)}\left(\boldsymbol{F}^{(1)}\right) - \mathbb{L}^{(1)}\boldsymbol{F}^{(1)} \quad \text{and} \quad \boldsymbol{T}^{(2)} := \mathcal{L}^{(2)}\left(\boldsymbol{F}^{(2)}\right) - \mathbb{L}^{(2)}\boldsymbol{F}^{(2)} + \boldsymbol{M}^{(2)} \tag{7.33}$$

in expression (F.15) of Appendix F. Thus, we get

$$\bar{\boldsymbol{F}} - \bar{\boldsymbol{F}}^{(2)} = (1-c_0)\,\mathbb{P}\left[\mathbb{L}^{(1)}\left(\boldsymbol{F}^{(1)} - \bar{\boldsymbol{F}}^{(2)}\right) + \boldsymbol{M}^{(2)} - \mathcal{L}^{(1)}\left(\boldsymbol{F}^{(1)}\right) + \mathcal{L}^{(2)}\left(\boldsymbol{F}^{(2)}\right)\right], \tag{7.34}$$

where the microstructural tensor $\mathbb{P}$ is defined in Appendix F, and encodes information about the details of the microstructure. In obtaining this last expression we have used the fact that the fluctuation of the deformation gradient in the inclusion phase is identically zero (i.e., $\boldsymbol{C}_{\boldsymbol{F}}^{(2)} = 0$), because of the Hashin-Shtrikman type estimates used in the computation of the effective energy for linear two-phase thermoelastic composites (see Appendix F for more details).

To obtain the unknowns $\hat{\boldsymbol{F}}^{(1)}$ and $\hat{\boldsymbol{F}}^{(2)}$, we make use of the stationary conditions (7.25) and (7.26). First, we note that $\boldsymbol{C}_{\boldsymbol{F}}^{(2)} = 0$, and therefore the stationary condition

(7.27) for phase two implies

$$\hat{\boldsymbol{F}}^{(2)} = \bar{\boldsymbol{F}}^{(2)}. \tag{7.35}$$

Using (7.35), the stationary condition (7.26) for $r = 2$, can be shown to lead to an equation to the effect that the modulus $\mathbb{L}^{(2)}$ of phase two in the LCC is given by the tangent modulus of nonlinear phase two, evaluated at $\boldsymbol{F}^{(2)}$. On the other hand, for $r = 1$ it reduces to

$$\mathcal{L}^{(1)}\left(\hat{\boldsymbol{F}}^{(1)}\right) - \mathcal{L}^{(1)}\left(\boldsymbol{F}^{(1)}\right) = \mathbb{L}^{(1)}\left(\hat{\boldsymbol{F}}^{(1)} - \boldsymbol{F}^{(1)}\right). \tag{7.36}$$

Finally, the stationary condition (7.25) for phase one of the composite can be further simplified by using the prescriptions of Lopez-Pamies & Ponte Castañeda (2006*b*) for the modulus tensor $\mathbb{L}^{(1)}$. Thus, the the modulus tensor $\mathbb{L}^{(1)}$ will be taken to have the following form

$$L^{(1)}_{ijkl} = Q^{(1)}_{rm} Q^{(1)}_{jn} Q^{(1)}_{sp} Q^{(1)}_{lq} R^{(1)}_{ir} R^{(1)}_{ks} L^{*}_{mnpq}, \tag{7.37}$$

where it is assumed that $\mathbb{L}^{*}$ has only nine independent components, denoted here by $l_\alpha$ ($\alpha = 1, 2, \cdots, 9$). Then the stationary condition (7.25) for $r = 1$ reduces to

$$\left(\hat{\boldsymbol{F}}^{(1)} - \boldsymbol{F}^{(1)}\right) \cdot \frac{\partial \mathbb{L}^{(1)}}{\partial l_\alpha}\left(\hat{\boldsymbol{F}}^{(1)} - \boldsymbol{F}^{(1)}\right) = \frac{2}{1 - c_0} \left.\frac{\partial \hat{W}_{*T}}{\partial l_\alpha}\right|_{\boldsymbol{F}^{(1)}}. \tag{7.38}$$

The right side of the above equation can be computed (see Lopez-Pamies & Ponte Castañeda 2006*b*, for more details) as follows

$$\begin{aligned}
\left.\frac{2}{1 - c_0} \frac{\partial \hat{W}_{*T}}{\partial l_\alpha}\right|_{\boldsymbol{F}^{(1)}} &= \frac{1}{1 - c_0}\left(\boldsymbol{F}^{(1)} - \bar{\boldsymbol{F}}\right) \cdot \frac{\partial \mathbb{L}^{(1)}}{\partial l_\alpha}\left(\boldsymbol{F}^{(1)} - \bar{\boldsymbol{F}}\right) \\
&\quad - \frac{c_0}{1 - c_0}\left(\boldsymbol{F}^{(1)} - \bar{\boldsymbol{F}}^{(2)}\right) \cdot \frac{\partial \mathbb{L}^{(1)}}{\partial l_\alpha}\left(\boldsymbol{F}^{(1)} - \bar{\boldsymbol{F}}^{(2)}\right) \\
&\quad - \frac{c_0}{(1 - c_0)^2}\left(\bar{\boldsymbol{F}} - \bar{\boldsymbol{F}}^{(2)}\right) \cdot \left[\mathbb{P}^{-1} \frac{\partial \mathbb{P}}{\partial l_\alpha} \mathbb{P}^{-1}\right]\left(\bar{\boldsymbol{F}} - \bar{\boldsymbol{F}}^{(2)}\right)
\end{aligned} \tag{7.39}$$

In summary, for a given $\boldsymbol{M}^{(2)}$, equations (7.34), (7.36), and (7.38) can be solved to obtain the components of $\hat{\boldsymbol{F}}^{(1)}$ and $\bar{\boldsymbol{F}}^{(2)}$, and the moduli $l_\alpha$ ($\alpha = 1, 2, \cdots, 9$).

In the analysis that follow the reference deformation gradients $\boldsymbol{F}^{(1)}$ and $\boldsymbol{F}^{(2)}$ are

taken to be equal to $\bar{\boldsymbol{F}}$ and $\bar{\boldsymbol{F}}^{(2)}$, respectively.

### 7.3.2 Specialization to two-phase particulate composites consisting of rigid inclusions

The above general results for two-phase particulate composites with compliant phases can be easily specialized for the case of composites with rigid inclusions, Thus, for two-phase composites reinforced by a rigid inclusion phase, the effective energy (7.30), reduces to

$$\hat{W}_* = (1-c_0)\left\{W^{(1)}\left(\hat{\boldsymbol{F}}^{(1)}\right) + \mathcal{L}^{(1)}\left(\bar{\boldsymbol{F}}\right)\cdot\left(\bar{\boldsymbol{F}}^{(1)} - \hat{\boldsymbol{F}}^{(1)}\right)\right\} + c_0\boldsymbol{M}^{(2)}\cdot\bar{\boldsymbol{R}}^{(2)}, \tag{7.40}$$

where we used the fact that $\hat{\boldsymbol{F}}^{(2)} = \bar{\boldsymbol{F}}^{(2)} = \bar{\boldsymbol{R}}^{(2)}$ for the rigid phase. The evolution equation (7.34) for the average particle rotations can also be further simplified (Lopez-Pamies & Ponte Castañeda 2006*b*, Lopez-Pamies & Ponte Castañeda 2006*a*) as follows

$$\begin{aligned}
&(1-c_0)\left[\left(\bar{\boldsymbol{R}}^{(2)}\right)^T\boldsymbol{M}^{(2)} - \left(\boldsymbol{M}^{(2)}\right)^T\bar{\boldsymbol{R}}^{(2)}\right] = \cdots\\
&+\left(\bar{\boldsymbol{R}}^{(2)}\right)^T\left[\left(\mathbb{Q}-(1-c_0)\,\mathbb{L}^{(1)}\right)\left(\bar{\boldsymbol{F}}-\bar{\boldsymbol{R}}^{(2)}\right)\right] - \left[\left(\mathbb{Q}-(1-c_0)\,\mathbb{L}^{(1)}\right)\left(\bar{\boldsymbol{F}}-\bar{\boldsymbol{R}}^{(2)}\right)\right]^T\left(\bar{\boldsymbol{R}}^{(2)}\right)\\
&+(1-c_0)\left[\left(\bar{\boldsymbol{R}}^{(2)}\right)^T\mathcal{L}^{(1)}\left(\bar{\boldsymbol{F}}\right) - \left(\mathcal{L}^{(1)}\left(\bar{\boldsymbol{F}}\right)\right)^T\bar{\boldsymbol{R}}^{(2)}\right],
\end{aligned} \tag{7.41}$$

where $\mathbb{Q} := \mathbb{P}^{-1}$. In obtaining the above identity we have used the fact that (see Lopez-Pamies & Ponte Castañeda 2006*b*, for more details)

$$\left[\left(\bar{\boldsymbol{R}}^{(2)}\right)^T\mathcal{L}^{(2)}\left(\bar{\boldsymbol{F}}^{(2)}\right) - \left(\mathcal{L}^{(2)}\left(\bar{\boldsymbol{F}}^{(2)}\right)\right)^T\bar{\boldsymbol{R}}^{(2)}\right] = 0, \tag{7.42}$$

when the particles become rigid.

### 7.3.3 Specialization to fiber-reinforced composites undergoing 2D plane-strain deformations

When the composite is constrained to undergo 2D plane-strain deformations the above general results can be further simplified. Thus, assuming that the deformation of the

composite is constrained to remain in the $X_1$-$X_2$ plane of the laboratory axes, it can be argued (see Lopez-Pamies & Ponte Castañeda 2006*a*, for more details) that only six in-plane components of $\mathbb{L}^*$ enter the calculations, namely, $L^*_{1111} := l_1$, $L^*_{2222} := l_2$, $L^*_{1212} = L^*_{2121} := l_3$, $L^*_{1122} := l_4$, and $L^*_{1221} := \sqrt{(l_1 - l_3)(l_2 - l_3)} - l_4$. We emphasize that as pointed out by (Lopez-Pamies & Ponte Castañeda 2006*a*) the above choices for the six independent components of $\mathbb{L}^*$ are not unique. Next, given an underlying coordinate system (e.g., the laboratory axes $\{X_1, X_2, X_3\}$) the macroscopic 2D plane-strain deformation of the composite in the $X_1$-$X_2$ plane can be represented as follows

$$\big[\bar{\boldsymbol{F}}\big] = \big[\bar{\boldsymbol{R}}\big]\big[\bar{\boldsymbol{U}}\big] \quad \text{and} \quad \big[\bar{\boldsymbol{U}}\big] = \big[\bar{\boldsymbol{Q}}\big]\big[\bar{\boldsymbol{\Lambda}}\big]\big[\bar{\boldsymbol{Q}}\big]^T, \tag{7.43}$$

where

$$\big[\bar{\boldsymbol{R}}\big] = \begin{bmatrix} \cos\bar{\psi} & -\sin\bar{\psi} \\ \sin\bar{\psi} & \cos\bar{\psi} \end{bmatrix}, \quad \big[\bar{\boldsymbol{Q}}\big] = \begin{bmatrix} \cos\bar{\theta} & -\sin\bar{\theta} \\ \sin\bar{\theta} & \cos\bar{\theta} \end{bmatrix}, \quad \text{and} \quad \big[\bar{\boldsymbol{\Lambda}}\big] = \begin{bmatrix} \bar{\lambda}_1 & 0 \\ 0 & \bar{\lambda}_2 \end{bmatrix}. \tag{7.44}$$

Here the angle $\bar{\psi}$ denotes the macroscopic in-plane rotation of the sample, $\bar{\theta}$ denotes the in-plane loading angle, and $\bar{\lambda}_1$ and $\bar{\lambda}_2$ denote the principal in-plane stretches. In the case of rigid inclusions $\bar{\boldsymbol{F}}^{(2)} = \bar{\boldsymbol{R}}^{(2)}$ takes the following form in the underlying coordinate system

$$\big[\bar{\boldsymbol{R}}^{(2)}\big] = \begin{bmatrix} \cos\bar{\psi}^{(2)} & -\sin\bar{\psi}^{(2)} \\ \sin\bar{\psi}^{(2)} & \cos\bar{\psi}^{(2)} \end{bmatrix}, \tag{7.45}$$

where $\bar{\psi}^{(2)}$ denotes the average in-plane (equilibrium) rotation of the inclusions.

With the above choices for the components of $\mathbb{L}^*$ and the following definition for the second-order tensor $\boldsymbol{Y}$

$$\boldsymbol{Y} := \bar{\boldsymbol{Q}}^T \bar{\boldsymbol{R}}^T \big(\hat{\boldsymbol{F}}^{(1)} - \bar{\boldsymbol{F}}\big)\bar{\boldsymbol{Q}} \tag{7.46}$$

the fluctuation equation (7.39) for the special case of 2D plane-strain deformations

can be re-written as follows

$$\begin{aligned} Y_{11}^2 + 2f_1 Y_{12} Y_{21} &= \frac{2}{1-c_0}\frac{\partial \hat{W}_{*T}}{\partial l_1^*} := k_1 \\ Y_{22}^2 + 2f_2 Y_{12} Y_{21} &= \frac{2}{1-c_0}\frac{\partial \hat{W}_{*T}}{\partial l_2^*} := k_2 \\ Y_{11}^2 + Y_{22}^2 + 2f_3 Y_{12} Y_{21} &= \frac{2}{1-c_0}\frac{\partial \hat{W}_{*T}}{\partial l_3^*} := k_3 \\ 2Y_{11}Y_{22} - 2Y_{12}Y_{21} &= \frac{2}{1-c_0}\frac{\partial \hat{W}_{*T}}{\partial l_4^*} := k_4, \end{aligned} \tag{7.47}$$

where the following definitions have been used

$$f_1 := \frac{\partial L_{1221}^*}{\partial l_1^*}, \quad f_2 := \frac{\partial L_{1221}^*}{\partial l_2^*}, \quad \text{and} \quad f_3 := \frac{\partial L_{1221}^*}{\partial l_3^*}. \tag{7.48}$$

Equations (7.47) can be solved for $Y_{11}$ and $Y_{22}$ as follows

$$Y_{11} = \pm\frac{f_1 k_4 + k_1}{\sqrt{4f_1^2 k_2 + 2f_1 k_4 + k_1}} \quad \text{and} \quad Y_{22} = \pm\frac{2f_1 k_2 + k_4/2}{\sqrt{4f_1^2 k_2 + 2f_1 k_4 + k_1}}. \tag{7.49}$$

Note that the combinations $Y_{12}Y_{21}$ and $Y_{12}^2 + Y_{21}^2$ can then be uniquely determined in terms of $Y_{11}$ and $Y_{22}$. Next, each of the two solutions in (7.49) can be used to obtain $\hat{\boldsymbol{F}}^{(1)} = \bar{\boldsymbol{F}} + \bar{\boldsymbol{R}}\bar{\boldsymbol{Q}}\boldsymbol{Y}\bar{\boldsymbol{Q}}^T$, which in turn can be substituted into the stationary condition (7.26) to obtain four non-linear equations for the five unknowns of the problem, namely $l_1$, $l_2$, $l_3$, $l_4$, and $\bar{\psi}^{(2)}$. These four equations along with equation (7.41) for the evolution of the microstructure form a closed system of five non-linear equations which can be solved for the five unknowns, mentioned earlier.

The above expression can be significantly simplified for the limit when the matrix phase becomes incompressible. For such limits we can make use of the asymptotic analysis of Lopez-Pamies & Ponte Castañeda (2006*a*) to obtain an analytical expression for the effective energy $\hat{W}_*$ in the incompressibility limit. Thus, after performing the asymptotic analysis (refer to Appendix G for more details), we obtain the follow-

ing estimate for the effective energy

$$\hat{W}_*\left(\bar{\boldsymbol{F}}\right) = \hat{W}_*\left(\bar{\lambda}_1, \bar{\theta}; \boldsymbol{M}^{(2)}\right) = (1-c_0)\, g^{(1)}\left(\hat{I}^{(1)}\right) + c_0\left(M_{11}^{(2)} + M_{22}^{(2)}\right)\cos\varphi_0 - c_0\left(M_{12}^{(2)} - M_{21}^{(2)}\right)\sin\varphi_0, \tag{7.50}$$

where

$$\hat{I}^{(1)} = \frac{c_0\left(1+\bar{\lambda}_1^2\right)^2 + \left[1 + 2\left(c_0-2\right)c_0\bar{\lambda}_1^2 + \bar{\lambda}_1^4\right]w + c_0\left(1+\bar{\lambda}_1^2\right)w^2}{\left(1-c_0\right)^2\bar{\lambda}_1^2 w} - \frac{c_0\left(\bar{\lambda}_1^4-1\right)\left(w^2-1\right)}{\left(1-c_0\right)^2\bar{\lambda}_1^2 w}\sin\left(\varphi_0\right)\sin\left(\varphi_0 - 2\bar{\theta}\right) - \frac{2c_0\left(1+\bar{\lambda}_1^2\right)\left(1+w^2\right)}{\left(1-c_0\right)^2\bar{\lambda}_1 w}\cos\left(\varphi_0\right). \tag{7.51}$$

In the above expressions $\varphi_0 = \bar{\psi}^{(2)} - \bar{\psi}$ denotes the relative rotation of the fibers with respect to the macroscopic rotation and satisfies the identity

$$\bar{\boldsymbol{\tau}}_{12} = \frac{\hat{g}'\left(1+\bar{\lambda}_1^2\right)}{w\bar{\lambda}_1^2\left(1-c_0\right)}\left[2\bar{\lambda}_1\left(1+w^2\right)\sin\varphi_0 - \left(\bar{\lambda}_1^2-1\right)\left(w^2-1\right)\sin\left(2\varphi_0 - 2\bar{\theta}\right)\right], \tag{7.52}$$

where the definition

$$\bar{\boldsymbol{\tau}}_{12} := \left(M_{12}^{(2)} - M_{21}^{(2)}\right)\cos\varphi_0 + \left(M_{11}^{(2)} + M_{22}^{(2)}\right)\sin\varphi_0 \tag{7.53}$$

has been used for conciseness.

## 7.4 Estimates for the effective purely mechanical energy for given rotation of the fibers

Thus far, we have obtained an explicit estimate for the effective energy of two-phase composites with rigid fibers and modified phase energies of the form (7.8). The results for incompressible composites undergoing 2D deformations in the plane perpendicular to the long axes of the fibers are summarized in expression (7.50) for the effective energy $\hat{W}_*\left(\bar{\boldsymbol{F}}; \boldsymbol{M}^{(2)}\right)$ and expression (7.52) for the evolution of the microstructure. In this section we make use of the above result in order to obtain an estimate for

the effective energy of fiber-reinforced composites when a macroscopic deformation is specified on the boundary and (average) in-plane rotations are prescribed for the fibers.

Thus, we note that the effective energy $\hat{W}_*\left(\bar{\boldsymbol{F}}\right)$ obtained in the previous section can be interpreted as the (total) potential energy, that is the strain energy stored in the matrix phase with potential $W\left(\boldsymbol{F}\right)$ under the combined actions of the macroscopic deformation $\bar{\boldsymbol{F}}$ and eigen-stress $\boldsymbol{M}^{(2)}$, plus the work done by the eigen-stress $\boldsymbol{M}^{(2)}$. To see this more clearly, let us denote the minimizer of the variational problem (7.7), by $\boldsymbol{F}^*$, such that

$$\boldsymbol{F}^*\left(\mathbf{X}\right) = \boldsymbol{F}\left(\mathbf{X}\right) \text{ for } \mathbf{X} \in \Omega_0^{(1)} \quad \text{and} \quad \boldsymbol{F}^*\left(\mathbf{X}\right) = \bar{\boldsymbol{R}}^{(2)} \text{ for } \mathbf{X} \in \Omega_0^{(2)} \tag{7.54}$$

where

$$\left[\bar{\boldsymbol{R}}^{(2)}\right] := \begin{bmatrix} \cos\bar{\psi}^{(2)} & -\sin\bar{\psi}^{(2)} \\ \sin\bar{\psi}^{(2)} & \cos\bar{\psi}^{(2)} \end{bmatrix}. \tag{7.55}$$

Substituting $\boldsymbol{F}^*\left(\mathbf{X}\right)$, given above, into the right side of equation (7.7) and simplifying the resulting expression, we obtain

$$\hat{W}_*\left(\bar{\boldsymbol{F}}\right) = \left\langle W\left(\boldsymbol{F}^*, \mathbf{X}\right)\right\rangle_0 + c_0 \boldsymbol{M}^{(2)} \cdot \bar{\boldsymbol{R}}^{(2)}. \tag{7.56}$$

Note that the first term on the right side of (7.56) corresponds to the (effective) energy stored in the composite when macroscopic deformation is applied on the boundary and (average) rotations $\bar{\boldsymbol{R}}^{(2)}$ are specified for the fibers, i.e.,

$$\left\langle W\left(\boldsymbol{F}^*, \mathbf{X}\right)\right\rangle_0 = \hat{W}\left(\bar{\boldsymbol{F}}; \bar{\boldsymbol{R}}^{(2)}\right). \tag{7.57}$$

Furthermore, and as mentioned earlier, the second term on the right side of (7.56) corresponds to the work done by the eigen-stress $\boldsymbol{M}^{(2)}$. Therefore, to obtain an expression for $\hat{W}\left(\bar{\boldsymbol{F}}; \bar{\boldsymbol{R}}^{(2)}\right)$ we can simply solve (7.56), i.e.,

$$\hat{W}\left(\bar{\boldsymbol{F}}; \bar{\boldsymbol{R}}^{(2)}\right) = \hat{W}_*\left(\bar{\boldsymbol{F}}\right) - c_0 \boldsymbol{M}^{(2)} \cdot \bar{\boldsymbol{R}}^{(2)} = \left(1 - c_0\right) g^{(1)}\left(\hat{I}^{(1)}\right), \tag{7.58}$$

where $\hat{I}^{(1)}$ is given by (7.51). It is important to emphasize that the final expression for $\hat{W}\left(\bar{\boldsymbol{F}};\bar{\boldsymbol{R}}^{(2)}\right)$, obtained above, is exactly identical to the corresponding expression in Lopez-Pamies & Ponte Castañeda (2006*a*), except that now the relative in-plane rotation of the fibers is prescribed, and therefore need not satisfy the evolution equation (30) in Lopez-Pamies & Ponte Castañeda (2006*a*).

## 7.5 Concluding remarks

In this chapter we have provided a general homogenization framework for the effective (purely mechanical) response of particulate composites with prescribed rotations (or equivalently body couples) for the inclusions phase. The newly developed homogenization framework takes advantage of a uniform eigen-stress on the inclusion phase to account for the effects of external body couples, and results in a new variational problem with modified phase energies. Using the fact that the form of the new variational problem is exactly identical to the standard problem addressed in Lopez-Pamies & Ponte Castañeda (2006*b*), we were able to obtain homogenization estimates for the new variational problem by replacing the standard phase energies with the modified phases energies in appropriate expressions of Lopez-Pamies & Ponte Castañeda (2006*b*).

Next, we have provided explicit expressions for the effective energy and microstructure evolution of elastomers reinforced by very long rigid fibers under 2D plane-strain deformations when a uniform eigen-stress is prescribed on the fibers. Thus the effective energy of such composites under macroscopic mechanical deformations and prescribed eigen-stress on the fiber phase is obtained by expression (7.50), while the in-plane rotation of the fibers is obtained by expression (7.52). Note that in the absence of external eigen-stresses (i.e., when the fibers are free to rotate), the above-mentioned expression reduce to the corresponding expressions in Lopez-Pamies & Ponte Castañeda (2006*a*), as expected.

Finally, we have obtained explicit expressions for the effective energy of fiber-constrained composites with prescribed in-plane rotation for the fibers, as given by

(7.58). The effective energy (7.58) is seen to be exactly identical to the corresponding result in Lopez-Pamies & Ponte Castañeda (2006*a*) (cf. equation (27) in that reference), with the only difference that the rotation of the fibers need not satisfy the evolution equation. This special property is not in general expected to be the consequence of the "second-order" homogenization procedure or an exclusive feature of fiber-constrained composites undergoing 2D plane-strain deformations, and may as well hold for more general cases. Whether this special property continues to hold for more general cases remains to be proven more formally in future works. However, it is worthwhile to mention that by using this special property we can conveniently obtain homogenization estimates for composites with prescribed evolution for the microstructure, given that the corresponding estimates are available when the microstructure of the composite is freely evolving as a result of the macroscopic loading.

# Chapter 8

# Fiber-constrained DECs: Finite Deformation Response and Instabilities Under Non-aligned Loading Conditions

In this chapter we obtain the effective electromechanical response of fiber-constrained DECs under general non-aligned loading conditions. For such cases the average in-plane rotations of the fibers are no longer zero. Recall that the fibers may undergo in-plane rotations as a consequence of non-aligned mechanical or electrostatic loads. Obtaining the effective response of DECs under general non-aligned conditions requires the use of the Partial Decoupling Strategy (PDS) of section 3.2, as given by equations (3.51). In the context of fiber-constrained DECs of chapters 5 and 6, the partial decoupling strategy may simply be rewritten as follows

$$\tilde{W}\left(\bar{\boldsymbol{F}}, \bar{\mathbf{D}}\right) = \min_{\bar{\psi}^{(2)}} \left\{ \tilde{W}_{me}\left(\bar{\boldsymbol{F}}; \bar{\psi}^{(2)}\right) + \tilde{W}_{el}\left(\bar{\mathbf{D}}, \bar{\boldsymbol{F}}; \bar{\psi}^{(2)}\right) \right\}, \tag{8.1}$$

where $\tilde{W}_{me}\left(\bar{\boldsymbol{F}}; \bar{\psi}^{(2)}\right)$ and $\tilde{W}_{el}\left(\bar{\mathbf{D}}, \bar{\boldsymbol{F}}; \bar{\psi}^{(2)}\right)$ are, respectively, the purely mechanical and electrostatic effective energies for a given (in-plane) rotation of the fibers, denoted here by $\bar{\psi}^{(2)}$. For the perfectly aligned cases of chapters 5 and 6, the in-plane rotations of

the fibers could be easily argued to be identically zero (i.e., $\bar{\psi}^{(2)} = 0$) at least up-to the point of possible development of instabilities, and therefore there was no need to deal with the general form (8.1) for the effective total energy. For such cases the effective energy is conveniently obtained via

$$\tilde{W}\left(\bar{\boldsymbol{F}}, \bar{\mathbf{D}}\right) = \tilde{W}_{me}\left(\bar{\boldsymbol{F}}\right) + \tilde{W}_{el}\left(\bar{\mathbf{D}}, \bar{\boldsymbol{F}}\right), \tag{8.2}$$

where one can use available estimates for the effective purely mechanical energy and Hashin-Shtrikman type estimate for the effective electrostatic energy. We refer to the estimate (8.2) for the perfectly aligned case as the "principal" solutions (see chapter 5 for details of obtaining such solutions). For the general case of non-aligned DECs and when the matrix material is stiff enough (compared to the size of the electrostatic interactions), we argued that one may be able to use the Partial Decoupling Approximation (PDA) of section 3.2 to estimate the evolution of the microstructure by using the solution of the purely mechanical problem, and therefore obtain the approximated solution

$$\tilde{W}\left(\bar{\boldsymbol{F}}, \bar{\mathbf{D}}\right) \simeq \tilde{W}_{me}\left(\bar{\boldsymbol{F}}; \bar{\psi}^{(2)}_{me}\right) + \tilde{W}_{el}\left(\bar{\mathbf{D}}, \bar{\boldsymbol{F}}; \bar{\psi}^{(2)}_{me}\right), \tag{8.3}$$

for the effective energy of DECs under non-aligned conditions. Here $\bar{\psi}^{(2)}_{me}$ is the (in-plane) rotation of the fibers, obtained form the purely mechanical homogenization problem. The approximation (8.3) significantly simplifies the analysis of the DECs, since, once again, it enables the use of available purely mechanical estimates. However, such an approximation becomes less accurate as the matrix phase becomes softer (compared to the size of the electrostatic interactions).

The first objective of this chapter is to use the general form (8.1) in order to obtain the effective response of DECs under non-aligned loading conditions, which are expected to be valid for both soft and stiff matrix phases. We will also compare the effective response of DECs under non-aligned conditions as obtained by the PDA and PDS schemes, and provide a quantitative measure for the range of validity of the former.

The second objective of this chapter is to re-evaluate the instability regions for

DECs under aligned loading conditions of chapters 5 and 6 by making use of the more accurate effective energy obtained via the PDS scheme[3]. Note that even though the effective energy is not expected to change in the perfectly aligned case when using the more accurate PDS results, the second derivatives of the energy with respect to $\bar{\boldsymbol{F}}$ and $\bar{\mathbf{D}}$ (used in the evaluation of the instability conditions) may change. Therefore, using the "principal" solutions of chapters 5 and 6, and the newly obtained effective energy, we re-calculate the instability regions of aligned DECs and compare them with the previous results.

## 8.1 Effective response of DECs under non-aligned loading conditions

Obtaining the effective response of DECs via the above decoupling strategy requires the computation of the mechanical and electrostatic energies on the right side of expression (8.1) for given loadings, $\bar{\boldsymbol{F}}$ and $\bar{\mathbf{D}}$, and in-plane rotation of the fibers, $\bar{\psi}^{(2)}$. Explicit expressions for these energies will be provided next.

### 8.1.1 Effective mechanical energy for a given in-plane rotation of the fibers

An explicit expression for the effective purely mechanical energy of fiber-constrained composites, as defined by the variational problem

$$\tilde{W}_{me}\left(\bar{\boldsymbol{F}};\bar{\psi}^{(2)}\right)=\tilde{W}_{me}\left(\bar{\lambda},\bar{\theta};\bar{\psi}^{(2)}\right)=\min_{\boldsymbol{F}\in\mathcal{K}'\left(\bar{\boldsymbol{F}},\bar{\psi}^{(2)}\right)}\left\langle W_{me}\left(\boldsymbol{F},\mathbf{X}\right)\right\rangle \tag{8.4}$$

is provided in chapter 7. Thus, as shown in Fig. 8.1, we consider a reinforced elastomer consisting of a single family of rigid cylindrical fibers with elliptical cross-sections, that are distributed with elliptical symmetry in the plane perpendicular to

[3]Recall that in the above-mentioned sections we studied the DECs with aligned microstructures under aligned electromechanical loading conditions. In particular, we investigated the effective response as well as instabilities by using the "principal" solution.

the long axes of the fibers. The initial orientation of the fibers is characterized by the angle $\beta$ (measured form the positive $X_1$ direction in a counter-clock-wise fashion) in the reference configuration. As shown in the figure we assume that in the deformed

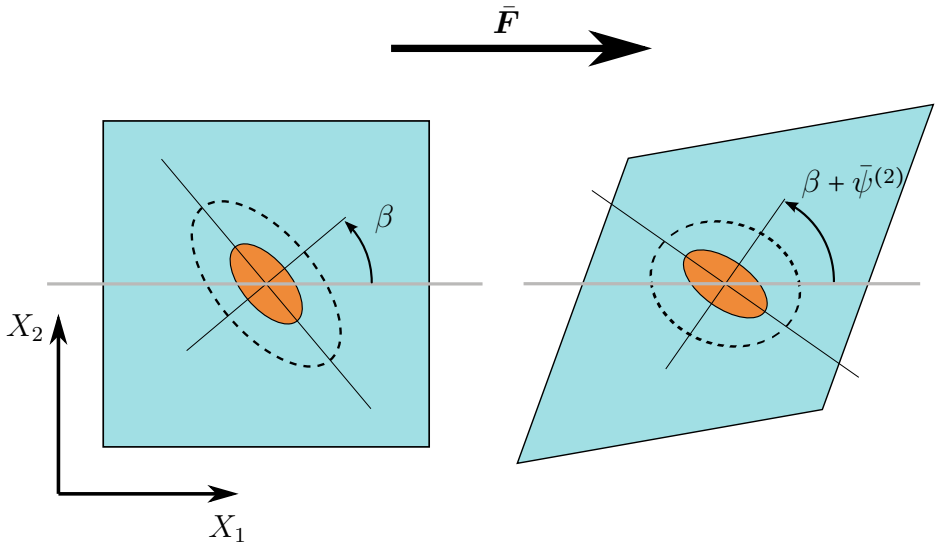


Figure 8.1: Schematics describing the variational problem (8.4). (left) Microstructure of the composite in the reference configuration, and (right) microstructure of the composite in the deformed configuration with prescribed rotation $\bar{\psi}^{(2)}$ for the fibers.

configuration the in-plane rotation of the fibers, $\bar{\psi}^{(2)}$, is prescribed. The effective purely mechanical energy of the above-described composite when the matrix phase is an (incompressible) Gent elastomer with stored energy of the form given by (2.14) may be obtained as follows

$$\tilde{W}_{me}\left(\bar{\boldsymbol{F}};\bar{\psi}^{(2)}\right)=\tilde{W}_{me}\left(\bar{\lambda},\bar{\theta};\bar{\psi}^{(2)}\right)=\left(c_0-1\right)\frac{\mu^{(1)}J_m}{2}\ln\left[1-\frac{\hat{I}-2}{J_m}\right], \tag{8.5}$$

where

$$\begin{aligned}\hat{I}=&\frac{c_0\left(1+\bar{\lambda}^2\right)^2+\left[1+2\left(c_0-2\right)c_0\bar{\lambda}^2+\bar{\lambda}^4\right]w+c_0\left(1+\bar{\lambda}^2\right)^2w^2}{\left(1-c_0\right)^2\bar{\lambda}^2w}\\&-\frac{c_0\left(\bar{\lambda}^4-1\right)\left(w^2-1\right)}{\left(1-c_0\right)^2\bar{\lambda}^2w}\sin\left(\varphi\right)\sin\left(\varphi+2\beta-2\bar{\theta}\right)-\frac{2c_0\left(1+\bar{\lambda}^2\right)\left(1+w^2\right)}{\left(1-c_0\right)^2\bar{\lambda}\,w}\cos\left(\varphi\right),\end{aligned} \tag{8.6}$$

and $\varphi$ denotes the relative rotation of the fibers with respect to the macroscopic rotation, as defined by

$$\varphi := \bar{\psi}^{(2)} - \bar{\psi}. \tag{8.7}$$

The loading parameters $\bar{\lambda}$, $\bar{\theta}$, and $\bar{\psi}$ in the above expressions characterize the macroscopic 2D (in the $X_1$-$X_2$ plane) deformation

$$\left[\bar{\boldsymbol{F}}\right] = \left[\bar{\boldsymbol{R}}\right]\left[\bar{\boldsymbol{Q}}\right]\left[\bar{\boldsymbol{\Lambda}}\right]\left[\bar{\boldsymbol{Q}}\right]^T, \tag{8.8}$$

where

$$\left[\bar{\boldsymbol{R}}\right] = \begin{bmatrix} \cos\bar{\psi} & -\sin\bar{\psi} \\ \sin\bar{\psi} & \cos\bar{\psi} \end{bmatrix}, \quad \left[\bar{\boldsymbol{Q}}\right] = \begin{bmatrix} \cos\bar{\theta} & -\sin\bar{\theta} \\ \sin\bar{\theta} & \cos\bar{\theta} \end{bmatrix}, \quad \text{and} \quad \left[\bar{\boldsymbol{\Lambda}}\right] = \begin{bmatrix} \bar{\lambda} & 0 \\ 0 & \bar{\lambda}^{-1} \end{bmatrix}. \tag{8.9}$$

It is remarked here that expression (8.5) for the effective purely mechanical energy of fiber-reinforced composites with prescribed rotations ($\bar{\psi}^{(2)}$) for the fibers is exactly identical (in form) with the corresponding expression when the fibers are allowed to rotate freely (see equations (5.13) and (5.14) in chapter 5), with the only difference that now the relative rotation $\varphi$ need not satisfy the evolution equation (5.16) and must be treated as an independent variable.

### 8.1.2 Effective electrostatic energy for a given in-plane rotation of the fibers

Estimates for the effective electrostatic energy of DECs with a given in-plane rotation of the fibers have already been obtained in subsection 5.1.4. For completeness we summarized the final results in the following. Thus, the effective electrostatic energy of the DEC may be written as follows

$$\tilde{W}_{el}\left(\bar{\lambda}, \bar{\theta}, \bar{\mathbf{D}}; \bar{\psi}^{(2)}\right) = \frac{1}{2}\bar{\mathbf{D}} \cdot \left[\bar{\boldsymbol{U}}\tilde{\boldsymbol{\mathcal{E}}}^{-1}\left(\bar{\boldsymbol{U}}; \bar{\psi}^{(2)}\right)\bar{\boldsymbol{U}}\right]\bar{\mathbf{D}}, \tag{8.10}$$

where the effective deformation-dependent permittivity is given by

$$\tilde{\boldsymbol{\mathcal{E}}}\left(\bar{\boldsymbol{U}};\bar{\psi}^{(2)}\right)=\varepsilon^{(1)}\boldsymbol{I}+\frac{c_0}{\bar{J}}\left\{\boldsymbol{R}^p\left(\boldsymbol{\mathcal{E}}^{(2)}-\varepsilon^{(1)}\boldsymbol{I}\right)^{-1}\boldsymbol{R}^{p^T}+\frac{1}{\varepsilon^{(1)}}\hat{\boldsymbol{P}}_0\left(\bar{\boldsymbol{U}}\right)\right\}^{-1}. \tag{8.11}$$

In this last expression for the effective permittivity

$$[\boldsymbol{R}^p]=\begin{bmatrix}\cos\varphi & -\sin\varphi\\ \sin\varphi & \cos\varphi\end{bmatrix}\quad\text{with}\quad\varphi=\bar{\psi}^{(2)}-\bar{\psi}. \tag{8.12}$$

It is emphasized, once again, that here $\bar{\psi}^{(2)}$ is treated as an independent variable.

### 8.1.3 Equilibrium rotation of the fibers under general non-aligned loading conditions

Having obtained explicit expressions for the effective mechanical and electrostatic energies in terms of the in-plane rotation of the fibers $\bar{\psi}^{(2)}$, we can use (8.1) in order to obtain the equilibrium in-plane rotation of the fibers under the simultaneous action of mechanical and electrostatic effects. Thus, for a given macroscopic deformation $\bar{\boldsymbol{F}}$ and electric displacement $\bar{\mathbf{D}}$ the equilibrium rotation, denoted here by $\bar{\psi}^{(2)}_{eq}$, is the minimizer of the following problem

$$\tilde{W}\left(\bar{\lambda},\bar{\theta},\bar{\mathbf{D}}\right)=\min_{\bar{\psi}^{(2)}}\tilde{W}\left(\bar{\lambda},\bar{\theta},\bar{\mathbf{D}};\bar{\psi}^{(2)}\right), \tag{8.13}$$

where

$$\tilde{W}\left(\bar{\lambda},\bar{\theta},\bar{\mathbf{D}};\bar{\psi}^{(2)}\right):=\tilde{W}_{me}\left(\bar{\lambda},\bar{\theta};\bar{\psi}^{(2)}\right)+\tilde{W}_{el}\left(\bar{\lambda},\bar{\theta},\mathbf{D};\bar{\psi}^{(2)}\right). \tag{8.14}$$

Therefore, we can easily conclude that

$$\tilde{W}\left(\bar{\lambda},\bar{\theta},\bar{\mathbf{D}}\right)=\tilde{W}\left(\bar{\lambda},\bar{\theta},\bar{\mathbf{D}};\bar{\psi}^{(2)}=\bar{\psi}^{(2)}_{eq}\right), \tag{8.15}$$

where the equilibrium rotation $\bar{\psi}^{(2)}_{eq}$ satisfies the stationary condition

$$\frac{\partial}{\partial \bar{\psi}^{(2)}} \tilde{W}\left(\bar{\lambda}, \bar{\theta}, \bar{\mathbf{D}}; \bar{\psi}^{(2)}\right)\Big|_{\bar{\psi}^{(2)}=\bar{\psi}^{(2)}_{eq}} = 0. \tag{8.16}$$

Note that the equilibrium rotation would in general depend on mechanical loading parameters $\bar{\lambda}$ and $\bar{\theta}$, as well as the electrostatic loading parameter, $\bar{\mathbf{D}}$, as it is evident from equation (8.16).

It is emphasized that the energy $\tilde{W}\left(\bar{\lambda}, \bar{\theta}, \bar{\mathbf{D}}; \bar{\psi}^{(2)}\right)$ may in general be non-convex in $\bar{\psi}^{(2)}$, and therefore the (stationary) condition (8.16) is not sufficient for determining the equilibrium value for $\bar{\psi}^{(2)}$. In general, $\bar{\psi}^{(2)}_{eq}$ has to satisfy the following conditions for a global minimum

$$\begin{aligned} &\frac{\partial}{\partial \bar{\psi}^{(2)}} \tilde{W}\left(\bar{\lambda}, \bar{\theta}, \bar{\mathbf{D}}; \bar{\psi}^{(2)}\right)\Big|_{\bar{\psi}^{(2)}=\bar{\psi}^{(2)}_{eq}} = 0, \quad \text{and} \\ &\tilde{W}\left(\bar{\lambda}, \bar{\theta}, \bar{\mathbf{D}}; \bar{\psi}^{(2)}_{eq}\right) \leq \tilde{W}\left(\bar{\lambda}, \bar{\theta}, \bar{\mathbf{D}}; \bar{\psi}^{(2)}\right) \text{ for all } \bar{\psi}^{(2)}. \end{aligned} \tag{8.17}$$

Other solutions of the stationary condition $(8.17)_1$, if they exist, would correspond to local minima or maxima of the effective rotation-dependent energy $\tilde{W}\left(\bar{\lambda}, \bar{\theta}, \bar{\mathbf{D}}; \bar{\psi}^{(2)}\right)$ (see further below for more details).

### 8.1.4 Constitutive relations for fiber-constrained DECs under non-aligned loading conditions

Having obtained the effective energy, as given by (8.15) we may then obtain the constitutive relations of the DECs under non-aligned conditions by means of relations (2.11), or their Eulerian equivalents. This requires the computation of the derivatives of the effective energy with respect to the macroscopic deformation gradient $\bar{\boldsymbol{F}}$ and macroscopic electric displacement field $\bar{\mathbf{D}}$, which will be provided in the following.

For the energy functions of the form given by equation (8.15), the macroscopic Cauchy stress may be conveniently obtained in terms of the derivatives of the energy

function with respect to the loading parameters $\bar{\lambda}$ and $\bar{\theta}$. Thus, we can show that

$$\bar{\boldsymbol{T}} = 2\bar{\boldsymbol{R}}\bar{\boldsymbol{T}}_B\bar{\boldsymbol{R}}^T - \bar{p}\boldsymbol{I}, \tag{8.18}$$

where $\bar{p}$ is the pressure-like Lagrange multiplier accounting for the overall incompressibility of the DEC, and $\bar{\boldsymbol{T}}_B$ is the Biot-like stress defined by

$$\bar{\boldsymbol{T}}_B := \frac{\partial}{\partial\bar{\lambda}}\tilde{W}\left(\bar{\lambda},\bar{\theta},\bar{\mathbf{D}};\bar{\psi}_{eq}^{(2)}\right)\times\left[\bar{\boldsymbol{U}}\frac{\partial\bar{\lambda}}{\partial\bar{\boldsymbol{C}}}\bar{\boldsymbol{U}}\right] + \frac{\partial}{\partial\bar{\theta}}\tilde{W}\left(\bar{\lambda},\bar{\theta},\bar{\mathbf{D}};\bar{\psi}_{eq}^{(2)}\right)\times\left[\bar{\boldsymbol{U}}\frac{\partial\bar{\theta}}{\partial\bar{\boldsymbol{C}}}\bar{\boldsymbol{U}}\right]. \tag{8.19}$$

Here $\bar{\boldsymbol{C}} = \bar{\boldsymbol{F}}^T\bar{\boldsymbol{F}} = \bar{\boldsymbol{U}}^2$ is the right Cauchy-Green tensor and

$$\left[\frac{\partial\bar{\lambda}}{\partial\bar{\boldsymbol{C}}}\right] = \frac{1}{2\bar{\lambda}}\begin{bmatrix}\cos^2\bar{\theta} & \sin\bar{\theta}\cos\bar{\theta}\\ \sin\bar{\theta}\cos\bar{\theta} & \sin^2\bar{\theta}\end{bmatrix},\qquad \left[\frac{\partial\bar{\theta}}{\partial\bar{\boldsymbol{C}}}\right] = \frac{\bar{\lambda}^2}{2-2\bar{\lambda}^4}\begin{bmatrix}\sin 2\bar{\theta} & -\cos 2\bar{\theta}\\ -\cos 2\bar{\theta} & -\sin 2\bar{\theta}\end{bmatrix}. \tag{8.20}$$

Finally, the derivatives of the effective energy with respect to the loading parameters $\bar{\lambda}$ and $\bar{\theta}$ can be evaluated as follows

$$\begin{aligned}\frac{\partial}{\partial\bar{g}}\tilde{W}\left(\bar{\lambda},\bar{\theta},\bar{\mathbf{D}}\right) &= \frac{\partial}{\partial\bar{g}}\tilde{W}\left(\bar{\lambda},\bar{\theta},\bar{\mathbf{D}};\bar{\psi}_{eq}^{(2)}\right) + \frac{\partial}{\partial\bar{\psi}_{eq}^{(2)}}\tilde{W}\left(\bar{\lambda},\bar{\theta},\bar{\mathbf{D}};\bar{\psi}_{eq}^{(2)}\right)\times\frac{\partial\bar{\psi}_{eq}^{(2)}}{\partial\bar{g}}\\ &= \frac{\partial}{\partial\bar{g}}\tilde{W}\left(\bar{\lambda},\bar{\theta},\bar{\mathbf{D}};\bar{\psi}_{eq}^{(2)}\right)\quad\text{for}\quad\bar{g}\in\left\{\bar{\lambda},\bar{\theta}\right\}.\end{aligned} \tag{8.21}$$

In obtaining the second line we have used the stationary condition $(8.17)_1$. In summary, equations (8.18) and (8.19) along with the derivative of the energy with respect to $\bar{\lambda}$ and $\bar{\theta}$ given by (8.21) will be used in this work to compute the effective macroscopic stress inside DEC samples. Similarly, we can obtain the macroscopic electric field of the composite as follows

$$\begin{aligned}\bar{\mathbf{E}} = \frac{\partial}{\partial\bar{\mathbf{D}}}\tilde{W}\left(\bar{\lambda},\bar{\theta},\bar{\mathbf{D}}\right) &= \frac{\partial}{\partial\bar{\mathbf{D}}}\tilde{W}\left(\bar{\lambda},\bar{\theta},\bar{\mathbf{D}};\bar{\psi}_{eq}^{(2)}\right) + \frac{\partial}{\partial\bar{\psi}_{eq}^{(2)}}\tilde{W}\left(\bar{\lambda},\bar{\theta},\bar{\mathbf{D}};\bar{\psi}_{eq}^{(2)}\right)\times\frac{\partial\bar{\psi}_{eq}^{(2)}}{\partial\bar{\mathbf{D}}}\\ &= \frac{\partial}{\partial\bar{\mathbf{D}}}\tilde{W}\left(\bar{\lambda},\bar{\theta},\bar{\mathbf{D}};\bar{\psi}_{eq}^{(2)}\right),\end{aligned} \tag{8.22}$$

where the stationary condition (8.17) is used, once again, in order to arrive at the second line.

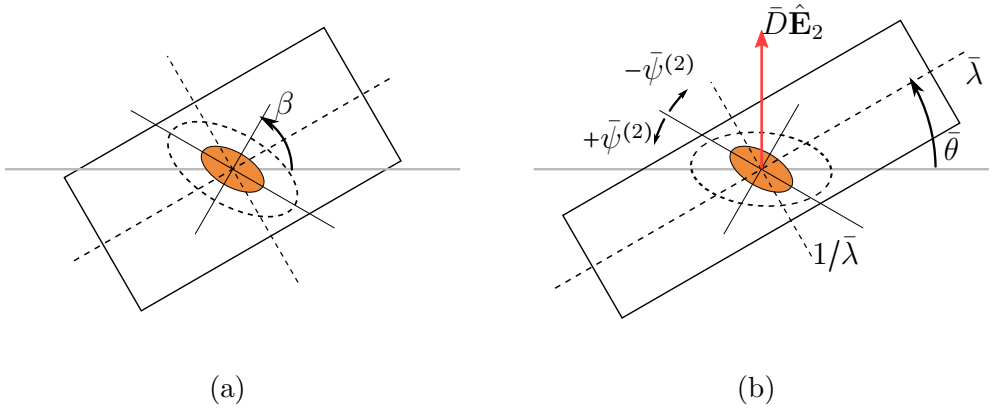


(a) (b)

Figure 8.2: Schematics of the non-aligned setup in the reference (a) and deformed (b) configurations.

Next we will investigate different aspects of the new estimate obtained in this chapter in the context of fiber-constrained DECs, defined previously in chapter 5. In particular, in subsection 8.2.1 we study the equilibrium rotation of the fibers for given $\bar{\boldsymbol{F}}$ and $\bar{\mathbf{D}}$, while in subsection 8.2.2 we study the response of DECs under the electrode boundary conditions. We also compare the results obtained via the partial decoupling strategy (PDS) of this section, with the corresponding results obtained via the partial decoupling approximation (PDA), and provide a quantitative measure for the range of validity of the PDA scheme. Finally, in subsection 8.2.3 we study the instability maps for the perfectly aligned case when the more accurate PDS energy is used for the computations of the second derivatives.

## 8.2 Results for non-aligned DECs

### 8.2.1 Equilibrium rotation of the fibers

As mentioned earlier, due to the non-convex nature of the energy $\tilde{W}\left(\bar{\lambda}, \bar{\theta}, \bar{\mathbf{D}}; \bar{\psi}^{(2)}\right)$, the solution of the stationary condition $(8.17)_1$ for the equilibrium rotation, may not be unique for a given loading. To further illustrate this, in the following we consider an example in which the mechanical and electrostatic loads are not aligned with each other or with the symmetry axis of the fibers. Thus, as can be seen in Fig. 8.2, we

consider a DEC under generally non-aligned conditions, where the initial orientation of the fibers is characterized by the angle $\beta$. The loading conditions are as follows

$$\bar{\mathbf{D}} = \bar{D}\hat{\mathbf{E}}_2 \quad \text{and} \quad \left[\bar{\boldsymbol{F}}\right] = \left[\bar{\boldsymbol{U}}\right] = \left[\bar{\boldsymbol{Q}}\right]\left[\bar{\boldsymbol{\Lambda}}\right]\left[\bar{\boldsymbol{Q}}\right]^T, \tag{8.23}$$

where

$$\left[\bar{\boldsymbol{\Lambda}}\right] = \begin{bmatrix} \bar{\lambda} & 0 \\ 0 & \bar{\lambda}^{-1} \end{bmatrix} \quad \text{and} \quad \left[\bar{\boldsymbol{Q}}\right] = \begin{bmatrix} \cos\bar{\theta} & -\sin\bar{\theta} \\ \sin\bar{\theta} & \cos\bar{\theta} \end{bmatrix} \tag{8.24}$$

with $\bar{\lambda}$ and $\bar{\theta}$ being the loading parameters. It is emphasized that the true electric displacement field is obtained using the transformation rule $\bar{\mathbf{d}} = J^{-1}\bar{\boldsymbol{F}}\bar{\mathbf{D}}$ as follows

$$\bar{\mathbf{d}} = \left[\sin\bar{\theta}\cos\bar{\theta}\left(\bar{\lambda} - \bar{\lambda}^{-1}\right)\bar{D}\right]\hat{\mathbf{E}}_1 + \left[\left(\bar{\lambda}\sin^2\bar{\theta} + \bar{\lambda}^{-1}\cos^2\bar{\theta}\right)\bar{D}\right]\hat{\mathbf{E}}_2, \tag{8.25}$$

and is not in general aligned with the $X_2$ direction.

We begin the discussion of our results by considering the perfectly aligned case. Thus, Fig. 8.3 shows the effective energy as a function of the in-plane rotation of the fibers $\bar{\psi}^{(2)}$ for different values of the electric displacement $\bar{D}/\sqrt{\varepsilon^{(1)}\mu^{(1)}} = 0, 1, 2, 3, 4, 5$. As can be seen in Fig. 8.3(a) at no deformations (i.e., when $\bar{\lambda} = 1$) the energy $\tilde{W}$ is minimized for $\bar{\psi}^{(2)}_{eq} = \bar{\psi}^{(2)} = 0$, independent of the value of the macroscopic electric displacement field. As we increase the macroscopic stretch this trend continues to hold for both $\bar{\lambda} = 1.5$ and $\bar{\lambda} = 2.0$, for the specific example shown in Fig. 8.3. For larger stretches, however, a more complicated behavior is observed, as can be seen in Fig 8.3(d) for $\bar{\lambda} = 2.5$. For the specific example shown in this figure, we observe that the effective energy $\tilde{W}$ is non-convex for $\bar{D}/\sqrt{\varepsilon^{(1)}\mu^{(1)}} = 0, 1, 2, 3$, while it becomes convex for larger values of the electric displacement field. The fact that the effective energy for the purely mechanical case ($\bar{D} = 0$), or for cases where the electric fields are relatively small, is non-convex for large values of the macroscopic stretch (in this case $\bar{\lambda} = 2.5$), implies that the composite has lost strong ellipticicty (as will be seen later). Next, recalling the stabilizing effect of the electric fields for cases when the larger in-plane axis of the fibers is aligned with the fields, we can readily justify the observation that for large enough values of $\bar{D}$ the effective total energy becomes convex.

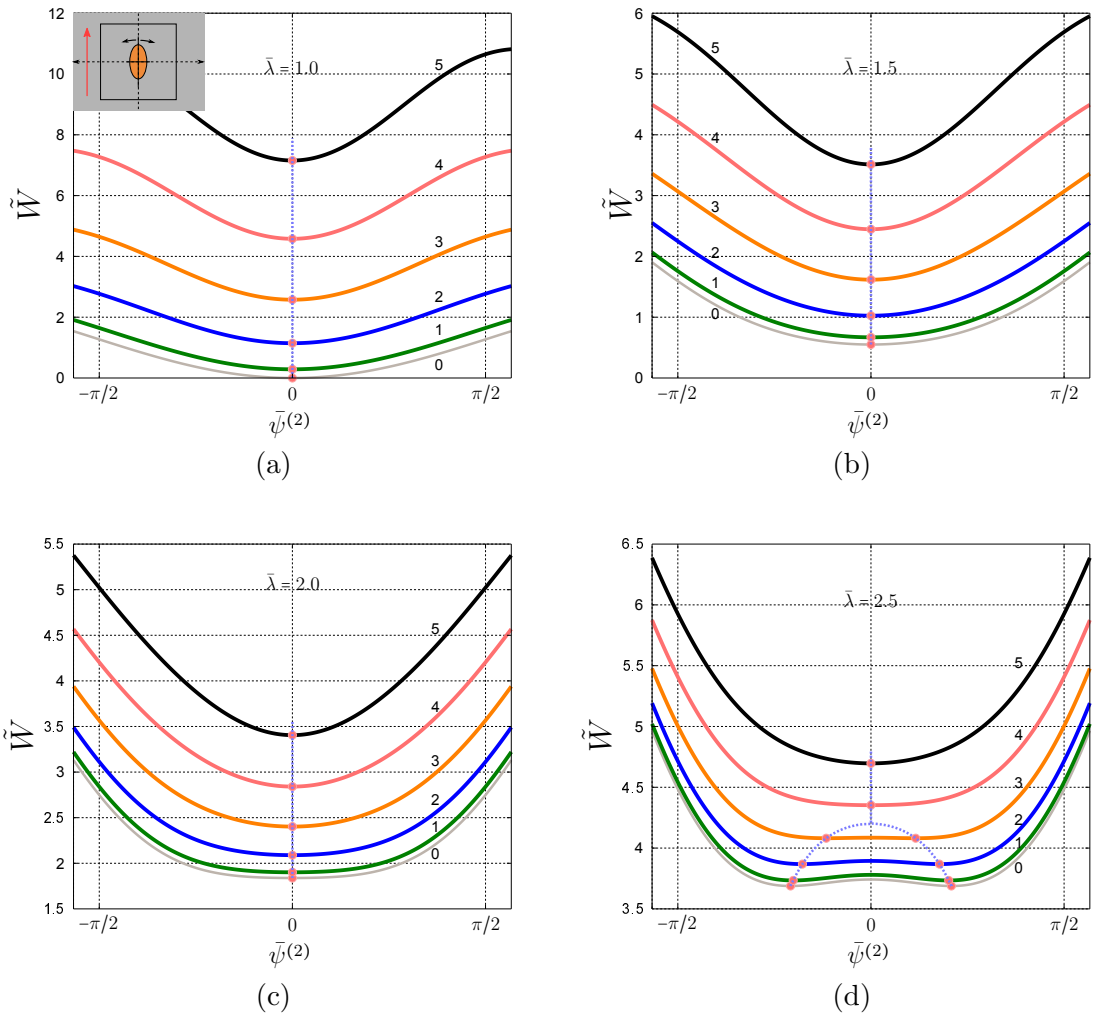


Figure 8.3: This figure shows the dependence of the effective energy $\tilde{W}\left(\bar{\lambda}, \bar{\theta}, \bar{\mathbf{D}}; \bar{\psi}^{(2)}\right)$ on the in-plane rotation of the fibers for $\beta = 0°$, $\bar{\theta} = 0°$, and different values of the electric displacement field. The minima of the energy for each case are marked by the symbol "•". (a) $\bar{\lambda} = 1.0$, (b) $\bar{\lambda} = 1.5$, (c) $\bar{\lambda} = 2.0$, and (d) $\bar{\lambda} = 2.5$. In this figure $w = 2$, $J_m = 100$, $c = 0.2$, and $\mathcal{E}^{(2)}/\varepsilon^{(1)} = 1000$.

Figure 8.4 shows the results for DECs with $\beta = 0$, when a pure shear deformation, characterized by the macroscopic stretch $\bar{\lambda}$, is applied at an angle $\bar{\theta} = 30°$. For the purely mechanical cases, we observe that the equilibrium rotations are negative (i.e., fibers undergo clock-wise rotation) and they increase in magnitude as the macroscopic stretch becomes larger. As the Lagrangian electric displacement field, $\bar{D}$, increases the equilibrium rotation decreases (becomes more negative) monotonically for all values of $\bar{\lambda}$ shown in this figure. This can be explained by noting that the equilibrium

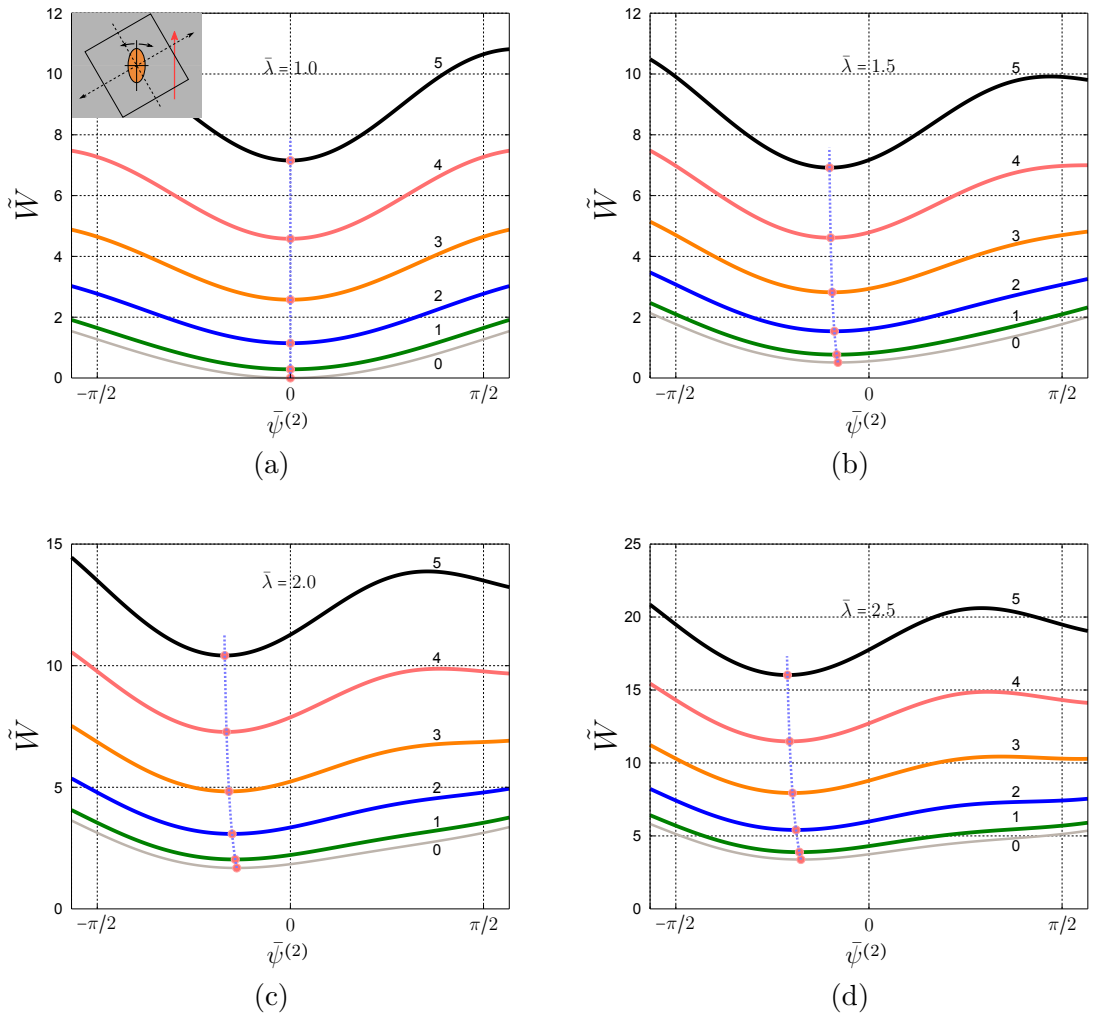


Figure 8.4: This figure shows the dependence of the effective energy $\tilde{W}\left(\bar{\lambda}, \bar{\theta}, \bar{\mathbf{D}}; \bar{\psi}^{(2)}\right)$ on the in-plane rotation of the fibers for $\beta = 0°$, $\bar{\theta} = 30°$, and different values of the electric displacement field. The minima of the energy for each case are marked by the symbol "•". (a) $\bar{\lambda} = 1.0$, (b) $\bar{\lambda} = 1.5$, (c) $\bar{\lambda} = 2.0$, and (d) $\bar{\lambda} = 2.5$. In this figure $w = 2$, $J_m = 100$, $c = 0.2$, and $\mathcal{E}^{(2)}/\varepsilon^{(1)} = 1000$.

electrostatic orientation of the fibers is determined by the direction of the true electric displacement field. As explained earlier (see equation (8.25) for more details) under non-aligned loading conditions the true electric displacement field may have a component in the $X_1$ direction, despite the fact that the Lagrangian electric displacement field is taken to be in the $X_2$ direction. For the specific example of Fig. 8.4 the direction of the true electric displacement is such that it causes negative rotations in the fibers.

Figure 8.5 shows the corresponding results for DECs with $\beta = 60°$, under a pure shear deformation, characterized by the macroscopic stretch $\bar{\lambda}$, applied at $\bar{\theta} = 30°$. Note that for this specific example the mechanical loading (pure shear at 30°) tends

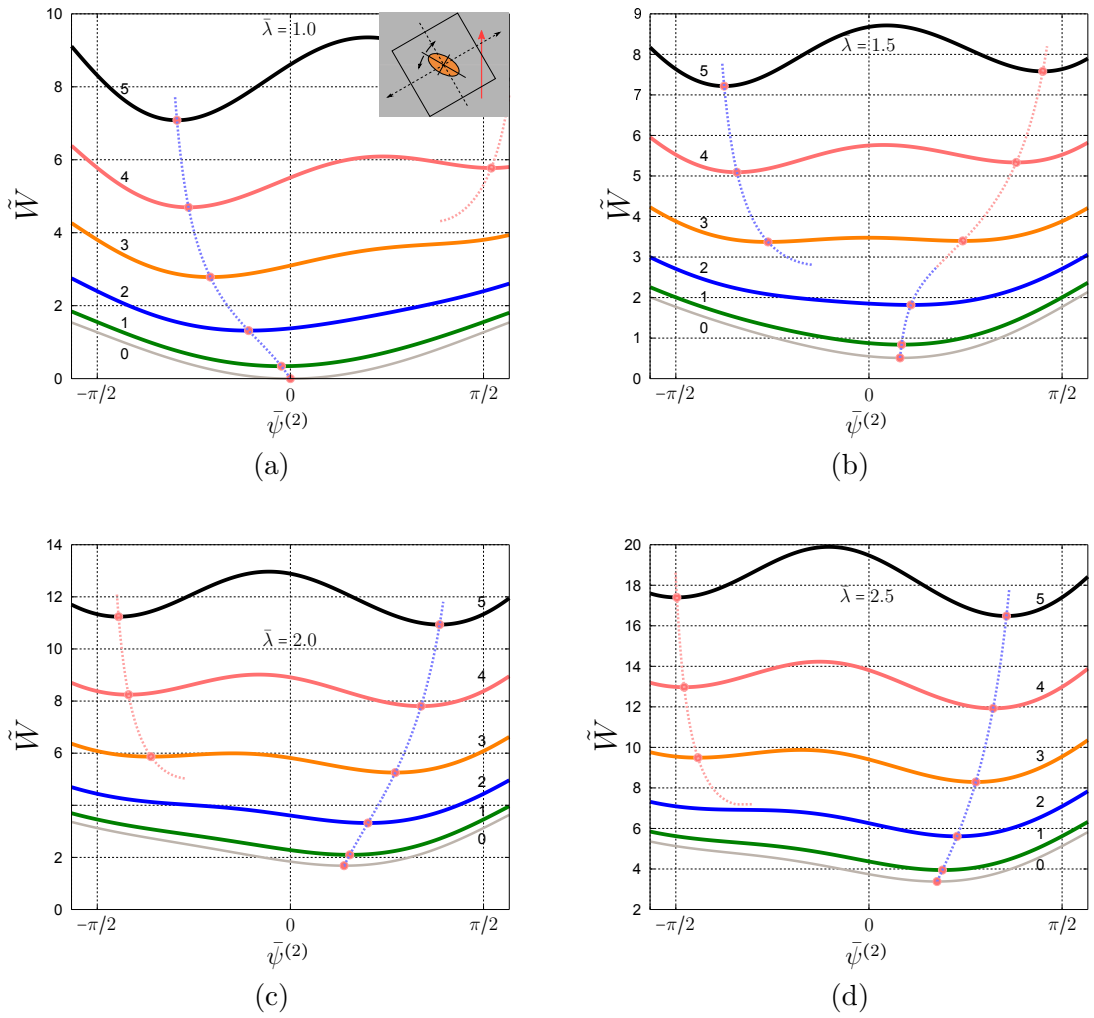


Figure 8.5: This figure shows the dependence of the effective energy $\tilde{W}\left(\bar{\lambda}, \bar{\theta}, \bar{\mathbf{D}}; \bar{\psi}^{(2)}\right)$ on the in-plane rotation of the fibers for $\beta = 60°$, $\bar{\theta} = 30°$, and different values of the electric displacement field. The minima of the energy for each case are marked by the symbol "•". (a) $\bar{\lambda} = 1.0$, (b) $\bar{\lambda} = 1.5$, (c) $\bar{\lambda} = 2.0$, and (d) $\bar{\lambda} = 2.5$. In this figure $w = 2$, $J_m = 100$, $c = 0.2$, and $\mathcal{E}^{(2)}/\varepsilon^{(1)} = 1000$.

to rotate the fibers in the positive direction, while the electrostatic loading (electric displacement field in the $X_2$ direction) tends to rotate the fibers in the negative direction. Thus, as can be seen in Fig. 8.5(a), in the absence of mechanical loadings (i.e., when $\bar{\lambda} = 1$) the equilibrium rotation of the fibers is always negative and its magni-

tude increases by increasing the electrostatic loading. This shows the tendency of the fibers to align themselves with the external electric fields. Figure 8.5(b) shows the corresponding results for the case where both mechanical and electrostatic loadings are present at the same time. As can be seen in this figure when $\bar{\lambda} = 1.5$ and $\bar{D} = 0$, the equilibrium rotation of the fibers is in the positive directions. As the electric displacement field increases, up-to a critical value, the equilibrium rotation of the fibers increases while staying on the positive side. For values of the electric displacement field larger than this critical value, the effective energy becomes non-convex with the global minimum on the negative side. Thus increasing the electric displacement beyond this critical value causes the orientation of the fibers to suddenly jump form the positive side to the negative side. For larger values of the deformation (i.e., for $\bar{\lambda} = 2, 2.5$) the fibers always tend to attain positive rotations even after the effective energy becomes non-convex, see Figs. 8.5(c) and 8.5(d).

In summary, we observe that the interplay between the mechanical and electrostatic effects determines the equilibrium rotation of the fibers in a DEC under generally non-aligned conditions. Depending on the specific parameters chosen, the electrostatic and elastic effects may tend to reorient the fibers in opposite directions, and therefore as the electric fields increase form zero to a large value while the macroscopic stretch is held fixed, the equilibrium rotation of the fibers may undergo a sudden jump from a state more favorable when the mechanical effects are more significant to another state when the electrostatic effects become more significant.

### 8.2.2 Effective response

In this subsection we study the effective response of DECs under generally non-aligned loading conditions as obtained by the partial decoupling strategy (PDS) described earlier in this chapter. We also provide the corresponding results obtained by means of the partial decoupling approximation (PDA) as well as the "principal" solutions of chapter 5 and 6 (in the perfectly aligned cases) for comparison purposes.

Thus, for the purposes of this subsection we consider a dielectric actuator made out of a DEC sample with initially non-aligned (with the coordinate axes) microstruc-

ture, as can be seen in Fig. 8.6. In the absence of external tractions and after the

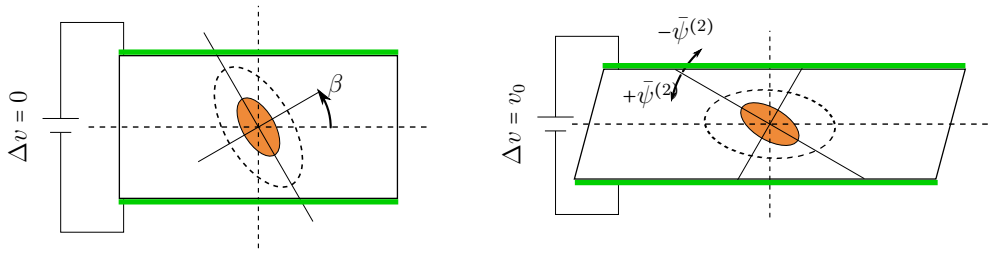


(a) (b)

Figure 8.6: Schematics of a dielectric actuator made out of a DEC with non-aligned (with the coordinate axes) microstructure sandwiched between two compliant electrodes. (a) The actuator in the reference configuration and (b) the actuator in the deformed configuration (i.e., after the application of the voltage). Note that the external tractions are assumed to be zero.

application of the voltage, the composite is expected to undergo an in-plane deformation of the form

$$\bar{\boldsymbol{F}} = \begin{bmatrix} \bar{F}_{11} & \bar{F}_{12} \\ 0 & 1/\bar{F}_{11} \end{bmatrix}, \tag{8.26}$$

where

$$\begin{aligned} \bar{F}_{11} &= \frac{\sqrt{1 + \left(\bar{\lambda}^4 - 1\right)\cos^2\bar{\theta}}}{\bar{\lambda}} \\ \bar{F}_{12} &= \frac{\sin\bar{\theta}\cos\bar{\theta}\left(\bar{\lambda}^3 - \bar{\lambda}^{-1}\right)}{\sqrt{1 + \left(\bar{\lambda}^4 - 1\right)\cos^2\bar{\theta}}}. \end{aligned} \tag{8.27}$$

On the other hand, due to the presence of the conducting electrodes, the Eulerian and Lagrangian electric fields are aligned with the $X_2$ direction, such that

$$\bar{\mathbf{e}} = \frac{\bar{F}_{11} v_0}{h_0}\hat{\mathbf{E}}_2 \quad \text{and} \quad \bar{\mathbf{E}} = \frac{v_0}{h_0}\hat{\mathbf{E}}_2, \tag{8.28}$$

where $h_0$ denotes the height of the sample in the reference configuration. Note that both the Eulerian and Lagrangian electric displacement fields will have a component in the $X_1$ direction when $\beta \neq 0, \pi/2$, since for such cases the principal axes of the effective permittivity are no longer aligned with the coordinate axes.

As discussed earlier in the previous subsection at certain points in a given load-

ing path the effective energy of the composite may become non-convex. For such non-convex energies the stationary condition $(8.17)_1$ can at most have three distinct solutions. In the following results, the stationary value corresponding to the global minimum of (8.15) will be used to compute the effective response of DECs. Results will be provided for both PDA and PDS schemes as well as the principal solution of chapters 5 and 6, for comparison purposes.

We begin our discussion by considering the perfectly aligned case (i.e., $\beta = 0°$). Thus, Fig. 8.7, shows the effective response of a DEC consisting of fibers with aspect ratio $w = 2$ under the perfectly aligned conditions. Figures 8.7(a) and 8.7(b) show the Lagrangian electric and electric displacement fields as functions of the stretch $\bar{\lambda}$, while Figs. 8.7(c) and 8.7(d) show the corresponding results for the loading angle $\bar{\theta}$ and the shear component of the macroscopic deformation, $\bar{F}_{12}$. Finally Figs. 8.7(e) and 8.7(f) show the evolution of the microstructure as determined by the in-plane rotation of the fibers $\bar{\psi}^{(2)}$ or the relative rotation $\bar{\psi}^{(2)} - \bar{\psi}$. As can be seen in these figures, up-to a certain deformation ($\bar{\lambda} = \bar{\lambda}_{\text{Br}} \simeq 2.2$ for the specific example shown here), the response of the DEC obtained via the PDA scheme (the red solid curves) coincides exactly with the principal solution (black dashed curves). For larger deformations, however, the response obtained by the PDA scheme branches out (from the principal solution) into a lower energy solution. Recall that in the PDA scheme the rotation of the fibers are obtained from the solution of the purely mechanical problem, and for large values of the deformation ($\bar{\lambda} \gtrsim 2.2$ for the specific example shown in this figure) such solutions are known to bifurcate. In fact, the purely mechanical energy can be shown to be non-convex with two local minima at $\bar{\psi}^{(2)}_{eq} = \pm\psi^*$, corresponding to the additional PDA branches seen in the figures. Note that even though the two branches corresponding to $\bar{\psi}^{(2)}_{eq} = \pm\psi^*$ are different in their microstructural states, as can be seen in Figs. 8.7(e) and 8.7(f), they have the same $\bar{E}$-$\bar{\lambda}$ (or $\bar{D}_2$-$\bar{\lambda}$) response curves, as can be seen in Figs. 8.7(a) and 8.7(b). It is also worthwhile to mention that the branching of the PDA results always happens after the loss of strong ellipticity of the purely mechanical energy. As will be seen in the next subsection, for the specific DEC of Fig. 8.7, loss of ellipticity of the purely mechanical energy happens for $\bar{\lambda} = \bar{\lambda}_{\text{LE}} \simeq 1.88$,

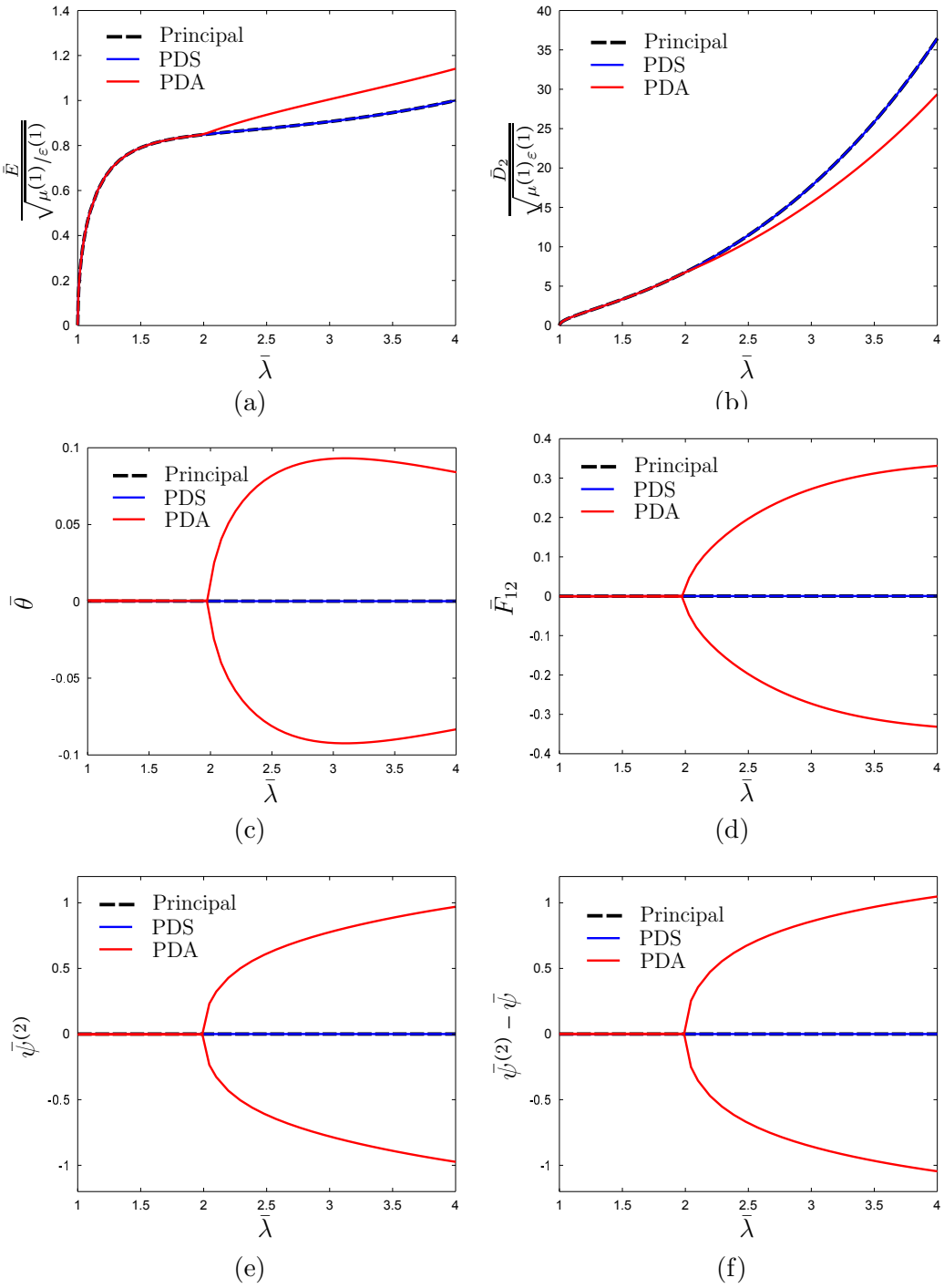


Figure 8.7: The response of a DEC with $\beta = 0°$ under the electrode boundary condition and zero external tractions. (a) Electric field, (b) electric displacement field, (c) loading angle, (d) $\bar{F}_{12}$, (e) equilibrium rotation, and (f) relative rotation as functions of $\bar{\lambda}$. In this figure $J_m = 100$, $\mathcal{E}^{(2)}/\varepsilon^{(1)} = 1000$, and $w = 2$, $c = 0.2$.

which is seen to be smaller than $\bar{\lambda}_{\rm Br}$. On the other hand, the response of the DEC as obtained by the PDS scheme (solid blue curves) never bifurcates from the principal solution, at least for the range of stretches shown in the figure, due to the stabilizing effect of the electric fields (recall that particles tend to align their longer in-plane axis with the external electric fields).

Figure 8.8 shows the corresponding results for a DEC consisting of fibers with aspect ratio $w = 3$. As can be seen from these figures the branching of the PDA response curves from the principal solution occurs at a smaller stretch ($\bar{\lambda} = \bar{\lambda}_{\rm Br} \simeq 1.7$ for the example shown in this figure). This can be explained by noting that fiber-constrained composites consisting of fibers with larger aspect ratios are mechanically less stable under the pure shear loading conditions considered here. The loss of ellipticity for the purely mechanical energy of the composite considered in Fig. 8.8 happens for $\bar{\lambda} = \bar{\lambda}_{\rm LE} \simeq 1.5$, which is seen to be smaller than the branching stretch.

For the DEC considered in Fig. 8.8 the PDS response curves branch out into a lower energy solution, as well. Note that even though the differences between the PDS and principal solutions in Figs. 8.8(a) and 8.8(b) are very small, the branching of the PDS solution can be easily observed in Figs. 8.8(c)-8.8(f). As can be seen in the figures, the branching of the PDS results happens at larger stretches (compared to the PDA results) due to the stabilizing effects of the electric fields. Furthermore, the branching of the PDS solutions is seen to happen more smoothly. Finally, unlike the PDA results, for which the branching happens after the loss of ellipticity of the purely mechanical energy, the branching of the PDS results happens before the loss of ellipticity of the principal solution. For the specific DEC shown in this figure, the branching of the PDS response curves occurs for $\bar{\lambda} = \bar{\lambda}_{\rm Br} \simeq 2.75$ while the principal solution loses ellipticity for $\bar{\lambda} = \bar{\lambda}_{\rm LE} \simeq 3.0$. Recall that in a displacement-controlled experiment loss of ellipticiy is known to be the first instability observed. The fact that the branching of the PDS results happens before the loss of ellipticity of the principal solution suggests that the material may be undergoing a different type of instability due to the unconventional electrode boundary conditions considered in our problem. Understanding the nature of the instabilities resulting in the branching of

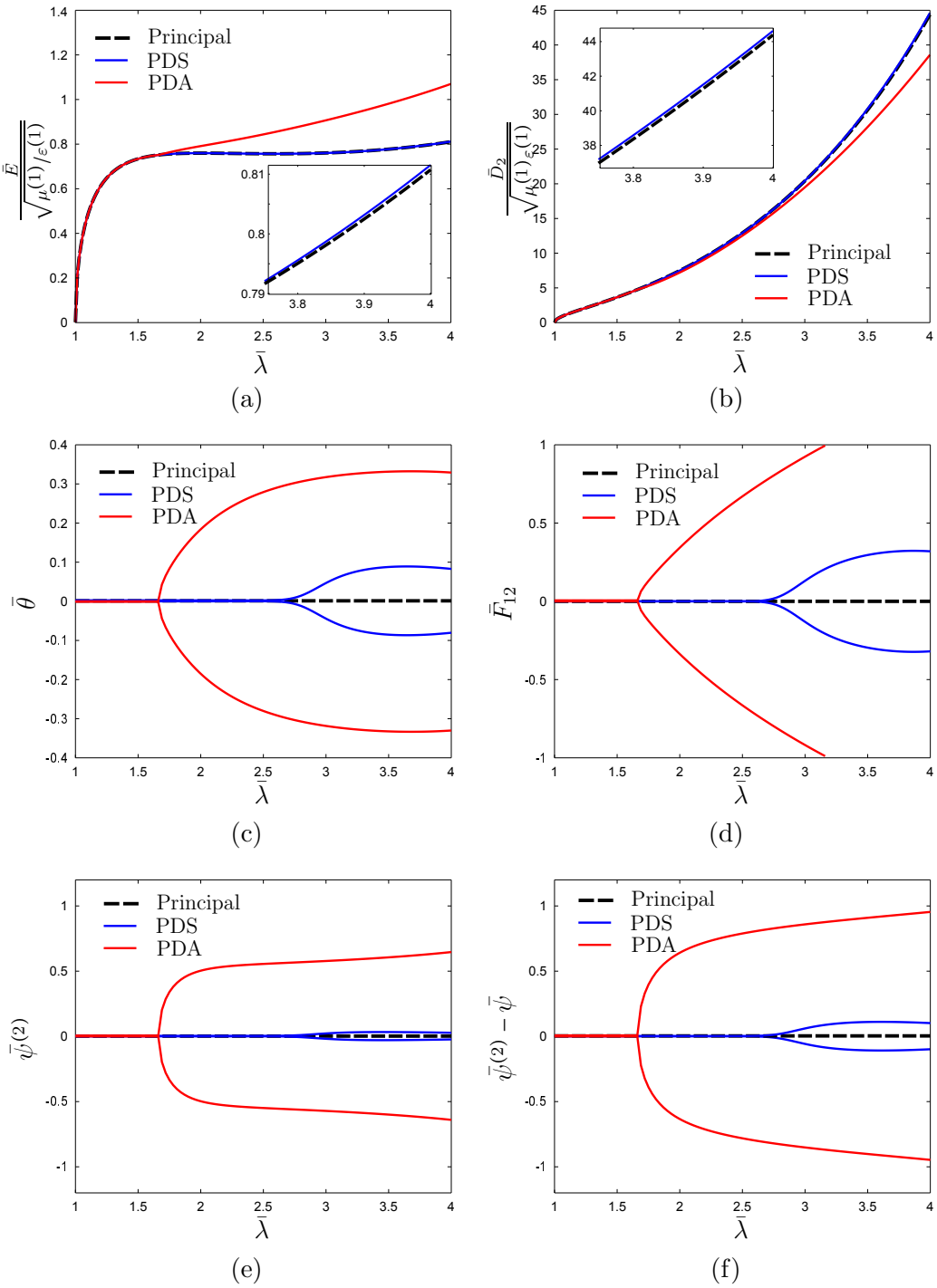


Figure 8.8: The response of a DEC with $\beta = 0°$ under the electrode boundary condition and zero external tractions. (a) Electric field, (b) electric displacement field, (c) loading angle, (d) $\bar{F}_{12}$, (e) equilibrium rotation, and (f) relative rotation as functions of $\bar{\lambda}$. In this figure $J_m = 100$, $\mathcal{E}^{(2)}/\varepsilon^{(1)} = 1000$, and $w = 3$, $c = 0.2$.

the PDS solutions requires a more through investigation of the instabilities under the electrode boundary condition and will be addressed in future works.

Figure 8.9 shows the results for DECs with $\beta = 22.5°$, while Fig. 8.10 shows the zoomed in versions. As shown in Figs. 8.9(a) and 8.9(b) the response of the DECs as obtained by the PDA scheme is initially in good agreement with the response obtained by the more accurate PDS scheme. This suggests that for small values of the fields (i.e., when the mechanical effects are dominant) the PDA scheme can provide accurate estimates for the effective response of the DECs. However, as the electric fields increase, and therefore the electrostatic effects become dominant, the PDA scheme loses its accuracy. In fact, as can be seen from Fig. 8.10(b), one can define

$$\kappa := \frac{1}{\mu^{(1)}} \times \frac{\bar{D}_2^2}{\varepsilon^{(1)}} \tag{8.29}$$

as a measure for the relative strength of the electrostatic and mechanical effects. When $\kappa \ll 1$, the mechanical effects are stronger (relative to the electrostatic effects), and therefore the difference between the response curves, as obtained by the PDA and PDS schemes, are negligible. On the other hand, when $\kappa \gtrsim 1$ the electrostatic effects are comparable with or stronger than the mechanical effects, and therefore the difference between the PDA and PDS schemes may not be ignored.

It is emphasized that at the microstructre level the two schemes result in different solutions, even for very small electric fields (i.e., when $\kappa \ll 1$). In particular, as can be seen in Figs. 8.9(c)-8.9(f) (or the corresponding zoomed in versions), according to the PDA results the fibers tend to undergo positive in-plane rotations, while according to the PDS results the fibers tend to undergo negative rotations. Note that when using the PDA scheme the fiber rotations are determined by the purely mechanical problem. (Recall that in the purely mechanical problem fibers tend to align their longer in-plane axes with the direction of the larger principal stretch, i.e., the $X_1$ direction for the example shown here.) For the specific example of Figs. 8.9 and 8.10, this causes the fibers to undergo positive rotations in the purely mechanical problem, and therefore the rotation of the fibers as determined by the PDA scheme is

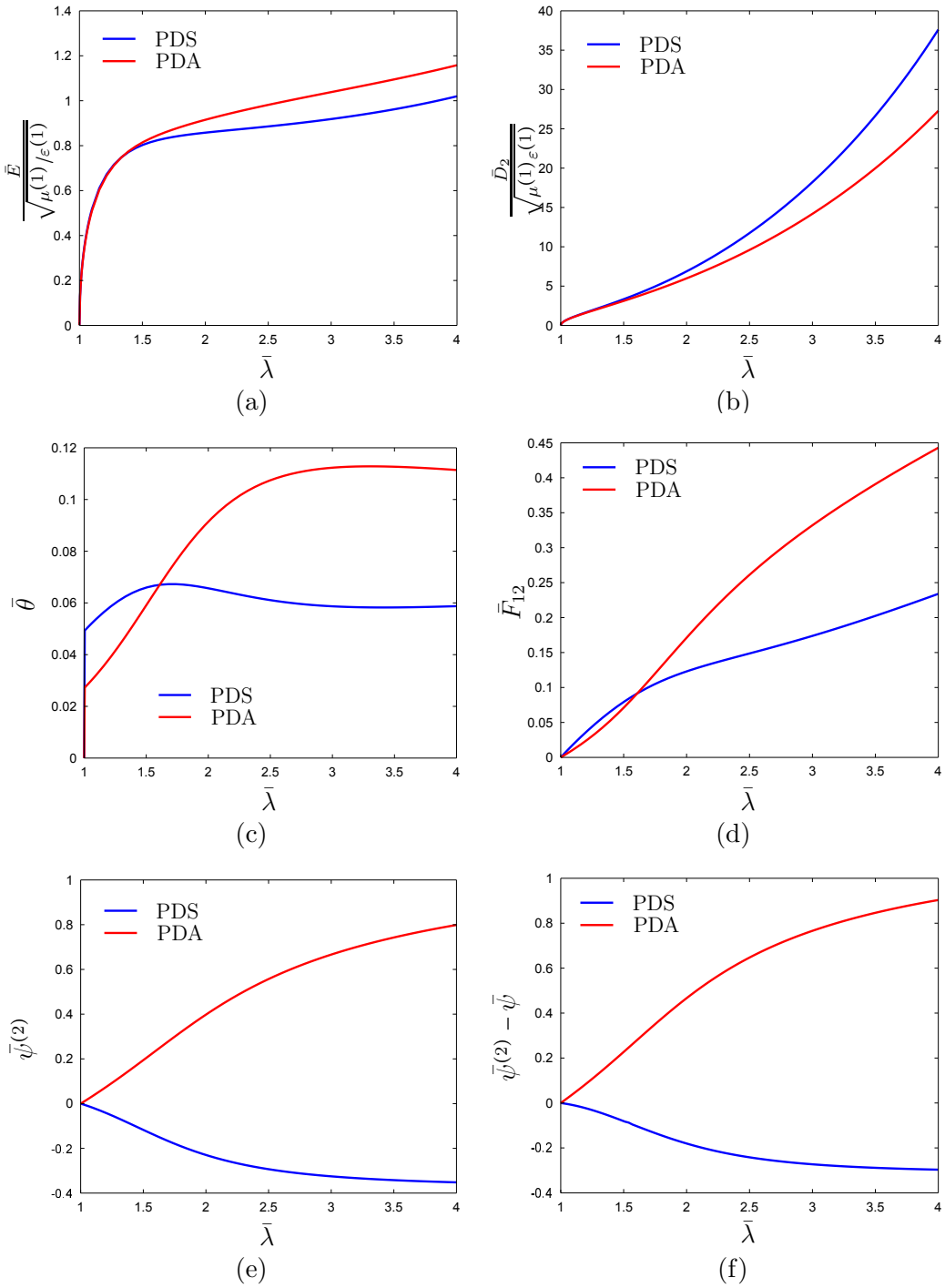


Figure 8.9: The response of a DEC with $\beta = 22.5°$ under the electrode boundary condition and zero external tractions. (a) Electric field, (b) electric displacement field, (c) loading angle, (d) $\bar{F}_{12}$, (e) equilibrium rotation, and (f) relative rotation as functions of $\bar{\lambda}$. In this figure $J_m = 100$, $\mathcal{E}^{(2)}/\varepsilon^{(1)} = 1000$, and $w = 2$, $c = 0.2$.

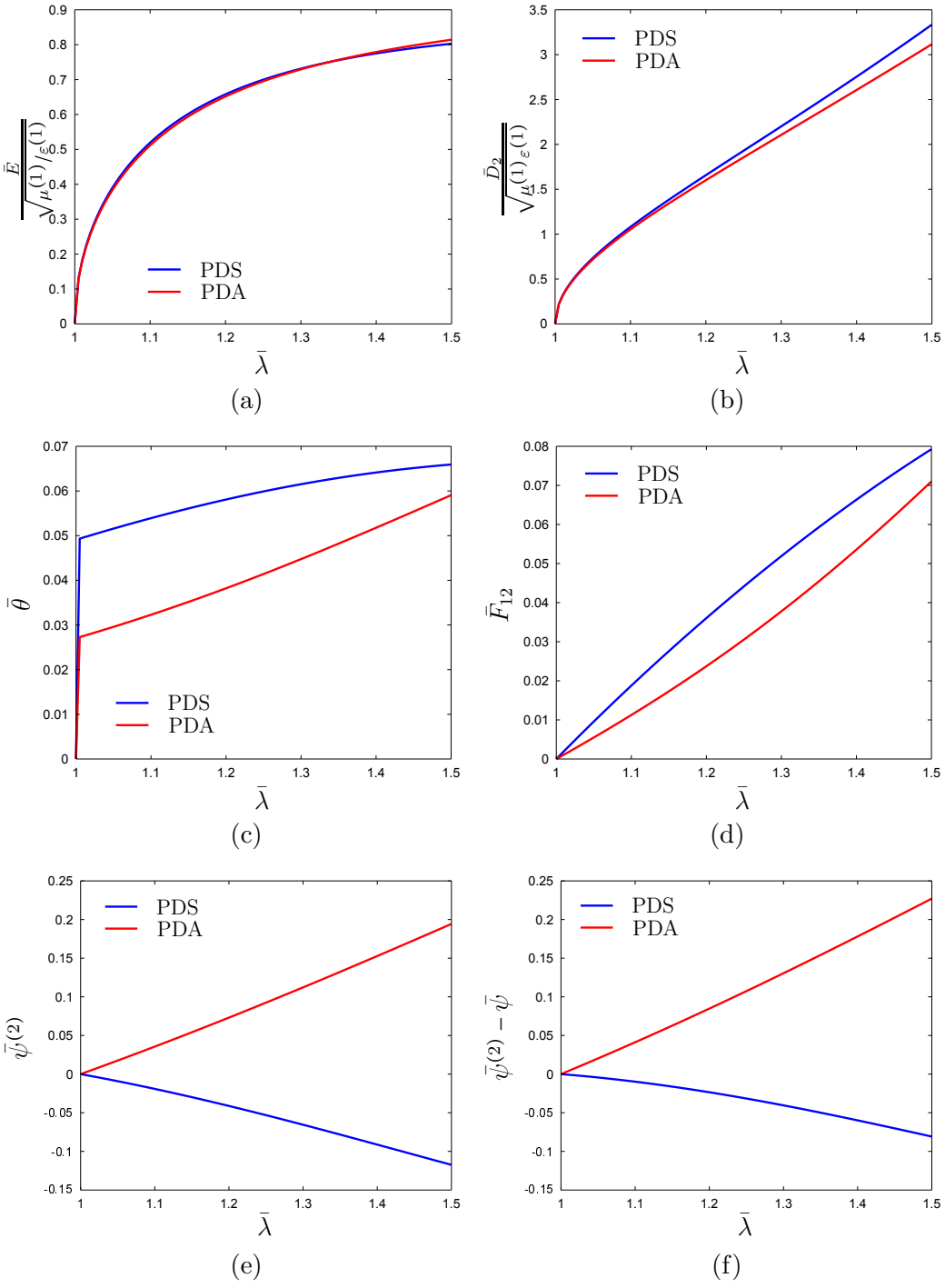


Figure 8.10: Zoomed in version of Fig. 8.9. (a) Electric field, (b) electric displacement field, (c) loading angle, (d) $\bar{F}_{12}$, (e) equilibrium rotation, and (f) relative rotation as functions of $\bar{\lambda}$. In this figure $J_m = 100$, $\mathcal{E}^{(2)}/\varepsilon^{(1)} = 1000$, and $w = 2$, $c = 0.2$.

positive. On the other hand, when using the PDS scheme the rotations are obtained from the coupled electromechanical problem in which both mechanical and electrical effects are present. In particular, in the presence of both mechanical and electrical loadings, there exist at most two favorite orientations for the fibers; a mechanical orientation and an electrostatic orientation. The mechanical orientation characterizes the tendency of the fibers for aligning their longer in-plane axes with the direction of the larger principal stretch (i.e., $X_1$ direction for the example shown here), while the electrostatic orientation characterizes the tendency of the fibers for aligning their longer axes with the direction of the applied electric field (i.e., $X_2$ direction for the example shown here). Thus, the equilibrium orientation of the fibers is the result of the complex interplay between these two effects. For the specific example of Figs. 8.9 and 8.10, the electrostatic orientation turns out to be the more favorable one, and therefore when using the PDS scheme fibers tend to undergo negative rotations, even for very small fields.

Figures 8.11 and 8.12 show the corresponding results for a DEC with $\beta = 45°$. As can be seen from the figures both PDA and PDS responses are qualitatively similar to the corresponding results for DECs with $\beta = 22.5°$. However, when $\beta = 45°$ the magnitude of the fiber rotations as obtained by the PDA scheme are smaller than the corresponding values for DECs with $\beta = 22.5°$. This can be explained by noting that in the purely mechanical problem fibers tend to align their longer axes with the $X_1$ direction, and therefore smaller initial misalignment with the $X_1$ direction (i.e., larger $\beta$) results in a smaller rotation. On the other hand, when $\beta = 45°$, the magnitude of the fiber rotations as obtained by the PDS scheme is larger than the corresponding values for DECs with $\beta = 22.5°$. This is due to the fact that in the PDS scheme the rotations are determined by the direction of the applied electric fields (i.e., $X_2$ direction), and therefore a larger misalignment with this direction (i.e., larger $\beta$) results in a larger electrostatic torque and consequently a larger rotation.

Figures 8.13 and 8.14 show the corresponding results for a DEC with $\beta = 67.5°$. Note that the magnitude of the fiber rotations as obtained by the PDA scheme is very small for this case due to the very small misalignment of the fibers with the $X_1$

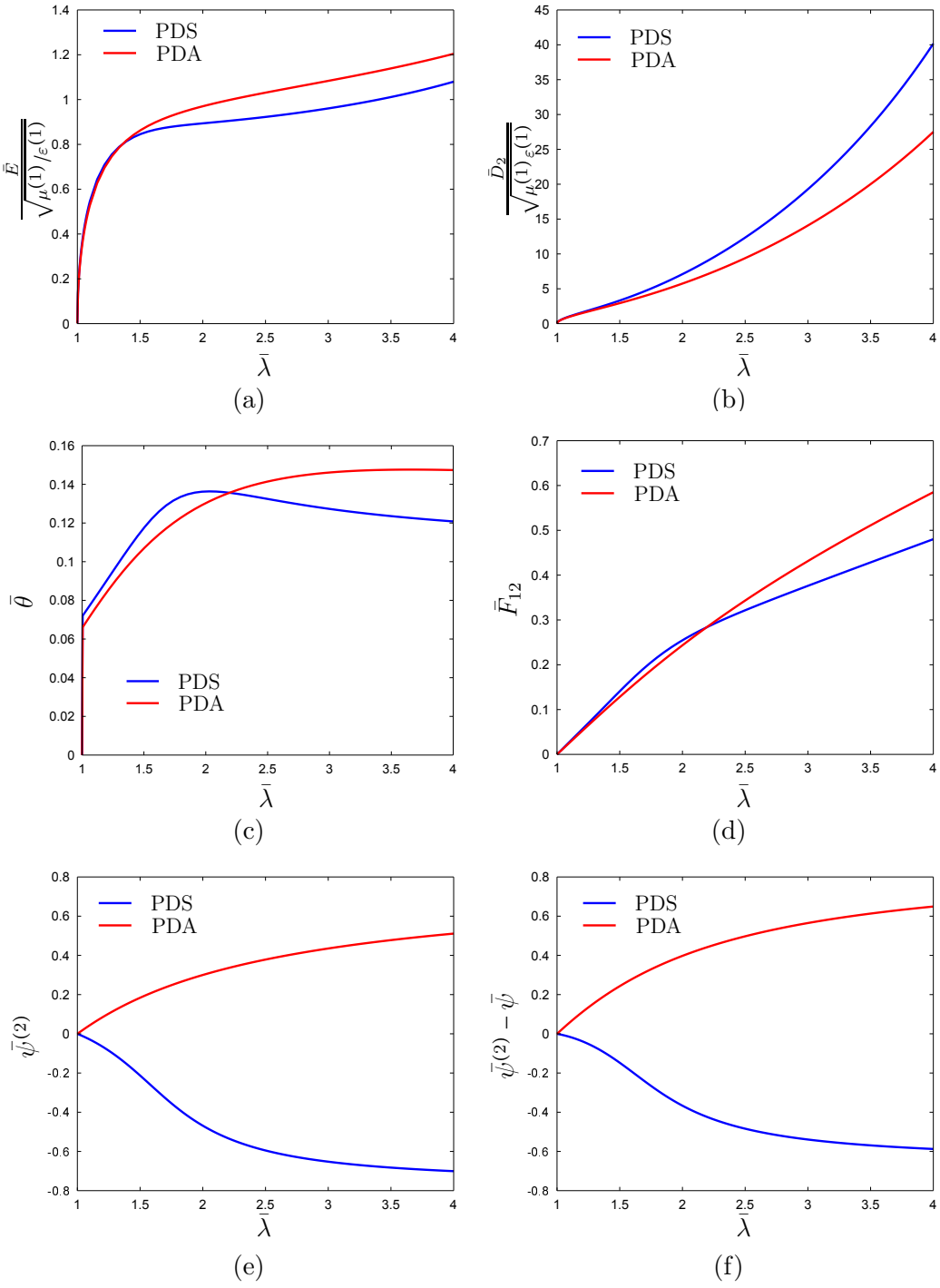


Figure 8.11: The response of a DEC with $\beta = 45°$ under the electrode boundary condition and zero external tractions. (a) Electric field, (b) electric displacement field, (c) loading angle, (d) $\bar{F}_{12}$, (e) equilibrium rotation, and (f) relative rotation as functions of $\bar{\lambda}$. In this figure $J_m = 100$, $\mathcal{E}^{(2)}/\varepsilon^{(1)} = 1000$, and $w = 2$, $c = 0.2$.

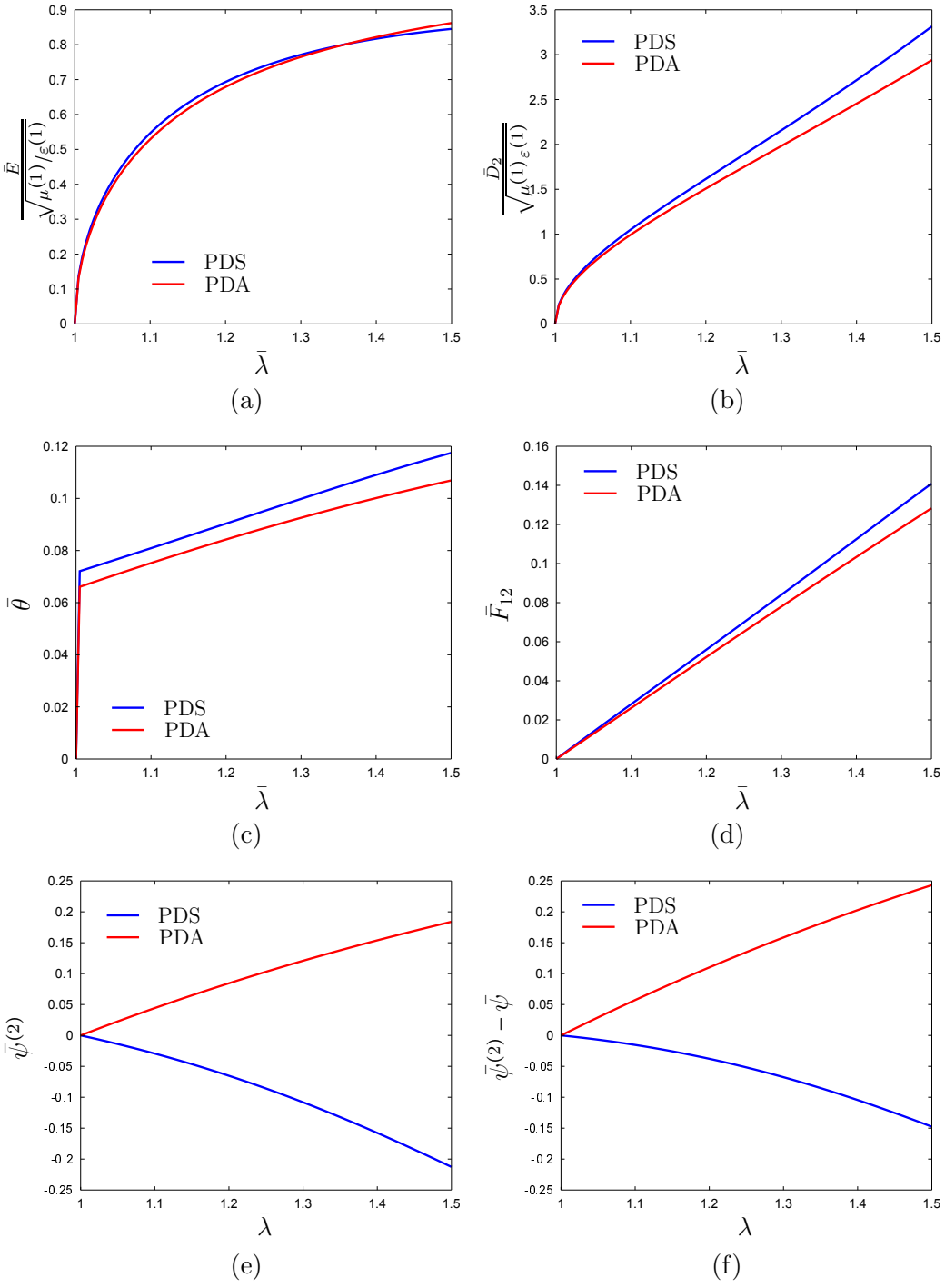


Figure 8.12: Zoomed in version of Fig. 8.11. (a) Electric field, (b) electric displacement field, (c) loading angle, (d) $\bar{F}_{12}$, (e) equilibrium rotation, and (f) relative rotation as functions of $\bar{\lambda}$. In this figure $J_m = 100$, $\mathcal{E}^{(2)}/\varepsilon^{(1)} = 1000$, and $w = 2$, $c = 0.2$.

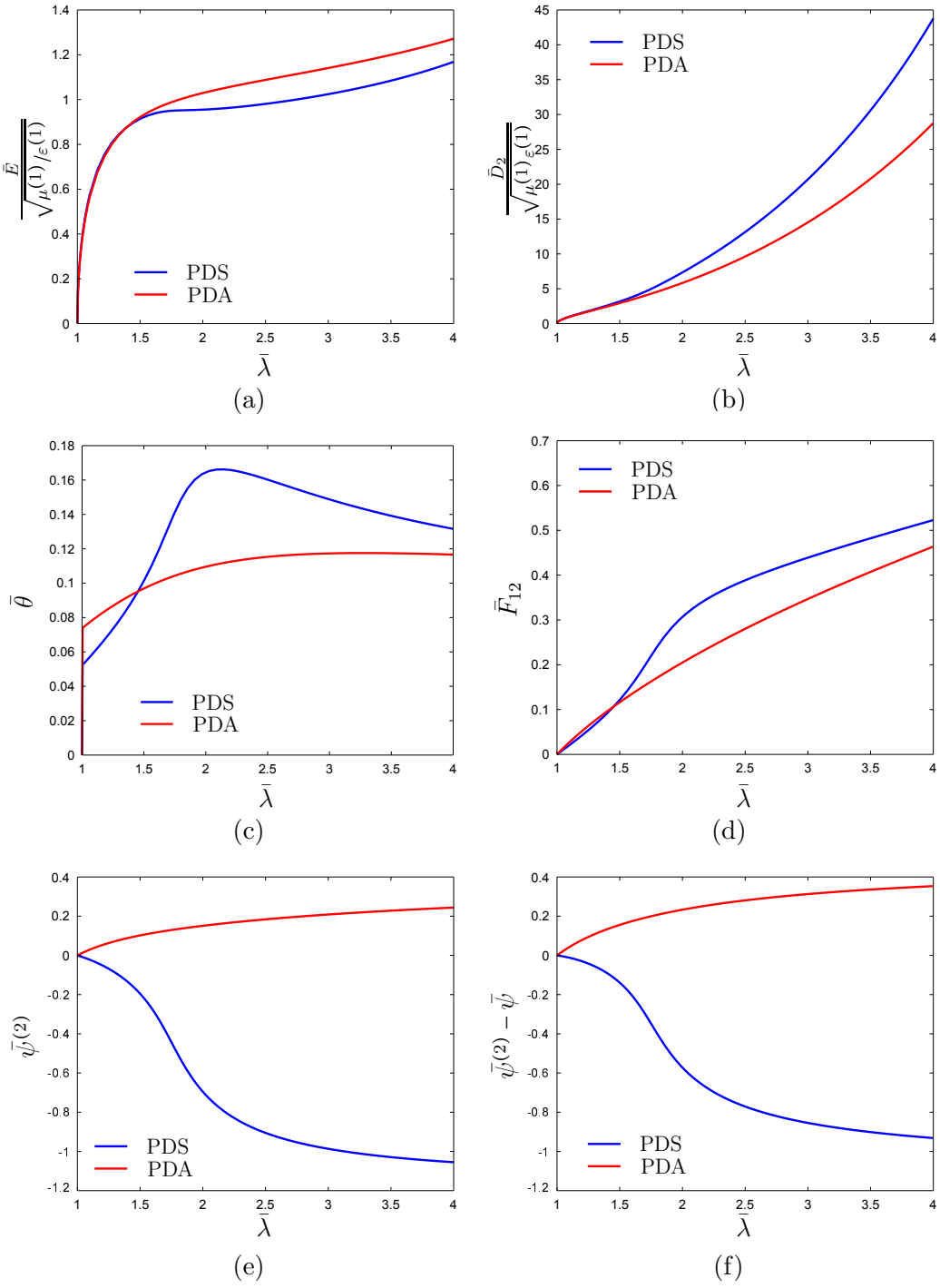


Figure 8.13: The response of a DEC with $\beta = 67.5°$ under the electrode boundary condition and zero external tractions. (a) Electric field, (b) electric displacement field, (c) loading angle, (d) $\bar{F}_{12}$, (e) equilibrium rotation, and (f) relative rotation as functions of $\bar{\lambda}$. In this figure $J_m = 100$, $\mathcal{E}^{(2)}/\varepsilon^{(1)} = 1000$, and $w = 2$, $c = 0.2$.

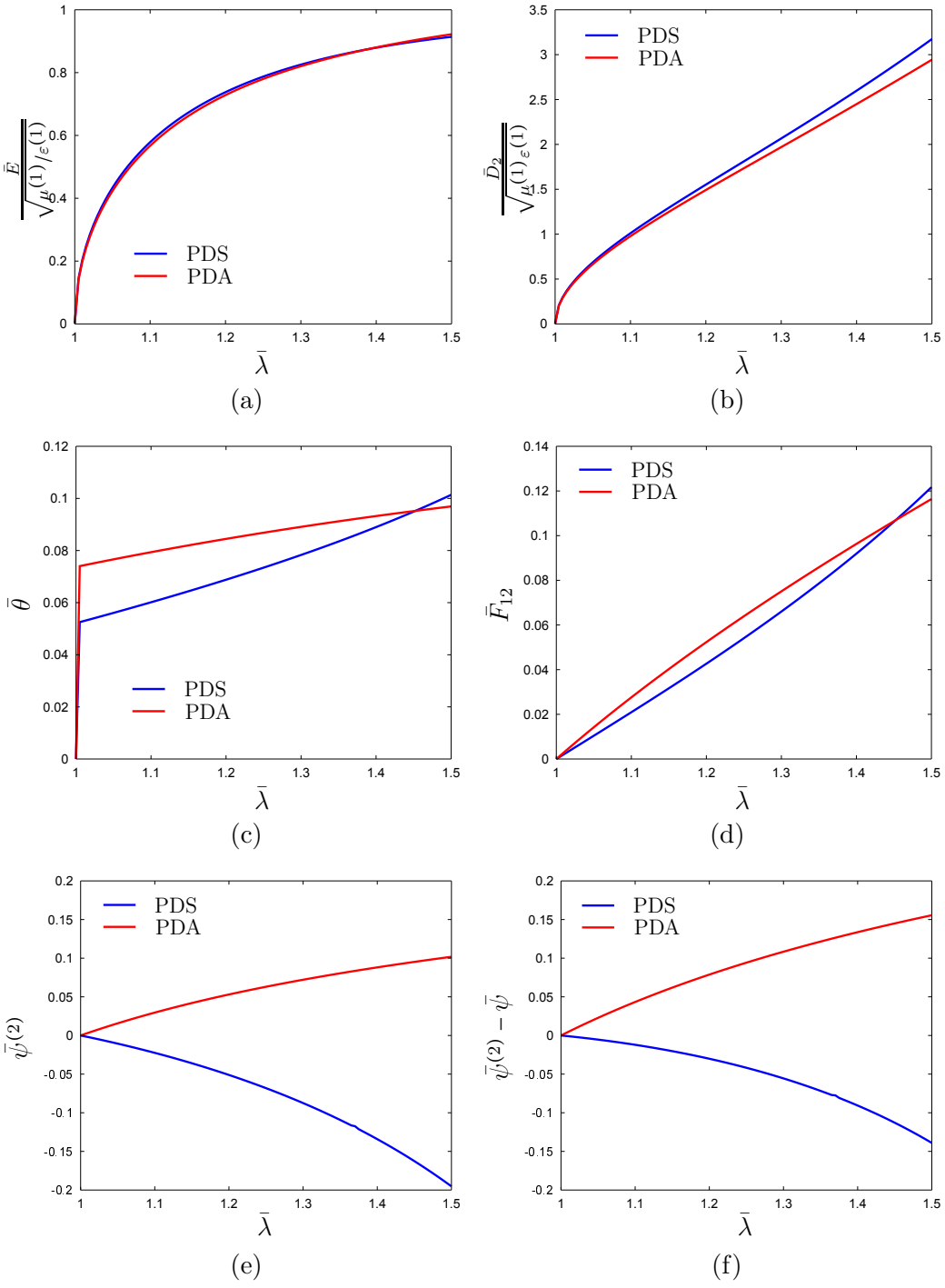


Figure 8.14: Zoomed in version of Fig. 8.13. (a) Electric field, (b) electric displacement field, (c) loading angle, (d) $\bar{F}_{12}$, (e) equilibrium rotation, and (f) relative rotation as functions of $\bar{\lambda}$. In this figure $J_m = 100$, $\mathcal{E}^{(2)}/\varepsilon^{(1)} = 1000$, and $w = 2$, $c = 0.2$.

direction (i.e., the direction of the larger principal stretch). On the other hand, the rotations as obtained by the PDS scheme are very large when $\beta = 67.5°$, due to the very large misalignment between the fibers and the $X_2$ direction (i.e., the direction of the applied electric fields).

Figure 8.15 shows the corresponding results for DECs with $\beta = 90°$ and $w = 2$. As can be seen in this figure, the response of the DEC as obtained by the PDA scheme coincides exactly with the principal solution. Recall that in the PDA scheme the rotation of the fibers is obtained from the purely mechanical problem. Thus, for DECs with $\beta = 90°$ (i.e., when the longer axes of the fibers is aligned with the $X_1$ direction), the rotation of the fibers is identically zero. For this reason, the PDA results are exactly identical to the principal solution, when $\beta = 90°$.

The PDS results coincide with the principal solution up-to a certain deformations ($\bar{\lambda} = \bar{\lambda}_{\text{Br}} \simeq 2.4$, for the example shown here). As the deformation progresses beyond this value, the PDS solution branches out into two lower energy solutions with identical electric fields but different microstructural details. These new lower energy solutions correspond to cases where the in-plane rotations of the fibers are approximately equal to $\pm\frac{\pi}{2}$, as can be seen in Fig. 8.15(e). This is easily explained by recalling the tendency of the fibers to reorient their longer in-plane axes with the external electric fields.

Finally, Fig. 8.16 shows the corresponding results for a DEC with $\beta = 90°$ and $w = 3$. It is seen from this figure that the branching of the PDS solutions happens earlier (for the specific example shown here the branching happens for $\bar{\lambda} = \bar{\lambda}_{\text{Br}} \simeq 1.9$). This is due to the fact that fibers with larger aspect ratios experience larger electrostatic torques, and therefore are (electrostatically) less stable.

Thus far we have studied the response of DECs with both aligned and non-aligned microstructures as obtained by the PDA and PDS schemes. We have shown that both PDA and PDS solutions branch out from the principal solution for the perfectly aligned case (i.e., when $\beta = 0°$), while only the PDS solutions branch out from the principal solution when $\beta = 90°$. As mentioned earlier the branching of the PDA solutions is seen to happen after the onset of the loss of ellipticity for the purely

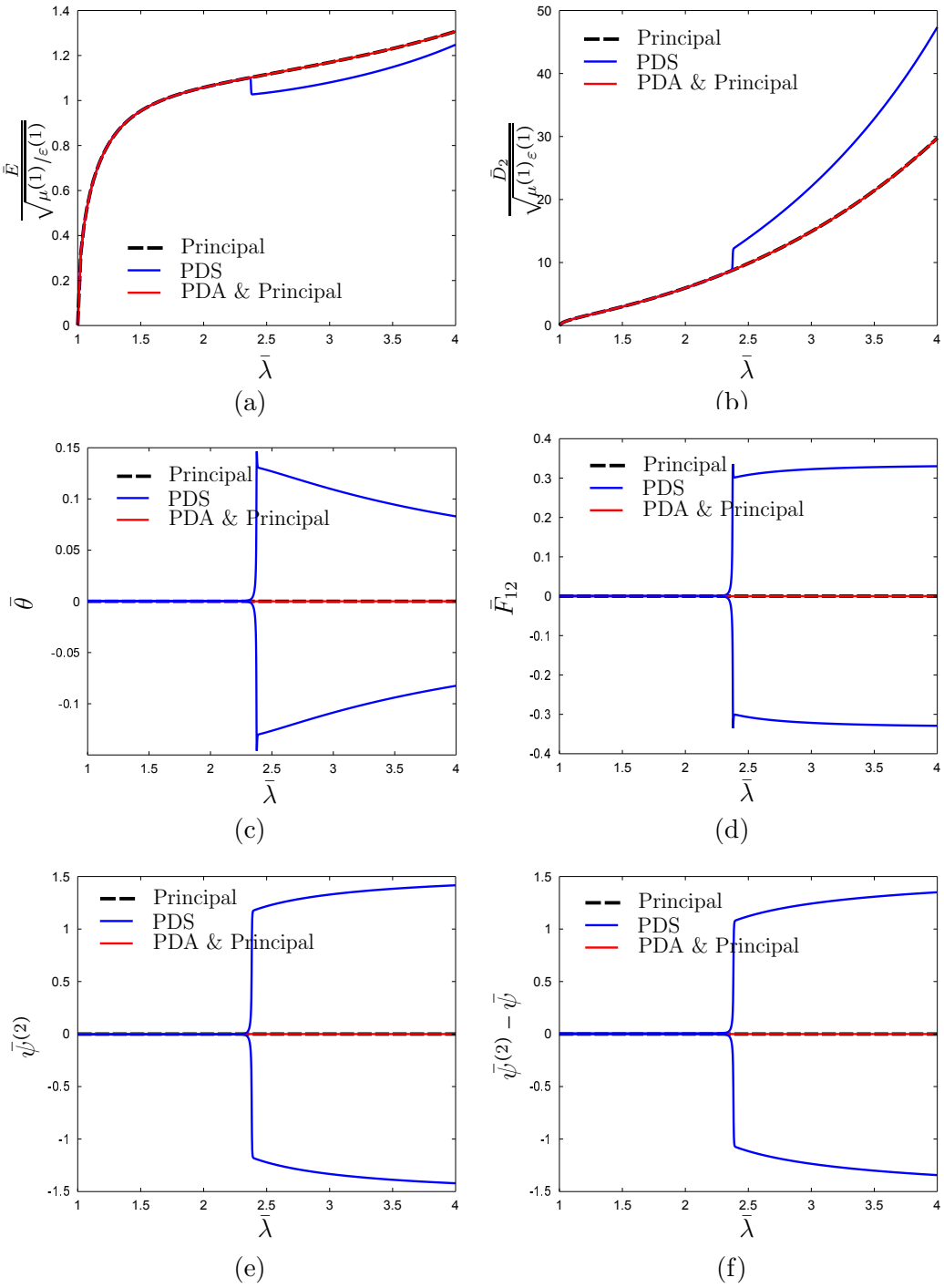


Figure 8.15: The response of a DEC with $\beta = 90°$ under the electrode boundary condition and zero external tractions. (a) Electric field, (b) electric displacement field, (c) loading angle, (d) $\bar{F}_{12}$, (e) equilibrium rotation, and (f) relative rotation as functions of $\bar{\lambda}$. In this figure $J_m = 100$, $\mathcal{E}^{(2)}/\varepsilon^{(1)} = 1000$, and $w = 2$, $c = 0.2$.

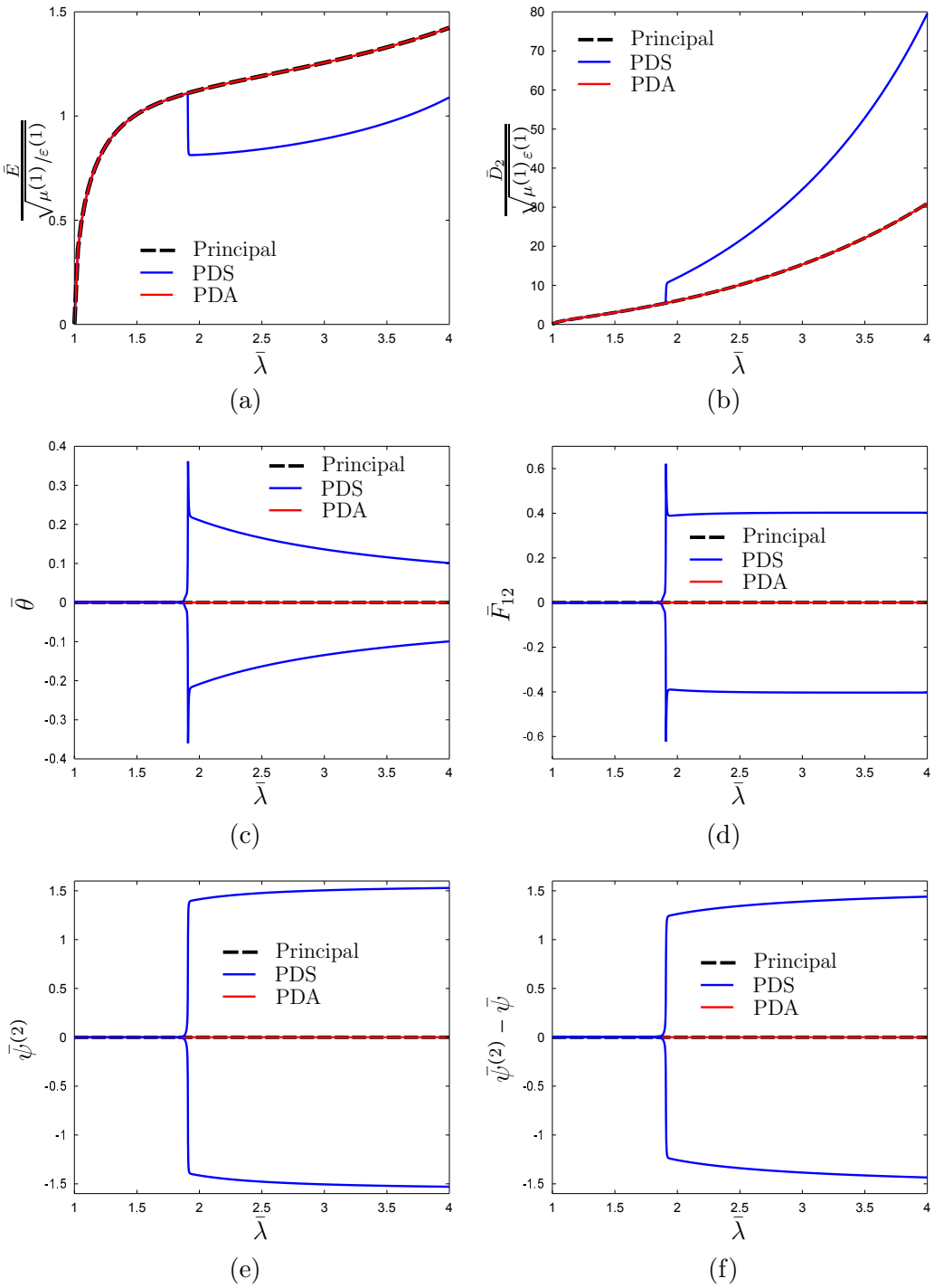


Figure 8.16: The response of a DEC with $\beta = 90°$ under the electrode boundary condition and zero external tractions. (a) Electric field, (b) electric displacement field, (c) loading angle, (d) $\bar{F}_{12}$, (e) equilibrium rotation, and (f) relative rotation as functions of $\bar{\lambda}$. In this figure $J_m = 100$, $\mathcal{E}^{(2)}/\varepsilon^{(1)} = 1000$, and $w = 3$, $c = 0.2$.

mechanical energy, and therefore corresponds to an instability of the shear band type. On the other hand, the branching of the PDS solutions for the electrode boundary conditions considered here, is seen to happen before the onset of loss of ellipticity for the principal solution, and therefore does not necessarily correspond to a shear band type instability. In the following subsection, we investigate in more details the instabilities using the more accurate PDS scheme.

### 8.2.3 Instabilities

In chapter 5 we have studied instabilities for DECs with aligned microstructures under aligned loading conditions. In this subsection we investigate such instabilities for the principal solution of aligned DECs under aligned loading conditions by using the more accurate PDS effective energies. In particular, the components of the effective electromechanical moduli (which are used in the instability conditions) will be computed by using the effective energies obtained by the PDS scheme.

Figure 8.17 shows the principal solution along with the (newly computed) instability regions for DECs with different aspect ratios, while Fig. 8.18 shows the corresponding results as computed by the prescriptions of chapter 5, for comparison purposes. Note that the aligned LPD regions are exactly identical to the corresponding results provided in chapter 5, as can be seen in Figs. 8.17 and 8.18. This is due to the fact that the second derivatives of the effective energy when computed along the loading directions are the same for the new PDS calculations and old calculations of chapter 5. On the other hand the non-aligned LPD and LE regions, as shown in Fig. 8.17, change dramatically from the corresponding calculations of chapter 5, shown in Fig. 8.18, when using the more accurate PDS energy to compute the electromechanical moduli of the DEC. Note that the non-aligned LPD and LE conditions involve second derivatives of the effective energy in directions orthogonal to the macroscopic loading directions, and such derivatives may change dramatically when using the new PDS energies.

To better understand the difference between the results shown in Figs. 8.17 and 8.18, it is useful to look at the behavior of $\tilde{A}_{1212}$ as a function of $\bar{\lambda}$ for different

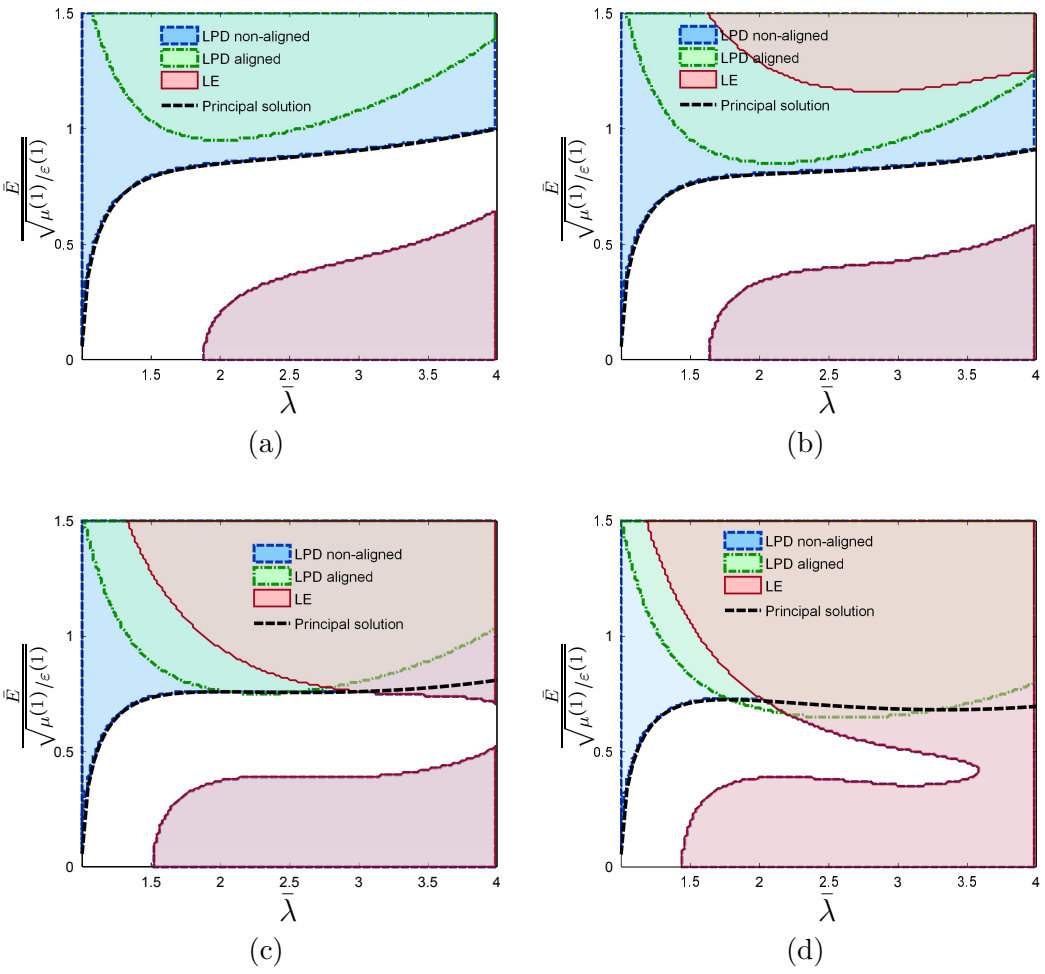


Figure 8.17: This figure shows the response curve (normalized voltage vs $\bar{\lambda}$) along with the instability regions as computed by using the new PDS effective energies. (a) $w = 2$, (b) $w = 2.5$, (c) $w = 3$, and (d) $w = 3.5$. In this figure $c = 0.2$, $J_m = 100$, and $\mathcal{E}^{(2)}/\varepsilon^{(1)} = 1000$.

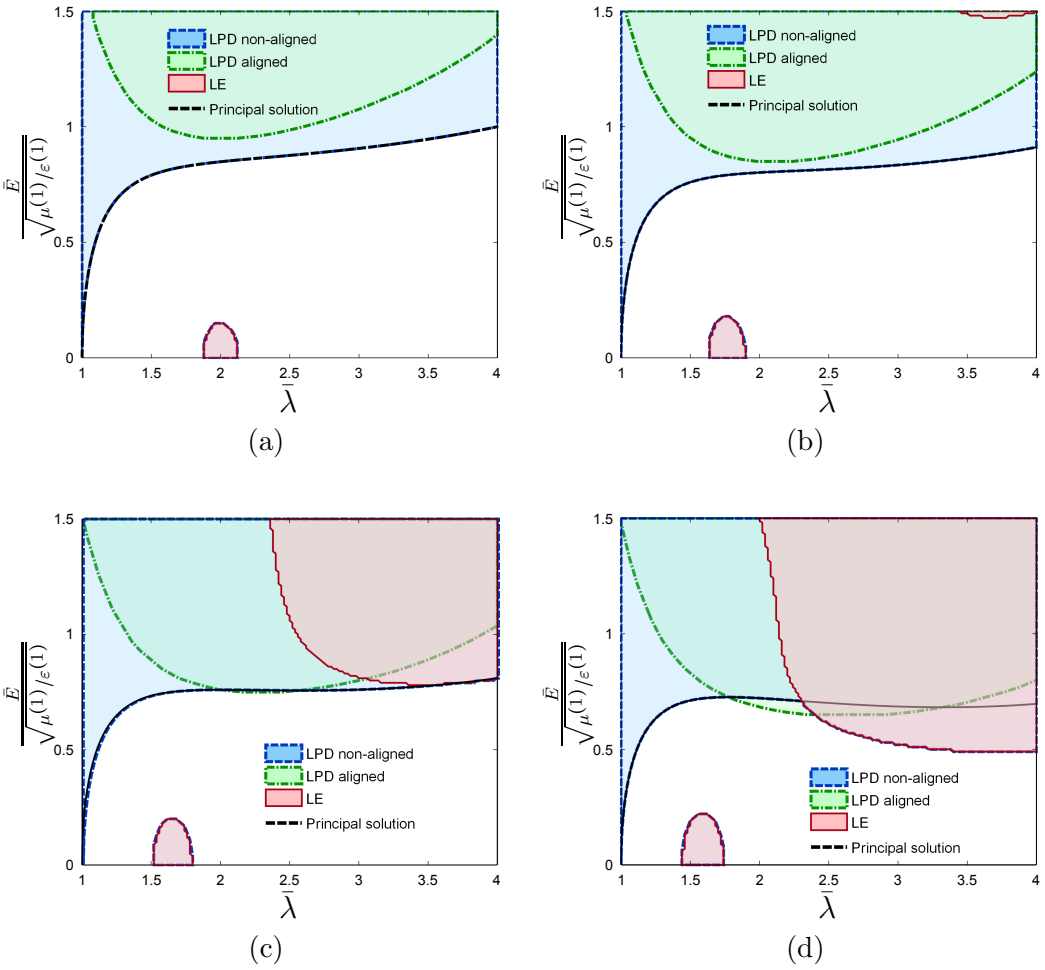


Figure 8.18: This figure shows the response curve (normalized voltage vs $\bar{\lambda}$) along with the instability regions as computed by the prescriptions of chapter 5. (a) $w = 2$, (b) $w = 2.5$, (c) $w = 3$, and (d) $w = 3.5$. In this figure $c = 0.2$, $J_m = 100$, and $\mathcal{E}^{(2)}/\varepsilon^{(1)} = 1000$.

macroscopic electric displacement fields $\bar{\mathbf{D}} = \bar{D}_2\hat{\mathbf{E}}_2$. Thus, Fig. 8.19 shows the moduli

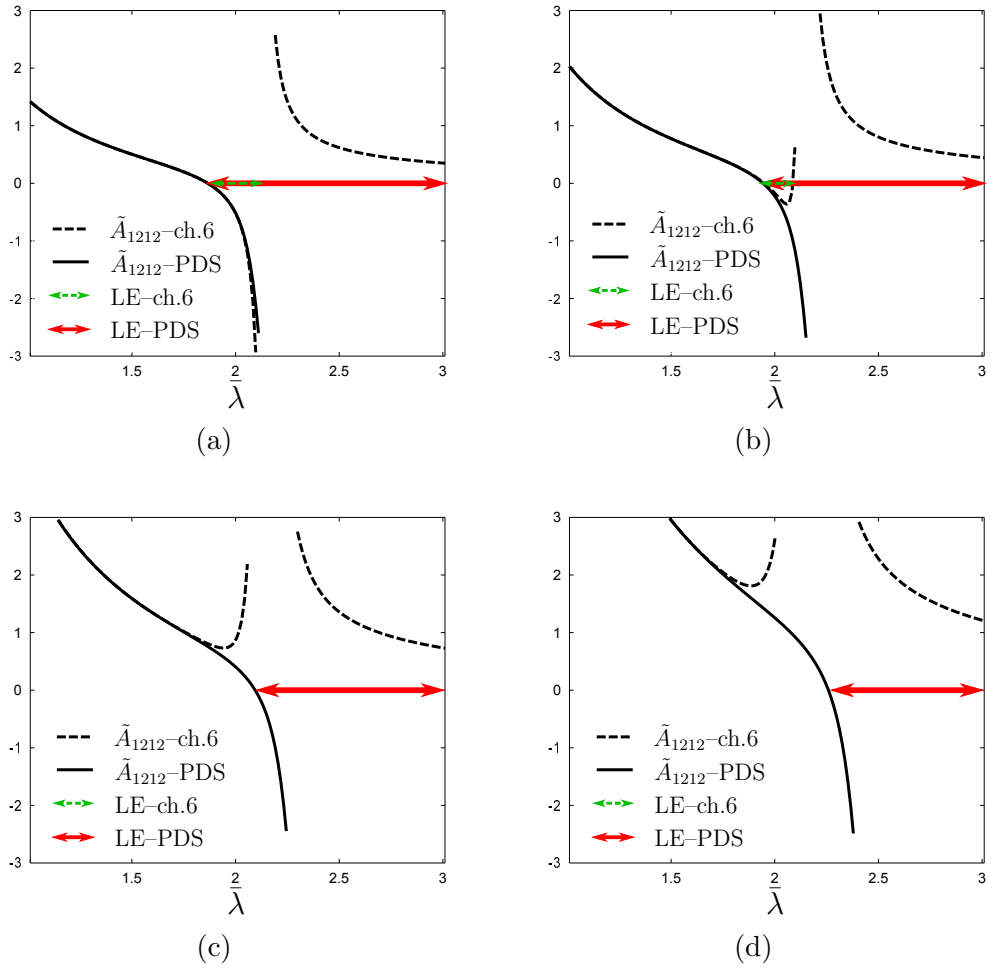


Figure 8.19: This figure shows the behavior of $\tilde{A}_{1212}$ as computed by the prescriptions of chapter 5 (dashed black line) and the new PDS scheme (solid black line). The non-elliptic regions are shown for comparison. (a) $\bar{D}_2/\sqrt{\mu^{(1)}\varepsilon^{(1)}} = 0$, (b) $\bar{D}_2/\sqrt{\mu^{(1)}\varepsilon^{(1)}} = 1$, (c) $\bar{D}_2/\sqrt{\mu^{(1)}\varepsilon^{(1)}} = 2$, and (d) $\bar{D}_2/\sqrt{\mu^{(1)}\varepsilon^{(1)}} = 3$. In this figure $c = 0.2$, $w = 2$, $J_m = 100$, $\bar{D}_1 = 0$, and $\mathcal{E}^{(2)}/\varepsilon^{(1)} = 1000$.

component $\tilde{A}_{1212}$ as obtained by the prescriptions of chapter 5 and the new PDS prescriptions. Note that the onset of an LE instability can be recognized when the moduli component $\tilde{A}_{1212}$ becomes zero. As can be seen in Fig. 8.19(a), in the absence of electric fields $\tilde{A}_{1212}$ becomes negative (for the first time) at $\bar{\lambda}_{\text{LE}} \approx 1.7$, for both calculations. However, it is seen that for larger values of the stretch (i.e., $\bar{\lambda} \gtrsim 2.2$) $\tilde{A}_{1212}$ as computed by the prescription of chapter 5 become positive, while $\tilde{A}_{1212}$ as computed by the new PDS scheme remains negative. Similar trends are observed for

$\bar{D}_2/\sqrt{\mu^{(1)}\varepsilon^{(1)}} = 1$, as shown in Fig. 8.19(b). As can be seen in Figs. 8.19(c) and 8.19(d), for larger values of the applied electric displacement (i.e., $\bar{D}_2/\sqrt{\mu^{(1)}\varepsilon^{(1)}} = 2, 3$), $\tilde{A}_{1212}$ as computed by the prescriptions of chapter 5 never becomes negative. Therefore, for certain ranges of the applied voltage fiber-constrained DECs under the electrode boundary conditions never lose ellipticity according to the calculations of chapter 5 (e.g., the DEC shown in Fig. 8.18(c) never loses ellipticity for fixed $\bar{E}/\sqrt{\mu^{(1)}/\varepsilon^{(1)}} = 0.5$). On the other hand, $\tilde{A}_{1212}$ as computed by the PDS scheme becomes negative for large enough values of $\bar{\lambda}$, even for relatively large applied fields. For this reason, according to the new calculations the principal solution is seen to lose ellipticity for large stretches (e.g., the DEC shown in Fig. 8.17(c) loses ellipticiy for $\bar{\lambda} \simeq 4.0$ at fixed $\bar{E}/\sqrt{\mu^{(1)}/\varepsilon^{(1)}} = 0.5$).

It is emphasized here that one-sided derivatives are used in the old calculations of chapter 5 for the computation of the 2nd derivatives of the energy. Such an interpretation results in positive values for the second 2nd derivatives (or curvatures) of the energy when the energy develops a kink. For this reason, the modulus component $\tilde{A}_{1212}$, as computed by the prescriptions of chapter 5, becomes positive (again) as the deformation progresses (see Figs. 8.19(a) and 8.19(b)). For the same reason $\tilde{A}_{1212}$, as computed by the prescription of chapter 5, never becomes negative for larger values of the field, as can be seen in Figs. 8.19(c) and 8.19(d). On the other hand, in the new calculations we consider a more correct "sub-differential" interpretation for the 2nd derivatives, which provide negative values for the curvature when the energy develops a kink. Therefore, $\tilde{A}_{1212}$ as computed by the new prescriptions always becomes negative for large enough deformations.

Finally, Fig. 8.20, shows the instability regions in the $\bar{t}_1$-$\bar{t}_2$ plane for different values of the electric displacement field in the $X_2$ direction. As can be seen in Figs. 8.20(a) and 8.20(b), when the applied field is zero or small (i.e., for $\bar{D}/\sqrt{\varepsilon^{(1)}\mu^{(1)}} = 0, 1.15$), the instability regions are qualitatively similar to the corresponding results of chapter 6. On the other hand, when the applied fields are larger (i.e., for $\bar{D}/\sqrt{\varepsilon^{(1)}\mu^{(1)}} = 3.45, 5.75$), the non-aligned LPD regions are seen to be different from the corresponding results of chapter 6, as shown in Figs. 8.20(c) and 8.20(d). As mentioned earlier,

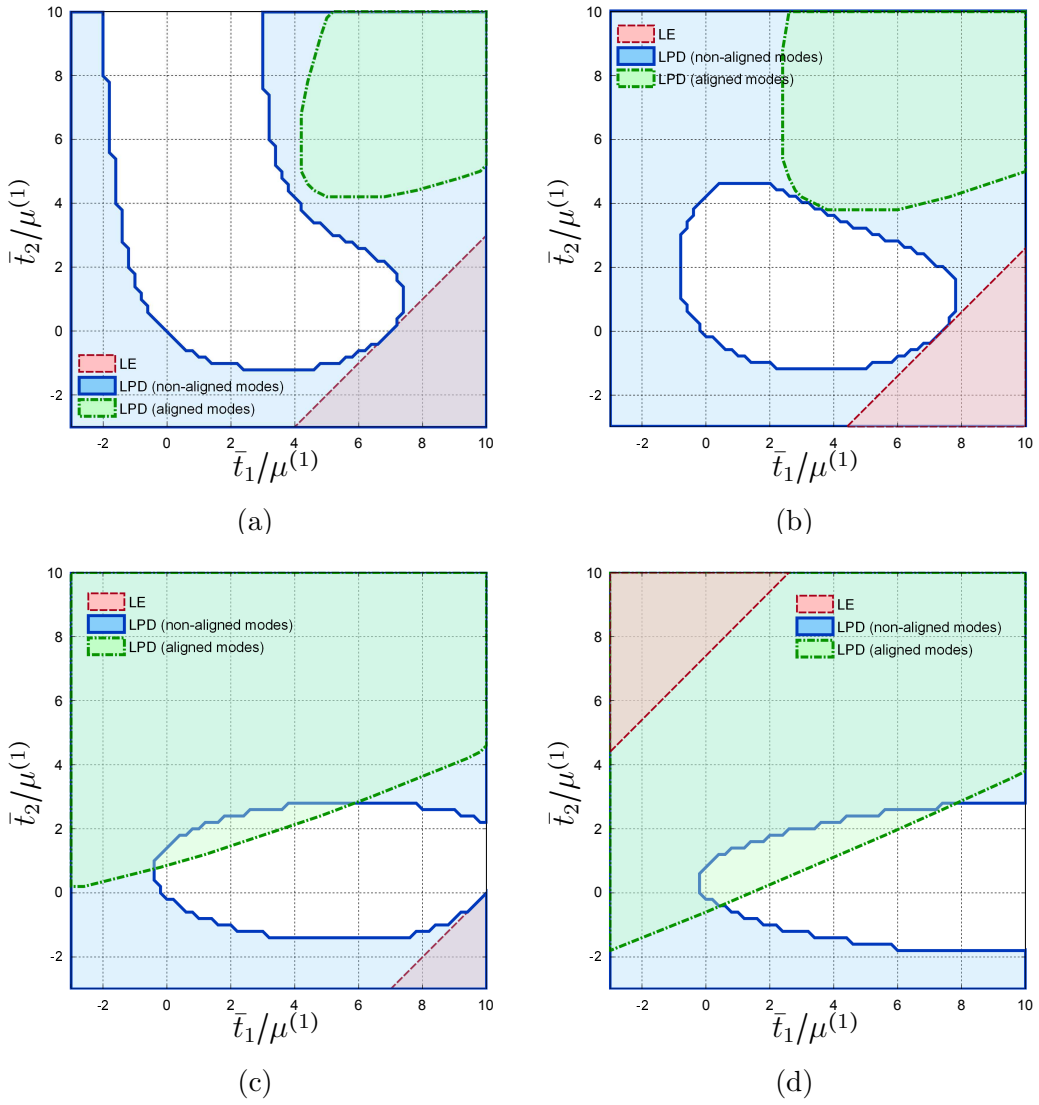


Figure 8.20: This figure shows the stability and various instability regions (on the $\bar{t}_1$-$\bar{t}_2$ plane), as computed by the new PDS scheme, for different values of the electric displacement. (a) $\bar{D}/\sqrt{\varepsilon^{(1)}\mu^{(1)}} = 0$, (b) $\bar{D}/\sqrt{\varepsilon^{(1)}\mu^{(1)}} = 1.15$, (c) $\bar{D}/\sqrt{\varepsilon^{(1)}\mu^{(1)}} = 3.45$, and (d) $\bar{D}/\sqrt{\varepsilon^{(1)}\mu^{(1)}} = 5.75$. In this figure $w = 2$, $c = 0.355$, $J_m = 100$, and $\mathcal{E}^{(2)}/\varepsilon^{(1)} = 1000$.

this is due to the fact that the non-aligned LPD condition involves second derivatives of the effective energy in directions perpendicular to the macroscopic loading directions, and such derivatives are expected to change when using the new PDS scheme.

## 8.3 Concluding remarks

In this chapter we have studied the effective response and evolution of the microstructure for fiber-constrained DECs under general non-aligned loading conditions. We have considered both the PDA scheme, in which the rotations are obtained from the solution of the purely mechanical problem, and the PDS scheme, in which the rotations are obtained via the more general conditions (8.17). We have also studied instabilities for perfectly aligned DECs under aligned loadings by using the more accurate PDS energies.

Our results show that both PDA and PDS schemes bifurcate from the principal solution for cases where $\beta = 0°$. For such cases, we have seen that the branching of the PDA solutions happens after the loss of ellipticity of the purely mechanical energy, and therefore can be recognized as a shear-band type instability. On the other hand, we have seen that the branching of the PDS results when $\beta = 0°$ happens after the loss of ellipticity of the principal solution. Thus, we have argued that the branching of the PDS solutions might be a signal for a different type of instability which happens before the loss of strong ellipticity of the principal solution, due to the electrode boundary conditions considered here. For cases where $\beta = 90°$, our results show that the PDS solutions bifurcate from the principal solution, due to the tendency of the fibers to align their longer in-plane axes with the direction of the applied field.

Finally, it is worthwhile to mention that the effective response of non-aligned DECs, as obtained in this chapter, may be used to obtain the effective response of DECs in the post-bifurcated deformation regime, which may be consisting of laminated microstructures with equal and opposite orientations for the fibers in each layer (Avazmohammadi & Ponte Castañeda 2014). As depicted in Fig. 8.21, as the

loading increases on a given loading path, the DEC follows the principal solution, in which all the fibers are aligned with each other, until the onset of an instability (e.g., loss of ellipticity). Increasing the loads beyond the onset of this instability, may

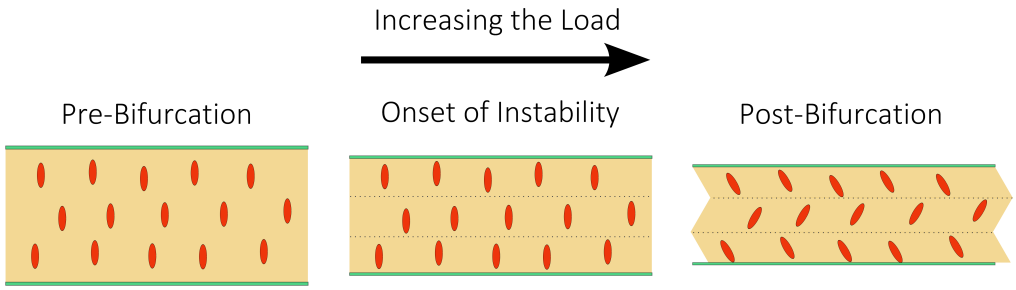


Figure 8.21: Schematics for a DEC sample developing shear band instabilities as the load increases, and a candidate form for the post-bifurcated solution which consists of a two-scale layered microstructure.

cause the initially aligned fibers to reorient themselves in such a way that a lower energy configuration is achieved. As mentioned in the introduction, this opens up the possibility of operating DECs in their post-bifurcated (and mechanically softer) deformation regimes to achieve higher electrostrictive strains.

# Chapter 9

# Closure

In this thesis we have developed a coupled homogenization framework for the effective response and stability of dielectric elastomer composites at finite deformations when subjected to coupled electromechanical loading conditions. Our homogenization framework is based on a partial decoupling strategy in which the general coupled electroelastic problem is split into a purely mechanical and an electrostatic problem which are linked together by a set of kinematical parameters–serving to characterize the evolved microstructure of the composite. The framework developed here is capable of accounting for (mechanical or electrical) inter-particle interactions. More importantly, the decoupling strategy introduced in this work enables us to accurately capture the effect of extra rotations due to the electrostatic torques exerted on the inhomogeneities by the external electric fields.

After reviewing the background materials of electroelasticity in **chapter 2**, in **chapter 3**, we have proposed the coupled homogenization framework for electroelastic composite materials at finite strains. Furthermore, this framework has been used to develop constitutive models for electro-active composites consisting of initially aligned, rigid dielectric particles distributed randomly or periodically in a dielectric elastomer matrix. A decoupling strategy has been proposed in this chapter for DECs with ideal dielectric matrix phases. The strategy consists in writing the electroelastic homogenization problem in terms of a "purely mechanical" homogenization problem in the reference configuration and a "purely electrostatic" homogenization

problem in the deformed configuration, coupled only through a set of kinematical parameters serving to describe the deformed microstructure of the DECs. For random composites or for periodic composites with a single inclusion in each unit-cell the only kinematical parameter which couples the purely mechanical and electrostatic problems is the rotation of the particles. For periodic DECs with more than one inclusion per unit-cell (e.g., in the post-bifurcation deformation regime) the set of kinematical parameters includes the new positions and orientations of all the inclusions in the unit-cell. For DECs with random microstructures, and before the onset of instabilities, the effective behavior is determined by expression (3.35) for the effective electro-elastic energy, in terms of the mechanical energy function (3.36) of a composite with prescribed particle rotations and given deformation on its boundary, and the corresponding electrostatic energy (3.50) in the deformed configuration. The corresponding expression for periodic DECs with only one inclusion in the unit cell (i.e., before the onset of instabilities), are given by (3.80), while the corresponding results for cases where each unit cell includes more than one inclusion are given by (3.74). These results may be simplified further by taking the particle rotations to be given by the solution of the corresponding purely mechanical problems when the particles are allowed to rotate freely with the imposed deformation. Such a "partial decoupling" approximation (first introduced by Ponte Castañeda & Galipeau 2011, in the context of magneto-elastic composites) has been shown recently by Siboni & Ponte Castañeda (2012) to be exact for infinitesimal deformations in the "stiff matrix" limit (i.e., when the matrix stiffness is large compared to the electric effects, so that the additional rotations due to the presence of the electric fields are negligible compared to the rotations induced by the deformation).

The new estimates for the DECs developed in **chapter 3** rely on corresponding estimates for the purely mechanical behavior of such material systems consisting of elastomers reinforced by aligned rigid inclusions. Such estimates may be obtained by means of the "second-order" linear comparison homogenization methods (Ponte Castañeda & Tiberio 2000) for both random and periodic composites (Lopez-Pamies & Ponte Castañeda 2006*b*, Brun et al. 2007, Michel et al. 2010*b*). On the other

hand, estimates for the electrostatic energy function in the deformed configuration are obtained in this chapter by adaptation of the Hashin-Shtrikman-type estimates for random or periodic DECs (Ponte Castañeda & Willis 1995, Nemat-Nasser et al. 1982) with linear dielectric behaviors for the inclusion phase. The resulting estimates lead to deformation-dependent predictions for the effective dielectric permittivity of the DECs, giving rise to "extra" stresses beyond the purely mechanical stress and the Maxwell-like stress in the composite. In other words, the macroscopic electromechanical response of the composite is not that of an "ideal dielectric elastomer" (Zhao & Suo 2008), even when the matrix material is assumed to be an ideal dielectric elastomer itself. We argue in this chapter that this phenomenon is linked to the deformation-induced configurational changes in the microstructure of the DEC. Thus, it has been found that changes in the volume fraction, distribution (i.e., the shape of the unit cell in the periodic case and the shape of the distributional ellipsoids in the random case), and orientation of the inclusions, all contribute to the electrostrictive stresses developed in DECs. While the distributional changes have an effect of order quantity squared in the initial volume fraction of the particles on the macroscopic stress, changes in the particle orientation induced by the applied deformation can be of order volume fraction, and therefore more significant for small concentrations. (This last observation is important because larger particle volume fraction although enhancing the electro-mechanical coupling in the composite also leads to a stiffer overall mechanical response for the composite, and therefore does not necessarily lead to improved actuation capabilities.)

In **chapter** 4 we have developed a general homogenization framework for DECs in the limit of infinitesimal deformations. The framework has been used to obtain estimates for the effective response of two-phase DECs with random particulate microstructures. Our results show that the addition of highly dielectric yet stiff particles can enhance the electromechanical response of DECs, for appropriate choices of the relevant microstructural parameters. This is not a trivial result since the addition of highly dielectric but stiff particles to the dielectric elastomer matrix increases both the overall permittivity and the stiffness of the DEC. While a higher overall permit-

tivity leads to an increased attractive force between the electrodes, the higher stiffness limits the overall electrostrictive strains that can be achieved. Consistent with the early theoretical results for electrostriction (Landau et al. 1984, Shkel & Klingenberg 1998), the framework developed in this work expresses the effective electromechanical coupling of the composite in terms of the derivative of the permittivity with respect to the strain, also incorporating the effect of particle rotations. In addition, it accounts for dipolar interactions between particles, as well as for the nonlinear coupling between the electric and mechanical fields. For these reasons, the new framework is expected to produce more accurate estimates than earlier estimates (Li & Rao 2004, Rao & Li 2004), especially when the field fluctuation in the matrix phase become significant (Li et al. 2004). On the other hand, while the framework developed in this chapter should be equivalent to the recently developed homogenization framework of Tian et al. (2012), the alternative expression for the electromechanical coupling in terms of the strain-dependent permittivity (instead of third moments of the electric and mechanical fields) has allowed the computation of such coupling constants for composites with general distributions of ellipsoidal inclusions, which is something that has not yet been possible with the formulation of Tian et al. (2012).

The specific estimates developed in **chapter 4** are based on homogenization estimates of Ponte Castañeda & Willis (1995) for the effective stiffness and permittivity of a certain class of random particulate microstructures consisting of aligned ellipsoidal inclusions of a stiff dielectric material distributed in an soft elastomeric matrix with "ellipsoidal" two-point statistics. For the special case of spherical particles and isotropic (spherical) distributions, the estimate for the effective permittivity reduces to the well-known Maxwell-Garnett approximation (Garnett 1904), while both estimates for the effective permittivity and elasticity are known to be rigorous lower bounds (Hashin & Shtrikman 1962, 1963) for the class of statistically isotropic microstructures in this case. In addition, for the case of rigid, perfectly conducting inclusions, the estimates do not "percolate" until 100% concentration of the inclusions, which suggests that the estimates are more appropriate for polydisperse microstructures, such as the Hashin (Hashin & Shtrikman 1962) composite-sphere as-

semblage microstructure, than for monodisperse microstructures. Our results show that the electrostriction under "soft electrode" conditions is compressive, and becomes strongest when the electric field is aligned with the long axis of the particles. This is because when the particles are not aligned with the field they tend to reorient themselves with the field producing a tensile contribution to the overall strain which tends to oppose the compression applied by the electrodes. The results also show that for a fixed, sufficiently large dielectric coefficient for the particles (compared to that of the matrix) the strongest electrostriction is achieved for certain optimal values of the particle concentration ($0 < c_0^* < 1$) and aspect ratio ($1.2 < w^* < 1.6$). Moreover, it was found that the dipole interactions tend to become dominant (over the intrinsic effect of the particles on the Maxwell stress) at sufficiently large particle concentrations, and this is why the optimal particle concentration $c_0^*$ tends to be fairly high. In addition, it was found that the electrostriction increases monotonically with the dielectric coefficient of the particles (in fact, linearly, for large values of the particle dielectric coefficient), with the optimal values of the particle concentration and aspect ratio tending to 100% and ~ 1.3, respectively. This result is consistent with earlier findings (Huang et al. 2004), which suggest that the strongest electrostrictive effect occurs near percolation of the inclusion phase. However, as already noted, the estimates used in this chapter do not "percolate" until reaching 100% of the inclusion phase, and in this sense the results are consistent. On the other hand, high particle volume fractions would tend to produce dielectric breakdown of the elastomeric matrix phase, and it would be expected that lower concentrations of the inclusion phase should be used in practical applications. In any event, the results of this chapter should serve to provide some guidelines for the design of DECs with optimal electrostriction, at least for the special class of particulate microstructures used in this work. The general theory could also be used in combination with other types of homogenization estimates, such as the effective medium approximation (Bruggeman 1935), that would be perhaps more realistic for systems that percolate at a lower concentration of the inclusion phase.

In **chapter 5** we have obtained homogenization estimates for the electromechani-

cal response of fiber-constrained DECs consisting of one family of aligned rigid dielectric fibers firmly embedded in an ideal dielectric matrix. Toward this end, we have used the decoupling strategy/approximation of Ponte Castañeda & Siboni (2012), together with analytical estimates of Lopez-Pamies & Ponte Castañeda (2006*a*) for the purely mechanical response of fiber-reinforced composites at finite strains. Using the homogenization estimates obtained in this work, we have thoroughly investigated the effects of microstructural parameters, such as the concentration and aspect ratio of the fibers, as well as of the dielectric contrast, on the overall response of DECs. In particular, we have shown that increasing the volume fraction or aspect ratio (in the direction of the applied field) of the fibers significantly enhances the electromechanical coupling in fiber-constrained DECs, due to the effects of dipolar interactions. Therefore, DECs consisting of high concentrations of fibers or large aspect ratios for the fibers require, in general, smaller voltages to achieve a given deformation state.

In addition, we have investigated the effect of microstructure on the stability and failure of fiber-constrained DECs. It has been shown that while low concentrations of fibers, serving to constrain the deformation in the plane transverse to the fibers, can be used to prevent the development of electromechanical instabilities, sufficiently high concentrations of fibers can lead to the generation of such instabilities, which are manifested by a snap-through behavior, similar to that observed in pure dielectric elastomers undergoing more general 3D deformations. In addition, it has been found that high fiber concentrations and/or large fiber aspect ratios can lead to a dramatic reduction on the overall breakdown field that the DEC can withstand, due to the field-magnification effect of the fibers. As a consequence, dielectric breakdown has been identified as the main limiting factor in the performance of these fiber-reinforced DECs. For this reason, we have also considered the effect of the fiber permittivity on the macroscopic response and failure instabilities in these DECs. According to our theoretical predictions, composites with smaller contrasts in the dielectric constant of the phases can actually achieve higher overall electrostrictive strains before failure. In fact, for composites with vanishingly small dielectric contrast, the overall breakdown field becomes that of the pure matrix phase, and as a consequence such composites

can withstand larger applied electric fields and achieve larger electrostrictive strains.

We have also considered the effect of externally applied mechanical tractions on the response and stability of DECs. Our results show that the application of external tractions in the direction perpendicular to the applied electric field (and to the fibers) can be used to reduce, or eliminate altogether the possible development of electromechanical (or snap-through) instabilities, characterized by loss of positive definiteness with aligned eigenmodes, in agreement with similar findings for homogeneous ideal dielectrics under 3D equal-biaxial loading conditions (Lu et al. 2012). However, although the terminal stretch before breakdown increases with increasing traction, the portion of the stretch that is solely due to the electric potential (i.e., the electrostriction) is still relatively small. In this context, it is also important to note that for composites consisting of elliptical fibers with the longer (in-plane) axis aligned with the electric field, the mechanical traction cannot be increased arbitrarily since the composite may experience shear localization instabilities, as determined by the loss of strong ellipticity condition. This suggest the possibility of using electric fields to control the onset of these instabilities, which may be desirable in certain applications.

Inspired by the above findings for the effect of the various material and microstructural parameters, we have developed a systematic procedure for the optimal design of DECs that are capable of achieving large electrostrictions—in excess of 100% strain—before failure. Due to the severe restrictions imposed by dielectric breakdown, composites consisting of a very small concentration of rigid circular fibers with vanishing contrast in the dielectric properties can achieve the largest electrostrictive strains. It is emphasized, however, that although smaller fiber concentrations result in larger electrostrictive strains, the concentration of the fibers cannot be arbitrarily small. In fact, there exists a critical value for the concentration, which depends on the tensile strength of the fiber material, to ensure that the fibers do not break and the constraint of 2D plane-strain deformations is satisfied for the DECs. The optimized microstructures suggested by our analytical model are found to be generally consistent with recent experimental findings of Lu et al. (2012) and Bolzmacher et al. (2006).

In **chapter 6** we have carried out a preliminary investigation on the possible development of instabilities in a certain class of fiber-constrained dielectric elastomer composites subjected to all-around dead electromechanical loading under plane-strain conditions. Three types of "material" instabilities were considered: loss of positive definiteness (LPD) with "aligned" eigenmodes, loss of positive definiteness with "non-aligned" eigenmodes, and loss of strong ellipticity (LE). Loss of positive definiteness simply corresponds to the loss of local convexity of the homogenized electro-elastic stored-energy function for the DECs (Bertoldi & Gei 2011). For the aligned cases, the (local) convexity is lost for increments that are aligned with the loading direction, and typically manifest themselves as "limit load" behavior either in the mechanical or electrical response, while for the non-aligned case the convexity is lost for increments that are orthogonal to the loading direction, and could correspond to bifurcations from the principal solution. The loss of strong ellipticity, on the other hand, corresponds to loss of positive definiteness of the electromechanical acoustic tensor (Dorfmann & Ogden 2010*a*) and manifests itself by the onset of highly localized shear band instabilities. Loss of ellipticity normally takes place after loss of convexity, but the two can occur simultaneously for special circumstances.

Our results show that the stability of the DECs depends sensitively on the loading conditions (i.e., the applied tractions on the sample and electric displacement fields in the $X_2$ direction) and is also affected by the microstructure of the DECs (i.e., the volume fraction of the fibers and their aspect ratio). It is worth mentioning that for the range of tractions considered in our work, the strain-locking parameter does not have a significant effect on the onset of instabilities. According to our results, only the first two types of LPD instabilities are normally observed for DECs with in-plane isotropic microstructures, corresponding to randomly distributed fibers of circular cross-section, including as a special case the ideal dielectric matrix phase. However, anisotropy of the in-plane microstructure—in the form of fibers of elliptical cross section that are aligned with the loading directions—allows for the possible development of shear localization instabilities under conditions involving compressive electromechanical stresses along the long (in-plane) axis of the fibers. More specifically, it

is found that the non-aligned LPD instabilities typically precede aligned LPD and LE instabilities, especially for in-plane isotropic microstructures, but aligned (limit load) LPD and LE instabilities can also be critical for composites with anisotropic microstructures. In this context, it should be noted that the possible development of non-aligned LPD bifurcation instabilities appears to have been ignored in prior analysis of the problem for ideal dielectric (Zhao & Suo 2007, Zhao et al. 2007) and layered dielectrics (Bertoldi & Gei 2011, Rudykh & deBotton 2011). Fortunately, however, such instabilities can usually be avoided by orienting the long (in-plane) axis of the fibers parallel to the tensile stress direction and orthogonal to the applied electric field. It should also be noted that our work can be considered a generalization of the plane-strain works of Huang, Li, Foo, Zhu, Clarke & Suo (2012) for (isotropic) ideal dielectric elastomers and of Bertoldi & Gei (2011) for (anisotropic) layered dielectrics in that both limits can be recovered in principle by taking the elliptical cross section of the fibers to be circular ($w = 1$) or flat ($w = 0$), respectively. (In the first case, the fiber concentration $c$ must also be taken to be infinitesimal to compare with the corresponding results of Huang, Li, Foo, Zhu, Clarke & Suo (2012).) Our work also provides new results in the purely mechanical context for all-around dead tractions of the fiber-reinforced elastomers with non-circular (i.e., elliptical) cross section, where the in-plane response is orthotropic (Hill & Hutchinson 1975). Thus, our work also provides a specific example generalizing the results of Ogden (1985) for in-plane isotropic response, although a global analysis was not attempted here.

We have found that for uni-axial tension loadings in the $X_1$ direction, the presence of an electric displacement field in the $X_2$ direction has no effect on the stability of DECs with $w \leq 1$ (see Figs. 6.2 and 6.4, for example). For DECs with $w > 1$, however, the effect of the electric displacement field on the stability is more complicated, as shown in Fig. 6.3. In particular, we have shown that for such composites the onset of first instability is delayed for larger values of the electric displacement field up to a limiting value. For values of the electric displacement field beyond the limiting value, the composites is shown to remain stable as the traction $\bar{t}_1 = \bar{t} > 0$ increases. Therefore, one can say that for small and moderate fields, the presence of an electric

displacement field has an stabilizing effect on DECs. On the other hand, large electric displacement fields can have a destabilizing effect on the DEC. In fact, we have shown that the specific DEC considered in Fig. 6.3 can become unstable (via an aligned instability mode) by only increasing the electric displacement field at zero external tractions.

For uni-axial tension loadings in the $X_2$ direction, we have shown that the presence of an electric displacement field in the $X_2$ direction always has destabilizing effects on the DECs. The first instability observed on such a loading path depends on the microstructure. More specifically, for isotropic DECs (and also for the homogeneous ideal dielectrics) the first instability observed is the loss of positive definiteness with a non-aligned eigenmode, as shown in Fig. 6.2. Similar to the isotropic composites, the first instability for DECs consisting of elliptical fibers with $w > 1$ is loss of positive definiteness. The mode for the instability, however, depends on the intensity of the electric field. More specifically, for smaller fields the first instability is of the non-aligned type (see Fig. 6.3(b), for example), while for larger fields the first instability encountered is of the aligned type (see Figs. 6.3(c) and 6.3(d), for example). For DECs consisting of elliptical fibers with $w < 1$, the first instability on uni-axial tension loadings in the $X_2$ direction is loss of positive definiteness with a non-aligned eigenmode, independent of the magnitude of the electric displacement field. At zero field, however the first instability encountered on the above-mentioned loading path is of the shear band type, as can be seen in Fig. 6.4(a).

For symmetric loadings of the form $\bar{t}_1 = \bar{t}_2 = \bar{t} > 0$, our results show that the presence of an electric displacement field has a destabilizing effect independent of the microstructure, such that the magnitude of the critical (symmetric) traction at the bifurcation point decreases by increasing the electric displacement field. For isotropic DECs the first instability encountered is the loss of positive definiteness. As shown in Fig. 6.2 both aligned and non-aligned modes happen at the same time when an isotropic DEC loses positive definiteness for the first time. For this reason any linear combination of these two eigenmodes is also an eigenmode for instability. For the purely mechanical case (i.e., in the absence of the electric fields) this implies that the

incremental deformation at this critical point is a pure shear in the $X_1$-$X_2$ plane with an arbitrary angle (consistent with the findings of Ogden 1985). Similarly, when an electric displacement field is present, the increments generally consist of a pure shear and an electric displacement with one arbitrary parameter which specifies their orientation in the $X_1$-$X_2$ plane. For DECs consisting of elliptical fibers with $w > 1$, the first instability encountered on a symmetric loading path is loss of positive definiteness, however, the eigenmode depends strongly on the intensity of the electric displacement field. In particular, as can be seen in Fig. 6.3, for small electric displacement fields the first instability has a non-aligned eigenmode, while for large enough fields the first instability encountered on a symmetric loading path has an aligned eigenmode. Finally, our results show that composites consisting of elliptical fibers with $w < 1$ always lose positive definiteness with a non-aligned mode on a symmetric loading path, as shown in Fig. 6.4.

Our results also show that composites with a fixed concentration of fibers with larger aspect ratios lose ellipticity for a smaller critical traction $\bar{t}_1 = \bar{t}_1^c > 0$, when the electric displacement field is held fixed below a limiting value. Furthermore, as can be seen in Fig. 6.5, composites consisting of fibers with large aspect ratios may lose positive definiteness (via the aligned modes) by increasing the electric displacement field, while the traction $\bar{t}_1$ is held fixed. On the other hand, our results show that for a fixed aspect ratio $w > 1$, DECs with larger concentration of rigid fibers can withstand larger tractions in the $X_1$ direction before the onset of shear bands. Similar to the DECs consisting of fibers with large aspect ratios, DECs consisting of large concentrations of fibers may become unstable (via the aligned modes) by just increasing the electric displacement field, while the traction $\bar{t}_1$ is held fixed (see Fig. 6.6, for example).

Finally, our results indicate that the points on the boundary of the aligned regions correspond to a maximum in the electrostatic response (characterized by the nominal electric field as a function of the nominal electric displacement) of DECs when the external nominal traction is held fixed (refer to Fig. 6.7, for the details). This result can be considered as the generalization of the corresponding observation for and ideal

dielectric under 3D equal-biaxial dead (nominal) tracitons considered by Zhao & Suo (2007).

In particular, it was found out that, at a fixed applied electric field, composites with higher volume fraction of fibers can actually sustain higher levels of applied tractions before failure, while composites containing fibers with higher aspect ratios tend to become unstable at lower levels of applied tractions. Moreover, our analysis indicate that application of an electric field always tends to destabilize the DECs when subjected to a tensile traction aligned with the field direction. However, application of an electric field perpendicular to the tensile traction may have a stabilizing or destabilizing effect depending on the shape of fibers. For the case of circular fibers ($w = 1$), we found that the composite under a tensile traction remains stable when an electric filed is applied perpendicular to the traction axis. For the case of elongated fibers ($w > 1$), the results indicate that macroscopic instabilities characterized by the LE of the homogenized behavior may develop when the traction transverse to the long axis of particles reaches a critical value $\bar{t}^{cr}$. In this case, although application of an electric fields with small magnitudes along the long axis of the fibers can prevent development of macroscopic instabilities, sufficiently higher magnitudes of the electric field may drive instabilities associated with the LPD of the homogenized behavior even for the case of zero traction ($\bar{t}_1 = 0$). We showed that these inabilities correspond to the maximum in $E$ in the $\bar{D} - \bar{E}$ response curve, similar to finding in homogeneous ideal dielectrics subjected to 3-D tractions and an electric field (Suo's paper). In contrast, for the case of flat fiber ($w < 1$), it was found out that application of an electric field perpendicular to the long axis of the fibers can never destabilize the composite, when subjected to a tensile load along the long axis of the fibers.

In **chapter 7** we have provided an explicit expression for the effective purely mechanical response of fiber-constrained composites with prescribed in-plane rotations for the fibers. This was done by introducing a new variational problem with modified phase energies to account for the effects of external body couples. The final expression for effective energy of two-phase composites consisting of incompressible Gent matrix phases and rigid fibers undergoing 2D plane-strain deformations is given in (7.58).

This expression was seen to be identical in form with the corresponding expression in Lopez-Pamies & Ponte Castañeda (2006*a*), with the only difference that the rotation of the fibers in (7.58) is prescribed. We have also argued that the above property is not an exclusive feature of the problem addressed in this chapter, and may as well hold for other cases.

In **chapter** 8 we have studied DECs under non-aligned loading conditions by using the partial decoupling approximation (PDA) and partial decoupling strategy (PDS) schemes. Our results for the effective response of non-aligned DECs under the electrode boundary condition show that for small fields the differences between the PDA and PDS response curves are negligible, while for larger fields such differences are more significant. We have also studied the instabilities for aligned DECs under the electrode boundary condition using the new PDS effective energy to compute the second derivatives of the energy (required for the evaluation of the instability criteria), and compared them with the corresponding results of chapters 5 and 6. Our results show that the aligned LPD regions remain unchanged when using the new PDS energy, while the non-aligned LPD and LE regions undergo dramatic changes. The results of this chapter for non-aligned cases are necessary to obtain the effective response of DECs in the post-bifurcated deformation regimes, which are expected to consist of two-scale layered microstructures (see Avazmohammadi & Ponte Castañeda 2014, for the corresponding problem in the purely mechanical context).

# Appendix

# Appendix A

# Incremental stability conditions: purely mechanical case

In this appendix, we consider the incremental stability of the orthotropic DECs subjected to aligned purely mechanical loadings (i.e, $\bar{\mathbf{D}} = \mathbf{0}$) under plane-strain conditions. For this special case, the incremental stability condition (2.37) simplifies to

$$\mathcal{Q} = \left(A_{1111} + A_{2222} - 2A_{1122} + 2p\right) H_{11}^2 + A_{1212} H_{12}^2 + A_{2121} H_{21}^2 + 2\left(A_{1221} + p\right) H_{12} H_{21} > 0, \tag{A.1}$$

where the $H_{ij} = u_{i,j}$ $(i, j = 1, 2)$ denote the components of the displacement gradient. In obtaining (A.1) we used the fact that the non-aligned components of the tangent moduli tensor are identically zero ($A_{1112} = A_{1121} = A_{2212} = A_{2221} = 0$) for aligned loadings. The quadratic form $\mathcal{Q}$ is positive definite if all the eigenvalues of the associated Hessian matrix, defined in (5.33), are positive. Thus, the necessary and sufficient conditions for the positive definiteness of $\mathcal{Q}$ are

$$\begin{aligned} &0 < \left(A_{1212} + A_{2121}\right) \pm \sqrt{\left(A_{1212} - A_{2121}\right)^2 + \left[2\left(A_{1221} + p\right)\right]^2}, \quad \text{and} \\ &0 < A_{1111} + A_{2222} - 2A_{1122} + 2p. \end{aligned} \tag{A.2}$$

Defining the shear moduli

$$\mu := \frac{1}{2}\left(A_{1212} + A_{2121}\right) \quad \text{and} \quad \mu^* := \frac{1}{4}\left[2\mu + A_{1111} + A_{2222} - 2\left(A_{1122} + A_{1221}\right)\right], \tag{A.3}$$

conditions, (A.2) can be shown to be equivalent to

$$2\mu^* > \mu - \left(A_{1221} + p\right), \quad \mu > 0, \quad \text{and} \quad 2\mu > \sqrt{\left(A_{1212} - A_{2121}\right)^2 + \left[2\left(A_{1221} + p\right)\right]^2}. \tag{A.4}$$

We remark that $\mu$ and $\mu^*$ are the same shear moduli introduced by Hill & Hutchinson (1975) to characterize the incremental response of a general class of initially orthotropic, incompressible solids subjected to aligned plane-strain loading. This can be verified by comparing the incremental constitutive relations (2.28) with the corresponding relations provided by equation (2.6) of Hill & Hutchinson (1975). Furthermore, comparison of relation (2.28) with relation (2.6) of Hill & Hutchinson (1975) reveals the following relations between the Cauchy tractions $t_1$, $t_2$ and the pertinent components of the tangent moduli tensor

$$t_1 - t_2 = A_{2121} - A_{1212}, \quad \text{and} \quad t_1 + t_2 + 2p = 2\mu - 2A_{1221}. \tag{A.5}$$

Making use of the above relations, inequalities (A.4) can be rewritten as

$$4\mu^* > t_1 + t_2, \quad \mu > 0, \quad \text{and} \quad 2\mu\left(t_1 + t_2\right) > t_1^2 + t_2^2, \tag{A.6}$$

which can be shown to be equivalent to

$$4\mu^* > t_1 + t_2 > 0, \quad \text{and} \quad 2\mu > \frac{t_1^2 + t_2^2}{t_1 + t_2}. \tag{A.7}$$

These exclusion conditions were obtained by Hill & Hutchinson (1975) when considering the incremental stability of the above-mentioned class of orthotropic solids subjected to aligned, in-plane tractions $t_1$ and $t_2$ (see equation (3.9) in Hill & Hutchinson (1975)).

For the special case of *isotropic* hyperelastic solids with stored-energy function $W(\lambda)$, the shear moduli $\mu$ and $\mu^*$ in (A.3) can be written as

$$\mu = \frac{1}{2}\frac{\lambda^4+1}{\lambda^4-1}\times\lambda\frac{dW}{d\lambda} = \frac{1}{2}\frac{\lambda^4+1}{\lambda^4-1}(t_1-t_2) \quad \text{and} \quad \mu^* = \frac{\lambda}{4}\left(\frac{dW}{d\lambda}+\lambda\frac{d^2W}{d\lambda^2}\right), \tag{A.8}$$

respectively. Substituting these two expressions into the conditions (A.7), we obtain

$$\lambda\left(\frac{dW}{d\lambda}+\lambda\frac{d^2W}{d\lambda^2}\right) > t_1+t_2, \quad \text{and} \tag{A.9}$$

$$t_1+t_2>0, \quad \frac{\lambda^4+1}{\lambda^4-1}(t_1-t_2) > \frac{t_1^2+t_2^2}{t_1+t_2}. \tag{A.10}$$

These conditions are equivalent to those provided by Ogden (1985) for the case of initially isotropic incompressible solids subjected to in-plane tractions $t_1$ and $t_2$. More specifically, condition (A.9) can be seen to be identical with condition (29) of Ogden (1985). Also, the two conditions in (A.10) can be equivalently expressed as

$$t_1+\lambda^2 t_2>0 \quad \text{and} \quad \frac{t_1-\lambda^2 t_2}{\lambda^2-1}>0, \tag{A.11}$$

which are identical to conditions (30) and (31), respectively, in Ogden's paper. In this regard, note that the Biot stresses $t_1^{(1)}$ and $t_2^{(1)}$ used in Ogden's conditions are related to the Cauchy stresses via the identities $t_1^{(1)} = t_1/\lambda$ and $t_2^{(1)} = \lambda t_2$.

Finally, returning to the case of orthotropic hyperelastic solids, we emphasize that the stability conditions (A.4) depend, in general, on the pressure $p$, which can be determined from traction boundary conditions. For instance, for the special case of a uniaxial tension test in the $X_1$ direction (i.e., when $t_2 = 0$), the pressure $p$ can be determined from relations (A.5), together with $(A.3)_1$, as follows

$$p = A_{1212} - A_{1221}. \tag{A.12}$$

Substituting $p$ from (A.12) into the conditions (A.4) for positive definiteness, it follows

that

$$A_{1212} > 0, \quad A_{2121} > A_{1212}, \quad \text{and} \quad \frac{1}{2}\left(A_{1111} + A_{2222}\right) - \left(A_{1122} + A_{1221}\right) + A_{1212} > 0. \tag{A.13}$$

For comparison purposes, we recall the strong ellipticity conditions for an incompressible hyperelastic solid under aligned loading conditions. They are given by (Hill 1979)

$$A_{1212} > 0, \quad A_{2121} > 0, \quad \text{and} \quad \frac{1}{2}\left(A_{1111} + A_{2222}\right) - \left(A_{1122} + A_{1221}\right) + \sqrt{A_{1212}A_{2121}} > 0. \tag{A.14}$$

It is interesting to note that conditions (A.13) for the incremental stability of the DECs under purely mechanical uniaxial tensile loadings are more restrictive than conditions (A.14) for the strong ellipticity of the composite material.

For a stored-energy function of the form $W(\lambda, \theta)$, the pertinent traces of the instantaneous moduli tensor $\mathbb{A}$ can be expressed as

$$\begin{aligned} A_{1212} &= \frac{\lambda}{\left(\lambda^4-1\right)^2}\left[\left(\lambda^4-1\right)\frac{\partial}{\partial\lambda} + \lambda^3\frac{\partial^2}{\partial\theta^2}\right]W, \; A_{2121} = \frac{\lambda^4}{\left(\lambda^4-1\right)^2}\left[\lambda\left(\lambda^4-1\right)\frac{\partial}{\partial\lambda} + \frac{\partial^2}{\partial\theta^2}\right]W, \\ \left(A_{1111}+A_{2222}\right) - 2\left(A_{1122}+A_{1221}\right) &= \frac{\lambda}{\left(\lambda^4-1\right)^2}\left[\lambda\left(\lambda^4-1\right)^2\frac{\partial^2}{\partial\lambda^2} - 2\left(\lambda^4-1\right)\frac{\partial}{\partial\lambda} - 2\lambda^3\frac{\partial^2}{\partial\theta^2}\right]W, \end{aligned} \tag{A.15}$$

where all derivatives are evaluated at $\theta = 0$ (i.e., the aligned loading condition.) Making use of the above moduli traces, the stability conditions (A.13) reduce to

$$\left(\lambda^4 - 1\right)\frac{\partial W}{\partial\lambda} + \lambda^3\frac{\partial^2 W}{\partial\theta^2} > 0, \quad \frac{\partial W}{\partial\lambda} > 0, \quad \text{and} \quad \frac{\partial^2 W}{\partial\lambda^2} > 0, \tag{A.16}$$

Similarly, making use of (A.15), the strong ellipticity conditions (A.14) may be written

as

$$
\begin{aligned}
&(\lambda^4-1)\frac{\partial W}{\partial \lambda}+\lambda^3\frac{\partial^2 W}{\partial \theta^2}>0, \quad \lambda(\lambda^4-1)\frac{\partial W}{\partial \lambda}+\frac{\partial^2 W}{\partial \theta^2}>0,\\
&\frac{1}{2}\left[\lambda(\lambda^4-1)^2\frac{\partial^2 W}{\partial \lambda^2}-2(\lambda^4-1)\frac{\partial W}{\partial \lambda}-2\lambda^3\frac{\partial^2 W}{\partial \theta^2}\right]\\
&+\lambda\sqrt{\lambda}\left[\lambda(\lambda^4-1)^2\left(\frac{\partial W}{\partial \lambda}\right)^2+\lambda^3\left(\frac{\partial^2 W}{\partial \theta^2}\right)^2+(\lambda^8-1)\frac{\partial W}{\partial \lambda}\frac{\partial^2 W}{\partial \theta^2}\right]^{\frac{1}{2}}>0, \qquad \text{(A.17)}
\end{aligned}
$$

# Appendix B

# The single inclusion problem

This appendix deals with the problem of an isolated, rigid inclusion with linear-magnetic behaviour embedded in a linear-elastic matrix. Under the hypothesis of infinitesimal deformations, an analytical expression is obtained for the equilibrium rotation of the magnetic inclusion under general magneto-mechanical loading conditions. The results show that the inclusion undergoes an 'extra' rotation due to the presence of the non-aligned magnetic fields (even in the absence of mechanical loadings). Moreover, this extra rotation is found to depend on the shape of the inclusion, as well as on its magnetic anisotropy. Thus, the extra rotation increases monotonically to an asymptote with increasing magnetic anisotropy of the inclusion, while, for the fixed magnetic behavior of the inclusion, the extra rotation increases up to a maximum with increasing aspect ratio, and then decays to zero. It is remarked that, even though the results of this chapter are for the magnetic problem, they can be easily translated into the corresponding results in the electro-active case.

## B.1 Introduction

The problem of an isolated inclusion in an infinite surrounding matrix, also known as the single-impurity problem, is a central problem in the theory of composite materials, and other heterogeneous media. In the context of linear elasticity, a general solution for a single ellipsoidal inclusion of one material embedded in a matrix of a

second material was provided by Eshelby in a highly-cited paper (Eshelby 1957) . The main feature of this solution—which was known much earlier in the context of electrostatics (e.g. Maxwell 1873) —is that the stress and strain fields are uniform inside the ellipsoidal inclusion. This feature has made possible the development of dilute and effective medium theories for composites containing random distributions of such inclusions (Willis 1981) . Because of this, generalizations of Eshelby's solution, and of some of the methods that are based on it, have been developed for magneto-elastic composites with piezomagnetic coupling in recent years (e.g. Benveniste 1992, Dunn & Taya 1993, Huang et al. 1998).

This work is concerned with magneto-elastic systems of a different type, involving coupled behavior through the Maxwell stress. It is well-known (e.g. Landau et al. 1984) that an externally applied magnetic field gives rise to forces and torques on magnetically susceptible particles. When such particles are embedded in an elastic matrix (even if it is not itself magnetically susceptible), the externally applied magnetic field can generate stress and strain fields in the matrix material, as a consequence of the forces and torques that are transmitted by the particles to the surrounding matrix. These stresses and strains can combine with corresponding stresses and strains arising solely from purely mechanical sources to produce interesting coupled magneto-elastic behavior, such as magnetostriction. In this connection, it should be noted that the magnitude of the Maxwell stresses that are generated in the matrix material are quadratic in the magnetic field and can therefore be significant for large values of the fields (even if the effect is limited by the magnetic saturation of the particles).

Magnetorheological elastomers, which consist of very stiff magnetic inclusions embedded in relatively soft elastic matrices (Ginder et al. 1999, 2002, Guan et al. 2008), are composite materials which attempt to exploit the above described mechanism to generate large field-induced (i.e. magnetostrictive) strains. These materials are examples of 'smart' materials, which can be useful in many applications as actuators and sensors, as well as artificial analogues of muscles. Recent papers by Borcea & Bruno (2001) and Yin et al. (2006) have addressed the effects of dipole forces between particles, and their implications for the constitutive behavior of such materials. In

addition, Liu et al. (2006) have generated variational estimates for elastic-matrix composites with a dilute concentration of a certain type of (deformable) magnetostrictive particles. However, it appears that, to date, no systematic attempts have been made to describe the effects of the magnetic torques that would be expected to develop when the particles have a geometric shape and/or magnetic anisotropy. To this end, we develop in this appendix, building on the work of Eshelby and others, an analytical solution for a single, rigid inclusion with linear, anisotropic magnetic behavior that is embedded in a non-magnetic, linear-elastic matrix.

The appendix is organized as follows. Section B.2 provides a quick review of magneto-elasticity, where we present the governing equations, as well as the constitutive equations for the two special classes of materials involved: rigid materials with linear magnetic behavior and elastomers with linear elastic, non-magnetic behavior. In addition, the problem for the magnetic ellipsoidal inclusion in an elastic matrix is formulated, and the general strategy for solving the problem in terms of two auxiliary problems in magnetostatics and linear elasticity is introduced. In Section B.3 we address the magnetostatics problem of the single rigid inclusion with linear magnetic behavior in the deformed configuration, by means of the integral equation formulation of Willis (1977). Furthermore, we obtain an explicit formula for the force and torque exerted on the inclusion by the external magnetic field. Section B.4 is devoted to the elasticity problem of a single rigid inclusion in an infinite elastic matrix under the combined action of an externally applied deformation and a prescribed rotation of the inclusion (Walpole 1991) . Using the results of Section B.3 and Section B.4 for the magnetic and mechanical inclusion problems, together with the fact that the Maxwell stress in the surrounding elastic matrix is self-equilibrated, we obtain an expression in Section B.5 for the equilibrium rotation of a rigid inclusion with general ellipsoidal shape and magnetic anisotropy in an infinite elastic matrix under both mechanical and magnetic loading of the system. More specifically, we show that, in the presence of an external magnetic field, the inclusion can undergo an extra rotation in addition to the Eshelby-type, mechanically driven rotation. In Section B.6 an analytical expression is obtained for the in-plane rotation of the isolated inclusion

under appropriate loading conditions, and the results are analyzed for some special cases. In addition, the analytical results are compared with the results of a simple finite element (FE) analysis for some two-dimensional examples. Finally, we conclude the appendix in Section B.7 with a brief discussion of the results and possible future applications.

## B.2 Problem formulation

Magneto-elastic materials are defined as materials exhibiting coupled magnetic and mechanical behaviors. Characterizing the constitutive behavior of magneto-elastic materials requires a model for the interaction of the magnetic fields and matter. Modeling the response of deformable bodies to magnetic fields (or in general, to electromagnetic fields) has been a challenging scientific issue (see, for example, Maxwell 1873), and, as a consequence, different formulations have been proposed in the literature, which do not seem consistent at first glance. Despite the fact that there exist different formulations, it can be shown that under certain assumptions, all these formulations are equivalent (see, for example, Hutter et al. 2006). In the following, we present a brief summary of the governing equations that are required for the purposes of this appendix (see Kovetz 1990, Hutter et al. 2006, for more general formulations).

### B.2.1 Governing equations

Under application of mechanical and magnetic loadings a typical magneto-elastic material deforms from its original, reference configuration to a new, current configuration. This deformation can be parametrized by a continuous map, $\mathbf{x} = \mathbf{x}(\mathbf{X})$, which is a one-to-one correspondence between the position of material points in the reference configuration, $\mathbf{X}$, and in the current configuration, $\mathbf{x}$. In the infinitesimal limit, such deformations can be characterized by the displacement gradient $\nabla\mathbf{u}$, where $\mathbf{u} := \mathbf{x} - \mathbf{X}$ denotes the infinitesimal displacement. Its symmetric part, with Cartesian components $\epsilon_{ij} = \frac{1}{2}(u_{i,j} + u_{j,i})$, and antisymmetric part, $\omega_{ij} = \frac{1}{2}(u_{i,j} - u_{j,i})$, correspond respectively to the infinitesimal strain and rotation tensors.

In the absence of electric and relativistic effects, as well as external current densities, Maxwell's equations for the case of static magnetic fields are given by

$$\operatorname{div} \mathbf{b} = 0, \quad \text{and} \quad \operatorname{curl} \mathbf{h} = \mathbf{0}, \tag{B.1}$$

where $\mathbf{b}$ and $\mathbf{h}$ are the magnetic induction and magnetic fields, respectively. In the classical theory of electromagnetism for magnetizable materials, it is standard to introduce the magnetization, denoted by $\mathbf{m}$, such that

$$\mathbf{m} = \frac{1}{\mu_0}\mathbf{b} - \mathbf{h}. \tag{B.2}$$

Neglecting inertial and external forces, the conservation of linear and angular momentum for a homogeneous, magneto-elastic material may be written as

$$\operatorname{div} \boldsymbol{T} = \mathbf{0}, \quad \text{and} \quad \boldsymbol{T}^T = \boldsymbol{T}, \tag{B.3}$$

where $\boldsymbol{T}$ is the total stress, including magnetic effects. In the presence of material interfaces (between two different phases in a composite), the following set of jump conditions has to be satisfied: $[\![\mathbf{u}]\!] = \mathbf{0}$, $[\![\boldsymbol{T}]\!]\,\mathbf{n} = \mathbf{0}$, $[\![\mathbf{b}]\!] \cdot \mathbf{n} = 0$, and $[\![\mathbf{h}]\!] \times \mathbf{n} = \mathbf{0}$, where $\mathbf{n}$ is the unit normal to the interface in the current configuration.

The above set of governing equations is completed by appropriate constitutive relations between the pairs, $\mathbf{b}$ and $\boldsymbol{T}$, and $\mathbf{h}$ and $\nabla\mathbf{u}$. As already mentioned, in this investigation, a rigid magnetically linear inclusion is embedded in a linear-elastic, magnetically insensitive material. Their constitutive responses are described as follows (Kovetz 1990, Hutter et al. 2006).

*Magnetically impermeable, linear-elastic materials.* For elastic materials, which are not susceptible to magnetic fields, the magnetization is always zero. Therefore, for this class of materials, the constitutive behavior reduces to

$$\mathbf{b} = \mu_0 \mathbf{h} \quad \text{and} \quad \boldsymbol{T} := \boldsymbol{T}^{el} + \boldsymbol{T}^{M}, \tag{B.4}$$

where $\mu_0$ is the permeability of vacuum, and $\boldsymbol{T}^{el}$ and $\boldsymbol{T}^{M}$ denote the "purely mechanical" and Maxwell stresses, given respectively by the expressions

$$\boldsymbol{T}^{el} = \mathbb{C}^{(1)}\boldsymbol{\epsilon}, \quad \text{and} \quad \boldsymbol{T}^{M} = \frac{\mathbf{b}\otimes\mathbf{b}}{\mu_0} - \frac{\mathbf{b}\cdot\mathbf{b}}{2\mu_0}\boldsymbol{I}. \tag{B.5}$$

In the first of these equations, $\mathbb{C}^{(1)}$ is the stiffness of the material, which in general is a fully symmetric, fourth-order tensor, but for isotropic material behavior reduces to an isotropic tensor depending only on the elastic shear modulus, $\mu_{el}$, and the Poisson's ratio, $\nu$.

*Rigid magnetic materials.* A rigid material can only undergo a rigid displacement (a translation and a rotation). Therefore, in the context of infinitesimal deformations, the displacement gradient in the rigid particles is given by an infinitesimal rotation, i.e.

$$\nabla\mathbf{u} = \bar{\boldsymbol{\omega}}^{(2)}, \tag{B.6}$$

while the total stress is indeterminate.

In the current configuration, the magnetic response of the rigid material will be taken to be described by the relation

$$\mathbf{b} = \boldsymbol{\mu}^{(2)}\mathbf{h}, \tag{B.7}$$

where $\boldsymbol{\mu}^{(2)}$ is the magnetic permeability of the material. This linear model is appropriate for diamagnetic and paramagnetic materials. However, it should be noted that the analysis may be generalized for nonlinear responses of the type that may be exhibited by a soft ferromagnetic material (with small hysteresis). We will come back to this point in the concluding remarks. It should also be noted (see e.g., Ponte Castañeda & Galipeau 2011) in the context of expression (B.7) that the permeability in the current configuration $\boldsymbol{\mu}^{(2)}$ is related to the corresponding permeability in the reference configuration $\boldsymbol{M}^{(2)}$ via

$$\boldsymbol{\mu}^{(2)} = \boldsymbol{M}^{(2)} + \bar{\boldsymbol{\omega}}^{(2)}\boldsymbol{M}^{(2)} - \boldsymbol{M}^{(2)}\bar{\boldsymbol{\omega}}^{(2)}, \tag{B.8}$$

where terms of order $\left(\bar{\boldsymbol{\omega}}^{(2)}\right)^2$ and higher have been neglected because of the small deformation approximation.

### B.2.2 Solution procedure

We consider a single rigid magnetic inclusion, denoted by $\Omega_0$, embedded in an infinite elastic, and non-magnetic matrix, occupying $\mathbb{R}^3 \backslash \Omega_0$. For the inclusion, we assume a general ellipsoidal shape in the reference configuration $\Omega_0 = \{\mathbf{X} : |\boldsymbol{Z}_0^{-T}\mathbf{X}| \leq 1\}$, where $\boldsymbol{Z}_0$ is a symmetric, second-order tensor representing the shape of the inclusion. In addition, we assume a general, anisotropic, reference permeability tensor, $\boldsymbol{M}^{(2)}$, for the magnetic behavior of the inclusion. The rigid inclusion in the presence of mechanical and magnetic loadings is expected to undergo an infinitesimal rotation until reaching an equilibrium point at which the infinitesimal rotation is $\bar{\boldsymbol{\omega}}_e^{(2)}$ (see Fig. B.1). It is important to note that even in the absence of the external magnetic fields the inclusion may undergo an infinitesimal rotation (see Eshelby 1957). Since the inclusion is

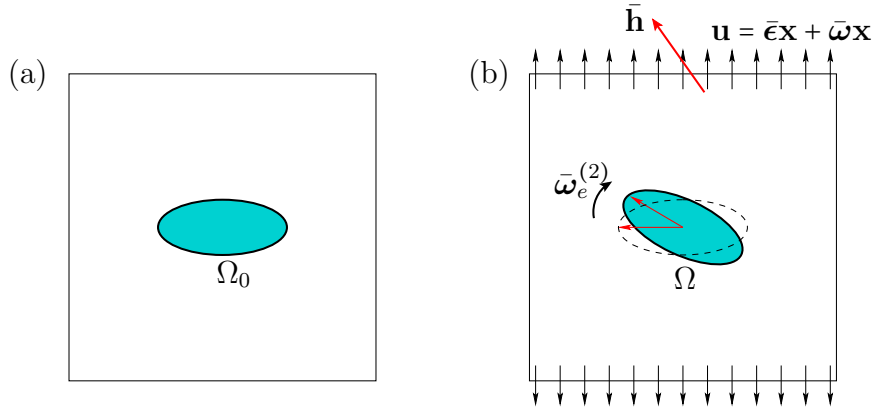


Figure B.1: Schematic of the single inclusion's magneto-elasticity problem. (a) The reference configuration, and (b) the deformed configuration.

rigid, its shape in the deformed configuration is characterized by $\Omega = \{\mathbf{x} : |\boldsymbol{Z}^{-T}\mathbf{x}| \leq 1\}$, where, on account of the small rotations involved, the shape tensor $\boldsymbol{Z}$ in the current configuration is related to the corresponding reference shape tensor $\boldsymbol{Z}_0$ by

$$\boldsymbol{Z} = \boldsymbol{Z}_0 + \bar{\boldsymbol{\omega}}^{(2)}\boldsymbol{Z}_0 - \boldsymbol{Z}_0\bar{\boldsymbol{\omega}}^{(2)}. \tag{B.9}$$

To determine the equilibrium rotation of the inclusion, we note that for static equilibrium, the global versions of the conservation laws of linear and angular momentum must be satisfied for any part of the body. In particular, for the domain $\Omega$ enclosing the rigid particle with boundary surface $\partial\Omega$, we have that the total force $\mathbf{f}$ and torque $\mathbf{l}$ on $\Omega$ must vanish identically, or

$$\mathbf{f} = \frac{1}{V}\int_{\partial\Omega} \boldsymbol{T}\mathbf{n}\ dS = \mathbf{0}, \quad \text{and} \quad \mathbf{l} = \frac{1}{V}\int_{\partial\Omega} \mathbf{x}\times\boldsymbol{T}\mathbf{n}\ dS = \mathbf{0}, \tag{B.10}$$

where $\boldsymbol{T}$ is the total stress defined in the previous section (which includes *both* mechanical and magnetic contributions), $V$ is the volume of the inclusion and $\mathbf{n}$ is the unit outward normal to $\partial\Omega$.

Noting that the inclusion $\Omega$ is surrounded by the matrix material (i.e., the surface $\partial\Omega$ in equation (B.10) is just outside the inclusion, and therefore in the matrix), the stress $\boldsymbol{T}$ in the total force and torque integrals correspond to the total stress in the matrix which is given by equation (B.4) in terms of the elastic stress, $\boldsymbol{T}^{el}$, and the Maxwell stress, $\boldsymbol{T}^{M}$, as defined by equations (B.5). In conclusion, equation (B.10) can be rewritten as

$$\mathbf{f}^{el} + \mathbf{f}^{mg} = \mathbf{0}, \quad \text{and} \quad \mathbf{l}^{el} + \mathbf{l}^{mg} = \mathbf{0}, \tag{B.11}$$

where $\mathbf{f}^{el}$ and $\mathbf{f}^{mg}$, and $\mathbf{l}^{el}$ and $\mathbf{l}^{el}$ denote the "elastic" and "magnetic" components of the forces and the torques (per unit volume) acting on the inclusion due to the elastic matrix and the magnetic field, respectively. They are given by the same integrals as in (B.10) with $\boldsymbol{T}$ being replaced by $\boldsymbol{T}^{el}$ (or $\boldsymbol{T}^{M}$) for the elastic (or magnetic) force and torque.

Independent of the rotation of the inclusion, the elastic and magnetic forces acting on it will turn out to vanish (as will be discussed in more detail below). Thus, equation $(B.11)_1$ is automatically satisfied. On the other hand, for an arbitrary rotation of the inclusion, $\bar{\boldsymbol{\omega}}^{(2)}$, both elastic and magnetic torques in equation $(B.11)_2$ can be thought of as functions of the rotation (i.e. $\mathbf{l}^{el} = \mathbf{l}^{el}(\bar{\boldsymbol{\omega}}^{(2)})$ and $\mathbf{l}^{mg} = \mathbf{l}^{mg}(\bar{\boldsymbol{\omega}}^{(2)})$). Noting that the sum of these two torques must be zero at equilibrium, the following equation for

the equilibrium rotation of the inclusion is obtained

$$\mathbf{l}^{el}\left(\bar{\boldsymbol{\omega}}^{(2)}\right)+\mathbf{l}^{mg}\left(\bar{\boldsymbol{\omega}}^{(2)}\right)=\mathbf{0},\quad \text{for}\quad \bar{\boldsymbol{\omega}}^{(2)}=\bar{\boldsymbol{\omega}}_{e}^{(2)}. \tag{B.12}$$

As will be shown in more detail in Section B.3, it is possible to obtain the magnetic fields for a given rotation of the inclusion, $\bar{\boldsymbol{\omega}}^{(2)}$, independent of the deformation field in the matrix. Having the solution for the magnetic fields, the magnetic torque can be obtained as a function of $\bar{\boldsymbol{\omega}}^{(2)}$ in terms of the Maxwell stress tensor (B.5), evaluated immediately outside the inclusion, by means of the integral appearing in $(\text{B.10})_1$ with $\boldsymbol{T}$ replaced by the Maxwell stress $\boldsymbol{T}^{M}$.

Similarly, as will be shown in Section B.4, since the matrix is not responsive to the magnetic fields, for the given rotation of the inclusion, $\bar{\boldsymbol{\omega}}^{(2)}$, the elasticity problem can be solved independent of the magnetic fields. Moreover, the elastic torque applied on the inclusion can be obtained in terms of the same integral appearing in $(\text{B.10})_1$ with $\boldsymbol{T}$ replaced by the elastic stress $\boldsymbol{T}^{el}=\mathbb{C}^{(1)}\boldsymbol{\epsilon}\left(\mathbf{x}\right)$ (for $\mathbf{x}\in\partial\Omega$).

In the following two sections, the magnetic and elastic problems described above will be solved independently in order to determine the elastic and magnetic torques acting on the inclusion. Then, the equilibrium rotation of the inclusion under combined mechanical and magnetic loadings will be determined by means of (B.12).

## B.3 Rigid magnetizable inclusion in an external magnetic field

In this section, we address the solution of the magnetostatic problem consisting of a magnetic inclusion (denoted by $\Omega$ in the deformed configuration) placed in an external magnetic field, $\bar{\mathbf{h}}$, which is the field in the absence of the inclusion, or simply the magnetic field at infinity. Recalling equations (B.1) and (B.2), the magnetostatic

problem reduces to the following boundary value problem

$$\begin{aligned} &\mu_0 \nabla^2 \phi + \mu_0 \nabla \cdot \mathbf{m} = 0 \qquad \mathbf{x} \in \mathbb{R}^3, \\ &\phi \to \bar{\mathbf{h}} \cdot \mathbf{x} \qquad\qquad\qquad\quad |\mathbf{x}| \to \infty, \end{aligned} \tag{B.13}$$

where $\phi$ is the magnetic potential, such that $\mathbf{h} = \nabla\phi$, and where $\mathbf{m}$ is the magnetization, given by

$$\mu_0 \mathbf{m} = \left(\boldsymbol{\mu}^{(2)} - \mu_0 \boldsymbol{I}\right) \nabla\phi, \quad \text{when} \quad \mathbf{x} \in \Omega, \tag{B.14}$$

and zero otherwise.

There are well-known solutions for the case of isotropic permeability tensors and simple geometries, such as spheres (Reitz & Milford 1962) and ellipsoids (Landau et al. 1984) . For the general case of anisotropic magnetic properties, it is possible to rewrite the governing equations of magnetostatics (i.e. the Maxwell's equations) in an integral equation form analogous to the Eshelby problem in elasticity (see Willis 1977) in order to find the magnetic fields. The main advantage of the integral equation approach is the compact form of the solution, inside and outside of the inclusion, for the most general case of anisotropic magnetic behaviors and ellipsoidal shapes of the inclusion. Therefore, by application of the procedure of (Willis 1977) to deal with anisotropic magnetic behavior for the inclusions, it can be shown that for ellipsoidal shapes of the inclusion, the magnetization, magnetic field and magnetic induction are constant inside the inclusion and therefore equal to their averages, i.e.

$$\bar{\mathbf{m}}^{(2)} = \boldsymbol{\alpha}^{(2)} \bar{\mathbf{h}}, \quad \bar{\mathbf{h}}^{(2)} = \boldsymbol{\beta}^{(2)} \bar{\mathbf{h}}, \quad \text{and} \quad \bar{\mathbf{b}}^{(2)} = \boldsymbol{\mu}^{(2)} \boldsymbol{\beta}^{(2)} \bar{\mathbf{h}}, \tag{B.15}$$

where $\boldsymbol{\mu}^{(2)}$ is the permeability of the inclusion, and $\boldsymbol{\alpha}^{(2)}$ and $\boldsymbol{\beta}^{(2)}$ are symmetric, second-order tensors denoting the magnetization and magnetic field concentration tensors, respectively, and are given by

$$\boldsymbol{\alpha}^{(2)} = \mu_0^{-1} \left\{ \left(\boldsymbol{\mu}^{(2)} - \mu_0 \boldsymbol{I}\right)^{-1} + \boldsymbol{P} \right\}^{-1}, \text{ and } \quad \boldsymbol{\beta}^{(2)} = \left\{ \boldsymbol{I} + \boldsymbol{P} \left(\boldsymbol{\mu}^{(2)} - \mu_0 \boldsymbol{I}\right) \right\}^{-1}. \tag{B.16}$$

Here the second-order, symmetric tensor $\boldsymbol{P}$ describes the magnetic microstructural

tensor of the inclusion and is defined by

$$\boldsymbol{P} := \frac{\det \boldsymbol{Z}}{4\pi\mu_0} \int_{|\boldsymbol{\xi}|=1} \boldsymbol{\xi} \otimes \boldsymbol{\xi} \, |\boldsymbol{Z}\boldsymbol{\xi}|^{-3} \; dS. \tag{B.17}$$

Note that it depends only on the magnetic properties of the matrix (i.e. $\mu_0$) and shape of the inclusion. It is also important to note that the above results are given in the current configuration which differs from the reference configuration by a rigid rotation, as already mentioned in the previous section.

The net force and torque on the inclusion due to the magnetic field can be determined via the Maxwell stress tensor as explained in Section B.2 *b*, i.e.

$$\mathbf{f}^{mg} = \frac{1}{V} \int_{\partial\Omega} \boldsymbol{T}^M \mathbf{n} \; dS, \quad \text{and} \quad \mathbf{l}^{mg} = \frac{1}{V} \int_{\partial\Omega} \mathbf{x} \times \left( \boldsymbol{T}^M \mathbf{n} \right) \; dS, \tag{B.18}$$

where $\boldsymbol{T}^M$ is given by equation (B.5) with $\mathbf{b}$ denoting the magnetic field just outside the inclusion. For the single inclusion problem, it is given by (see Reitz & Milford 1962, for the details)

$$\mathbf{b}\left(\mathbf{x}\right) = \mu_0 \bar{\mathbf{h}} - \frac{\mu_0}{4\pi} \int_{\mathbf{x}' \epsilon \Omega} \left\{ \frac{\bar{\mathbf{m}}^{(2)}}{r^3} - \frac{3\left(\bar{\mathbf{m}}^{(2)} \cdot \mathbf{r}\right)\mathbf{r}}{r^5} \right\} \; d\mathbf{x}', \quad \mathbf{r} = \mathbf{x} - \mathbf{x}'. \tag{B.19}$$

After a long, but straightforward calculation (Landau et al. 1984) , it can be shown that the force and torque (per unit volume) exerted on the inclusion by the magnetic field are given by

$$\mathbf{f}^{mg} = \mathbf{0} \quad \text{and} \quad \mathbf{l}^{mg} = \mu_0 \bar{\mathbf{m}}^{(2)} \times \bar{\mathbf{h}}. \tag{B.20}$$

Note that the magnetic force on the inclusion vanishes as expected. On the other hand, using expression $(B.15)_1$, and the fact that the torque is an axial vector, we can write the components of the torque in terms of a skew-symmetric, second-order tensor, $\boldsymbol{\tau}^{mg}$, such that the Cartesian components of $\mathbf{l}^{mg}$ read

$$l_i^{mg} = \epsilon_{ijk} \tau_{kj}^{mg}, \quad \text{with} \quad \boldsymbol{\tau}^{mg} = -\frac{\mu_0}{2} \left\{ \left( \boldsymbol{\alpha}^{(2)} \bar{\mathbf{h}} \right) \otimes \bar{\mathbf{h}} - \bar{\mathbf{h}} \otimes \left( \boldsymbol{\alpha}^{(2)} \bar{\mathbf{h}} \right) \right\}. \tag{B.21}$$

To make the dependence of $\boldsymbol{\tau}^{mg}$ (or equivalently $\mathbf{l}^{mg}$) on the rotation of the inclu-

sion more explicit, we note that the magnetization concentration tensor $\boldsymbol{\alpha}^{(2)}$, which in the current configuration is given by $(B.16)_1$, can be written in terms of its reference counterpart, $\boldsymbol{A}^{(2)}$, and the rotation, $\bar{\boldsymbol{\omega}}^{(2)}$, as follows

$$\boldsymbol{\alpha}^{(2)} = \boldsymbol{A}^{(2)} + \bar{\boldsymbol{\omega}}^{(2)}\boldsymbol{A}^{(2)} - \boldsymbol{A}^{(2)}\bar{\boldsymbol{\omega}}^{(2)}, \tag{B.22}$$

where

$$\boldsymbol{A}^{(2)} = \mu_0^{-1}\left\{\left(\boldsymbol{M}^{(2)} - \mu_0\boldsymbol{I}\right)^{-1} + \boldsymbol{P}_0\right\}^{-1}, \tag{B.23}$$

and $\boldsymbol{P}_0$ is given by the same expression (B.17), except that $\boldsymbol{Z}$ should be replaced by $\boldsymbol{Z}_0$, as defined in (B.9).

Then, substituting (B.22) into $(B.21)_2$, and ignoring higher order terms in $\bar{\boldsymbol{\omega}}^{(2)}$, we obtain the result

$$\boldsymbol{\tau}^{mg}\left(\bar{\boldsymbol{\omega}}^{(2)}\right) = \boldsymbol{\tau}_0^{mg} + \frac{\mu_0}{2}\,\mathbb{T}\,\bar{\boldsymbol{\omega}}^{(2)}, \tag{B.24}$$

where $\boldsymbol{\tau}_0^{mg}$ denotes the magnetic torque in the reference (unrotated) configuration of the inclusion and is given by

$$\boldsymbol{\tau}_0^{mg} = -\frac{\mu_0}{2}\left\{\left(\boldsymbol{A}^{(2)}\bar{\mathbf{h}}\right)\otimes\bar{\mathbf{h}} - \bar{\mathbf{h}}\otimes\left(\boldsymbol{A}^{(2)}\bar{\mathbf{h}}\right)\right\}, \tag{B.25}$$

and where the Cartesian components of the fourth-order tensor $\mathbb{T}$ are given by

$$T_{ijst} = \delta_{is}A^{(2)}_{tq}\bar{h}_q\bar{h}_j - \delta_{js}A^{(2)}_{tq}\bar{h}_q\bar{h}_i + \bar{h}_i\bar{h}_tA^{(2)}_{js} - \bar{h}_j\bar{h}_tA^{(2)}_{is}. \tag{B.26}$$

Note that they satisfy the symmetries $T_{ijkl} = -T_{jikl} = -T_{ijlk}$.

## B.4 Rigid ellipsoidal inclusion in an infinite elastic matrix

In the previous section, we found the torque produced by an external magnetic field on the rigid inclusion $\Omega$, as a function of its rotation (i.e., $\mathbf{l}^{mg}\left(\bar{\boldsymbol{\omega}}^{(2)}\right)$). In this section, we would like to obtain the corresponding torque applied by the surrounding elastic

medium on the inclusion as a function of the rotation $\bar{\boldsymbol{\omega}}^{(2)}$. Toward this goal, it is first noted that the Maxwell stress $\boldsymbol{T}^M$, as given by (B.5), is divergence-free for a non-magnetic matrix. This can be easily shown by means of the Maxwell's equations, given by (B.1), and the fact that for a non-magnetic material $\mathbf{b} = \mu_0 \mathbf{h}$. Therefore, the magnetic fields do not appear explicitly in the equilibrium equation, and we can solve for the displacement field in the matrix independent of the magnetic fields. Thus, for the infinite elastic matrix with stiffness tensor $\mathbb{C}^{(1)}$, subjected to an affine displacement boundary condition at infinity, and an arbitrary rotation $\bar{\boldsymbol{\omega}}^{(2)}$ just outside the inclusion, we have the following "purely mechanical" boundary value problem (BVP) for the displacement field $\mathbf{u}$ in the elastic matrix material:

$$\begin{aligned} &\operatorname{div}\left(\mathbb{C}^{(1)} \nabla \mathbf{u}\right) = \mathbf{0} && \mathbf{x} \in \mathbb{R}^3 \backslash \Omega_0, \\ &\mathbf{u}(\mathbf{x}) \to \bar{\boldsymbol{\epsilon}} \mathbf{x} + \bar{\boldsymbol{\omega}} \mathbf{x} && |\mathbf{x}| \to \infty, \\ &\mathbf{u}(\mathbf{x}) = \bar{\boldsymbol{\omega}}^{(2)} \mathbf{x} && \mathbf{x} \in \partial \Omega_0, \end{aligned} \tag{B.27}$$

where $\bar{\boldsymbol{\epsilon}}$ is a constant symmetric second-order tensor denoting the macroscopic strain and $\bar{\boldsymbol{\omega}}$ is a constant antisymmetric second-order tensor representing the macroscopic rotation of the system.

For the special case of $\bar{\boldsymbol{\epsilon}} = \bar{\boldsymbol{\omega}} = \mathbf{0}$, the BVP (B.27) has been solved by making use of an orthogonal ellipsoidal coordinate system (Kachanov et al. 2002) . On the other hand, for $\bar{\boldsymbol{\omega}} = \mathbf{0}$ and $\bar{\boldsymbol{\omega}}^{(2)}$ not prescribed, it reduces to the well-known Eshelby problem which can be solved by using the so-called simple set of imaginary cutting, straining and welding operations, as described by (Eshelby 1957). The above more general problem has been addressed by Walpole (1991) . For completeness, the solution for the above BVP is briefly summarized in the last section B.8 of this appendix.

Thus, it is shown in this appendix that the "mechanical" traction $\boldsymbol{T}^{el}\mathbf{n}$ on the surface of the inclusion is given by

$$\boldsymbol{T}^{el}\mathbf{n} = (\boldsymbol{\sigma} + \boldsymbol{\tau})\,\mathbf{n}, \tag{B.28}$$

where $\boldsymbol{\sigma}$ and $\boldsymbol{\tau}$ are respectively symmetric and skew-symmetric, second-order tensors,

given by

$$\begin{aligned}\boldsymbol{\sigma} &= \mathbb{P}^{-1}\bar{\boldsymbol{\epsilon}} - \mathbb{P}^{-1}\mathbb{Q}\left\{\mathbb{S} - \mathbb{R}\mathbb{P}^{-1}\mathbb{Q}\right\}^{-1}\left(\bar{\boldsymbol{\omega}} - \bar{\boldsymbol{\omega}}^{(2)} - \mathbb{R}\mathbb{P}^{-1}\bar{\boldsymbol{\epsilon}}\right),\\ \boldsymbol{\tau} &= \left\{\mathbb{S} - \mathbb{R}\mathbb{P}^{-1}\mathbb{Q}\right\}^{-1}\left(\bar{\boldsymbol{\omega}} - \bar{\boldsymbol{\omega}}^{(2)} - \mathbb{R}\mathbb{P}^{-1}\bar{\boldsymbol{\epsilon}}\right),\end{aligned} \tag{B.29}$$

where $\mathbb{P}$, $\mathbb{Q}$, $\mathbb{R}$ and $\mathbb{S}$ are mechanical microstructural (Eshelby) tensors, defined by relations (B.48) and (B.47). Note that the stress is indeterminate inside the rigid inclusion, and hence the need for the traction on the boundary of the inclusion in order to compute the force and torque exerted by the surrounding elastic medium on the inclusion. Then, by means of expressions of the form (B.18) (with $\boldsymbol{T}^{mg}$ replaced by $\boldsymbol{T}^{el}$), it can be shown that the elastic force is zero (i.e. $\mathbf{f}^{el} = \mathbf{0}$) and that the torque (per unit volume) exerted by the surrounding elastic medium on the inclusion is given by

$$l_i^{el}\left(\bar{\boldsymbol{\omega}}^{(2)}\right) = \epsilon_{ijk}\tau_{kj}, \tag{B.30}$$

where $\boldsymbol{\tau}$ is given in terms of $\bar{\boldsymbol{\omega}}^{(2)}$ by equation $(B.29)_2$.

## B.5 Equilibrium rotation of inclusion in an infinite elastic matrix subjected to an external magnetic field

It is recalled from Section B.2 *b* that the magnetic and elastic torques must add up to zero at equilibrium. Thus, substituting the magnetic and elastic torque from expressions $(B.21)_1$ and (B.30), respectively, into equation (B.12), the following equation for the equilibrium rotation, $\bar{\boldsymbol{\omega}}_e^{(2)}$ is obtained

$$\boldsymbol{\tau}^{mg}\left(\bar{\boldsymbol{\omega}}^{(2)}\right) + \boldsymbol{\tau}\left(\bar{\boldsymbol{\omega}}^{(2)}\right) = \mathbf{0}, \quad \text{for} \quad \bar{\boldsymbol{\omega}}^{(2)} = \bar{\boldsymbol{\omega}}_e^{(2)}, \tag{B.31}$$

where $\boldsymbol{\tau}^{mg}$ and $\boldsymbol{\tau}$ are given in terms of the particle rotation $\bar{\boldsymbol{\omega}}^{(2)}$ by expressions (B.24) and $(B.29)_2$, respectively. Therefore, solving for the equilibrium rotation we obtain

the result

$$\bar{\boldsymbol{\omega}}_e^{(2)} = \left(\mathbb{I} - \frac{\mu_0}{2}\mathbb{V}\mathbb{T}\right)^{-1}\left(\bar{\boldsymbol{\omega}} - \mathbb{R}\mathbb{P}^{-1}\bar{\boldsymbol{\epsilon}} + \mathbb{V}\boldsymbol{\tau}_0^{mg}\right), \tag{B.32}$$

where $\mathbb{V} := \{\mathbb{S} - \mathbb{R}\mathbb{P}^{-1}\mathbb{Q}\}$ and it is recalled that $\boldsymbol{\tau}_0^{mg}$ denotes the magnetic torque exerted on the inclusion in its reference configuration. It is important to note that $\bar{\boldsymbol{\omega}}_e^{(2)}$ depends linearly on $\bar{\boldsymbol{\epsilon}}$ and $\bar{\boldsymbol{\omega}}$ and quadratically on the external magnetic field $\bar{\mathbf{h}}$.

Introducing dimensionless parameter

$$\kappa = \frac{\mu_0 \bar{h}^2}{2\mu_{el}}, \tag{B.33}$$

serving to characterize the relative strength of the magnetic versus the elastic effects, and the dimensionless variables

$$\hat{\mathbb{T}} = \mathbb{T}/\bar{h}^2, \quad \hat{\mathbb{V}} = \mu_{el}\mathbb{V}, \quad \text{and} \quad \hat{\boldsymbol{\tau}}_0^{mg} = 2\boldsymbol{\tau}_0^{mg}/\left(\mu_0 \bar{h}^2\right), \tag{B.34}$$

the following asymptotic result is obtained for the equilibrium rotation

$$\bar{\boldsymbol{\omega}}_e^{(2)} = \bar{\boldsymbol{\omega}} - \mathbb{R}\mathbb{P}^{-1}\bar{\boldsymbol{\epsilon}} + \kappa\,\hat{\mathbb{V}}\left[\hat{\boldsymbol{\tau}}_0^{mg} + \hat{\mathbb{T}}\left(\bar{\boldsymbol{\omega}} - \mathbb{R}\mathbb{P}^{-1}\bar{\boldsymbol{\epsilon}}\right)\right] + \mathcal{O}\left(\kappa^2\right), \tag{B.35}$$

which is valid for $\kappa \ll 1$. In this connection, it should be noted that $\kappa \ll 1$ is the typical situation in applications. Indeed, in most of the recent experimental studies on two-phase, magnetorheological composites, the choices of the materials and the actuating fields are such that the largest value of $\kappa$ is in the order of 0.1 (see Ginder et al. 1999, 2002, Guan et al. 2008, , where the elastic matrix is made of silicon or natural rubber with a shear modulus of $1.0 - 1.2MPa$, and the magnetic induction fields are of magnitude $0 - 1.2T$). In any case, it is useful to distinguish three different limiting cases in reference to the above expressions for the particle rotation:

*Case 1*: $\kappa$ is small compared to $|\bar{\boldsymbol{\epsilon}}|$ and $|\bar{\boldsymbol{\omega}}|$. In this limit, terms of order one or higher in the parameter $\kappa$ can be neglected, compared to the zeroth-order term, and the equilibrium rotation of the inclusion is given by the (purely mechanical) Eshelby

result

$$\bar{\boldsymbol{\omega}}_e^{(2)} = \bar{\boldsymbol{\omega}} - \mathbb{R}\mathbb{P}^{-1}\bar{\boldsymbol{\epsilon}}. \tag{B.36}$$

Clearly, this case corresponds to situations where the matrix is so stiff compared to the strength of the magnetic field that the rotation of the inclusion is independent of the magnetic field.

*Case 2*: $\kappa$ is of the same order as $|\bar{\boldsymbol{\epsilon}}|$ and $|\bar{\boldsymbol{\omega}}|$. In this case the second- and higher-order terms in equation (B.35) can be neglected, and the equilibrium rotation of the inclusion is given by

$$\bar{\boldsymbol{\omega}}_e^{(2)} = \bar{\boldsymbol{\omega}} - \mathbb{R}\mathbb{P}^{-1}\bar{\boldsymbol{\epsilon}} + \kappa\hat{\mathbb{V}}\hat{\boldsymbol{\tau}}_0^{mg}. \tag{B.37}$$

It is important to emphasize that the small- strain and rotation assumptions that are implicit in this linearized deformation approximation essentially require that $\kappa$ be at most of the same order as $|\bar{\boldsymbol{\epsilon}}|$ and $|\bar{\boldsymbol{\omega}}|$, for otherwise the resulting particle rotation and associated strain distributions would violate the small deformation approximation. In addition, it is evident from expression (B.37), which depends on the magnetic torque $\hat{\boldsymbol{\tau}}_0^{mg}$ in the reference configuration that in this limit the differences between the reference and deformed configuration become irrelevant, as far as the computation of the equilibrium rotation $\bar{\boldsymbol{\omega}}_e^{(2)}$ is concerned.

*Case 3*: *nearly aligned magnetic fields*. For the special cases where the magnetic field is almost aligned with the inclusion (or its magnetic anisotropy axes), the equilibrium rotation of the inclusion would be infinitesimally small, independent of the parameter $\kappa$. Therefore, for these special cases the general expression (B.32) should be used to obtain the equilibrium rotation of the inclusion.

## B.6 Applications for in-plane particle rotations

In this section, the general results of the previous section are specialized for magnetic loading applied on a plane of symmetry of the inclusion (with $\bar{\boldsymbol{\epsilon}} = \bar{\boldsymbol{\omega}} = 0$), so that the rigid inclusion undergoes an in-plane rotation. For simplicity, the matrix is assumed to be isotropic with stiffness tensor $\mathbb{C}^{(1)}$, depending on the elastic moduli, $\mu_{el}$ and

$\nu$, and the rigid, ellipsoidal inclusion to be magnetically anisotropic with magnetic permeability $\boldsymbol{\mu}$, such that the principal permeabilities are $\mu_1'$, $\mu_2'$ and $\mu_3'$. As depicted in Fig. B.2, the geometric axes of the inclusion, defined by $\{x_1, x_2, x_3\}$, are initially aligned with the laboratory axes, characterized by $\{X_1, X_2, X_3\}$, but rotate about the $X_3$-axis by an angle $\phi$ under the magnetic loading $\bar{\mathbf{h}}$, which in turn is applied on the $X_1 - X_2$ plane at an angle $\psi_0$ relative to the $X_1$ axis. Note that in order for the rotation of the particle to remain in the plane (so that $x_3 = X_3$), the magnetic axes of the inclusion, defined by $\{x_1', x_2', x_3'\}$, must be oriented such that $x_3' = x_3 = X_3$. For some generality, however, we assume that the magnetic axes may differ from the geometric axes by an angle $\theta$ (about the $x_3$ axis). Finally, we label the semi-axes of the ellipsoidal inclusion in the 1, 2, and 3 directions, $a$, $b$ and $c$, respectively.

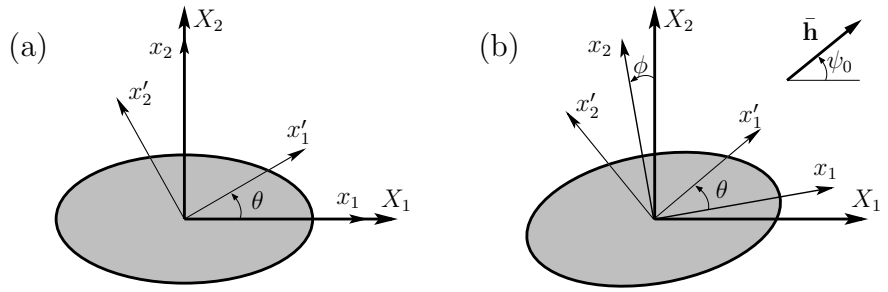


Figure B.2: Schematic representation of the in-plane rotation of the particle under magnetic loading. (a) The inclusion in the reference configuration and (b) the inclusion in the current configuration (after application of the external magnetic field $\bar{\mathbf{h}}$). Note that here the coordinate systems $\{x_1, x_2, x_3\}$ and $\{x_1', x_2', x_3'\}$ defining the geometric and magnetic axes of the inclusion are fixed on the rigid inclusion and are such that $x_3' = x_3$.

Under the above-mentioned hypotheses with the external magnetic fields $\bar{\mathbf{h}}$ being applied on the $X_1 - X_2$ plane at an angle $\psi_0$ relative to the $X_1$ axis, it can be shown that the only non-zero components of the antisymmetric magnetic moment tensor, $\hat{\boldsymbol{\tau}}_0^{mg}$, in equation (B.37) are

$$(\hat{\tau}_0^{mg})_{21} = -(\hat{\tau}_0^{mg})_{12} = \frac{1}{2}\Big(A_{11}^{(2)} - A_{22}^{(2)}\Big)\sin(2\psi_0) - A_{12}^{(2)}\cos(2\psi_0), \tag{B.38}$$

where $A_{ij}^{(2)}$ are the components of the magnetization concentration tensor defined by expression (B.23). On the other hand, it follows from expression (B.37) for $\bar{\boldsymbol{\omega}}_e^{(2)}$

that the in-plane particle rotation $\phi = \left(\bar{\omega}_e^{(2)}\right)_{21}$ is given by $\phi = 2\kappa \hat{V}_{2121} \left(\hat{\tau}_0^{mg}\right)_{21}$, where $\hat{V}_{2121} = \hat{S}_{2121} - \hat{Q}_{2121}^2 / \hat{P}_{2121}$ is the relevant component of the fourth-order tensor $\hat{\mathbb{V}} = \mu_{el} \{\mathbb{S} - \mathbb{R}\mathbb{P}^{-1}\mathbb{Q}\}$, defined earlier. Then, substituting expression (B.38) for $\left(\hat{\tau}_0^{mg}\right)_{21}$ into this expression for $\phi$, it can be readily shown that

$$\phi = \frac{\kappa\alpha}{\cos\xi} \sin\left(2\psi_0 - \xi\right), \tag{B.39}$$

where

$$\alpha = \left(A_{11}^{(2)} - A_{22}^{(2)}\right) \hat{V}_{2121}, \quad \text{and} \quad \tan\xi := \frac{A_{12}^{(2)}}{A_{11}^{(2)} - A_{22}^{(2)}}. \tag{B.40}$$

Note that the equilibrium particle rotation $\phi$ is periodic on the magnetic field angle $\psi_0$, with period $\pi$. It is also linear on the dimensionless parameter $\kappa$, and therefore quadratic in the magnetic field $\bar{h}$ and inversely proportional to the shear modulus $\mu_{el}$. In addition, it depends on both the "mechanical" microstructural tensors , $\mathbb{P}, \mathbb{Q}, \mathbb{R}$, and $\mathbb{S}$ (through $\hat{\mathbb{V}}$), as well as on the corresponding "magnetic" microstructural tensor $\boldsymbol{P}_0$ (through $\boldsymbol{A}$), and therefore also depends on the Poisson's ratio $\nu$, the magnetic permeabilities $\mu_1'$, $\mu_2'$ and $\mu_3'$, the particle shape, as determined by $a$, $b$ and $c$, and the orientation of the magnetic axis relative to the geometric axes, as specified by $\theta$. In an effort to elucidate the dependence of the inclusion rotation on all these variables and parameters, results will be provided next for cylindrical inclusions of elliptical cross-section aligned with the $x_3$ axis, and for spheroidal inclusions with their axis of symmetry lying in the rotation plane.

### B.6.1 Cylindrical (2D) inclusions

We begin by considering cylindrical inclusions with elliptical cross-section of aspect ratio $w = a/b$, and with in-plane (principal) magnetic permeabilities, $\mu_1', \mu_2'$, and generally non-aligned magnetic axes, as determined by $\theta$. As shown in Fig. B.3, the theoretical results are also compared to numerical results obtained using the general purpose FEM software COMSOL. These numerical simulations have been carried out for a square cell of finite length $L$. The length $L$ is chosen in the following manner.

We start with length $L_0$ ($\sim 4 \times a$ for the above specific example). Then we double the length until the condition $\frac{\phi_{n+1}-\phi_n}{\phi_n} < 0.0001$ is satisfied, where $\phi_n$ and $\phi_{n+1}$ are respectively the equilibrium rotations when $L = L_n$ and $L = L_{n+1} = 2L_n$.

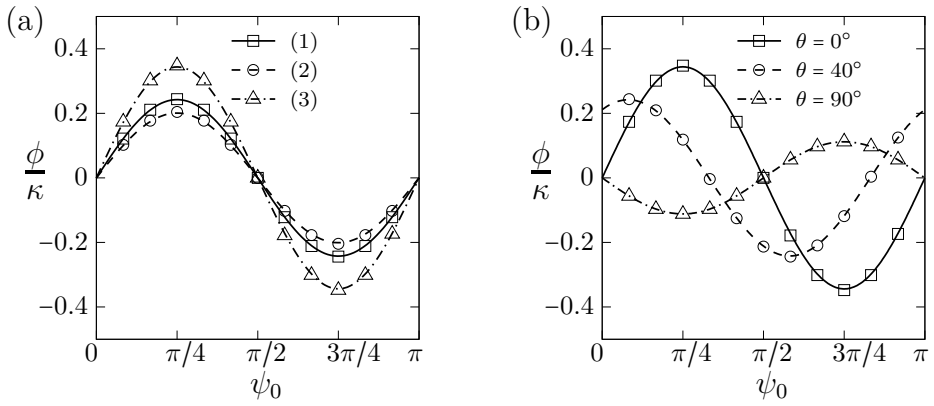


Figure B.3: Analytical predictions (lines) and FE results (symbols) for the equilibrium rotation $\phi$ as a function of the magnetic loading angle $\psi_0$. (a) Cylindrical inclusion with aligned magnetic and geometric axes ($\theta = 0°$) for three different cases: (1) circular cross-section and principal permeabilities ${}^{\mu'_1}/_{\mu_0} = 10$ and ${}^{\mu'_2}/_{\mu_0} = 2$, (2) elliptic cross-section with aspect ratio $w = a/b = 2$ and isotropic permeability ${}^{\mu'_1}/_{\mu_0} = {}^{\mu'_2}/_{\mu_0} = 10$, and (3) elliptic cross-section with aspect ratio $w = 2$ and principal permeabilities ${}^{\mu'_1}/_{\mu_0} = 10$ and ${}^{\mu'_2}/_{\mu_0} = 2$. (b) Cylindrical inclusion with aspect ratio $w = 2$ and principal permeabilities ${}^{\mu'_1}/_{\mu_0} = 10$ and ${}^{\mu'_2}/_{\mu_0} = 2$, for $\theta = 0°$, $\theta = 40°$, and $\theta = 90°$.

In Fig. B.3(a), results are shown for $\theta = 0°$ corresponding to aligned geometric and magnetic axes, such that the largest axis of the elliptical inclusion (if it is not circular) is always aligned with the largest principal permeability (if the magnetic properties of the inclusion are not isotropic). Results are presented for three cases: (1) circular cross-section ($w = 1$) and principal permeabilities ${}^{\mu'_1}/_{\mu_0} = 10$ and ${}^{\mu'_2}/_{\mu_0} = 2$, (2) elliptic cross-section with aspect ratio $w = a/b = 2$ and isotropic permeability ${}^{\mu'_1}/_{\mu_0} = {}^{\mu'_2}/_{\mu_0} = 10$, and (3) elliptic cross-section with aspect ratio $w = 2$ and principal permeabilities ${}^{\mu'_1}/_{\mu_0} = 10$ and ${}^{\mu'_2}/_{\mu_0} = 2$. The main observation from the results presented in this figure is that the particle always tends to align the magnetic axis with the largest permeability (if not magnetically isotropic), or its largest geometric axis (if it is isotropic) with the applied magnetic field (i.e. $\phi > 0$ for $0 < \psi_0 < \pi/2$). Note also that the particle rotation $\phi$ is periodic in $\psi_0$, with period $\pi$, as already mentioned in connection with equation (B.39), and that $\phi = 0$ when the magnetic field is aligned

with the particle axes ($\psi_0 = 0$, $\pi/2$ or $\pi$). The second important observation is that the particle shape and magnetic anisotropy have a synergistic effect for these case when the largest geometric axis is aligned with the largest principal permeability. Thus, the amplitude of the particle rotation is largest for case (3) above.

In Fig. B.3(b), results are shown for elliptical particles with fixed aspect ratio $w = 2$ and magnetic permeabilities ${}^{\mu_1'}/_{\mu_0} = 10$ and ${}^{\mu_2'}/_{\mu_0} = 2$, for three values of $\theta$ between 0 and $\pi/2$. Note that changing $\theta$ changes the components $A_{ij}^{(2)}$, and therefore, $\alpha$ and $\xi$ in equation (B.39). For $\theta = 0°$, the magnetization concentration tensor $\boldsymbol{A}^{(2)}$ is diagonal (i.e. $A_{12}^{(2)} = 0$), which implies that $\xi = 0$, consistent with what is shown in the figure. For $0° < \theta < 90°$, we have $A_{12}^{(2)} \neq 0$ which results in a non-zero $\xi$, and therefore, a phase shift in the plot for the equilibrium rotation of the inclusion. Finally, for $\theta = 90°$, the magnetic concentration tensor is diagonal which again implies that $\xi = 0$; however, $\alpha < 0$ for the specific choice of the parameters in Fig. B.3. Consequently, the inclusion no longer tends to align its largest geometric axis with the applied field, but instead prefers, for this specific choice of parameters, to align its largest magnetic axis with the applied field, resulting in $\phi < 0$ for $0 < \psi_0 < \pi/2$. In this case the magnetic and geometric effects oppose each other and the amplitude of the resulting particle rotation is also the smallest. In this connection, it should be noted that when $\theta = 90°$ it is possible to choose $w \neq 1$, $\mu_1'$ and $\mu_2' \neq \mu_1'$ such that the equilibrium rotation of the inclusion is zero for all values of $\psi_0$.

For a more detailed analysis of the effect of inclusion shape or magnetic behavior, we focus our attention on $\theta = 0°$ since in this case $\xi = 0$ and the equilibrium rotation simplifies to

$$\phi = \alpha\,\kappa\,\sin(2\psi_0)\,. \tag{B.41}$$

Then, the effect of the shape and magnetic behavior on the rotation of the cylindrical inclusion with aspect ratio $w = a/b$, and magnetic permeabilities, $\mu_1', \mu_2'$, is completely described by $\alpha$. We consider the following two cases:

*Case 1: Cylindrical inclusion with circular cross-section ($w = 1$) and anisotropic permeability ($\mu_1' \neq \mu_2'$).* Then, the amplitude coefficient $\alpha$, as given by expression

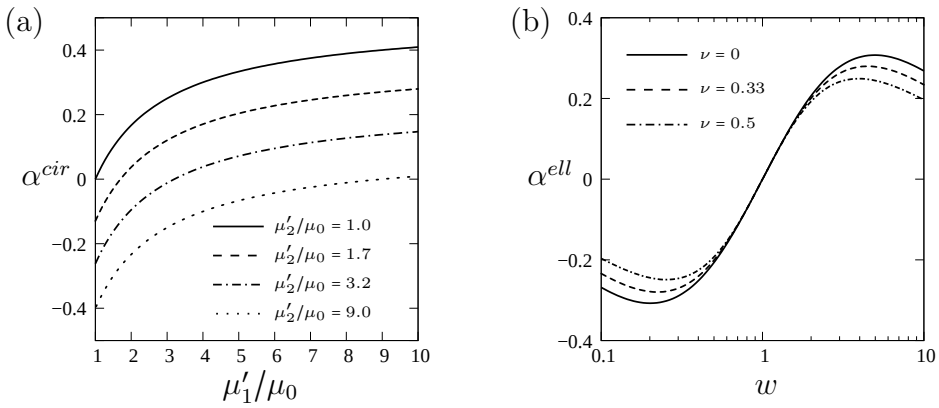


Figure B.4: The effects of magnetic anisotropy and inclusion shape on the magnitude of the particle rotation in an aligned external magnetic fields. (a) The coefficient $\alpha^{cir}$ for different values of the parameter ${}^{\mu_2'}/_{\mu_0}$ as a function of ${}^{\mu_1'}/_{\mu_0}$, and (b) the coefficient $\alpha^{ell}$ for fixed permeability ${}^{\mu}/_{\mu_0} = 10$, and different values of the Poisson's ratio of the matrix.

$(B.40)_1$, simplifies to

$$\alpha^{cir}\left({}^{\mu_1'}/_{\mu_0}, {}^{\mu_2'}/_{\mu_0}\right) = \frac{1}{2}\left(\frac{{}^{\mu_1'}/_{\mu_0} - 1}{{}^{\mu_1'}/_{\mu_0} + 1} - \frac{{}^{\mu_2'}/_{\mu_0} - 1}{{}^{\mu_2'}/_{\mu_0} + 1}\right).$$

Note that for this special case there is no dependence on the Poisson's ratio of the matrix $\nu$. Plots of $\alpha^{cir}$ as a function of ${}^{\mu_1'}/_{\mu_0}$, for fixed values of ${}^{\mu_2'}/_{\mu_0}$, are shown in Fig. B.4(a). It can be seen that $\alpha^{cir}$ increases monotonically with increasing the magnetic anisotropy, ${}^{\mu_1'}/_{\mu_0}$, and saturates for large values of ${}^{\mu_1'}/_{\mu_0}$. In addition, note that the graphs corresponding to the larger values of ${}^{\mu_2'}/_{\mu_0}$, can be obtained by translations in the negative vertical direction.

*Case 2: Cylindrical inclusion with aspect ratio $w = a/b$ and isotropic in-plane magnetic behavior ($\mu_1' = \mu_2' = \mu$).* The coefficient $\alpha$ in this case reduces to

$$\alpha^{ell}\left({}^{\mu}/_{\mu_0}, w, \nu\right) = \frac{w - {}^{w}/_{4(1-\nu)}}{(w+1)^2 - {}^{w}/_{(1-\nu)}} \frac{(w^2-1)\left({}^{\mu}/_{\mu_0} - 1\right)^2}{\left(w + {}^{\mu}/_{\mu_0}\right)\left(1 + {}^{\mu}/_{\mu_0} w\right)},$$

which does depend on the Poisson's ratio $\nu$. Plots of $\alpha^{ell}$ as a function of $w$, for $\mu/\mu_0 = 10$, are shown in Fig. B.4(b). In this figure, it can be seen that $\alpha^{ell}$ increases up to a maximum, and then decays to zero as the aspect ratio is further increased

(for $w > 1$). This is due to the fixed displacement boundary condition at infinity, and the fact that as the aspect ratio tends to infinity the rigid inclusion approaches the boundary. Note that $\alpha^{ell}(w) = -\alpha^{ell}(1/w)$, due to the symmetry of the problem.

### B.6.2 Spheroidal (3D) inclusions

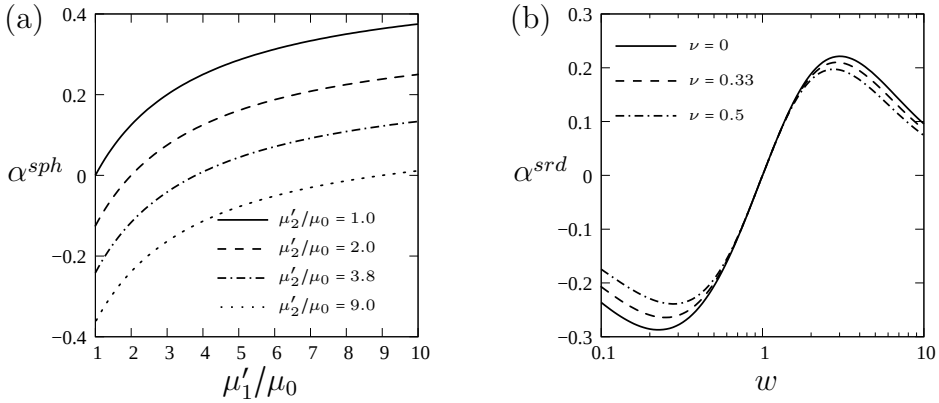


Figure B.5: The effect of anisotropy, due to the magnetic behavior and shape of the inclusion, on the response of the single inclusion to the external magnetic field. (a) The coefficient $\alpha^{sph}$ as a function of $\mu_1'/\mu_0$ for different values of the parameter $\mu_2'/\mu_0$ and (b) the coefficient $\alpha^{srd}$ for fixed permeability $\mu/\mu_0 = 10$, and different values of the Poisson's ratio of the matrix.

In this subsection, we consider spheroidal ($c = b$) inclusions of aspect ratio $w = a/b$ with aligned magnetic and geometric axes ($\theta = 0^\circ$) in the plane of the rotation. In this case, the equilibrium rotation also satisfies the relation (B.41) with $\alpha$ serving to describe the amplitude of the particle rotation as a function of the various geometric and material parameters. For simplicity here, we consider the following two cases:

*Case 1: Spherical inclusion ($w = 1$) with anisotropic permeability ($\mu_1' \neq \mu_2'$).* In this case, the coefficient $\alpha$ reduces to

$$\alpha^{sph}\left(\mu_1'/\mu_0, \mu_2'/\mu_0\right) = \frac{1}{2}\left(\frac{\mu_1'/\mu_0 - 1}{\mu_1'/\mu_0 + 2} - \frac{\mu_2'/\mu_0 - 1}{\mu_2'/\mu_0 + 2}\right),$$

which is independent of the Poisson's ratio of the matrix $\nu$. As it is shown in Fig. B.5(a), similar to the cylindrical inclusion with circular cross-section case, $\alpha^{sph}$ increases monotonically with increasing the magnetic anisotropy, $\mu_1'/\mu_0$, and saturates

for large values of $\mu'_1/\mu_0$.

*Case 2: Prolate spheroidal inclusion with aspect ratio $w = a/b > 1$ and isotropic in-plane magnetic behavior ($\mu'_1 = \mu'_2 = \mu$).* The coefficient $\alpha$ for this case can be written as

$$\alpha^{srd}\left(\mu/\mu_0, w, \nu\right) = \left(\hat{S}_{2121} - \frac{\hat{Q}^2_{2121}}{\hat{P}_{2121}}\right) \frac{\left(\mu/\mu_0 - 1\right)^2 \left(\hat{P}_{22} - \hat{P}_{11}\right)}{\left[1 + \hat{P}_{11}\left(\mu/\mu_0 - 1\right)\right]\left[1 + \hat{P}_{22}\left(\mu/\mu_0 - 1\right)\right]},$$

where

$$\hat{P}_{11} = \frac{w}{k^2}\left\{\frac{\sinh^{-1} k}{k} - \frac{1}{w}\right\}, \quad \hat{P}_{22} = \frac{w}{2k^2}\left\{w - \frac{\sinh^{-1} k}{k}\right\},$$

$$\hat{P}_{2121} = \frac{w}{8k^4}\left\{\frac{(1-\nu)\,k^4 + (2+\nu)\,k^2 + 3}{(1-\nu)\,w} - \frac{1+\nu}{1-\nu} k \sinh^{-1} k - \frac{3}{1-\nu}\frac{\sinh^{-1} k}{k}\right\},$$

$$\hat{Q}_{2121} = \frac{w}{8k^2}\left\{\frac{3\sinh^{-1} k}{k} - \frac{k^2+3}{w}\right\}, \qquad \hat{S}_{2121} = \frac{w}{8k^2}\left\{\frac{\sinh^{-1} k}{k} + \frac{k^2-1}{w}\right\}.$$

In these expressions, $k = \sqrt{w^2 - 1}$, where $w = a/b$ is the aspect ratio of the spheroid. As shown in Fig. B.5(b) (for $w > 1$), and similar to the elliptical particle, $\alpha^{srd}$ increases up to a maximum and then decays to zero with increasing the aspect ratio. However, for the spheroidal particles, the results for oblate ($w < 1$) spheroidal inclusions and the corresponding ones for prolate inclusions ($w > 1$) do *not* satisfy the symmetry relation $\alpha^{srd}(w) = -\alpha^{srd}(1/w)$ for $w < 1$, because oblate and prolate spheroids are geometrically different. Nonetheless, the general shape of the curve for oblate inclusions is similar to that of prolate inclusions, except for the sign of the rotation, of course.

## B.7 Concluding Remarks

In this appendix, we have addressed the magneto-elasticity problem of a single rigid inclusion with linear magnetic behavior embedded in a non-magnetic, and linear-elastic matrix. The main result is given by equation (B.32), which shows that the magnetic torque induced by an externally applied magnetic field will affect the overall rotation of the ellipsoidal inclusion embedded in a matrix that is being subjected to

a remotely applied deformation, as long as the inclusion is not both spherical and magnetically isotropic, and provided that the magnetic field is not aligned with one of its geometric, or magnetic axes.

To shed some light on the range of validity of the resulting expression for the equilibrium rotation of the inclusion, an asymptotic expansion in terms of the dimensionless parameter $\kappa = \mu_0 \bar{h}^2 / 2\mu_{el}$, serving to describe the relative strengths of the magnetic and elastic fields, was obtained (see equation (B.35) in Section B.5). It is shown that in order to be consistent with the assumption of infinitesimal deformations the parameter $\kappa$ can be at most of the order of the displacement gradient (i.e. $\kappa \sim |\nabla \mathbf{u}|$). Because of this, it is possible to neglect second-order terms in $\kappa$ in the expression for the equilibrium rotation of the inclusion.

The effect of magnetic anisotropy and inclusion shape on the particle rotation is investigated in some detail for both cylindrical (2D) and spheroidal (3D) inclusions, subjected to an in-plane magnetic field. The dependence of the particle rotation on the orientation of the applied magnetic field is found to be sinusoidal with period $\pi$, and it vanishes when the field is aligned with the symmetry axes of the particle, when both the magnetic and geometric axes coincide, and for some other intermediate orientations, when they are not. In addition, it is shown that the amplitude of the magnetically induced rotation monotonically increases and asymptotes to a constant value with increasing magnetic anisotropy of the inclusion. On the other hand, for magnetically isotropic inclusions with non-spherical shape, the equilibrium rotation increases up to a maximum, and then decays to zero, as the aspect ratio is increased.

The results of this appendix can be used to determine the effective behavior of magnetorheological composites consisting of a dilute concentration of rigid, magnetic inclusions distributed randomly in a non-magnetic elastomeric matrix in the small-deformation limit. The details of such a study are beyond the scope of this appendix and are left for a future publication. Furthermore, the results of this appendix provide some justification for the "stiff matrix" approximation in the work of Ponte Castañeda & Galipeau (2011) , which consists in the approximation that the particles are convected by the purely mechanical deformation in the limit when $\kappa \ll 1$. Indeed, when

a magnetorheological composite is subjected to finite strains, the additional rotations of the particles due to the applied magnetic fields would still be expected to be of order $\kappa$, and therefore small, compared to the mechanically driven particle rotations, which can be large compared to $\kappa$.

It should also be noted that the results of this appendix can be easily "translated" into corresponding results for the analogous problem of a stiff dielectric inclusion embedded in a soft dielectric matrix with a different dielectric coefficient which is assumed to be isotropic and deformation independent. Thus, identifying $\mathbf{h}$ with the electric field, $\mathbf{b}$ with the electric displacement, and $\mu_0$ and $\boldsymbol{\mu}^{(2)}$ with the dielectric coefficients of the matrix and inclusion, respectively, expression (B.25)—with an appropriate reinterpretation of $\boldsymbol{A}^{(2)}$—will correspond to the electric torque of the particle, while expression (B.35) will provide the rotation of the particle under the combined action of electric and mechanical loadings.

Finally, it is remarked that the results of this work for the particle rotation in a linear-elastic matrix under the action of a magnetic field could be generalized in at least two ways. First, the constitutive behavior of the particles could be taken to be non-linear, corresponding to ferromagnetic behavior, and second, the constitutive response of the elastomeric matrix material could be taken to be neo-Hookean, or some other suitably chosen hyperelasticity model to account for finite strains and rotations. The first would require generalization of the magnetostatic problem described in Section B.3 of this appendix to include nonlinear magnetization, which can be accomplished by application of the 'linear comparison' methods developed by Castaneda (1992) in the analogous context of nonlinear dielectric behavior (see also Ponte Castañeda et al. 1992). The second is a little more challenging and would require generalization of the elastic problem described in Section B.4 for the torque required to produce a finite rotation of the particle in the hyperelastic matrix. This could also be accomplished, at least in principle, by suitable application of the 'second-order' homogenization methods of Ponte Castañeda & Tiberio (2000) and Lopez-Pamies & Ponte Castañeda (2006*b*) for hyperelastic composites. These possible generalizations are under investigation and will be dealt with elsewhere.

## B.8 Solution of the BVP (B.27)

To find the solution of the BVP (B.27), we consider an auxiliary problem in which the whole space, $\mathbb{R}^3$, is filled with the elastic matrix material (see Fig. B.6). In this case, a part of the homogeneous body, $P_0$, which is geometrically the same as the inclusion but made up of the elastic matrix phase, undergoes a constant strain and a constant rotation due to the boundary condition $(B.27)_2$. To account for the fact that the strain in the actual rigid inclusion vanishes, it is necessary to apply a surface traction on the boundary of $P_0$ as follows

$$\mathbf{s}_1 = -\boldsymbol{\sigma}(\mathbf{x}')\,\mathbf{n}', \qquad \mathbf{x}' \in \partial P_0, \tag{B.42}$$

where $\boldsymbol{\sigma}(\mathbf{x}')$ is a divergence-free *symmetric* second-order tensor defined inside $P_0$. On the other hand, to satisfy the boundary condition $(B.27)_3$ and account for the rigid body rotation of the actual inclusion, it is required to apply a body torque distribution inside $P_0$ (i.e., $\mathbf{l} = \mathbf{l}(\mathbf{x}')$ for $\mathbf{x}' \in P_0$). However, to make the formulation more symmetric, instead of specifying the body torque to enforce the boundary condition $(B.27)_3$, we define a surface traction $\mathbf{s}_2$ on the boundary of $P_0$ as follows

$$\mathbf{s}_2 = -\boldsymbol{\tau}(\mathbf{x}')\,\mathbf{n}' \qquad \mathbf{x}' \in \partial P_0, \tag{B.43}$$

where $\boldsymbol{\tau}(\mathbf{x}')$ is a divergence-free, *skew-symmetric*, second-order tensor defined in $P_0$. Therefore, finding the solution of the BVP (B.27), shown schematically in Fig. B.6(a), is equivalent to finding the solution of the auxiliary problem depicted in B.6(b) with $\boldsymbol{\sigma}$ and $\boldsymbol{\tau}$ chosen such that

$$\boldsymbol{\epsilon}(\mathbf{x}) = 0, \quad \text{and} \quad \boldsymbol{\omega}(\mathbf{x}) = \bar{\boldsymbol{\omega}}^{(2)}, \qquad \mathbf{x} \in P_0. \tag{B.44}$$

Moreover, since the boundary conditions of the general BVP (B.27) are satisfied, the displacement field of the auxiliary problem, described above, is guaranteed to be the solution of (B.27) by the uniqueness theorem of elasticity (Love 1944) .

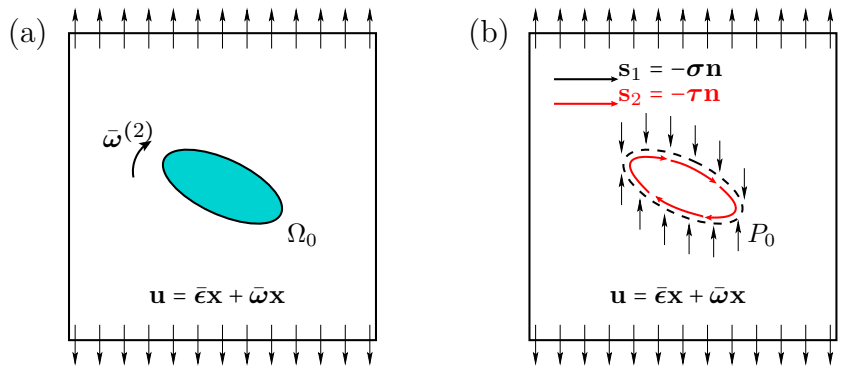


Figure B.6: Schematic of the problem given by the BVP (B.27). (a) The original problem, and (b) the auxiliary problem.

Using the linearity of the problem, the total displacement field for the above auxiliary problem can be divided into three parts. The first part is an affine displacement due to the boundary condition $(B.27)_3$ at infinity. Then, there is the displacement field due to the surface traction $\mathbf{s}_1$ which can be found by integration (over $\partial P_0$) from the solution of the concentrated force problem in an infinite elastic matrix (or the Green's tensor function of elasticity). Finally, there is the displacement field due to the traction $\mathbf{s}_2$. Noting that the surface traction $\mathbf{s}_2$ has a similar structure to $\mathbf{s}_1$, its contribution to the total displacement can be found by following the same procedure. It is important to note that, due to its singular character, the Green's function in the above computation has to be treated as a generalized function. However, to avoid the difficulties of dealing with such functions, it is useful to deploy the plane-wave decomposition of the delta function to generate alternative representations (in terms of the acoustic tensor) for the Green's function (see e.g., Willis 1977). Details for the calculations involved can be found in the works of Willis (1981) and Walpole (1991); the important results are summarized next.

Thus, it can be shown that the constraints (B.44) for inside the inclusion can be satisfied for constant $\boldsymbol{\sigma}$ and $\boldsymbol{\tau}$, i.e.

$$\boldsymbol{\sigma}(\mathbf{x}') = \boldsymbol{\sigma}, \quad \text{and} \quad \boldsymbol{\tau}(\mathbf{x}') = \boldsymbol{\tau}, \quad \mathbf{x}' \in P_0. \tag{B.45}$$

Therefore, the infinitesimal strain and rotation tensors for $\mathbf{x} \in P_0$ are uniform and

equal to

$$\boldsymbol{\epsilon} = \bar{\boldsymbol{\epsilon}} - \mathbb{P}\boldsymbol{\sigma} - \mathbb{Q}\boldsymbol{\tau}, \quad \text{and} \quad \boldsymbol{\omega} = \bar{\boldsymbol{\omega}} - \mathbb{R}\boldsymbol{\sigma} - \mathbb{S}\boldsymbol{\tau}, \tag{B.46}$$

where the fourth-order microstructural tensors $\mathbb{P}$, $\mathbb{Q}$, $\mathbb{R}$ and $\mathbb{S}$ are defined by

$$P_{ijpq} = X_{(ij)(pq)}, \;\; R_{ijpq} = X_{[ij](pq)}, \;\; Q_{ijpq} = X_{(ij)[pq]}, \text{ and } S_{ijpq} = X_{[ij][pq]} \tag{B.47}$$

in terms of

$$X_{ijpq} = \frac{\det \boldsymbol{Z}_0}{4\pi} \int_{|\boldsymbol{\xi}|=1} \xi_q \xi_j K_{ip}^{-1}(\boldsymbol{\xi}) \, |\boldsymbol{Z}_0 \boldsymbol{\xi}|^{-3} \;\; dS, \tag{B.48}$$

and depend only on the shape of the inclusion, through $\boldsymbol{Z}_0$, and on the elastic properties of the matrix, through the acoustic tensor $K_{ip}(\boldsymbol{\xi}) = C_{ijpq}^{(1)} \xi_j \xi_q$. Note that $\mathbb{P}$ and $\mathbb{R}$ are the usual Eshelby tensors characterizing the particle rotations in the small-strain/small-rotation limit, in the absence of external torque. On the other hand, $\mathbb{Q}$ and $\mathbb{S}$, which are such that $Q_{ijkl} = R_{klij}$, serve to account for the additional rotation of the inclusion due to the external torque.

Applying the constraints (B.44), the following system of equations is obtained

$$\bar{\boldsymbol{\epsilon}} = \mathbb{P}\boldsymbol{\sigma} + \mathbb{Q}\boldsymbol{\tau}, \quad \text{and} \quad \bar{\boldsymbol{\omega}} - \bar{\boldsymbol{\omega}}^{(2)} = \mathbb{R}\boldsymbol{\sigma} + \mathbb{S}\boldsymbol{\tau}, \tag{B.49}$$

which can be inverted for $\boldsymbol{\sigma}$ and $\boldsymbol{\tau}$ to yield the results in expressions (B.29). Having obtained expressions for $\boldsymbol{\sigma}$ and $\boldsymbol{\tau}$, it is now a simple matter to compute the total traction needed to produce the above-mentioned deformation in the auxiliary problem via $\mathbf{s} = \mathbf{s}_1 + \mathbf{s}_2 = -(\boldsymbol{\sigma} + \boldsymbol{\tau})\,\mathbf{n}$. This is of course the negative of the "mechanical" traction required to produce the needed rotation $\bar{\boldsymbol{\omega}}^{(2)}$ of the rigid particle in the original problem, as is given by expression (B.28) in terms of $\boldsymbol{\sigma}$ and $\boldsymbol{\tau}$.

# Appendix C

# Derivation of the linearized constitutive equations for electro-active materials

In this appendix, we provide a derivation of the constitutive response of a general homogeneous electro-active material in the limit of infinitesimal deformations by appropriately linearizing a thermodynamically consistent finite-strain formulation (Toupin 1956, Kovetz 1990, Hutter et al. 2006). The general form of the constitutive equations for a homogeneous electro-active material can thus be obtained by means of an energy-density (or potential) function $w(\boldsymbol{F}, \mathbf{d})$, where $\boldsymbol{F} := \partial \mathbf{x}(\mathbf{X}) / \partial \mathbf{X}$ is the deformation gradient. Then, the electric field and the total (Cauchy) stress for the material with potential $w(\boldsymbol{F}, \mathbf{d})$ are given by

$$\mathbf{e} = \frac{\partial w}{\partial \mathbf{d}}, \quad \text{and} \quad \boldsymbol{T} = \frac{\partial w}{\partial \boldsymbol{F}} \boldsymbol{F}^T + (w - \mathbf{d} \cdot \mathbf{e}) \boldsymbol{I} + \mathbf{e} \otimes \mathbf{d}. \tag{C.1}$$

The objectivity of the potential requires that $w(\boldsymbol{Q}\boldsymbol{F}, \boldsymbol{Q}\mathbf{d}) = w(\boldsymbol{F}, \mathbf{d})$ for any orthogonal matrix $\boldsymbol{Q}$. This implies (Kovetz 1990) that $w$ is a function of $\boldsymbol{F}^T\boldsymbol{F}$, $\boldsymbol{F}^T\mathbf{d}$, i.e.,

$$w = \hat{w}(\boldsymbol{F}^T\boldsymbol{F}, \boldsymbol{F}^T\mathbf{d}). \tag{C.2}$$

Therefore, by using the chain rule, equations (C.1), in terms of the modified potential $\hat{w}$, can be rewritten as

$$\mathbf{e} = \boldsymbol{F}\frac{\partial \hat{w}}{\partial \boldsymbol{F}^T \mathbf{d}}, \quad \text{and} \quad \boldsymbol{T} = 2\boldsymbol{F}\frac{\partial \hat{w}}{\partial \boldsymbol{F}^T \boldsymbol{F}}\boldsymbol{F}^T + (\hat{w} - \mathbf{d}\cdot\mathbf{e})\,\boldsymbol{I} + \mathbf{e}\otimes\mathbf{d} + \mathbf{d}\otimes\mathbf{e}. \tag{C.3}$$

Note that the stress $\boldsymbol{T}$, given by $(C.3)_2$, is obviously symmetric, as expected.

For small but finite deformations, linear-electrical response, and in the absence of piezo-electric effects, we can assume a general form for $w$ as follows

$$w(\boldsymbol{F}, \mathbf{d}) = \frac{1}{2}\boldsymbol{E} \cdot \mathbb{C}\boldsymbol{E} + \frac{1}{2}\mathbf{d}\cdot\boldsymbol{\varepsilon}^{-1}(\boldsymbol{F})\,\mathbf{d}, \tag{C.4}$$

where $\boldsymbol{E} = (\boldsymbol{F}^T\boldsymbol{F} - \boldsymbol{I})/2$ is the Green (or Lagrangian) strain tensor, $\mathbb{C}$ is the stiffness of the material and $\boldsymbol{\varepsilon}(\boldsymbol{F})$ is the corresponding (deformation-dependent) permittivity. Without loss of generality, $\mathbb{C}$ may be taken to be a constant (i.e., independent of the deformation and electric fields), fully symmetric, fourth-order tensor, while $\boldsymbol{\varepsilon}(\boldsymbol{F})$ is taken to be a symmetric, second-order tensor, characterizing the coupling of the electric and elastic effects. Alternatively, in terms of the modified potential, we can write

$$\hat{w}(\boldsymbol{F}^T\boldsymbol{F}, \boldsymbol{F}^T\mathbf{d}) = \frac{1}{2}\boldsymbol{E} \cdot \mathbb{C}\boldsymbol{E} + \frac{1}{2}\boldsymbol{F}^T\mathbf{d}\cdot\left(\boldsymbol{U}^{-1}\boldsymbol{\mathcal{E}}^{-1}(\boldsymbol{E})\,\boldsymbol{U}^{-1}\right)\boldsymbol{F}^T\mathbf{d}, \tag{C.5}$$

where we have made use of the polar decomposition $\boldsymbol{F} = \boldsymbol{R}\boldsymbol{U}$ to decompose the deformation gradient into a rotation $\boldsymbol{R}$ and a stretch $\boldsymbol{U} = (\boldsymbol{F}^T\boldsymbol{F})^{1/2}$, and we have introduced the "strain-dependent permittivity"

$$\boldsymbol{\mathcal{E}}(\boldsymbol{E}) = \boldsymbol{R}^T\,\boldsymbol{\varepsilon}(\boldsymbol{F})\boldsymbol{R}. \tag{C.6}$$

Note that $\boldsymbol{\mathcal{E}}(\boldsymbol{E})$ physically corresponds to the permittivity of the medium in a fictitious frame of reference that rotates with the material (particles).

We can then use equations (C.3) to obtain explicit expressions for the electric field $\mathbf{e}$ and the total stress $\boldsymbol{T}$ corresponding to the potential described above. These expressions can then be linearized to obtain the constitutive equations of the electro-active

materials in the limit of infinitesimal deformations. The result for the deformation-dependent electric constitutive equation is given by expression (4.4), where $\boldsymbol{\mathcal{E}}_0 = \boldsymbol{\mathcal{E}}(0)$ is the permittivity of the material in the reference (undeformed) configuration, and the electromechanical coupling constant $\mathbb{S}$ is given also in terms of $\boldsymbol{\mathcal{E}}$ by expression (4.5).

On the other hand, the total stress inside the electro-active materials in the limit of infinitesimal deformations is found to be of the form (4.8), where $\boldsymbol{T}^{me} = \mathbb{C}\boldsymbol{\epsilon}$ and

$$\boldsymbol{T}^{el} = \frac{1}{2}(\mathbf{e}\otimes\mathbf{d} + \mathbf{d}\otimes\mathbf{e}) - \frac{1}{2}(\mathbf{e}\cdot\mathbf{d})\,\boldsymbol{I} + \frac{1}{2}\mathbb{D}^{\dagger}(\mathbf{d}\otimes\mathbf{e})\,. \tag{C.7}$$

Here the fourth-order tensor $\mathbb{D}$ is given by

$$D^{\dagger}_{mnij} = D_{ijmn} = -\mathcal{E}^{-1}_{0_{ip}} S_{pjmn}, \tag{C.8}$$

and satisfies the symmetry property $D_{ijmn} = D_{ijnm}$. Note that in expression (4.8) for $\boldsymbol{T}$, terms of order $|\nabla\mathbf{u}|^2$ and $|\nabla\mathbf{u}||\mathbf{d}|^2$ or higher are ignored in order to be consistent with the general form (C.4) for the potential $w$. For the same reason, terms of order $|\nabla\mathbf{u}|^2$ or higher are ignored in expression $(4.3)_2$ for $\boldsymbol{\varepsilon}$.

It is noted that the result for the total stress provided by equation (4.8) is in agreement with the results of Landau et al. (1984). However, it should be emphasized that Landau et al. (1984) treat the effect of the macroscopic rotation as an additional contribution to the free energy, whereas in this work the effect of the macroscopic rotation is directly accounted for in the linearization of the potential energy $w$ (or $\hat{w}$).

It is important to emphasize that the result (4.8) is only valid for infinitesimal deformations. Therefore, the electric fields appearing on the right side of equation (4.8) cannot be arbitrarily large since they may result in large deformations. As discussed in section 4.4.2, the boundary conditions that are widely used in practical applications of DECs, require the total stress $\boldsymbol{T} = \mathbb{C}\boldsymbol{\epsilon} + \boldsymbol{T}^{el}$ inside to vanish (see (4.70)). In order to obtain a measure for the size of the electric fields that are consistent with the assumption of the infinitesimal deformations, we introduce the

dimensionless parameters

$$\check{\mathbb{C}} = \frac{1}{\mu}\mathbb{C}, \quad \check{\mathbf{d}} = \frac{1}{\varepsilon\bar{e}}\mathbf{d}, \quad \text{and} \quad \check{\mathbf{e}} = \frac{1}{\bar{e}}\mathbf{e}, \tag{C.9}$$

where $\mu$, $\varepsilon$ and $\bar{e}$ are appropriately chosen reference values for the shear modulus, permittivity and the electric field, respectively. Now equation (4.70) can be rewritten as $\check{\mathbb{C}}\boldsymbol{\epsilon} + \kappa\check{\boldsymbol{T}}^{el} = 0$, where $\check{\boldsymbol{T}}^{el}$ is given by (C.7) with $\mathbf{e}$ and $\mathbf{d}$ being replaced by $\check{\mathbf{e}}$ and $\check{\mathbf{d}}$, respectively, and satisfies $\check{\boldsymbol{T}}^{el} \sim O(1)$, and where the dimensionless parameter $\kappa$, defined by expression (4.7), serves to characterize the strength of the electrostatic effects relative to the elastic effects. It then becomes clear from equation (4.7) that unless $\kappa$ is of the same order as the strain (i.e., $\kappa \sim |\boldsymbol{\epsilon}|$), the assumption of infinitesimal deformations will be violated.

It is also important in this context to recall that $\mathbf{d}$ and $\mathbf{e}$ (or similarly $\check{\mathbf{d}}$ and $\check{\mathbf{e}}$) are Eulerian variables, which, in general, depend on the deformation. However, for cases where $\kappa \sim |\boldsymbol{\epsilon}|$, they can be replaced by their Lagrangian (referential) counterparts. This is due to the fact that Eulerian and Lagrangian variables differ at most by correction terms that are of first order in the strain, which translate into terms of order $\kappa^2$, or higher in the corresponding expressions for the total stress. The fact that all the electric fields in the expression for the total stress have to be computed in the reference configuration allows further simplification of the expression for the electric part of the total stress as follows

$$\boldsymbol{T}^{el} = -\frac{1}{2}\left(\mathbf{e}\cdot\mathbf{d}\right)\boldsymbol{I} + \frac{1}{2}\left(\mathbf{e}\otimes\mathbf{d} + \mathbf{d}\otimes\mathbf{e}\right) - \frac{1}{2}\mathbb{S}^{\dagger}\left(\mathbf{e}\otimes\mathbf{e}\right). \tag{C.10}$$

In the above result for the electric contribution to the total stress, the tensor $\mathbb{S}$ only depends on $\boldsymbol{\mathcal{E}}(\boldsymbol{\epsilon})$ via equation (4.5). Thus, the the constitutive relations (i.e., effective permittivity and the total stress) for a general electro-active material can be obtained solely in terms of the strain-dependent permittivity $\boldsymbol{\mathcal{E}}(\boldsymbol{\epsilon})$.

# Appendix D

# Microstructural tensors for spheroidal inclusions

The mechanical (or electric) microstructural tensors $\mathbb{P}$ and $\mathbb{R}$ (or $\boldsymbol{P}$ and $\hat{\mathbb{P}}$) for the special case of spherical inclusions with symmetry axis along the unit vector $\mathbf{n}$ exhibit transversely isotropic symmetry. For this reason, it is useful to define two elementary second-order tensors

$$\boldsymbol{\rho} = \mathbf{n} \otimes \mathbf{n} \quad \text{and} \quad \boldsymbol{\gamma} = \boldsymbol{I} - \mathbf{n} \otimes \mathbf{n}, \tag{D.1}$$

such that a general transversely symmetric second-order tensor $\boldsymbol{\sigma}$ can be written as $\boldsymbol{\sigma} = \sigma_r \boldsymbol{\rho} + \sigma_s \boldsymbol{\gamma}$, where $\sigma_r$ and $\sigma_s$ are the axial and transverse components of $\boldsymbol{\sigma}$, respectively.

A general transversely isotropic fourth-order tensor can then be expressed (Walpole 1981) in terms of four fully symmetric fourth-order tensors $\mathbb{E}^{[\alpha]}$ ($\alpha = 1, \cdots, 4$), two additional tensors with minor symmetries $\mathbb{E}^{[5]}$ and $\mathbb{E}^{[6]}$, and another tensor $\mathbb{F}$ with symmetry properties $F_{ijkl} = F_{ijlk} = -F_{jikl}$. They are defined, in terms of $\boldsymbol{\rho}$ and $\boldsymbol{\gamma}$, as

follows

$$\begin{aligned}
E^{[1]}_{ijkl} &:= \tfrac{1}{2}\gamma_{ij}\gamma_{kl}, \quad E^{[2]}_{ijkl} := \rho_{ij}\rho_{kl}, \\
E^{[3]}_{ijkl} &:= \tfrac{1}{2}\left(\gamma_{ik}\gamma_{jl} + \gamma_{jk}\gamma_{il} - \gamma_{ij}\gamma_{kl}\right), \\
E^{[4]}_{ijkl} &:= \tfrac{1}{2}\left(\gamma_{ik}\rho_{jl} + \gamma_{il}\rho_{jk} + \gamma_{jl}\rho_{ik} + \gamma_{jk}\rho_{il}\right), \\
E^{[5]}_{ijkl} &:= \rho_{ij}\gamma_{kl}, \quad E^{[6]}_{ijkl} := \gamma_{ij}\rho_{kl}, \text{ and} \\
F_{ijkl} &:= \tfrac{1}{4}\left(-\gamma_{ik}\rho_{jl} - \gamma_{il}\rho_{jk} + \gamma_{jl}\rho_{ik} + \gamma_{jk}\rho_{il}\right).
\end{aligned} \tag{D.2}$$

For future use, the auxiliary tensor $\mathbb{E}^{[a]}$ is also defined as follows

$$\mathbb{E}^{[a]} = \frac{1}{3}\mathbb{E}^{[1]} + \frac{2}{3}\mathbb{E}^{[2]} - \frac{1}{3}\left(\mathbb{E}^{[5]} + \mathbb{E}^{[6]}\right). \tag{D.3}$$

It is easily observed that the first four of the tensors in (D.2) are projections, i.e. they satisfy

$$\begin{aligned}
\textstyle\sum_{\alpha=1}^{4} \mathbb{E}^{[\alpha]} &= \mathbb{I}, \\
\mathbb{E}^{[\alpha]}\mathbb{E}^{[\alpha]} &= \mathbb{E}^{[\alpha]} \quad \text{for } \alpha \in \{1, \cdots, 4\}, \\
\mathbb{E}^{[\alpha]}\mathbb{E}^{[\beta]} &= 0 \qquad \text{for } \alpha \neq \beta \in \{1, \cdots, 4\}.
\end{aligned} \tag{D.4}$$

Also it can be shown that the following relations hold

$$\begin{aligned}
\mathbb{E}^{[a]}\mathbb{E}^{[a]} &= \mathbb{E}^{[a]}, \\
\mathbb{E}^{[a]}\mathbb{E}^{[\alpha]} &= \mathbb{E}^{[\alpha]}\mathbb{E}^{[a]} = 0 \text{ for } \alpha \in \{3, 4\}, \\
\mathbb{F}\mathbb{E}^{[\alpha]} &= \mathbb{F} \text{ for } \alpha = 4, \text{ and 0 otherwise.}
\end{aligned} \tag{D.5}$$

It can then be shown (Ponte Castañeda & Willis 1995) that for the special case of spheroidal inclusions with aspect ratio $w$ and symmetry axis $\mathbf{n}$, together with incompressible matrices with shear modulus $\mu^{(1)}$,

$$\mathbb{P} = 2m^p_p\mathbb{E}^{[3]} + 2m^p_n\mathbb{E}^{[4]} + 2m^p_a\mathbb{E}^{[a]} \text{ and } \mathbb{R} = r\mathbb{F}, \tag{D.6}$$

where

$$\begin{aligned}
m^p_p &= \tfrac{3h(w)-2w^2}{16(1-w^2)\mu^{(1)}}, \qquad m^p_n = \tfrac{\left[(1+w^2)(2-3h(w))\right]}{8(1-w^2)\mu^{(1)}}, \\
m^p_a &= \tfrac{3\left[h(w)-2w^2+2w^2h(w)\right]}{8(1-w^2)\mu^{(1)}}, \quad \text{and} \quad r = \tfrac{3h(w)-2}{2\mu^{(1)}},
\end{aligned} \tag{D.7}$$

for $w \neq 1$ and

$$m_p^p = m_n^p = m_a^p = \frac{1}{10\mu^{(1)}} \quad \text{and} \quad r = 0, \tag{D.8}$$

for $w = 1$. The function $h(w)$ is given by

$$h(w) = \begin{cases} \frac{w\left[\arccos(w) - w\sqrt{1-w^2}\right]}{(1-w^2)^{3/2}} & w < 1 \\ 2/3 & w = 1 \\ \frac{w\left[w\sqrt{w^2-1} - \operatorname{arccosh}(w)\right]}{(w^2-1)^{3/2}} & w > 1 \end{cases}. \tag{D.9}$$

The corresponding electric microstructural tensors are given by

$$\begin{aligned} \boldsymbol{P} &= p_r \boldsymbol{\rho} + p_s \boldsymbol{\gamma} \\ \hat{\mathbb{P}} &= 2\hat{k}_p^p \mathbb{E}^{[1]} + \hat{n}^p \mathbb{E}^{[2]} + 2\hat{m}_p^p \mathbb{E}^{[3]} + 2\hat{m}_n^p \mathbb{E}^{[4]} + \hat{l}^p \mathbb{E}^{[5]} + \hat{l}'^p \mathbb{E}^{[6]} \\ &= \left(2\hat{k}_p^p, \hat{n}^p, 2\hat{m}_p^p, 2\hat{k}_n^p, \hat{l}^p, \hat{l}'^p\right) \text{ in short,} \end{aligned} \tag{D.10}$$

where

$$\begin{aligned} p_r &= \tfrac{1-h(w)}{\varepsilon^{(1)}}, & p_s &= \tfrac{h(w)}{2\varepsilon^{(1)}}, \\ \hat{k}_p^p &= 2\hat{m}_p^p = \tfrac{3h(w)-2w^2}{4(w^2-1)\varepsilon^{(1)}}, & \hat{n}^p &= \tfrac{3w^2h(w)-3w^2+1}{(w^2-1)\varepsilon^{(1)}}, \\ \hat{l}^p &= \hat{l}'^p/w^2 = \tfrac{2-3h(w)}{2(w^2-1)\varepsilon^{(1)}}, & 2\hat{m}_n^p &= \tfrac{\left(1+w^2\right)(2-3h(w))}{2(w^2-1)\varepsilon^{(1)}}, \end{aligned} \tag{D.11}$$

for $w \neq 1$. For spherical inclusions we have

$$P_{ij} = \tfrac{1}{3\varepsilon^{(1)}}\delta_{ij} \quad \text{and} \quad \hat{P}_{ijkl} = \tfrac{-1}{5\varepsilon^{(1)}}\left(\delta_{ij}\delta_{kl} + \delta_{ik}\delta_{jl} + \delta_{il}\delta_{jk}\right). \tag{D.12}$$

Note that the correction tensor $\hat{\mathbb{P}}$ is defined only for the distribution while the other microstructural tensors are defined for both inclusions and the distribution. Therefore, when computing the microstructural tensors for the inclusions, $w_{\mathcal{I}_0}$ and $\mathbf{n}_{\mathcal{I}_0}$ corresponding to the geometry of the inclusions have to be used, while $w_{\mathcal{D}_0}$ and $\mathbf{n}_{\mathcal{D}_0}$ have to be used for the computation of the microstructural tensors for the distribution.

# Appendix E

# Eulerian expressions for the macroscopic stress and electric field

Here we provide the corresponding Eulerian forms of expressions (5.29) and (5.30) for the effective constitutive response of fiber-constrained DECs. Thus, we define the Eulerian energies

$$\tilde{w}_{me}\left(\bar{\boldsymbol{F}}\right) := \tilde{W}_{me}\left(\bar{\boldsymbol{F}}\right) \quad \text{and} \quad \tilde{w}_{el} := \frac{1}{2}\bar{\mathbf{D}} \cdot \tilde{\boldsymbol{\varepsilon}}^{-1}\left(\bar{\boldsymbol{F}}\right)\bar{\mathbf{D}}, \tag{E.1}$$

where $\tilde{\boldsymbol{\varepsilon}}\left(\bar{\boldsymbol{F}}\right)$ is the effective deformation-dependent permittivity given by $(5.17)_2$, and the replacement $\bar{J} = 1$ is made to account for the overall incompressibility of the DEC. Then, taking into account the objectivity of the effective energy, as well as the quadratic nature of $\tilde{w}_{el}$ on $\bar{\mathbf{D}}$, the Eulerian electric field and the total Cauchy stress can be shown to be given by

$$\bar{\mathbf{E}} = \tilde{\boldsymbol{\varepsilon}}^{-1}\left(\bar{\boldsymbol{F}}\right)\bar{\mathbf{D}} \quad \text{and} \quad \bar{\boldsymbol{T}} = \bar{\boldsymbol{T}}^{me} + \bar{\boldsymbol{T}}^{el}, \tag{E.2}$$

where

$$\bar{\boldsymbol{T}}^{me} = 2\bar{\boldsymbol{F}}\frac{\partial \tilde{u}_{me}}{\partial \bar{\boldsymbol{C}}}\bar{\boldsymbol{F}}^T - \bar{p}\boldsymbol{I}, \quad \text{and} \quad \bar{\boldsymbol{T}}^{el} = 2\bar{\boldsymbol{F}}\frac{\partial \tilde{u}_{el}}{\partial \bar{\boldsymbol{C}}}\bar{\boldsymbol{F}}^T - \frac{1}{2}\left(\bar{\mathbf{E}}\cdot\bar{\mathbf{D}}\right)\boldsymbol{I} + \bar{\mathbf{E}}\otimes\bar{\mathbf{D}} + \bar{\mathbf{D}}\otimes\bar{\mathbf{E}}. \tag{E.3}$$

In the above equations, $\tilde{u}_{me}\left(\bar{\boldsymbol{C}}\right)$ and $\tilde{u}_{el}\left(\bar{\boldsymbol{C}}, \bar{\boldsymbol{F}}^T\bar{\mathbf{D}}\right)$ are the corresponding objective forms of the effective energies $\tilde{w}_{me}\left(\bar{\boldsymbol{F}}\right)$ and $\tilde{w}_{el}\left(\bar{\boldsymbol{F}}, \bar{\mathbf{D}}\right)$, respectively, and $\bar{\boldsymbol{C}} \coloneqq \bar{\boldsymbol{F}}^T\bar{\boldsymbol{F}}$.

The derivative $\partial\tilde{u}_{el}/\partial\bar{\boldsymbol{C}}$ can be written in a more explicit form as follows

$$\frac{\partial \tilde{u}_{el}}{\partial \bar{\boldsymbol{C}}} = -\frac{1}{4}\tilde{\mathbb{S}}^{\dagger}\left[\left(\bar{\boldsymbol{R}}^T\bar{\mathbf{E}}\right)\otimes\left(\bar{\boldsymbol{R}}^T\bar{\mathbf{e}}\right)\right] - \mathbb{T}^{\dagger}\left[\left(\bar{\boldsymbol{R}}^T\bar{\mathbf{D}}\right)\otimes\left(\bar{\boldsymbol{R}}\bar{\mathbf{E}}\right)\right], \tag{E.4}$$

where the fourth-order tensors $\tilde{\mathbb{S}}$ and $\mathbb{T}$ are, respectively, defined by

$$\tilde{S}_{pqkl} \coloneqq 2\,\frac{\partial \tilde{\mathcal{E}}_{pq}}{\partial \bar{C}_{kl}}, \quad \text{and} \quad T_{pqkl} \coloneqq \frac{\partial \bar{U}_{pn}}{\partial \bar{C}_{kl}}\bar{U}^{-1}_{nq}, \tag{E.5}$$

and the symbol "†" denotes the diagonal transpose operator. Note that $\tilde{\mathbb{S}}$ is a material property characterizing the effective electromechanical coupling tensor of the composite. The expression for $\mathbb{T}$ can be further simplified by using an explicit expression for the derivative $\partial\bar{\boldsymbol{U}}/\partial\bar{\boldsymbol{C}}$ (see Hoger & Carlson 1984, for more details). Thus, we obtain

$$\begin{aligned} T_{pqkl} = \frac{1}{4\bar{I}_1\bar{I}_2}\Big\{&\left(\bar{U}_{pk}\delta_{lq} + \bar{U}_{pl}\delta_{kq}\right) + \left(\bar{I}_1^2 + \bar{I}_2\right)\left(\delta_{pk}\bar{U}^{-1}_{lq} + \delta_{pl}\bar{U}^{-1}_{kq}\right) \\ &-\bar{I}_1\left(\bar{U}_{pk}\bar{U}^{-1}_{lq} + \bar{U}_{pl}\bar{U}^{-1}_{kq} + \delta_{pk}\delta_{lq} + \delta_{pl}\delta_{kq}\right)\Big\}, \end{aligned} \tag{E.6}$$

where $\bar{I}_1 \coloneqq \operatorname{tr}\bar{\boldsymbol{U}}$ and $\bar{I}_2 \coloneqq \det\bar{\boldsymbol{U}}$. Finally, by substituting (E.4) into $(\text{E.3})_2$, we get

$$\begin{aligned} \bar{\boldsymbol{T}}^{el} = &-\frac{1}{2}\left(\bar{\mathbf{E}}\cdot\bar{\mathbf{D}}\right)\boldsymbol{I} + \bar{\mathbf{E}}\otimes\bar{\mathbf{D}} + \bar{\mathbf{D}}\otimes\bar{\mathbf{E}} \\ &- 2\bar{\boldsymbol{F}}\left\{\mathbb{T}^{\dagger}\left[\left(\bar{\boldsymbol{R}}^T\bar{\mathbf{D}}\right)\otimes\left(\bar{\boldsymbol{R}}^T\bar{\mathbf{E}}\right)\right] + \frac{1}{4}\tilde{\mathbb{S}}^{\dagger}\left[\left(\bar{\boldsymbol{R}}^T\bar{\mathbf{E}}\right)\otimes\left(\bar{\boldsymbol{R}}^T\bar{\mathbf{E}}\right)\right]\right\}\bar{\boldsymbol{F}}^T. \end{aligned} \tag{E.7}$$

The limit as $\bar{\boldsymbol{U}} \to \boldsymbol{I}$ is of special interest for infinitesimal deformations. In this limit, expression (E.6) reduces to

$$T_{pqkl} = \frac{1}{4}\left(\delta_{pk}\bar{U}^{-1}_{lq} + \delta_{pl}\bar{U}^{-1}_{kq}\right), \tag{E.8}$$

and the macroscopic stress correspondingly reduces to

$$\bar{\boldsymbol{T}} = \bar{\boldsymbol{T}}^{me}_{inf} + \frac{1}{2}\left(\bar{\mathbf{e}} \otimes \bar{\mathbf{d}} + \bar{\mathbf{d}} \otimes \bar{\mathbf{e}}\right) - \frac{1}{2}\left(\bar{\mathbf{e}} \cdot \bar{\mathbf{d}}\right)\boldsymbol{I} - \frac{1}{2}\tilde{\mathbb{S}}^{\dagger}_{inf}\left(\bar{\mathbf{e}} \otimes \bar{\mathbf{e}}\right), \tag{E.9}$$

where $\bar{\boldsymbol{T}}^{me}_{inf}$ is the purely mechanical contribution to the total stress in the limit of infinitesimal deformations, and $\tilde{\mathbb{S}}_{inf} = \tilde{\mathbb{S}}(\bar{\boldsymbol{C}} = \boldsymbol{I})$. Note that these results agree exactly with the results obtained in the recent work of Siboni & Ponte Castañeda (2013) for infinitesimal deformations, and therefore the finite-deformation estimates developed in this work are consistent with our earlier infinitesimal-deformation results.

# Appendix F

# Levine relations for two-phase linear thermoelastic composites

Here we provide explicit expressions for the effective energy of linear two-phase composites with particulate microstructures. Thus, consider a two-phase composite consisting of linear phases with the following quadratic energies

$$W_T^{(r)} = f^{(r)} + \boldsymbol{T}^{(r)} \cdot \boldsymbol{F} + \frac{1}{2}\boldsymbol{F} \cdot \mathbb{L}^{(r)}\boldsymbol{F}, \quad \text{for} \quad r = 1, 2. \tag{F.1}$$

At this stage $f^{(r)}$, $\boldsymbol{T}^{(r)}$, and $\mathbb{L}^{(r)}$ are given quantities which may be replaced by the corresponding coefficients obtained from the linearization of the non-linear phase energies. Using a generalization of the Levin relations for two-phase (i.e., $r = 1, 2$) thermoelastic composites, it is obtained that

$$\hat{W}_T = \tilde{f} + \tilde{\boldsymbol{T}} \cdot \bar{\boldsymbol{F}} + \frac{1}{2}\bar{\boldsymbol{F}} \cdot \tilde{\mathbb{L}}\bar{\boldsymbol{F}}, \tag{F.2}$$

where

$$\begin{aligned} \tilde{f} &:= \bar{f} + \frac{1}{2}\Delta\boldsymbol{T} \cdot \left[ (\Delta\mathbb{L})^{-1} \left( \tilde{\mathbb{L}} - \bar{\mathbb{L}} \right) (\Delta\mathbb{L})^{-1} \right] \Delta\boldsymbol{T} \\ \tilde{\boldsymbol{T}} &:= \bar{\boldsymbol{T}} + \left( \tilde{\mathbb{L}} - \bar{\mathbb{L}} \right) (\Delta\mathbb{L})^{-1} \Delta\boldsymbol{T}. \end{aligned} \tag{F.3}$$

Here $\Delta\boldsymbol{T} := \boldsymbol{T}^{(1)} - \boldsymbol{T}^{(2)}$, $\Delta\mathbb{L} := \mathbb{L}^{(1)} - \mathbb{L}^{(2)}$, and $\bar{f}$, $\bar{\boldsymbol{T}}$ and $\bar{\mathbb{L}}$ are the volume averages of the corresponding local variables. For *particulate* microstructures (e.g., see the

microstructures described in section 3.2), we make use of Hashin-Shtrikman type estimates for the effective modulus. Thus, $\tilde{\mathbb{L}}$ will be taken to be

$$\tilde{\mathbb{L}} = \mathbb{L}^{(1)} + c_0 \left[ (1 - c_0) \mathbb{P} - (\Delta \mathbb{L})^{-1} \right]^{-1}, \tag{F.4}$$

where $c_0$ is the volume fraction of the particle phase and $\mathbb{P}$ is the usual microstructural tensor (with major symmetries but not necessarily minor symmetries). The microstructural tensor $\mathbb{P}$ for composites consisting of inclusions with general ellipsoidal shapes, as characterized by the second-order shape tensor $\boldsymbol{Z}_0$ may be computed as follows

$$\mathbb{P} := \frac{\det \boldsymbol{Z}_0}{4\pi} \int_{|\boldsymbol{\xi}|=1} \mathbb{H}(\boldsymbol{\xi}) \left| \boldsymbol{Z}_0^T \boldsymbol{\xi} \right|^{-3} dS, \tag{F.5}$$

where the fourth-order tensor $\mathbb{H}$ is defined in terms of the acoustic tensor $K_{ik} = L^{(1)}_{ijkl} \xi_j \xi_l$, as follows

$$H_{ijkl}(\boldsymbol{\xi}) := K^{-1}_{ik} \xi_j \xi_l. \tag{F.6}$$

For composites consisting of long cylindrical fibers with elliptical shapes for the cross-section the above expression for the $\mathbb{P}$-tensor simplifies as follows

$$\mathbb{P} := \frac{\det \boldsymbol{Z}_0}{2\pi} \int_{\xi_1^2 + \xi_2^2 = 1} \mathbb{H}(\xi_1, \xi_2, \xi_3 = 0) \left| \boldsymbol{Z}_0^T \boldsymbol{\xi} \right|^{-1} dS. \tag{F.7}$$

Having the expression for the effective response of the above composite we can use the identity

$$\bar{\boldsymbol{F}}^{(2)} = \frac{1}{c_0} \frac{\partial \hat{W}_T}{\partial \boldsymbol{T}^{(2)}} \tag{F.8}$$

to obtain an expression to relate the deformation of the inclusion phase to the prescribed tensors $\boldsymbol{T}^{(1)}$ and $\boldsymbol{T}^{(2)}$. The computation of the derivative on the right side of (F.8), requires the computation of $\frac{\partial \tilde{f}}{\partial \boldsymbol{T}^{(2)}}$ and $\frac{\partial \tilde{\boldsymbol{T}} \cdot \bar{\boldsymbol{F}}}{\partial \boldsymbol{T}^{(2)}}$, which are easily obtained as follows

$$\frac{\partial}{\partial \boldsymbol{T}^{(2)}} \tilde{f} := -\mathbb{Y} \Delta \boldsymbol{T} \quad \text{and} \quad \frac{\partial}{\partial \boldsymbol{T}^{(2)}} \tilde{\boldsymbol{T}} \cdot \bar{\boldsymbol{F}} := c_0 \bar{\boldsymbol{F}} - \mathbb{Y} \Delta \mathbb{L} \bar{\boldsymbol{F}} \tag{F.9}$$

where

$$\mathbb{Y} := (\Delta \mathbb{L})^{-1} \left( \tilde{\mathbb{L}} - \bar{\mathbb{L}} \right) (\Delta \mathbb{L})^{-1}. \tag{F.10}$$

Therefore, we obtain

$$\begin{aligned}\bar{\boldsymbol{F}} - \bar{\boldsymbol{F}}^{(2)} &= \frac{\mathbb{Y}}{c_0}\left[\Delta \boldsymbol{T} + \Delta\mathbb{L}\bar{\boldsymbol{F}}\right] \\ &= \frac{\mathbb{Y}}{c_0}\left[\Delta \boldsymbol{T} + \Delta\mathbb{L}\bar{\boldsymbol{F}}^{(2)} + \Delta\mathbb{L}\left(\bar{\boldsymbol{F}} - \bar{\boldsymbol{F}}^{(2)}\right)\right].\end{aligned} \tag{F.11}$$

Solving the above equation for $\bar{\boldsymbol{F}} - \bar{\boldsymbol{F}}^{(2)}$, we get

$$\left\{\mathbb{I} - \frac{\mathbb{Y}\Delta\mathbb{L}}{c_0}\right\}\left(\bar{\boldsymbol{F}} - \bar{\boldsymbol{F}}^{(2)}\right) = \frac{\mathbb{Y}}{c_0}\left[\Delta \boldsymbol{T} + \Delta\mathbb{L}\bar{\boldsymbol{F}}^{(2)}\right] \tag{F.12}$$

or

$$\left(\bar{\boldsymbol{F}} - \bar{\boldsymbol{F}}^{(2)}\right) = \left\{\mathbb{I} - \frac{\mathbb{Y}\Delta\mathbb{L}}{c_0}\right\}^{-1}\frac{\mathbb{Y}}{c_0}\left[\Delta \boldsymbol{T} + \Delta\mathbb{L}\bar{\boldsymbol{F}}^{(2)}\right]. \tag{F.13}$$

Given the expression (F.4) and the definition (F.10), we can show that

$$\begin{aligned}\frac{1}{c_0}\mathbb{Y} &:= \left[\mathbb{I} - (1-c_0)^{-1}(\Delta\mathbb{L})^{-1}\mathbb{P}^{-1}\right]^{-1}(\Delta\mathbb{L})^{-1} \\ \left\{\mathbb{I} - \frac{\mathbb{Y}\Delta\mathbb{L}}{c_0}\right\}^{-1} &:= -(1-c_0)\mathbb{P}\Delta\mathbb{L}\left[\mathbb{I} - (1-c_0)^{-1}(\Delta\mathbb{L})^{-1}\mathbb{P}^{-1}\right].\end{aligned} \tag{F.14}$$

Hence, we obtain

$$\bar{\boldsymbol{F}} - \bar{\boldsymbol{F}}^{(2)} = -(1-c_0)\mathbb{P}\left[\Delta \boldsymbol{T} + \Delta\mathbb{L}\bar{\boldsymbol{F}}^{(2)}\right]. \tag{F.15}$$

# Appendix G

# Asymptotic analysis

To obtain the estimates for the incompressible limit, the following asymptotic expansions for $l^*$s, have been proven useful (Lopez-Pamies & Ponte Castañeda 2006*a*),

$$\begin{aligned} l_1^* &= \frac{a_{-1}}{\delta} + a_0 + a_1\delta + \mathcal{O}\left(\delta^2\right) \\ l_2^* &= \frac{b_{-1}}{\delta} + b_0 + b_1\delta + \mathcal{O}\left(\delta^2\right) \\ l_4^* &= d_0 + d_1\delta + d_2\delta^2 + \mathcal{O}\left(\delta^3\right) \\ l_3^* &= e_0 + e_1\delta + e_2\delta^2 + \mathcal{O}\left(\delta^3\right), \end{aligned} \tag{G.1}$$

where $\delta := \left(1/\kappa^{(1)}\right)^{1/3}$. Then taking the expansion

$$\varphi = \varphi_0 + \varphi_1\delta + \mathcal{O}\left(\delta^2\right), \quad \text{where} \quad \varphi_0 = \phi_0 - \bar{\psi}, \tag{G.2}$$

for the in-plane rotation (relative to the macroscopic rotation) of the fibers, the relevant components of the tensor $\boldsymbol{Y}$, are obtained as follows

$$\begin{aligned} Y_{11} &= x_0 + x_1\delta + x_2\delta^2 + \mathcal{O}\left(\delta^3\right) \\ Y_{22} &= y_0 + y_1\delta + y_2\delta^2 + \mathcal{O}\left(\delta^3\right) \\ Y_{12}Y_{21} &= p_0 + p_1\delta + p_2\delta^2 + \mathcal{O}\left(\delta^3\right) \\ Y_{11}^2 + Y_{22}^2 &= s_0 + s_1\delta + \mathcal{O}\left(\delta^2\right) \end{aligned} \tag{G.3}$$

By expanding (7.49) to the zeroth order we obtain

$$x_0 = \frac{c_0}{1-c_0}\left(\bar{\lambda} - \cos\varphi_0\right) \quad \text{and} \quad y_0 = \frac{c_0}{1-c_0}\left(\frac{1}{\bar{\lambda}} - \cos\varphi_0\right) \tag{G.4}$$

and by solving equations $(7.47)_{3,4}$, to the zeroth order, we obtain

$$\begin{aligned}
p_0 &= \frac{c_0}{\bar{\lambda}\left(1-c_0\right)^2}\left[\left(2-c_0\right)\bar{\lambda} - \left(\bar{\lambda}^2+1\right)\cos\varphi_0 + c_0\bar{\lambda}\cos^2\varphi_0\right] \\
s_0 &= \frac{c_0}{2w\bar{\lambda}\left(1-c_0\right)^2}\left\{-4\left[1+\left(w-1\right)w\right]\left(\bar{\lambda}+\bar{\lambda}^3\right)\cos\varphi_0\right. \\
&\quad + 2\left[w\left(c_0-4\right)\bar{\lambda}^2 + \left(1+w^2\right)\left(1+\bar{\lambda}^2\right)^2 - wc\bar{\lambda}^2\cos\left(2\varphi_0\right)\right] \\
&\quad \left.-2\left(w^2-1\right)\left(\bar{\lambda}^4-1\right)\cos\left(2\bar{\theta}\right)\sin^2\varphi_0 + \left(w^2-1\right)\left(\bar{\lambda}^4-1\right)\sin\left(2\bar{\theta}\right)\sin\left(2\varphi_0\right)\right\}.
\end{aligned} \tag{G.5}$$

(It is noted here that in obtaining the above expressions we used the identities $(G.7)_1$, $(G.9)_1$, and $(G.10)_2$, obtained later.)

To obtain the zeroth order relative rotation $\varphi_0$, we have to make use of the expansions of the secant condition (7.36) and the evolution equation (7.41). Thus, letting

$$\begin{aligned}
&k_4 = k_4^0 + k_4^1\delta + k_4^2\delta^2 + k_4^3\delta^3 + \cdots \\
&k_4^0 = \frac{-c_0}{1-c_0}\left[4 - 2\left(\bar{\lambda}_1 + \bar{\lambda}_1^{-1}\right)\cos\varphi_0\right] \quad \text{and} \quad k_4^1 = \frac{-c_0}{1-c_0}\left[2\varphi_1\left(\bar{\lambda}_1 + \bar{\lambda}_1^{-1}\right)\sin\varphi_0\right], \ \cdots,
\end{aligned} \tag{G.6}$$

the secant equation of order of $\delta^{-3}$ can be shown to result in

$$\bar{\lambda}_1\bar{\lambda}_2 = 1 \quad \text{and} \quad \bar{\lambda}_2 x_0 + \bar{\lambda}_1 y_0 + k_4^0/2 = 0. \tag{G.7}$$

Thus, to the $\delta^{-2}$ order, we obtain

$$\bar{\lambda}_2 x_1 + \bar{\lambda}_1 y_1 + k_4^1/2 = 0, \tag{G.8}$$

while to the $\delta^{-1}$ order, we obtain

$$\begin{aligned} &b_{-1} = \bar{\lambda}_1^4 a_{-1} \\ &a_{-1}\bar{\lambda}_1^3 y_0 + a_{-1}\bar{\lambda}_1 x_0 + \left(\bar{\lambda}_1^2 a_{-1} - d_{-1}\right) = 0 \\ &\bar{\lambda}_2 x_2 + \bar{\lambda}_1 y_2 + k_4^2/2 = d_{-1} - \bar{\lambda}_1^2 a_{-1}. \end{aligned} \tag{G.9}$$

Finally, to the order $\delta$, we obtain

$$\begin{aligned} &e_0 = 2\hat{g}' \\ &b_0 = \lambda_1^4 a_0 + \frac{2\left(1-\bar{\lambda}_1^4\right)}{d_{-1} - \bar{\lambda}_1^2 a_{-1}}\left[d_{-1}\hat{g}' + a_{-1}\left(\hat{g}' - 2\bar{g}\right)\right] \end{aligned}$$

$$\begin{aligned} 0 = &-a_{-1}^2\bar{\lambda}_1^4\left(\bar{\lambda}_1^2 a_{-1} - d_{-1}\right)\left(\bar{\lambda}_2 x_1 + \bar{\lambda}_1 y_1\right) + d_{-1}^2\bar{\lambda}_1^2\left(a_0 - 2\hat{g}'\right) \\ &- a_{-1}d_{-1}\left[\left(2\hat{g}' - 4\bar{g}\right)\bar{\lambda}_1^4 + \left(d_0 + \mu^{(1)} + a_0\bar{\lambda}_1^2\right)\bar{\lambda}_1^2 - 2\left(\hat{g}' - \bar{g}\right)\right] \\ &+ a_{-1}^2\bar{\lambda}_1\left\{2\left(\hat{g}' - \bar{g}\right)\left[\bar{\lambda}_1^5 + x_0\left(\bar{\lambda}_1^4 - 1\right)\right] + \left(\mu^{(1)} + d_0\right)\bar{\lambda}_1^2\right\} \end{aligned} \tag{G.10}$$

$$\bar{\lambda}_2 x_3 + \bar{\lambda}_1 y_3 + k_4^3/2 = d_0 + \mu^{(1)} - \frac{1}{2\bar{\lambda}_1^2}\left[b_0 + a_0\bar{\lambda}_1^4 - 2\hat{g}'\left(1 + \bar{\lambda}_1^4\right)\right],$$

where $\bar{g} \coloneqq g^{(1)}\left(\bar{I}\right)$ and $\hat{g}'$ denotes the leading (zeroth) order term in the expansion of $g_I^{(1)}\left(\hat{I}^{(1)}\right)$, where $\hat{I}^{(1)} = \hat{\boldsymbol{F}}^{(1)} \cdot \hat{\boldsymbol{F}}^{(1)}$.

The evolution equation to the order $\delta^{-1}$ reads as follows

$$\cos\varphi_0 = \frac{\left(c_0 - 1\right)d_{-1}}{c_0\bar{\lambda}_1\left(1 + \bar{\lambda}_1^2\right)a_{-1}} + \frac{\left(1 + c_0\right)\bar{\lambda}_1}{c_0\left(1 + \bar{\lambda}^2\right)}, \tag{G.11}$$

while to the order $\delta^0$, the expansion of the evolution equation provides and expression for $\varphi_1$ in terms of $\varphi_0$ and other parameters ($c_0$, $w$, $\bar{\lambda}_1$, $\bar{\theta}$, $\hat{g}'$, $\bar{g}$, $a_{-1}$, $a_0$, $d_0$, and the relevant components of the eigenstress $\boldsymbol{M}^{(2)}$).

Equation (G.7)$_2$ is identically satisfied for the values of $x_0$, $y_0$, and $k_4^0$ given by equations (G.4) and (G.6), while equations (G.9)$_3$ and (G.11) can be shown to be exactly identical. In order to obtain the relation between $\varphi_0$ and the relevant com-

ponents of the tensor $\boldsymbol{M}^{(2)}$, we can solve for the compound variable $\bar{\lambda}_2 x_1 + \bar{\lambda}_1 y_1$ from equations (G.8) and $(G.6)_3$, to get

$$\bar{\lambda}_2 x_1 + \bar{\lambda}_1 y_1 = \frac{c_0 \varphi_1}{1 - c_0} \left( \bar{\lambda}_1 + \bar{\lambda}_1^{-1} \right) \sin \varphi_0. \tag{G.12}$$

Substituting the above equation into $(G.10)_3$ and making use of the expression for $\varphi_1$ obtained from the expansion of the evolution equation to the order $\delta^0$, we obtain

$$\bar{\boldsymbol{\tau}}_{12} = \frac{\hat{g}' \left( 1 + \bar{\lambda}_1^2 \right)}{w \bar{\lambda}_1^2 \left( 1 - c_0 \right)} \left[ 2 \bar{\lambda}_1 \left( 1 + w^2 \right) \sin \varphi_0 - \left( \bar{\lambda}_1^2 - 1 \right) \left( w^2 - 1 \right) \sin \left( 2 \varphi_0 - 2 \bar{\theta} \right) \right], \tag{G.13}$$

where the definition

$$\bar{\boldsymbol{\tau}}_{12} := \left( M_{12}^{(2)} - M_{21}^{(2)} \right) \cos \phi_0 + \left( M_{11}^{(2)} + M_{22}^{(2)} \right) \sin \phi_0 \tag{G.14}$$

has been used for conciseness.

In summary, the effective energy of an incompressible matrix reinforced by long rigid fibers, undergoing finite strains in the plane perpendicular to the long axes of the fibers and in the presence of a uniform eigenstress $\boldsymbol{M}^{(2)}$ is obtained as follows

$$\begin{aligned} \hat{W}_* \left( \bar{\boldsymbol{F}} \right) = \hat{W}_* \left( \bar{\lambda}_1, \bar{\theta} \right) = \left( 1 - c_0 \right) g^{(1)} \left( \hat{I}^{(1)} \right) \\ + c_0 \left( M_{11}^{(2)} + M_{22}^{(2)} \right) \cos \phi_0 - c_0 \left( M_{12}^{(2)} - M_{21}^{(2)} \right) \sin \phi_0, \end{aligned} \tag{G.15}$$

where

$$\begin{aligned} \hat{I}^{(1)} = & \frac{c_0 \left( 1 + \bar{\lambda}_1^2 \right)^2 + \left[ 1 + 2 \left( c_0 - 2 \right) c_0 \bar{\lambda}_1^2 + \bar{\lambda}_1^4 \right] w + c_0 \left( 1 + \bar{\lambda}_1^2 \right) w^2}{\left( 1 - c_0 \right)^2 \bar{\lambda}_1^2 w} \\ & - \frac{c_0 \left( \bar{\lambda}_1^4 - 1 \right) \left( w^2 - 1 \right)}{\left( 1 - c_0 \right)^2 \bar{\lambda}_1^2 w} \sin \left( \varphi_0 \right) \sin \left( \varphi_0 - 2 \bar{\theta} \right) - \frac{2 c_0 \left( 1 + \bar{\lambda}_1^2 \right) \left( 1 + w^2 \right)}{\left( 1 - c_0 \right)^2 \bar{\lambda}_1 w} \cos \left( \varphi_0 \right) \end{aligned} \tag{G.16}$$

and $\varphi_0$ satisfies the evolution equation (G.13).

# Bibliography


Aschwanden, M. & Stemmer, A. (2006), 'Polymeric, electrically tunable diffraction grating based on artificial muscles', *Opt. Lett.* **31**, 2610–2612.

Avazmohammadi, R. & Ponte Castañeda, P. (2013), 'Tangent second-order estimates for the large-strain, macroscopic response of particle-reinforced elastomers', *J. of Elasticity* **112**(2), 139–183.

Avazmohammadi, R. & Ponte Castañeda, P. (2014), 'Macroscopic constitutive relations for short-fiber-reinforced elastomers with nematic order: instabilities and post-bifurcation response', *J. Mech. Phys. Solids* **to be submitted**.

Bar-Cohen, Y., ed. (2004), *Electroactive polymer (EAP) actuators as artificial muscles: reality, potential, and challenges*, 2nd edn, SPIE—The International Society for Optical Engineering, Bellingham, WA.

Benveniste, Y. (1992), 'The determination of the elastic and electric fields in a piezoelectric inhomogeneity', *Journal of Applied Physics* **72**, 1086–1095.

Benveniste, Y. & Dvorak, G. J. (1992), 'Uniform fields and universal relations in piezoelectric composites', *Journal of the Mechanics and Physics of Solids* **40**(6), 1295–1312.

Bertoldi, K. & Gei, M. (2011), 'Instabilities in multilayered soft dielectrics', *Journal of the Mechanics and Physics of Solids* **59**(1), 18–42.

Bolzmacher, C., Biggs, J. & Srinivasan, M. (2006), 'Flexible dielectric elastomer actu-

ators for wearable human-machine interfaces', *Proc. SPIE* **6168**, 616804–616804–12.

Borcea, L. & Bruno, O. (2001), 'On the magneto-elastic properties of elastomer-ferromagnet composites', *J. Mech. Phys. Solids* **49**, 2877–2919.

Braides, A. (1985), 'Homogenization of some almost periodic coercive functional', *Rend. Accad. Naz. Sci. XL* **103**, 313–322.

Brochu, P. & Pei, Q. (2010), 'Advances in dielectric elastomers for actuators and artificial muscles', *Macromol. Rapid Commun.* **31**, 10–36.

Bruggeman, D. A. G. (1935), 'Berechnung verschiedener physikalischer Konstanten von heterogenen Substanzen', *Ann. Phys. (Leipzig)* **24**, 636–679.

Brun, M., Lopez-Pamies, O. & Ponte Castañeda, P. (2007), 'Homogenization estimates for fiber-reinforced elastomers with periodic microstructures', *International journal of solids and structures* **44**(18), 5953–5979.

Bustamante, R., Dorfmann, A. & Ogden, R. W. (2009), 'Nonlinear electroelastostatics: a variational framework', *Zeitschrift für angewandte Mathematik und Physik* **60**(1), 154–177.

Carpi, F., Bauer, S. & De Rossi, D. (2010), 'Stretching dielectric elastomer performance', *Science* **330**, 1759–1761.

Carpi, F., De Rossi, D., Kornbluh, R., Pelrine, R. & Sommer-Larsen, P., eds (2008), *Dielectric elastomers as electromechanical transducersmodels and applications of an emerging electroactive polymer technology*, Elsevier, chapter High-performance acrylic and silicone elastomers, pp. 33–42.

Castañeda, P. P. & Suquet, P. (1997), 'Nonlinear Composites', *Advances in Applied Mechanics* **34**, 171–302.

Castaneda, P. P. (1992), 'Bounds and estimates for the properties of nonlinear heterogeneous systems', *Philosophical Transactions of the Royal Society of London. Series A: Physical and Engineering Sciences* **340**(1659), 531–567.

Cheng, Z. & Zhang, Q. (2008), 'Field-activated electroactive polymers', *MRS Bull.* **33**, 183–187.

deBotton, G., Tevet-Deree, L. & Socolsky, E. A. (2007), 'Electroactive Heterogeneous Polymers: Analysis and Applications to Laminated Composites', *Mech. Adv. Mater. Struct.* **14**(1), 13–22.

Dorfmann, A. & Ogden, R. W. (2005), 'Nonlinear electroelasticity', *Acta Mechanica* **174**, 167–183. 10.1007/s00707-004-0202-2.

Dorfmann, A. & Ogden, R. W. (2006), 'Nonlinear electroelastic deformations', *Journal of Elasticity* **82**(2), 99–127.

Dorfmann, A. & Ogden, R. W. (2010*a*), 'Electroelastic waves in a finitely deformed electroactive material', *IMA Journal of Applied Mathematics* **75**(4), 603–636.

Dorfmann, A. & Ogden, R. W. (2010*b*), 'Nonlinear electroelastostatics: Incremental equations and stability', *International Journal of Engineering Science* **48**(1), 1–14.

Dunn, M. L. & Taya, M. (1993), 'An analysis of piezoelectric composite materials containing ellipsoidal inhomogeneities', *Proceedings of the Royal Society of London. Series A: Mathematical and Physical Sciences* **443**(1918), 265–287.

Eringen, A. C. & Maugin, G. A., eds (1990), *Electrodynamics of continua. Volume 1 - Foundations and solid media. Volume 2 - Fluids and complex media*, Vol. 1.

Eshelby, J. D. (1957), 'The Determination of the Elastic Field of an Ellipsoidal Inclusion, and Related Problems', *Proc. R. Soc. Lond. A* **241**, 376–396.

Galipeau, E. & Ponte Castañeda, P. (2013), 'A finite-strain constitutive model for magnetorheological elastomers: Magnetic torques and fiber rotations', *Journal of the Mechanics and Physics of Solids* **61**(4), 1065–1090.

Garnett, J. C. M. (1904), 'Colours in Metal Glasses and in Metallic Films', *Phil. Trans. R. Soc. Lond., Ser. A* **203**, 385–420.

Gent, A. N. (1996), 'A New Constitutive Relation for Rubber', *Rubber Chemistry and Technology* **69**(1), 59–61.

Geymonat, G., Müller, S. & Triantafyllidis, N. (1993), 'Homogenization of nonlinearly elastic materials, microscopic bifurcation and macroscopic loss of rank-one convexity', *Archive for Rational Mechanics and Analysis* **122**(3), 231–290.

Ginder, J. M., Clark, S. M., Schlotter, W. F. & Nichols, M. E. (2002), 'Magnetostrictive phenomena in magnetorheological elastomers', *International Journal of Modern Physics B* **16**, 2412–2418.

Ginder, J. M., Nichols, M. E., Elie, L. D. & Tardiff, J. L. (1999), Magnetorheological elastomers: properties and applications, *in* 'Proc. SPIE1999 Symposium on Smart Structures and Materials', International Society for Optics and Photonics, pp. 131–138.

Guan, X., Dong, X. & Ou, J. (2008), 'Magnetostrictive effect of magnetorheological elastomer', *Journal of Magnetism and magnetic materials* **320**, 158–163.

Hashin, Z. & Shtrikman, S. (1962), 'A Variational Approach to the Theory of the Effective Magnetic Permeability of Multiphase Materials', *J. Appl. Phys.* **33**(10), 3125–3131.

Hashin, Z. & Shtrikman, S. (1963), 'A variational approach to the theory of the elastic behaviour of multiphase materials', *J. Mech. Phys. Solids* **11**(2), 127–140.

Hill, R. (1957), 'On uniqueness and stability in the theory of finite elastic strain', *Journal of the Mechanics and Physics of Solids* **5**(4), 229–241.

Hill, R. (1962), 'Acceleration waves in solids', *Journal of the Mechanics and Physics of Solids* **10**(1), 1–16.

Hill, R. (1967), 'Eigenmodal deformations in elastic/plastic continua', *Journal of the Mechanics and Physics of Solids* **15**(6), 371–386.

Hill, R. (1972), 'On Constitutive Macro-Variables for Heterogeneous Solids at Finite Strain', *Proceedings of the Royal Society of London. A. Mathematical and Physical Sciences* **326**(1565), 131–147.

Hill, R. (1979), 'On the theory of plane strain in finitely deformed compressible materials', *Mathematical Proceedings of the Cambridge Philosophical Society* **86**, 161–178.

Hill, R. & Hutchinson, J. W. (1975), 'Bifurcation phenomena in the plane tension test', *Journal of the Mechanics and Physics of Solids* **23**(45), 239–264.

Hoger, A. & Carlson, D. E. (1984), 'On the derivative of the square root of a tensor and Guo's rate theorems', *Journal of Elasticity* **14**(3), 329–336.

Huang, C. & Zhang, Q. (2004), 'Enhanced Dielectric and Electromechanical Responses in High Dielectric Constant All-Polymer Percolative Composites', *Adv. Funct. Mater.* **14**, 501–506.

Huang, C., Zhang, Q. M., deBotton, G. & Bhattacharya, K. (2004), 'All-organic dielectric-percolative three-component composite materials with high electromechanical response', *Appl. Phys. Lett.* **84**, 4391–4393.

Huang, J. H., Chiu, Y.-H. & Liu, H.-K. (1998), 'Magneto-electro-elastic eshelby tensors for a piezoelectric-piezomagnetic composite reinforced by ellipsoidal inclusions', *Journal of Applied Physics* **83**, 5364–5370.

Huang, J., Li, T., Foo, C. C., Zhu, J., Clarke, D. R. & Suo, Z. (2012), 'Giant, voltage-actuated deformation of a dielectric elastomer under dead load', *Appl. Phys. Lett.* **100**, 041911.

Huang, J., Lu, T., Zhu, J., Clarke, D. R. & Suo, Z. (2012), 'Large, uni-directional actuation in dielectric elastomers achieved by fiber stiffening', *Applied Physics Letters* **100**(21), 211901+.

Hutter, K., Ursescu, A. & van de Ven, A. A. F. (2006), *Electromagnetic Field Matter Interactions in Thermoelastic Solids and Viscous Fluids*, Springer.

Kachanov, M., Karapetian, E. & Sevostianov, I. (2002), *Multisclae deformation and fracture in materials and structures*, Springer, chapter Elastic space containing a rigid ellipsoidal inclusion subjected to translation and rotation, pp. 123–143.

Kailasam, M. & Ponte Castañeda, P. (1998), 'A general constitutive theory for linear and nonlinear particulate media with microstructure evolution', *J. Mech. Phys. Solids* **46**(3), 427–465.

Keplinger, C., Kaltenbrunner, M., Arnold, N. & Bauer, S. (2010), 'Röntgen's electrode-free elastomer actuators without electromechanical pull-in instability', *Proc. Natl. Acad. Sci.* **107**, 4505–4510.

Kovetz, A. (1990), *The Principles of Electromagnetic Theory*, Cambridge University Press.

Kovetz, A. (2000), *Electromagnetic Theory with 225 Solved Problems*, Oxford University Press, USA.

Krakovsky, I., Romijn, T. & de Boer, A. P. (1999), 'A few remarks on the electrostriction of elastomers', *J. Appl. Phys.* **85**(1), 628–629.

Landau, L. D., Lifshitz, E. M. & Pitaevskii, L. P. (1984), *Elecrodynamics of Continuous Media*, Pergamon Press.

Lee, H. Y., Peng, Y. & Shkel, Y. M. (2005), 'Strain-dielectric response of dielectrics as foundation for electrostriction stresses', *J. Appl. Phys.* **98**(7), 074104 –074104–9.

Levin, V. M. (1967), 'Thermal expansion coefficients of heterogeneous materials', *Mekh. Tverd. Tela.* **2**, 83–94.

Li, J. Y., Huang, C. & Zhang, Q. (2004), 'Enhanced electromechanical properties in all-polymer percolative composites', *Appl. Phys. Lett.* **84**, 3124–3126.

Li, J. Y. & Rao, N. (2004), 'Micromechanics of ferroelectric polymer-based electrostrictive composites', *J. Mech. Phys. Solids* **52**, 591–615.

Liu, L. P., James, R. D. & Leo, P. H. (2006), 'Magnetostrictive composites in the dilute limit', *Journal of the Mechanics and Physics of Solids* **54**(5), 951–974.

Lopez-Pamies, O. & Ponte Castañeda, P. (2006*a*), 'On the overall behavior, microstructure evolution, and macroscopic stability in reinforced rubbers at large deformations: II–Application to cylindrical fibers', *Journal of the Mechanics and Physics of Solids* **54**(4), 831–863.

Lopez-Pamies, O. & Ponte Castañeda, P. (2006*b*), 'On the overall behavior, microstructure evolution, and macroscopic stability in reinforced rubbers at large deformations: Itheory', *Journal of the Mechanics and Physics of Solids* **54**(4), 807–830.

Love, A. E. H. (1944), *The Mathematical Theory of Elasticity*, New York: Dover Publications.

Lu, T., Huang, J., Jordi, C., Kovacs, G., Huang, R., Clarke, D. R. & Suo, Z. (2012), 'Dielectric elastomer actuators under equal-biaxial forces, uniaxial forces, and uniaxial constraint of stiff fibers', *Soft Matter* **8**(22), 6167–6173.

Marcellini, P. (1978), 'Periodic solutions and homogenization of non linear variational problems', *Annali di matematica pura ed applicata* **117**(1), 139–152.

Maxwell, J. C. (1873), *A Treatise on Electricity and Magnetism*, Clarendon Press.

Mcmeeking, R. M. & Landis, C. M. (2005), 'Electrostatic Forces and Stored Energy for Deformable Dielectric Materials', *J. Appl. Mech.* **72**, 581–590.

Merlini, T. (1997), 'A variational formulation for finite elasticity with independent rotation and biot-axial fields', *Computational mechanics* **19**(3), 153–168.

Michel, J. C., Lopez-Pamies, O., Ponte Castañeda, P. & Triantafyllidis, N. (2010*a*), 'Microscopic and macroscopic instabilities in finitely strained fiber-reinforced elastomers', *Journal of the Mechanics and Physics of Solids* **58**(11), 1776–1803.

Michel, J.-C., Lopez-Pamies, O., Ponte Castañeda, P. & Triantafyllidis, N. (2010*b*), 'Microscopic and macroscopic instabilities in finitely strained fiber-reinforced elastomers', *Journal of the Mechanics and Physics of Solids* **58**(11), 1776–1803.

Milton, G. W. (2001), *The theory of composites*, Cambridge University Press.

Müller, S. (1987), 'Homogenization of nonconvex integral functionals and cellular elastic materials', *Archive for Rational Mechanics and Analysis* **99**(3), 189–212.

Nemat-Nasser, S. & Hori, M. (1993), *Micromechanics: Overall Properties of Heterogeneous Materials*, North-Holland.

Nemat-Nasser, S., Iwakuma, T. & Hejazi, M. (1982), 'On composites with periodic structure', *Mechanics of Materials* **1**(3), 239–267.

Ogden, R. W. (1985), 'Local and global bifurcation phenomena in plane-strain finite elasticity', *International Journal of Solids and Structures* **21**(2), 121–132.

Ogden, R. W. (1997), *Non-linear elastic deformations*, Courier Dover Publications.

Ozsecen, M. Y., Sivak, M. & Mavroidis, C. (2010), 'Haptic interfaces using dielectric electroactive polymers', *Proc. SPIE* **7647**, 764737.

Park, I.-S., Jung, K., Kim, D., Kim, S.-M. & Kim, K. J. (2008), 'Physical principles of ionic polymer–metal composites as electroactive actuators and sensors', *MRS Bull.* **33**, 190–195.

Pelrine, R. E., Kornbluh, R. D. & Joseph, J. P. (1998), 'Electrostriction of polymer dielectrics with compliant electrodes as a means of actuation', *Sens. Actuators, A: Phys.* **64**(1), 77–85.

Ponte Castañeda, P. (2001), 'Second-order theory for nonlinear dielectric composites incorporating field fluctuations', *Phys. Rev. B* **64**, 214205.

Ponte Castañeda, P., deBotton, G. & Li, G. (1992), 'Effective properties of nonlinear inhomogeneous dielectrics', *Phys. Rev. B* **46**, 4387–4394.

Ponte Castañeda, P. & Galipeau, E. (2011), 'Homogenization-based constitutive models for magnetorheological elastomers at finite strain', *J. Mech. Phys. Solids* **59**(2), 194 – 215.

Ponte Castañeda, P. & Siboni, M. H. (2012), 'A finite-strain constitutive theory for electro-active polymer composites via homogenization', *Int. J. Non-Linear Mech.* **47**(2), 293–306.

Ponte Castañeda, P. & Tiberio, E. (2000), 'A second-order homogenization method in finite elasticity and applications to black-filled elastomers', *Journal of the Mechanics and Physics of Solids* **48**(6), 1389–1411.

Ponte Castañeda, P. & Willis, J. R. (1995), 'The effect of spatial distribution on the effective behavior of composite materials and cracked media', *J. Mech. Phys. Solids* **43**(12), 1919–1951.

Racherla, V., Lopez-Pamies, O. & Ponte Castañeda, P. (2010), 'Macroscopic response and stability in lamellar nanostructured elastomers with "oriented" and "unoriented" polydomain microstructures', *Mechanics of Materials* **42**(4), 451–468.

Rao, N. & Li, J. Y. (2004), 'The electrostriction of P(VDF-TrFE) copolymers embedded with textured dielectric particles', *Int. J. Solids Struct.* **41**, 2995–3011.

Reitz, J. R. & Milford, F. J. (1962), *Foundations of Electromagnetism Theory*, Reading, MA: Addison-Wesley Publishing Company.

Ren, K., Liu, Y., Hofmann, H., Zhang, Q. M. & Blottman, J. (2007), 'An active energy harvesting scheme with an electroactive polymer', *Appl. Phys. Lett.* **91**, 132910.

Rice, J. R. (1976), *The localization of plastic deformation*, Division of Engineering, Brown University.

Rudykh, S. & deBotton, G. (2011), 'Stability of anisotropic electroactive polymers with application to layered media', *Zeitschrift für Angewandte Mathematik und Physik (ZAMP)* pp. 1–12.

Sarban, R., Oubaek, J. & Jones, R. W. (2009), 'Closed-loop control of a core free rolled EAP actuator', *Proc. SPIE* **7287**, 72870G–1+.

Shkel, Y. M. & Klingenberg, D. J. (1996), 'Material parameters for electrostriction', *J. Appl. Phys.* **80**(8), 4566–4572.

Shkel, Y. M. & Klingenberg, D. J. (1998), 'Electrostriction of polarizable materials: Comparison of models with experimental data', *J. Appl. Phys.* **83**(12), 7834 –7843.

Siboni, M. H. & Ponte Castañeda, P. (2012), 'A magnetically anisotropic, ellipsoidal inclusion subjected to a non-aligned magnetic field in an elastic medium', *C. R. Mécanique* **340**(4–5), 205 – 218.

Siboni, M. H. & Ponte Castañeda, P. (2013), 'Dielectric elastomer composites: small-deformation theory and applications', *Philosophical Magazine* **93**(21), 2769–2801.

Siboni, M. H. & Ponte Castañeda, P. (2014), 'Fiber-constrained, dielectric-elastomer composites: finite-strain response and stability analysis', *Journal of the Mechanics and Physics of Solids* .

Stark, K. & Garton, C. (1955), 'Electric Strength of Irradiated Polythene', *Nature* **176**, 1225–1226.

Sundar, V. & Newnham, R. E. (1992), 'Electrostriction and polarization', *Ferroelectrics* **135**(1), 431–446.

Suo, Z., Zhao, X. & Greene, W. (2008), 'A nonlinear field theory of deformable dielectrics', *Journal of the Mechanics and Physics of Solids* **56**(2), 467–486.

Tian, L., Tevet-Deree, L., deBotton, G. & Bhattacharya, K. (2012), 'Dielectric elastomer composites', *J. Mech. Phys. Solids* **60**(1), 181–198.

Toupin, R. A. (1956), 'The Elastic Dielectric', *J. Ration. Mech. Analysis* **5**, 849–915.

Triantafyllidis, N. & Maker, B. N. (1985), 'On the comparison between microscopic and macroscopic instability mechanisms in a class of fiber-reinforced composites', *ASME Journal of Applied Mechanics* **52**(4), 794–800.

Truesdell, C. & Noll, W. (2004), *The Non-Linear Field Theories of Mechanics*, The non-linear field theories of mechanics, 3rd edn, Springer.

Walpole, L. (1981), 'Elastic behavior of composite materials: Theoretical foundations', *Adv. Appl. Mech.* **21**, 169–242.

Walpole, L. J. (1991), 'A rotated rigid ellipsoidal inclusion in an elastic medium', *Proceedings of the Royal Society of London. Series A: Mathematical and Physical Sciences* **433**(1887), 179–207.

Willis, J. R. (1977), 'Bounds and self-consistent estimates for the overall properties of anisotropic composites', *Journal of the Mechanics and Physics of Solids* **25**(3), 185–202.

Willis, J. R. (1981), 'Variational and related methods for the overall properties of composites', *Advances in Applied Mechanics,* **21**, 1–78.

Wissler, M. & Mazza, E. (2007), 'Electromechanical coupling in dielectric elastomer actuators', *Sensors and Actuators A: Physical* **138**(2), 384–393.

Yin, H. M., Sun, L. Z. & Chen, J. S. (2006), 'Magneto-elastic modeling of composites containing chain-structured magnetostrictive particles', *Journal of the Mechanics and Physics of Solids* **54**(5), 975–1003.

Zhao, X., Hong, W. & Suo, Z. (2007), 'Electromechanical hysteresis and coexistent states in dielectric elastomers', *Phys. Rev. B* **76**, 134113.

Zhao, X. & Suo, Z. (2007), 'Method to analyze electromechanical stability of dielectric elastomers', *Appl. Phys. Lett.* **91**, 061921.

Zhao, X. & Suo, Z. (2008), 'Electrostriction in elastic dielectrics undergoing large deformation', *J. Appl. Phys.* **104**(12), 123530.

Zhao, X. & Suo, Z. (2010), 'Theory of Dielectric Elastomers Capable of Giant Deformation of Actuation', *Phys. Rev. Lett.* **104**, 178302.

Zhenyi, M., Scheinbeim, J. I., Lee, J. W. & Newman, B. A. (1994), 'High field electrostrictive response of polymers', *J. Polym. Sci., Polym. Phys.* **32**(16), 2721–2731.

Zhou, J., Hong, W., Zhao, X., Zhang, Z. & Suo, Z. (2008), 'Propagation of instability in dielectric elastomers', *International Journal of Solids and Structures* **45**(13), 3739–3750.